Atomic-resolution *In Situ* and *Operando* Visualization of Oxygen Transfer Reactions over CeO_2-supported Pt Catalysts

by

Joshua Lawrence Vincent

A Dissertation Presented in Partial Fulfillment
of the Requirements for the Degree
Doctor of Philosophy

Approved June 2021 by the
Graduate Supervisory Committee:

Peter A. Crozier, Chair
Jingyue Liu
Christopher Muhich
Brent Nannenga
Arunima Singh

ARIZONA STATE UNIVERSITY

August 2021

ABSTRACT

Oxygen transfer reactions are central to many catalytic processes, including those underlying automotive exhaust emissions control and clean energy conversion. The catalysts used in these applications typically consist of metal nanoparticles dispersed on reducible oxides (e.g., Pt/CeO_2), since reducible oxides can transfer their lattice oxygen to reactive adsorbates at the metal-support interface. There are many outstanding questions regarding the atomic and nanoscale spatial variation of the Pt/CeO_2 interface, Pt metal particle, and adjacent CeO_2 oxide surface during catalysis. To this end, a range of techniques centered around aberration-corrected environmental transmission electron microscopy (ETEM) were developed and employed to visualize and characterize the atomic-scale structural behavior of CeO_2-supported Pt catalysts under reaction conditions (*in situ*) and/or during catalysis (*operando*).

A model of the *operando* ETEM reactor was developed to simulate the gas and temperature profiles during conditions of catalysis. Most importantly, the model provides a tool for relating the reactant conversion measured with spectroscopy to the reaction rate of the catalyst that is imaged on the TEM grid. As a result, this work has produced a truly *operando* TEM methodology, since the structure observed during an experiment can be directly linked to quantitative chemical kinetics of the same catalyst.

This *operando* ETEM approach was leveraged to investigate structure-activity relationships for CO oxidation over Pt/CeO_2 catalysts. Correlating atomic-level imaging with catalytic turnover frequency reveals a direct relationship between activity and dynamic structural behavior that (a) destabilizes the supported Pt particle, (b) marks an enhanced rate of oxygen vacancy creation and annihilation, and (c) leads to increased strain and reduction in the surface of the CeO_2 support.

To further investigate the structural meta-stability (i.e., fluxionality) of 1 – 2 nm CeO_2-supported Pt nanoparticles, time-resolved *in situ* AC-ETEM was employed to visualize the catalyst's dynamical behavior with high spatiotemporal resolution. Observations are made under conditions relevant to the CO oxidation and water-gas shift (WGS) reactions. Finally, deep learning-based convolutional neural networks were leveraged to develop novel denoising techniques for ultra-low signal-to-noise images of catalytic nanoparticles.

To child-like curiosity.

"*The light microscope opened the first gate to microcosm. The electron microscope opened the second. What will we find opening the third?*"

– Ernst Ruska

ACKNOWLEDGEMENTS

First, I would like to express my gratitude to my advisor, Prof. Peter Crozier, for seeing potential in me and for inviting me to complete this thesis on *in situ* and *operando* TEM. It was my wildest dream as I entered graduate school and remains so as I leave it. Your expertise and creativity have been essential to completing this work. Additionally, your professional ethic has helped me to develop into the scientist I aim to be, and for all of this, I am deeply grateful.

I would like to express my sincere thanks to my committee, namely Professors Liu, Muhich, Nannenga, and Singh, for warmly accepting my invitations to mentor me on this thesis and for offering support and insight when it was needed.

There are many Crozier group members, too numerous to name here, who have made my time at ASU enjoyable and from whom I have learned much. Their support, guidance, and friendship, (as well as their creative feedback during the 3rd hour of Friday afternoon group meetings!), have all been instrumental to me in pursuing this thesis. To those still here with me, I look forward to completing this program with you, and to those future group members reading this at a later time – I wish you the best of luck.

I would like to thank the undergraduate students I was fortunate to mentor, namely Jarod Vance and Claire Block, who contributed substantially to work in this thesis.

I would also like to acknowledge those who mentored me while I completed my degree in Chemical Engineering at the University of Maryland, notably: Dr. Nicole Mogul and Prof. David Tomblin, who taught me how to think; Prof. Amy Karlsson, who always gave great career advice; and especially Dr. William Gibbons, who first introduced me to catalysis research and then showed me Peter's, starting all of this in motion.

During this thesis I was able to collaborate with Dr. Renu Sharma, who I gratefully acknowledge for hosting me – *twice*, nonetheless – at the National Institute of Standards

and Technology. The research I conducted there, as well as her wisdom and her guidance, added much to this this thesis. I would also like to thank Dr. David Yang and Dr. Canhui Wang from her group, who both assisted with the microscopy there and were fun to work with. In addition, I would like to acknowledge a few of the other outstanding scientists I have had the pleasure of collaborating with on this work, including Dr. Yuanyuan Li, Prof. Anatoly Frenkel, and Prof. Ralph Nuzzo; Prof. Carlos Fernandez-Granda, Prof. David Matteson, and their students, Sreyas Mohan and Binh Tang; Dr. Ben Miller, Jayse Langdon, and Dr. Ramon Manzorro; and finally, Dr. Karl Weiss, Dr. Fred Pena, Dr. David Wright, Dr. Dewight Williams, Dr. Shize Yang, and Dr. Shery Chang.

I would like to express my deep gratitude to my parents, Amy and Chris, and to my brother, Jake, for their unwavering support. I would also like to thank my grandmother, Carolyn Remley, as well, for gifting me my late grandfather's Jeep when I didn't have a car and for being overall the best person to talk with after a long week. Most importantly, I thank Rue, the love of my life, for the innumerable little ways you've supported me on this journey and for being my best friend.

This would work not have been possible without generous financial support from many different agencies. I gratefully acknowledge the Dean's Fellowship I received from ASU, as well as the NSF which enabled this research on *operando* TEM and its historical development (CBET–1604971). I am also thankful to the societies that supported my travel to share this work with the community, including the Microscopy Society of America, the International Federation of Societies for Microscopy, the Microanalysis Society, and the North American Catalysis Society, as well as the ASU Graduate College, and the ASU Graduate and Professional Student Association. Finally, I acknowledge the John M. Cowley Center, the Eyring Materials Center, and ASU High Performance Computing for access to characterization equipment and supercomputing resources.

TABLE OF CONTENTS

Page

LIST OF TABLES

LIST OF FIGURES

1. Introduction

1.1. Background and motivation

1.1.1. Motivation and fundamentals of heterogeneous catalysis

Heterogeneous catalysis is essential to the functioning and well-being of society. Catalysts are reactive materials that mediate chemical transformation pathways. They accelerate the rate of useful chemical reactions and can facilitate the selective generation of desirable products by decelerating the rate of others. Much of modern society relies on catalyzed processes, particularly those utilized in the production of fuels, fine chemicals, and value-added products, as much as 90% of which are generated from catalysts (Toulhoat, 2010; Grand View Research, 2019). Considering the overall importance of heterogeneous catalysis, a great deal of scientific effort has been directed at understanding the structure-function relationships that regulate activity and selectivity for catalysts of interest (Coq & Figueras, 1998).

Catalysts are also vital to environmental remediation and to clean energy conversion. Perhaps the most widely recognizable application of catalysts is the automotive catalytic converter, implemented on nearly every car in the US for exhaust emission control. The converter consists of a complex formulation of multiple catalysts that work together in order to minimize the emission of unburnt fuel, carbon monoxide, and oxidized nitrogen. The realization of the catalytic converter is considered one of the greatest environmental successes of the 20th century (Heck & Farrauto, 2001; Gandhi et al., 2003). Ongoing efforts aim at over-coming low temperature kinetic barriers that result in cold-start emissions, which now contribute the most overall to the total pollution emitted during a typical trip (Weilenmann et al., 2009; Roberts et al., 2014; Faria et al., 2018). Aside from such established technologies, catalysts play an indispensable role in

newly emerging clean energy applications, which include, for example, low-temperature solid oxide fuel cells (Stambouli & Traversa, 2002; da Silva & de Souza, 2017), electrolyzers (Paidar et al., 2016; Schmidt et al., 2017), and photocatalytic water splitters (Fajrina & Tahir, 2019; Wang et al., 2019). Notwithstanding ongoing political obstacles, the development of catalysts with suitable activity, stability, selectivity, and environmental availability remains one of the foremost challenges in the utilization of renewable energy sources and thus in the achievement of a sustainable future (Friend & Xu, 2017; Rodríguez-Padrón et al., 2019).

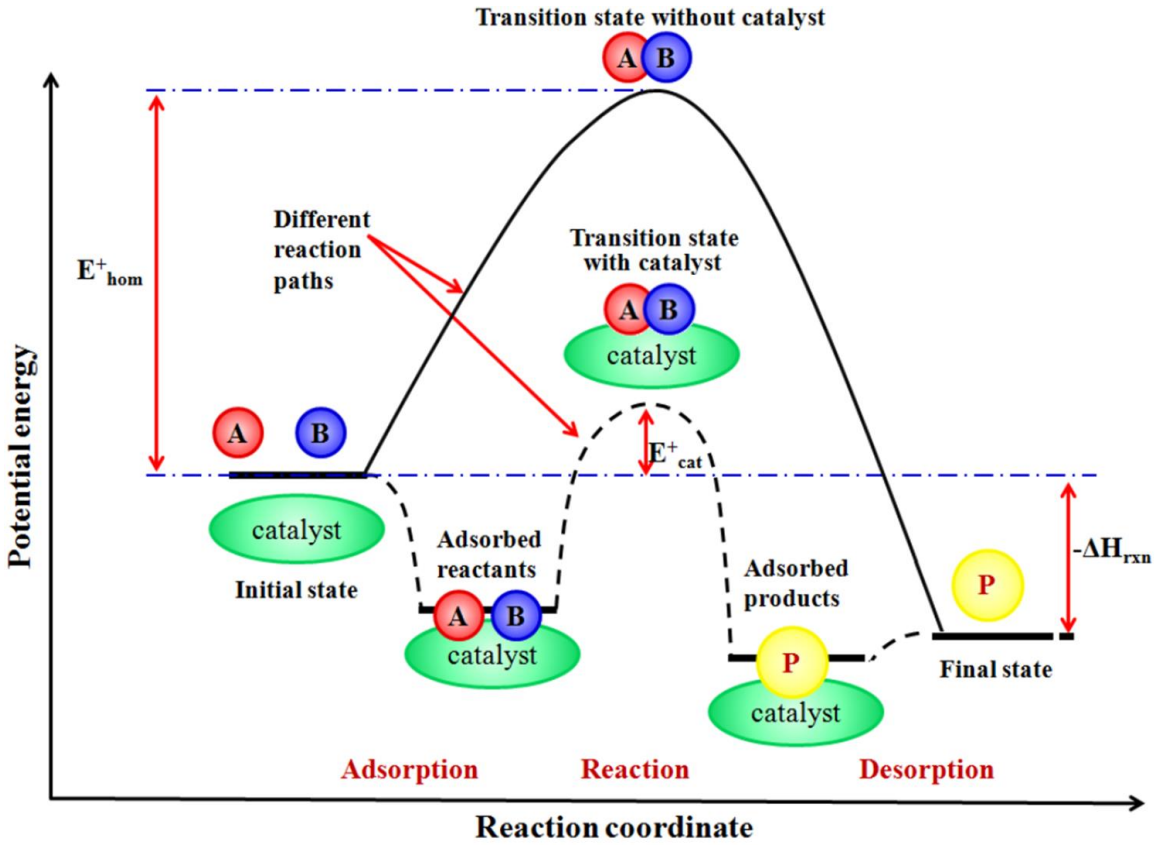

Figure 1.1. Schematic of potential energy diagram for the general reaction A + B → P without a catalyst (solid line) and in the presence of a catalyst (dashed line) showing that (i) the catalyst provides an alternative reaction pathway with a lower activation energy and (ii) this pathway involves the reaction of adsorbed complexes on the catalyst surface. Reprinted with permission from (Hussein, 2012).

To improve the performance of catalysts, a fundamental understanding must be attained as to how a given catalyst regulates the kinetics of a specific chemical reaction of interest. Comprehensive texts on the history and science of catalysis have been written by Ertl et al. (Ertl et al., 1997), Somorjai and Li (Somorjai & Li, 2010), and Nørskov et al. (Nørskov et al., 2014), to which the reader is referred for details beyond the brief overview about to be given on the general concepts. The general principle of catalysis is that the catalyst provides an alternative reaction pathway that enables the transformation of reactants into products to proceed at a faster rate. This kinetic enhancement originates in the interaction between the reactants and the catalyst surface. **Figure 1.1** illustrates a potential energy diagram for a general reaction A + B → P without a catalyst (solid line) and in the presence of a catalyst (dashed line) (Hussein, 2012). As the potential energy of the final state involving the product species P is lower than the potential energy of the initial state involving the individual reactant species A and B, this particular reaction is seen to be exothermic with a negative enthalpy of reaction ($-\Delta H_{rxn}$). For the sake of simplicity, consider that A, B, and P are gaseous molecules. In the absence of a catalyst (solid line), the generation of P occurs when reactants A and B collide with at least a minimum energy and an orientation that are both sufficient to facilitate the breaking of the bonds that define A and B and then the formation of the bonds that define P. The minimum energy required to accommodate this chemical transformation is known as the activation energy (E^{+}_{hom} in **Figure 1.1**). Additionally, the short-lived, activated molecular complex formed at the local potential energy maximum is known as the transition state.

In the presence of a catalyst (dashed line), the reaction proceeds at a faster rate because a different transition state can be reached that has a lower activation energy (E^{+}_{cat} in **Figure 1.1**). The reaction now takes place between adsorbed species on the catalyst surface. The adsorption of the reactants onto the catalyst surface is typically exothermic,

and in many cases it can itself involve a chemical reaction wherein pre-existing molecular bonds are broken and new bonds between the adsorbate and the surface are formed. This chemical adsorption, or chemisorption for short, often results in the formation of reaction intermediates that diffuse on the surface of the catalyst before transforming into secondary reaction intermediates or into the final product itself (Ertl et al., 1997; Nørskov et al., 2014). Finally, the adsorbed product P desorbs back into the gas phase. Note that this final state is energetically equivalent both with and without the catalyst, indicating that the overall thermodynamics of the reaction remain unchanged. In general, each step of the catalytic reaction (*i.e.,* adsorption, intermediate formation, diffusion, product formation, desorption) can be characterized with an activation energy barrier. The step with the highest activation energy relative to the initial state of the system often determines the overall rate of the reaction and is therefore called the rate-limiting step.

Since the catalytic reaction occurs on the surface of the catalytic material, technologically-relevant catalysts are often comprised of nanoparticles that offer large surface-to-volume ratios (Bell, 2003). A large degree of atomic-level structural heterogeneity can be present on nanoparticle surfaces, including, e.g., the presence of different exposed surface facets, surface atomic steps, close-packed terraces, adatoms, corner sites, vacancies, etc. (Ertl et al., 1997; Nørskov et al., 2014). Additionally, as will be discussed in Section 1.3, the structure of the catalyst is not static, but rather meta-stable, influenced by the presence of adsorbates and the local temperature, among other factors, and subject to substantial change (Somorjai, 1991; Ertl, 2001; Zhang et al., 2020). The overall macroscopic properties of the catalyst can thus be understood as a statistical average over the structural ensemble (Sun & Sautet, 2018; Cheula et al., 2020).

Reactant gases and/or intermediates interacting with the diverse population of available surface structures will give rise to multiple potential reaction pathways that each

exhibit varying degrees of activity. It is generally accepted that there exists a specific structural configuration that is present (if only momentarily) on the surface of working catalyst where the activation energy for the rate-limiting step of the reaction is lowest. This site is called the *active site*, and it may only account for a slim fraction of the overall sites available on the catalyst surface. Consider, for example, the synthesis of ammonia (N_2 + $3H_2$ → $2NH_3$) over a ruthenium catalyst. Nørskov and co-workers have calculated the potential energy diagram (**Figure 1.2a**) for the reaction on both a close-packed (100) Ru surface (dashed line, denoted *terrace*) and a (100)/(101) Ru step-edge (solid line, denoted *step*) (Honkala et al., 2005). In both cases, the dissociation of N_2 is the rate-limiting step (Logadóttir & Nørskov, 2003). On the terrace site, N_2 dissociation presents a large activation energy barrier of roughly 2 eV. On the step site, however, N_2 dissociation can proceed through a transition state with a much lower activation energy of roughly 1 eV.

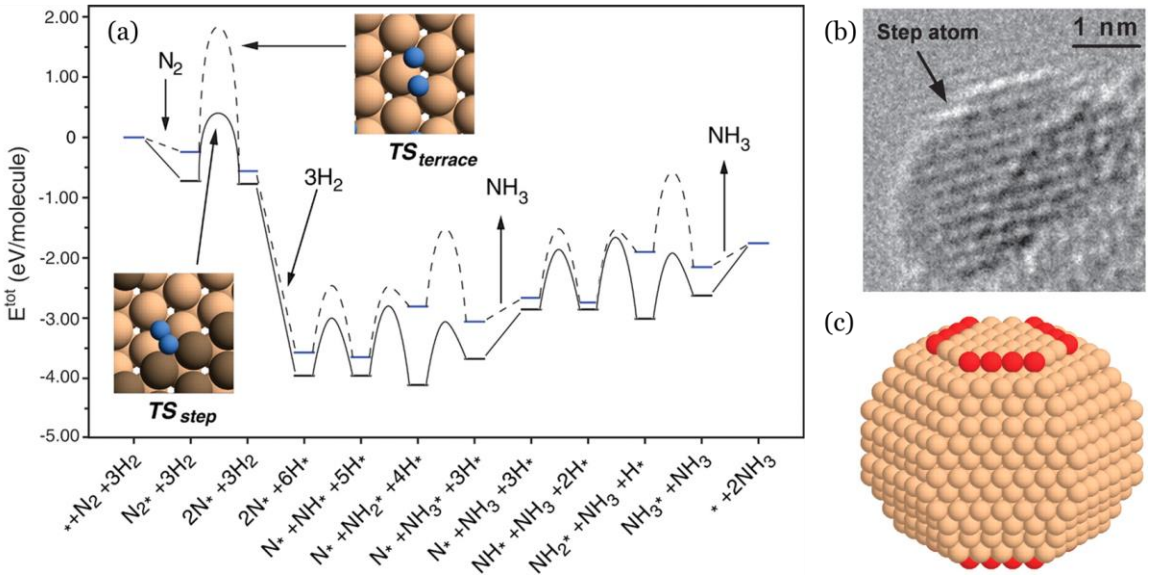

Figure 1.2. (a) Potential energy diagram for NH_3 synthesis over close-packed (dashed line) and stepped (solid line) Ru surfaces. **(b)** TEM image of a $MgAl_2O_4$-supported Ru nanoparticle with arrowed step-edge site visible. **(c)** Model of ~3 nm Ru nanoparticle with active (100)/(101) step-edge sites colored in red. Figures adapted from (Honkala et al., 2005). Reprinted with permission from AAAS.

While the difference in activation energy is only about 1 eV, the dissociation of N_2 on the step-edge site proceeds at a rate that is orders of magnitude faster than that of the terrace site. All else being equal, and assuming a simple Arrhenius dependence of the rate on the activation energy (i.e., $r \propto e^{-\frac{E_a}{kT}}$), at a catalytically-relevant temperature of 700 K, the rate of dissociation on the step is about *6,500 times faster* than that of the terrace site. Such a tremendous difference in rate implies that almost all of the N_2 dissociation that has taken place during the reaction has occurred at the active step-edge sites – even though these sites may be few in number and constitute only a minute portion of the entire Ru catalyst surface. A high-resolution transmission electron microscopy (HRTEM) image of the $MgAl_2O_4$-supported Ru nanoparticle catalyst is shown in **Figure 1.2b** (Honkala et al., 2005). Crystal lattice fringes are visible in the Ru nanoparticle and at the particle surface a step-like feature of contrast is visible, as arrowed. Energetics calculations can be employed to construct an atomic-level structural model of the Ru nanoparticle, which is shown for a particle ~3 nm in size in **Figure 1.2c** (Honkala et al., 2005). The active (100)/(101) step-edge sites are shaded red in the model. Note that these sites account for ~0.5% of the total present on the surface (about 24 out of 500). However, due to the much lower activation energy barrier available for the rate-limiting step of the reaction, these minority *active sites* virtually control the overall activity of the catalytic material.

In a few rare cases (e.g., NH_3 synthesis over Ru nanoparticle catalysts), decades of basic research have produced detailed insight as to how the atomic-level structure of the catalyst surface regulates the kinetics of the chemical reaction of interest. In the vast majority of cases, such knowledge remains unknown, and the general strategy towards improved catalytic performance involves large-scale materials screening experiments, which are time-consuming, expensive, and wasteful. Rationally engineering catalysts with the optimal properties for specific applications as of yet remains mostly out of reach

(Prieto & Schüth, 2015; Sharapa et al., 2019). This is largely due to a lack of information about the structures present on catalyst surfaces *under reaction conditions* and a similar lack of clarity about how such structures influence the catalyst's properties, e.g., their activity and/or stability.

Gaining such knowledge is considerably challenging. Catalytically significant surface structures are atomic-scale in size and are known to emerge and transform during catalysis, requiring characterization techniques that can provide information from controlled environments, i.e., under reaction conditions and/or during catalysis (*in situ*) or during a simultaneous quantitative measurement of the catalytic reaction rate (*operando*) (Belkacem et al., 2016). Aberration-corrected *in situ* and *operando* environmental TEM (ETEM) is thus far the only experimental technique capable of providing localized atomic-level information from nanoparticle catalysts under reaction conditions and during catalysis (Chee et al., 2021). An aspirational goal for ETEM research would be to establish a direct link between the observed structure and the functionality (e.g., activity) of the catalytic material. One of the primary motivations for the current work is to develop and apply quantitative *operando* TEM methods to determine structure-activity relationships for nanoparticle catalyst/reaction systems that are of importance to clean energy conversion. Extensive discussion on the technique will be given in Sections 1.2 and 2.3. An introduction to the reactions and CeO_2-based catalytic materials systems of interest to this thesis will be given first.

1.1.2. Oxygen transfer reactions over CeO_2-supported Pt nanoparticles

Oxygen transfer reactions are central to the functionality of many catalytic processes, including those underlying a variety of clean energy conversion and environmental remediation applications. In the catalytic converter, for example, the catalysts facilitate the transfer of oxygen from gaseous O_2 molecules to unburnt

hydrocarbons ($C_xH_y + O_2 \rightarrow CO_2 + H_2O$) and to carbon monoxide ($CO + ½O_2 \rightarrow CO_2$). At the same time, oxygen is transferred out of oxidized nitrogen species and back into molecular oxygen (e.g., $2NO \rightarrow N_2 + O_2$). Under operating conditions, the converter must maintain activity for these reactions in a highly variable gas atmosphere that may lack oxygen or contain excess amounts of it. The catalyst formulations employed in the converter include materials that can store and release oxygen and thus buffer fluctuations in the exhaust stoichiometry to maintain high activity. Cerium dioxide (ceria, CeO_2)-based materials are among the most popular, due to CeO_2's ability to undergo rapid and reversible oxygen uptake and release (Kašpar et al., 1999; Li et al., 2019). The attractive oxygen transfer capability of CeO_2 (historically called the oxygen storage capacity or OSC) has led to its inclusion in catalyst formulations used in a wide variety of applications, ranging from hydrocarbon cracking and reforming to waste water remediation and soot oxidation (Trovarelli, 2002; Gorte, 2010; Montini et al., 2016; Aneggi et al., 2016).

Oxygen transfer promoted by CeO_2-based catalysts is mediated by the cycling of oxygen vacancies in the ceria lattice. **Figure 1.3a** displays a crystal structure model of non-stoichiometric CeO_{2-x}. The perfect fluorite crystal (space group Fm-3m) consists of Ce^{4+} cations at face centered cubic sites and O^{2-} anions in the tetrahedral voids. As oxygen is transferred to a reactive adsorbate, an oxygen vacancy is generated in the CeO_2 lattice, producing CeO_{2-x}. To maintain charge neutrality, two neighboring Ce^{4+} cations are also reduced to Ce^{3+}. The utility of CeO_{2-x} arises in part from its ability to accommodate a large concentration of oxygen vacancies ($0 < x < \sim 0.2$) in conditions of relevance to chemical and energy conversion applications (Mogensen, 2000). The vacancy formation process can be described in Kröger-Vink notation, as written in **R. 1.1**:

R. 1.1 $$2Ce_{Ce}^{x} + O_{O}^{x} \leftrightarrow 2Ce'_{Ce} + V_{O}^{\cdot\cdot} + \frac{1}{2}O_{2(g)}$$

Where Ce_{Ce}^{x} represents Ce at a Ce lattice site, with an effective charge of 0 (Ce^{4+}), O_{O}^{x} represents O at an O lattice site, with an effective charge of 0 (O^{2-}), Ce'_{Ce} represents Ce at a Ce lattice site, with an effective charge of -1 (Ce^{3+}), and $V_{O}^{\cdot\cdot}$ represents a vacancy at an O lattice site, with an effective charge of +2.

The reversible Ce^{4+}/Ce^{3+} redox couple underpins ceria's activity for oxygen transfer reactions. An interesting pair of coupled redox reactions emerges when CeO_2 mediates oxygen transfer to reactive adsorbates. Take for example the oxidation of CO, which is of central importance to this work. The overall reaction can be written as follows in **R. 1.2**:

R. 1.2 $$CO + \frac{1}{2}O_2 \leftrightarrow CO_2$$

Due to the reversible redox couple between Ce^{4+} and Ce^{3+}, oxygen located in the CeO_2 lattice is available to serve as an oxidizing agent to produce CO_2. The overall reaction can thus be divided into a two-part, Mars-van Krevelen (MvK) redox mechanism wherein oxygen from the CeO_2 catalyst lattice enters into the desorbable products, so named after the researchers who originally described it in 1954 (Mars & van Krevelen, 1954; Doornkamp & Ponec, 2000). Written in Kröger-Vink notation (Kröger & Vink, 1956) to emphasize the participation of CeO_2, the first redox reaction involves lattice oxygen transfer to CO to produce CO_2 and a lattice oxygen vacancy:

R. 1.3 $$CO + O_{O}^{x} + 2Ce_{Ce}^{x} \leftrightarrow CO_2 + V_{O}^{\cdot\cdot} + 2Ce'_{Ce}$$

Secondly, molecular oxygen from the gas phase is activated on the CeO_2 surface and backfills the oxygen vacancy, completing the catalytic cycle:

R. 1.4 $$\frac{1}{2}O_2 + V_{O}^{\cdot\cdot} + 2Ce'_{Ce} \leftrightarrow O_{O}^{x} + 2Ce_{Ce}^{x}$$

Summing across **R. 1.3** and **R. 1.4** yields the overall CO oxidation process written in **R. 1.2**. These simplified reactions do not describe the elementary steps involved but are

presented to discuss the two-part MvK mechanism. Experiments with isotopically labeled oxygen show that the oxygen atom added to the CO does not originate directly from the gas phase but in fact does derive from the CeO_2 lattice (Penkala et al., 2015). Additional evidence comes from experiments wherein appreciable CO oxidation takes place over CeO_2 in the absence of gaseous O_2 (Mullins & Zhang, 2002; Mullins, 2015).

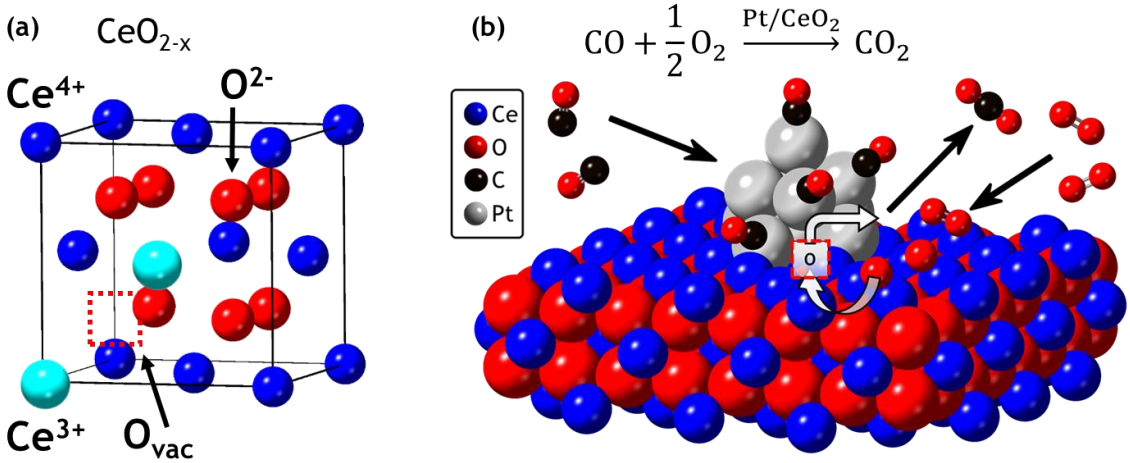

Figure 1.3. Schematic illustration of **(a)** fluorite structure of the slightly reduced CeO_{2-x} unit cell and its accommodation of an oxygen vacancy through Ce^{3+} formation (ionic radii not to scale), and **(b)** highly simplified mechanism of Mars-van Krevelen mediated oxygen transfer at a Pt/CeO_2 metal-support interface during CO oxidation, emphasizing the involvement of lattice oxygen vacancies in the CeO_{2-x} support.

In practical applications, CeO_2 is functionalized with metal nanoparticles (e.g., Pt) that improve the kinetics for the reactions of interest. The metal nanoparticles offer large specific surface areas and adsorption sites for gaseous reactants. They may also facilitate electronic charge transfer and reactant activation (Pacchioni, 2013). A special synergy exists at the metal-CeO_2 interface, recognized by the fact that the rates for oxygen transfer reactions can be considerably higher than the sum of the rates over CeO_2 and the metal alone (Bunluesin et al., 1995; Craciun et al., 1998; Ai-Ping Jia et al., 2010). The synergistic effect is further evidenced by kinetic studies that yield insight into the mechanism that controls the rate-limiting step for the overall reaction. For Pt supported on non-reducible

oxides (e.g., γ-Al_2O_3), kinetic measurements show that the rate of CO oxidation is inversely proportional to partial pressure of CO and approximately proportional to partial pressure of O_2 (Nibbelke et al., 1997). That is, $r \cong k_{app} P_{CO}^{-1} P_{O_2}$. In this case, the reaction proceeds with an appreciable rate only on the Pt, not on the Al_2O_3, so the reaction orders can be interpreted as indicating that the Pt surface is almost completely saturated with CO and that the competitive adsorption of oxygen onto Pt is involved in the rate-limiting step.

For Pt supported on CeO_2, on the other hand, kinetic measurements show that the rate of CO oxidation is nearly 0^{th} order with respect to both CO and O_2 (Cargnello et al., 2013; Liu et al., 2014). That is, $r \cong k_{app}$. The independence of the rate on the partial pressure of either reactant implies that gaseous CO and O_2 readily adsorb on the Pt and the CeO_2, respectively, with the rate-limiting step related to the transfer of oxygen at the metal-support interface. A highly simplified view of the Mars-van Krevelen interfacial oxygen transfer process is that the metal provides adsorption sites for CO while the CeO_2 provides lattice O to oxidize CO (**Figure 1.3b**). However, as will be discussed in the following paragraph, there is not a clear consensus on the fundamental details of the mechanism, and many outstanding questions remain unanswered regarding the atomic-level structure-activity relationships that underly the MvK interfacial oxygen transfer process. That being said, the highly simplified schematic illustration shown in **Figure 1.3b** for CO oxidation at a Pt/CeO_2 interface is not intended to convey information on the active structure of the working catalyst, but rather only to represent the overall processes of MvK-mediated oxygen transfer as reflected in **R. 1.3** and **R. 1.4**.

Attaining an atomic-level understanding of the catalytically-driven oxygen transfer process is of great interest to the scientific community and required to design more active catalysts. Despite the apparent simplicity of the CO oxidation reaction, the underlying details of the mechanism and structure-activity relationships for CeO_2-supported metal

catalysts remain unclear and are the focus of significant academic attention. Recent work by Lu et al. has demonstrated that the enhanced activity of CeO_2-supported Pt nanoparticles does not originate in the weakening of the CO-Pt bond, which would allow gaseous oxygen to compete effectively for adjacent adsorption sites (Lu et al., 2020). The involvement of Ce^{3+} in the reaction has been demonstrated with *in situ* X-ray spectroscopies, pointing to the importance of the Ce^{3+}/Ce^{4+} redox cycle and thus to the involvement of CeO_2 lattice oxygen vacancies (Kopelent et al., 2015; Pereira-Hernández et al., 2019). Elegantly designed studies by Cargnello and coworkers have provided compelling evidence that the active sites for CO oxidation are localized to the perimeter of the metal-support interface (Cargnello et al., 2013).

However, the structure and bonding of the active interfacial site that best facilitates the transfer of oxygen remains unresolved. For example, it is not presently known whether corner perimeter sites provide faster kinetic pathways for oxygen transfer than, say, edge perimeter sites. One may reason that the corner perimeter sites could be more active than the edge perimeter sites due to their lower coordination. Interestingly, very low coordination single Pt atoms supported on CeO_2 have been reported to have lower activities for CO oxidation (in terms of steady-state reactant conversion) compared to CeO_2-supported Pt nanoparticles 1 – 2 nm in size produced by sintering supported single-atoms (Ding et al., 2015; Gänzler et al., 2018). These results reveal that some degree of Pt reduction and sintering may be required to form an activated catalyst structure.

Using structure models derived from well-facetted, equilibrium Pt nanoparticle morphologies observed with HRTEM in vacuum, Cargnello and coworkers provide some evidence for corner sites being more active than other perimeter sites, but the results are inconclusive (Cargnello et al., 2013). Many authors implement well-facetted equilibrium shapes for CeO_2-supported Pt nanoparticles in their models, presumably due to their

simplicity and due to those shapes often being observed with HRTEM in vacuum (Cargnello et al., 2013; Kozlov & Neyman, 2016; Liu et al., 2017; Ren et al., 2018; Su et al., 2019; Wang et al., 2020). However, high resolution *in situ* TEM observations made a decade ago by Yoshida, Takeda, and coworkers revealed that ~4 nm CeO_2-supported Pt nanoparticles undergo rounding and other morphological changes in the presence of CO and at elevated temperatures of 100 °C (Yoshida et al., 2011). The particle size is expected to influence the morphology, but a systematic *in situ* investigation into the nanoscale structure of variously sized Pt/CeO_2 nanoparticles has not yet been done. Therefore, it is not clear to what extent such well-facetted equilibrium structures are relevant to the shape of 1 – 2 nm CeO_2-supported Pt nanoparticles under reaction conditions.

Independent measurements by Liu and Gänzler show that slightly reduced CeO_{2-x} enhance the kinetics of CO oxidation (Liu et al., 2014; Gänzler et al., 2017). However, it is not clear what CeO_{2-x}-adsorbate or CeO_{2-x}-metal species associations are responsible for the increase in activity. Some authors speculate that locally reduced CeO_{2-x} around the metal-support interface could accelerate the mobility of lattice oxygen vacancies and thus increase the reaction rate (Liu et al., 2014). Oxygen vacancies will introduce strain into the system, which could certainly promote the dissociative chemisorption of molecular oxygen (or the activation of another adsorbed compound). However, at present there is no high spatial resolution information about the locality and spatial extent of the reduction zone that may form under conditions relevant to CO oxidation, leaving such speculation purely hypothetical. Localized reduction zones 10 – 15 nm in size have been observed with *in situ* scanning TEM on 5 – 10 nm CeO_2-supported Ni nanoparticles under strongly reducing conditions in the absence of gaseous oxygen (Sharma et al., 2012; Lawrence & Crozier, 2018). Under the O_2-rich conditions typically employed for CO oxidation, the nature and spatial extent of the reduced zone may be very different due to the availability of molecular

oxygen, which may dissociate on the surface and backfill lattice O vacancies, preventing the build-up of a reduced zone around the metal-support interface.

On this topic, one fundamental question that remains unanswered concerns the nature and identity of the active site for molecular oxygen dissociation. Considering the 0^{th} order kinetics as well as the large coverage of CO on the Pt under reaction conditions (i.e., CO coverage > 0.6 – 0.8), the adsorption and thus the molecular dissociation of O_2 is unlikely to occur on the supported Pt nanoparticle (Lu et al., 2020). Molecular O_2 dissociation may be easily activated at interfacial sites containing an oxygen vacancy. Alternatively, dissociation may occur at vacant sites on the nearby CeO_{2-x} surface, followed by diffusion of O to the interface for reaction with CO. Which of these pathways dominates will depend on the surface and bulk oxygen vacancy diffusion rates as well as the oxygen reduction rate. To our knowledge experimental evidence for a dominant O_2 dissociation mechanism has not yet been reported for the Pt/CeO_2 system during CO oxidation.

1.1.3. Statement of purpose

There are many outstanding questions regarding the atomic and nanoscale spatial variation of the structure and composition of the Pt/CeO_2 interface, Pt metal particle, and adjacent CeO_2 oxide surface during catalysis. As such, still poorly understood effects involving the interaction of the metal particle, metal-support interface, and surrounding support surface are likely to play a role in describing the catalytically-driven oxygen transfer process at Pt/CeO_2 interfaces. At present there are very little observations of the atomic-scale structure of the surfaces and interfaces of CeO_2-supported Pt nanoparticle catalysts either under reaction conditions (*in situ*) and/or during catalysis (*operando*). One of the primary objectives of the following thesis is therefore to visualize and characterize Pt/CeO_2 catalysts under conditions relevant to oxygen transfer catalysis or during catalytic turnover itself. Overall, the atomic-level information generated by this

research program will contribute to our understanding of structure-activity relationships for catalytically-driven oxygen transfer at Pt/CeO_2 interfaces. These relationships are of fundamental interest to the heterogenous catalysis community, and in terms of broader impact they may facilitate the rational engineering of more active Pt/CeO_2 catalysts for clean energy conversion and environmental remediation applications.

Aberration-corrected environmental transmission electron microscopy (AC-ETEM) was the central methodology of this work, due to its ability to probe atomic-level structure and bonding with high spatiotemporal resolution. A brief introduction to AC-ETEM is given in the following section. A discussion of the methodological aspects specific to this thesis will be given in the next chapter.

1.2. Literature review of *in situ* and *operando* AC-ETEM for catalysis research

Aberration-corrected *in situ* ETEM is an extremely powerful characterization tool capable of providing atomic-level information from high surface area catalysts under reaction conditions. Modern instruments offer spatial resolutions better than 1 Å, and the ability to visualize the atomic-scale dynamics of catalysts under conditions relevant to their use has delivered insight into processes underlying catalyst activation (Chenna et al., 2011), active metal sintering (Liu et al., 2005; Y Nagai et al., 2006; Simonsen et al., 2010; Gänzler et al., 2017), metal-support interactions (Liu, 2011; Zhang et al., 2016; Lawrence & Crozier, 2018), surface reconstructions (Yoshida et al., 2012; Avanesian et al., 2017), and phase transformations (Ward et al., 2013; Dai et al., 2017), to name a few. For reviews of seminal research in applying *in situ* ETEM to heterogenous catalysis, see, for example: (Bell, 2003; Jinschek, 2014; Crozier & Hansen, 2015; Tao & Crozier, 2016; He et al., 2020; Ye et al., 2020; Chee et al., 2021). The historical development of the theory and technique of *in situ* ETEM has been excellently chronicled in *Controlled Atmosphere Transmission*

Electron Microscopy: Principles and Practice by Hansen and Wagner (Hansen & Wagner, 2016). Additional information providing a well-rounded overview to the technique can be found in the following references: (Gai, 1997; Sharma, 2001; Banhart, 2008; Sharma, 2012; Jungjohann & Carter, 2016; Taheri et al., 2016; Ross & Minor, 2019).

In the words of Henrik Topsøe, a pioneering researcher in the field of heterogeneous catalysis, "strictly speaking, the active state of the catalyst only exists *during catalysis*" (Topsoe, 2003). To elucidate catalytic structure-activity relationships, one would thus ideally employ an *operando* approach wherein one acquires atomic-resolution structural information *simultaneously* with data on the activity of the catalyst. Traditionally, it was not possible to verify that catalysis was in fact occurring in the ETEM, requiring researchers to make inferences about the activity of the observed catalyst. In the last decade there have been considerable advancements for studies under reaction conditions, including the development of in-line gas analysis (e.g., spectroscopy and/or mass spectrometry) that allows the gas composition in or downstream from the reaction cell to be monitored (Creemer et al., 2008, 2011; Crozier & Chenna, 2011; Miller & Crozier, 2014; Plodinec, Nerl, Farra, et al., 2020). Measurements of the gas composition can confirm that catalysis is actually taking place, and in favorable cases they may be used to quantify the *in situ* conversion of reactants to products.

Recent investigations have used AC-ETEM along with *in situ* microreactors coupled to in-line spectroscopy or downstream mass spectrometry in order to correlate observations of catalyst structure with changes in gas composition or conversion (Vendelbo et al., 2014; Li et al., 2015; Chee et al., 2020; Plodinec, Nerl, Girgsdies, et al., 2020; Miller & Crozier, 2021). While impressive, these experiments have often involved the observation of larger 10 – 100 nm metal nanoparticles that are dispersed on non-reducible supports (e.g., SiO_2) or on SiN_x thin films. In order to understand the Mars-van

Krevelen oxidation mechanism, however, the metal nanoparticles must be supported on a reducible oxide, since strong metal-support interactions play a significant role in the reaction mechanism. To the knowledge of the author, no such observations have been reported.

Additionally, in order to establish a truly *operando* connection between the observed structure and the catalyst's activity, it is necessary to directly correlate the TEM observations with the *reaction rate* of the working catalyst, as first argued by Bañares, Weckhuysen, Gaigneaux, and Mestl (M. Weckhuysen, 2003a, 2003b; Demoulin et al., 2003; Bañares, 2005; Guerrero-Pérez & Bañares, 2006). It is important to stress that an *in situ* measurement of conversion is not itself and in most cases is not directly related to the chemical reaction rate of the working catalyst (Ertl et al., 1997; Duprat, 2002). In the field of reaction engineering, this knowledge has led to the design of controlled catalytic reactors operated under easily modeled conditions wherein the conversion can be related to the kinetics of the catalytic reaction (Metcalf, 2011; Fogler, 2017).

The *in situ* reactors used for ETEM catalysis research are complex and generally differ greatly from the architectures typically employed in gas phase chemical reaction engineering. Two classes of *in situ* reactors have been developed thus far: the differentially-pumped open cell (Boyes & Gai, 1997; Sharma, 2001) and the windowed gas cell (Creemer et al., 2008, 2011). Windowed cells can achieve higher gas pressures (up to a few atmospheres) than open cell ETEM reactors (typically up to 10^{-2} – 10^{-3} atmospheres). The ability to extrapolate observations made from *in situ* TEM (or any other *in situ* characterization tool) to higher pressures will depend in part on the pressure sensitivity of the reaction and the detailed mechanism of the reaction pathway on the catalyst. As discussed earlier, the 0^{th}-order dependence of the CO and O_2 pressure on the rate of CO oxidation over Pt/CeO_2 provides a favorable case for *operando* ETEM as the reaction

kinetics the should not be significantly impacted by the gas pressure. A windowed gas cell was not used in this work, primarily to avoid losses in resolution and contrast associated with scattering from the electron transparent amorphous SiNx windows, which would make imaging the thin and dynamic surface and interfacial structures on 1 – 2 nm Pt/CeO_2 much more difficult. An open cell differentially-pumped ETEM was therefore used extensively for this work. The amount of reactant converted by the catalyst loaded on a typical ETEM sample grid is miniscule, which precludes measurements of chemical reaction kinetics. Special specimen preparation methods involving an *operando* pellet reactor have been developed to overcome this limitation, enabling quantification of the gas phase products of a catalytic reaction while achieving a stable platform for atomic-resolution imaging (Chenna & Crozier, 2012; Miller et al., 2015). The methodological design of the *operando* ETEM reactor is discussed in detail in Chapter 2, Section 2.3.5.

In order to determine steady-state reaction rates from catalytic conversion data, it is necessary to establish a detailed model for the *operando* ETEM reactor system. Mortensen et al. have conducted computational fluid dynamics (CFD) simulations of an ETEM in order to investigate the temperature distribution in a furnace-type holder for various pressures of single gases (Mølgaard Mortensen et al., 2015). Their model gives a good description of the temperature variation across a TEM grid for single gases of differing thermal conductivity at various pressures. However, it does not address the issues of catalysis or multi-component mass transport, both of which are essential to determining chemical reaction kinetics. Considering the impact that temperature and local gas environment have on determining a catalyst's structure and properties, it is highly desirable to understand the prevalence and extent of any thermal and compositional gradients that may exist during catalysis in an *operando* TEM experiment. One of the primary objectives of the present work was to establish a detailed chemical

engineering model of the *operando* ETEM reactor, so that quantitative chemical kinetics can be determined (Chapter 3). With this model, atomically-resolved structural dynamics occurring on CeO_2-supported catalysts can be directly correlated with activity for CO oxidation (Chapter 4).

1.3. Dynamic structural metastability during catalytic processes

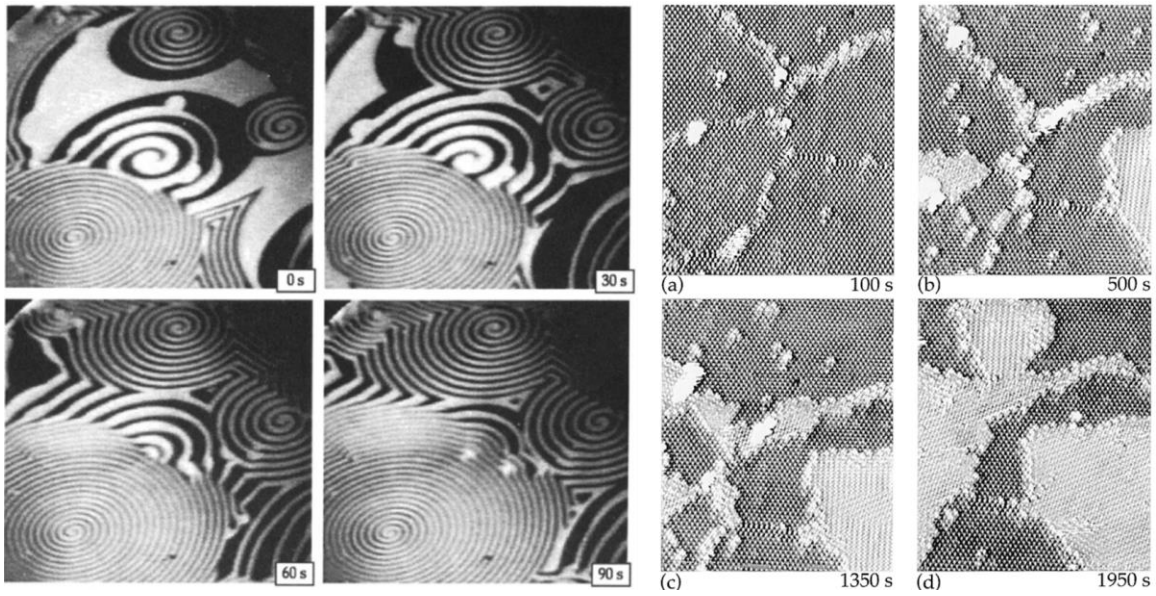

Figure 1.4. (left) Photoemission electron microscopy (PEEM) image time-series showing the spatiotemporal evolution and of spiral wave patterns on Pt (110) single crystal surface during CO oxidation at T = 448 K. Reactant pressures are $P_{CO} = 4 \times 10^{-5}$ mbar and $P_{O2} = 4 \times 10^{-4}$ mbar. Image size is approximately 450 x 450 μm. Dark contrast corresponds to O covered Pt surface while bright contrast corresponds to CO covered surface. Figure from (Imbihl & Ertl, 1995). **(right)** Scanning tunneling microscopy (STM) image time-series of a Pt (111) surface with pre-adsorbed O_{ad} showing the dynamic structural evolution during the process of CO oxidation at T = 244 K with $P_{CO} = 5 \times 10^{-7}$ mbar. Dark and bright contrast again correspond to O and CO-covered Pt, respectively. Figure from (Ertl, 2001).

Since the discovery of oscillatory reaction kinetics during CO oxidation on Pt surfaces by Wicke (Beusch et al., 1972), describing the dynamic structural metastability of catalyst surfaces and relating this behavior to the catalyst's activity has been one of the foremost scientific challenges of heterogenous catalysis research (Schlögl, 2015). Much

progress in this line of research was made by the group of Gerhard Ertl, whose *in situ* photoemission electron microscope (PEEM) and scanning tunneling microscope (STM) images of Pt single crystals revealed the emergence and continual transformation of complex surface structures during CO oxidation (Imbihl & Ertl, 1995: 199; Wintterlin et al., 1997; Ertl, 2001). The ability to directly visualize the dynamic structural evolution of the catalytic surface under reaction conditions (**Figure 1.4**) delivered spectacular insight into the metastable structure-activity relationships for extended Pt(110) and Pt(111) surfaces, for which Ertl received the Nobel prize in 2007 (Ertl, 2007).

While the surface science studies of Ertl and many others led in some cases to a detailed understanding of the relationship between structural metastability and activity on extended single crystal surfaces, such knowledge remains deeply limited for catalysts consisting of oxide-supported metal nanoparticles. The structural behavior of nanoparticles can differ significantly in comparison to extended surfaces due to the larger population of coordinatively unsaturated edge and corner sites. Energetics calculations of small (i.e., < 50) metallic nanoparticles demonstrate that many structural isomers may exist with shallow kinetic barriers separating distinct configurations that show similar thermodynamic stability (Ajayan & Marks, 1988; Marks & Peng, 2016). The structure of the metallic nanoclusters are also influenced by the coverage and interconversion of surface adsorbates as well as by interactions with the underlying support (Piccolo, 2020). Under reaction conditions, in the presence of chemisorbed species and applied heat, the cluster can easily cross activation energy barriers separating different structures, continually fluctuating between accessible local minima in the flattened potential energy landscape (Häkkinen et al., 2003; Xing et al., 2006; Zhai & Alexandrova, 2018).

Describing the fluctuating dynamic structural metastability, or *fluxionality*, of nanoparticle-adsorbate systems is increasingly becoming recognized as critical to

obtaining a fundamental understanding of catalytic activity (Zhang et al., 2020). Each configuration in the evolving ensemble of metastable structures contributes uniquely to the overall properties of the catalyst. Only a minority or even just one of them may be catalytically active for the reaction of interest. Advanced density functional theory (DFT) and *ab initio* molecular dynamics (AIMD) calculations are able to sample the potential energy (PE) landscape of supported metal nanoparticles interacting with gas at finite temperature, which can provide a detailed picture of the metastable states accessible under catalytic conditions. In a few cases involving clusters < 10 atoms in size, this approach has been successful in distinguishing more active metastable states from those that are merely effective spectators (Rehr & Vila, 2014; Baxter et al., 2017; Zandkarimi & Alexandrova, 2019; Zhang et al., 2020). However, first principles calculations are currently intractable for larger systems of practical relevance.

At the same time, there are very few experimental *in situ* observations of fluxional behavior at the single and sub-particle length scale. Many surface science characterization techniques measure ensemble-averaged signals, which may be dominated by the abundant metastable species, with weak contributions from the minority metastable species that may ultimately be the most catalytically important. Time-resolved and localized measurements from (sub)atomic and nanoscale regions are required to characterize fluxional behavior of catalysts. As discussed above in Section 1.2, aberration-corrected *in situ* ETEM is capable of providing sub-Ångstrom structural and chemical information from catalysts under reaction conditions. Recent advances in direct electron detector technology now enable atomically-resolved, shot noise-limited *in situ* ETEM image time-series to be acquired with a temporal resolution on the order of milliseconds (Faruqi & McMullan, 2018; Ciston et al., 2019). As many catalysts exhibit chemical reaction turnover frequencies on the order of 0.1 – 100 Hz, the emerging opportunity to

visualize atomic-level fluxional behavior with high spatiotemporal resolution holds much promise for understanding the structural/chemical transformation processes that take place on catalyst surfaces. To this end, one of the primary objectives of this work was to implement time-resolved *in situ* AC-ETEM to visualize the fluxional behavior of CeO_2-supported Pt nanoparticles with high spatiotemporal resolution (Chapter 5).

Although there is potentially much to be gained from applying these new detectors to catalytic nanomaterials characterization, acquiring *in situ* TEM image time series with very high temporal resolution produces datasets that can be severely degraded by noise (Lawrence et al., 2020). By carefully selecting and summing frames in a time-series, precise structural information on metastable states can be obtained with an improved signal-to-noise ratio (SNR). Averaging consecutive frames may reveal fluxional behavior provided the lifetime of each metastable state is longer that the averaging time. However, information on short-lived intermediate states, *which may ultimately underpin the material's functionality*, may no longer be resolved.

Thus, in order to advance the study of fluxional behavior in supported catalyst systems, there is a pressing need for sophisticated noise reduction techniques. Ideally the developed approaches should preserve the original temporal resolution of the image time-series and also facilitate the retrieval of structural features at the catalyst surface. In the field of machine learning, deep convolutional neural networks (CNNs) have been developed to achieve state-of-the-art denoising performance on natural photographic images corrupted with different types and varying degrees of noise. At present it is not clear what network architectures would be best suited for denoising the ultra-low SNR electron microscopy images. Overall, the application of deep CNNs to denoise electron microscopy images with a focus on atomic scale surface structure has not been adequately investigated. One of the primary objectives of the current work was to therefore explore

and evaluate new advances in deep CNNs in order to denoise large atomic-resolution *in situ* ETEM datasets (Chapter 6).

1.4. Objectives and outline

As illustrated in the previous sections, oxygen transfer catalyzed by CeO_2-supported Pt nanoparticles remains poorly understood. Significant progress has been made toward understanding the oxygen transfer process in terms of a Mars-van Krevelen mechanism in which CeO_2 lattice oxygen is transferred to CO adsorbed on Pt at the perimeter of the Pt/CeO_2 interface. However, there remain many outstanding questions regarding the atomic and nanoscale spatial variation of the structure and composition of the Pt/CeO_2 interface, Pt metal particle, and adjacent CeO_2 oxide surface during catalysis.

Attaining an atomic-level understanding of the catalytic process is of great interest to the scientific community and is required to design more active catalysts for clean energy conversion applications. In this work, atomic-resolution observations are made of CeO_2-supported Pt nanoparticle catalysts under conditions relevant to oxygen transfer catalysis (*in situ*) or during catalytic turnover itself (*operando*). A range of techniques centered around aberration-corrected environmental TEM were developed and employed to visualize and characterize local surface atomic structures with high spatiotemporal resolution. New advances in data science and machine learning were leveraged to develop novel denoising techniques for large image datasets of catalytic nanoparticles. **Key scientific questions** motivating this research include:

1. During an *operando* ETEM experiment, what are the gas and temperature distributions in and around the pellet reactor during catalysis? If gradients are present, how do they impact the experimental evaluation of the temperature and composition surrounding the catalyst that is imaged on the TEM grid? How can the EELS gas composition measurement be used to measure the conversion in the

ETEM cell, and more importantly, the catalytic reaction rate for particles imaged during an experiment?

2. What are the structure-activity relationships that regulate oxygen transfer at Pt/CeO_2 interfaces during CO oxidation? What role do surface sites near the metal particle play during oxidation at the metal-support interface? What type of structural dynamics occur under CO oxidation reaction conditions, and how does such fluxional behavior relate to the catalyst's activity?

3. Can we track the dynamic structural reconfigurations exhibited by CeO_2-supported Pt nanoparticles with high time resolution? How does the surrounding gas composition influence the degree and character of the fluxional behavior of the catalyst? What connection does such structural metastability have to the catalysts ability to regulate chemical transformation pathways?

4. By leveraging new advances in data science and machine learning (e.g., convolution neural networks), what innovative new approaches to image denoising can be developed and applied to atomic-resolution images of nanoparticle surfaces recorded with an extremely low signal-to-noise ratio (SNR)? What are the best conditions for training neural networks for this purpose, and how robust are the networks to unseen imaging conditions? How might one quantify the uncertainty of the atomic structure that appears in a denoised image produced by successfully trained networks? Can we access and understand the mechanisms by which the trained networks denoise the structure at the catalyst surface?

To this end, we first develop a finite element model of the ETEM and *operando* pellet reactor in order to explore the mass transport, chemical conversion, and heat transfer processes relevant to an *operando* catalysis experiment (Chapter 3). A

quantitative investigation is performed into the presence and potential effect of the gas and temperature gradients present during experimental conditions of catalysis. Additionally, a kinetic analysis is developed to establish exactly how the experimental EELS gas composition measurement can be used to evaluate the activity of the catalyst that is imaged on the TEM grid.

With this reactor model, a combined experimental and computational *operando* ETEM methodology is applied to investigate the structure-activity relationships for CO oxidation at Pt/CeO_2 interfaces (Chapter 4). Atomic-resolution imaging of the Pt/CeO_2 catalyst is conducted during the simultaneous measurement of the catalytic CO oxidation reaction rate, and fluxional behavior is correlated with the catalyst's turnover frequency for CO oxidation. Additionally, the catalyst is observed at 300 °C in an inert atmosphere of N_2 to differentiate structural dynamics associated with applied heat from those associated with catalysis.

A major finding of the aforementioned Chapter is that the 1 – 2 nm CeO_2-supported Pt catalysts exhibit dynamic structural meta-stability (i.e., fluxional behavior) in CO oxidation gas atmospheres. In Chapter 5, an aberration-corrected ETEM equipped with a fast and efficient direct electron detector is employed to visualize the structural dynamics with high spatiotemporal resolution. The influence of the gas composition is investigated, with observations conducted of Pt/CeO_2 catalysts exposed to inert N_2 gas, as well as CO oxidation ($CO + ½O_2 \rightarrow CO_2$) reactant gases and water-gas shift ($H_2O + CO \rightarrow H_2 + CO_2$) reaction conditions (i.e., reactant gases and an elevated temperature of 200 °C).

Finally, in Chapter 6, deep learning methods for denoising ultra-low SNR images of nanoparticle surfaces recorded from an aberration-corrected TEM are developed and evaluated. The network is trained on a large dataset of simulated images. The network's ability to correctly predict the atomic-scale structure of the nanoparticle surface was

critically assessed. An approach based on the log-likelihood ratio test is developed that provides a quantitative measure of the agreement between the noisy observation and the atomic-level structure present in the denoised image. Additionally, a gradient based analysis was conducted to investigate the filtering approach implemented by the network when it encounters non-periodic terminations or atomic-level defects at the nanoparticle surface. The approaches described here may be applicable to a wide range of atomic-resolution imaging applications that are characterized by ultra-low SNR, including the investigation of dynamic processes with time-resolved *in situ* microscopy or the study of beam sensitive systems.

2. Methods

2.1. Synthesis of CeO_2-supported Pt nanoparticles

The desire to engineer the size, shape, and exposed faceting of CeO_2 powders at the nanoscale has driven materials synthesis research to establish methods for preparing nanostructured CeO_2 particles. Standard preparation strategies, including combustion synthesis (Basu et al., 2004; Chen et al., 2006), sol-gel synthesis (Morris et al., 2006; Laberty-Robert et al., 2006), ultrasonic precipitation (Wang et al., 2002; Pinjari & Pandit, 2011), or spray drying (Blennow et al., 2009; Sharma et al., 2010), for example, typically offer little control over the morphology of the resultant CeO_2 nanopowder. Templating or adding structure-directing precursors during synthesis can improve the yield of particular nanostructured morphologies (Yang & Gao, 2006; Zhang et al., 2007). Alternatively, template-free, scalable, and simple synthesis of nanostructured CeO_2 particles (e.g., rods, cubes, octahedra, etc.) may be achieved with hydrothermal methods (Mai et al., 2005; Zhou et al., 2005). In this work, nanostructured CeO_2 with a cubic morphology was chosen as a model support structure due to its enhanced catalytic properties over irregularly shaped CeO_2 nanoparticles (Mai et al., 2005; Zhou et al., 2005; Qiao et al., 2013; Trovarelli & Llorca, 2017). Additionally, their well-defined shape also facilitates interpretable atomic-resolution TEM imaging: with the shape of the support well-defined (e.g., the projected shape of a cube is a square), it is feasible to rapidly ascertain whether a given particle is in a favorable zone axis orientation for HRTEM imaging.

Many methods exist for depositing active metal nanoparticles onto catalyst supports, including impregnation (van Dillen et al., 2003; Mehrabadi et al., 2017), coprecipitation (Munnik et al., 2015), microwave deposition (Hsieh et al., 2013), and exsolution (Kwon et al., 2017; Neagu et al., 2015). In this work, due to its simplicity, incipient wetness impregnation was used to deposit Pt onto nanostructured CeO_2 cubes.

2.1.1. Hydrothermal synthesis of CeO_2

Detailed descriptions of the synthesis procedures for producing nanostructured CeO_2 cubes have been published by Mai et al. (Mai et al., 2005). Generally, the synthesis involves the precipitation of crystalline CeO_2 from an aqueous basic solution when heated autogenously in a sealed hydrothermal vessel. In a typical synthesis, 1.38 g of $Ce(NO_3)_3 \cdot 6H_2O$ salt dissolved in 8 mL of deionized (DI) water was added to a 60 mL solution of 12 M NaOH, which was magnetically stirred for 30 minutes. The resultant pale-white slurry was added to an 85 mL Teflon-lined autoclave and heated for 24 hours at 200 °C. Upon cooling to room temperature, the white precipitates were isolated by filtration, washed multiple times with DI water, and dried at 60 °C in air overnight. After drying, the white CeO_2 powders were calcined in air at 350 °C for 4 hours.

2.1.2. Metal impregnation

An impregnation technique was used to deposit 17 wt.% Pt onto the CeO_2 nanocubes. A high weight loading of metal was desired to reduce the amount of time spent searching for Pt nanoparticles close to a zone-axis orientation during *in situ* and *operando* TEM experiments. In brief, a volume of CeO_2 powder was weighed, then an appropriate mass of H_2PtCl_6 was dissolved in DI water to achieve the desired weight loading. This Pt-containing solution was added dropwise to the CeO_2 to form a slurry. The slurry was mixed continuously in a mortar and pestle for 2 hours until complete evaporation of the DI water was achieved. The powder was dried overnight in air at 60 °C and then reduced in a flowing stream of 5% H_2/Ar for 2 hours at 400 °C, yielding a black powdered sample of Pt/CeO_2.

2.2. Characterization of catalytic activity

The catalyst's activity for CO oxidation ($CO + \frac{1}{2} O_2 \rightarrow CO_2$) was evaluated in a packed bed plug flow reactor. Plug flow reactor experiments were performed in a RIG-150

micro-reactor from In Situ Research Instruments (ISRI). The reactor consists of a 10 mm inner diameter quartz tube plumbed up to four mass flow controllers (MFCs) which provide control over the mass flow rate and composition of various inlet gases. The tubular micro-reactor is placed within a clamshell furnace capable of heating up to 900 °C. The furnace is equipped with an electronic proportional-integral-derivative (PID) controller to provide control over the temperature of the catalyst bed. A thermocouple is placed in the center of the catalyst bed within the quartz tube, providing a measurement of the catalyst temperature and feedback capability for controlling the furnace.

In a typical reaction, 20 mg of catalyst powder was diluted on 2.6 g of inert SiO_2 sand particles having size of 1 mm and loaded into the reactor. A reducing treatment was preformed prior to the introduction of reactants, wherein 40 standard cubic centimeters per minute (SCCM) of 5% H_2/Ar was flown while the reactor bed was held at 400 °C for 2 hours. The reactor was then cooled to room temperature with continued 5% H_2/Ar flow. Upon cooling to room temperature, the gas stream was switched to 8 SCCM of 10% CO/He and 22 SCCM of 5% O_2/He, balanced with 150 SCCM of pure He, corresponding to a gas hourly space velocity of 12,500 hr^{-1}. The reactor was then heated up to 400 °C at a rate of 1.5 °C/minute while the effluent gas composition was analyzed on-line with a Varian 3900 gas chromatograph (GC) equipped with a thermal conductivity detector (TCD).

The basic operating principles of GC relevant to this work are described briefly. For a comprehensive overview of the technique and instrumentation, the reader is referred to the following references: (Dettmer-Wilde & Engewald, 2014; Rosemount Analytical, 2012). In brief, GC is a technique for separating gaseous mixtures, permitting the composition of the mixture to be analyzed and quantified. A schematic showing the basic concept of the technique is given in **Figure 2.1a**. The gaseous mixture is separated by passing it through a tube coated with adsorbent material, which is called the column.

Small amounts (typically ~10 – 250 μL) of the mixture are diverted from the reactor effluent into the column by a gas sampling valve, which is a multi-port switching valve that contains a sampling loop. When operated in the loading state (see **Figure 2.1a**, top), the connections of the switching valve are set so the gaseous mixture flows into the sampling loop, filling it up, and then back out of the valve, to the waste. A carrier gas flows into the other side of the valve and back out again into the column. Upon sampling (see **Figure 2.1a**, bottom), the connections in the switching valve rotate, which causes the gas within the sampling loop to be pushed by the carrier gas into the column. The adsorbent coating on the inner walls of the column interacts differentially with the various gaseous components in the mixture, selectively retaining different species by a characteristic amount of time before they elute from the column, which effectively separates the mixture. A thermal conductivity detector (TCD) placed at the end of the column registers change in composition relative to the pure carrier gas, allowing the composition to be quantified.

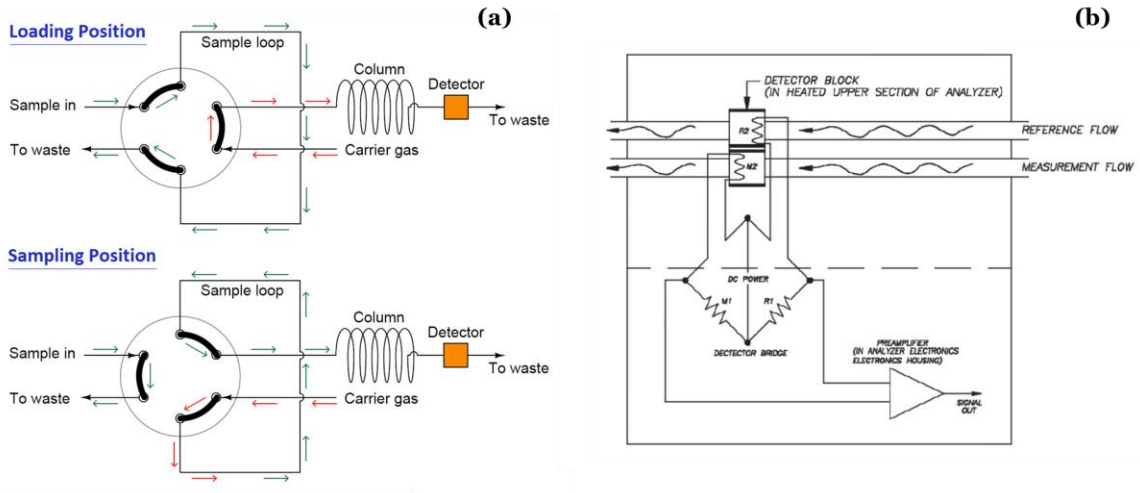

Figure 2.1. Schematic diagrams showing the basic operating principles behind **(a)** gas chromatography with sampling from a multi-port switching valve (Instrumentation Tools, 2018), and **(b)** a thermal conductivity detector based on a Wheatstone bridge circuit (Rosemount Analytical, 2012).

The TCD is based on a Wheatstone bridge circuit consisting of multiple heated filaments under applied direct current. The filaments typically consist of tungsten and rhenium, and thus the TCD should be purged before the filaments are heated, so as to prevent heating in the presence of air which could lead to embrittlement and potential failure due to oxidation. A simplified schematic diagram of the Wheatstone bridge circuit is given in **Figure 2.1b**. As seen at the top, pure carrier gas and the mixture stream are flown over two different heated filaments. When an analyte in the mixture stream flows over the mixture filament, the filament will heat or cool, depending on the thermal conductivity of the analyte relative to that of the carrier gas. A TCD signal is generated by measuring the change of resistance for the mixture filament relative to resistance of the reference filament, as the mixture filament heats up or cools down.

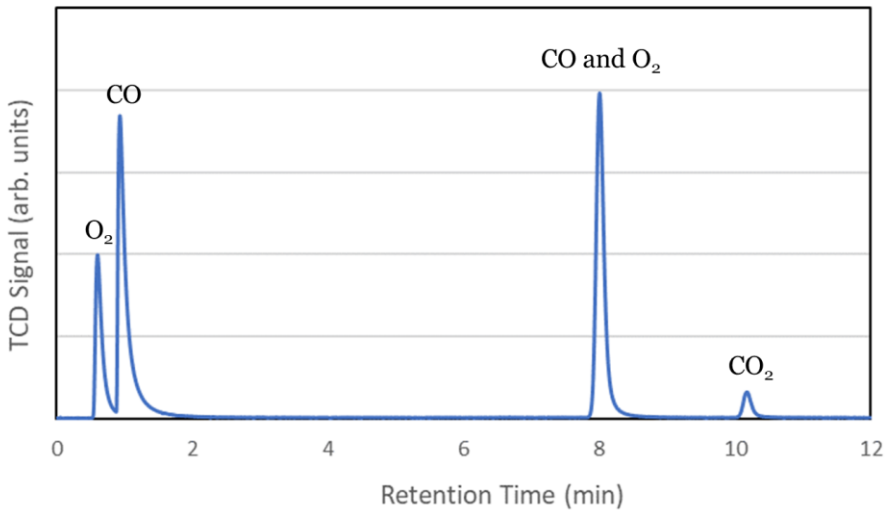

Figure 2.2. Example gas chromatogram recorded during CO oxidation, with peaks corresponding to CO, O_2, CO_2, as well as an unseparated mixture of CO and O_2. Figure is from own unpublished work.

Recording the TCD signal as a function of retention time produces a chromatogram, which ideally shows well-separated peaks corresponding to distinct components that are present in the sampled mixture. An example chromatogram taken during a CO oxidation experiment is shown in **Figure 2.2**, with labeled peaks

corresponding to CO, O_2, and CO_2. The area under each of these labeled peaks is proportional to the concentration of that component in the mixture stream. The chromatogram also shows a mixture peak containing both CO and O_2. In this experiment, a dual column configuration was used consisting of two parallel PLOT (Porous Layer Open Tubular) columns – one 10 m long, 0.32 mm diameter MolSieve5Å column designed for permanent gases (CO, O_2, N_2, H_2, etc.) and one 50 m long, 0.53 mm diameter PoraBOND Q column designed for CO_2. The sample is split between each column and the separated mixture is recombined before being sent to detector. Under these conditions, the short, 10 m long MolSieve5Å column elutes all of the sample before 8 minutes; this column cannot separate CO2 and thus a signal corresponding to CO_2 does not appear before 8 minutes. The much longer 50 m PoraBOND Q column requires a similarly longer retention time, and it cannot separate CO and O_2, thus a mixture peak appears corresponding to both components at around 8 minutes. However, this column is able to separate CO_2, which is detected in this case around 10 minutes.

For the experiments conducted in this thesis, He was used a carrier gas. The conversion of CO into CO_2, X_{CO}, was quantified by calculating $X_{CO} = (CO_{in}-CO_{out})/CO_{in}$, where CO_{in} and CO_{out} denote the molar flowrate of CO into and out of the reactor, respectively. The molar flowrate of CO into the reactor is known (0.8 SCCM, as mentioned above). The molar flowrate of CO out of the reactor is determined by integrating the peak corresponding to CO in a gas chromatogram recorded at a particular reactor temperature. The catalytic reaction rate, with units of mol CO sec^{-1}, was calculated by multiplying the conversion with the molar flow rate of CO into the reactor. Catalytic turnover frequencies (TOFs) were computed by normalizing the reaction rates to the estimated number of Pt atoms at the metal-support interfacial perimeter, as determined by the derivation described in the Appendix, Section C.2. We normalize to the number of Pt atoms at the

perimeter as we assume that the reaction occurs through a Mars-van Krevelen mechanism at the perimeter of the metal-support interface. We note that this normalization assumes that each perimeter Pt atom is active and that the number of perimeter Pt atoms is identical both in vacuum conditions, where the number is counted, and under reaction conditions, where the catalysis takes place. Essentially, though, the TOF reported here is linearly related to the mass-normalized rate of product formation. Activation energies for CO oxidation were calculated through an Arrhenius analysis of the activity data taken in the low-conversion regime (i.e., < 25%).

2.3. Electron microscopy and spectroscopy

Electron microscopy and spectroscopy are powerful characterization tools capable of providing a wealth of information on structural, elemental, chemical, and optical properties with atomic-scale spatial resolution. In the past two decades, the development of aberration correctors has led to considerable improvements in the imaging optics and pushed the spatial resolution beyond 1 Å. Recent advances in the realization of highly efficient direct electron detection systems now enable time-resolved series of images to be captured with frame rates in the kilohertz range. Such highly resolved spatio-temporal information is vital for fundamental studies of nanoparticle catalysts, as it is now well known that catalytic functionality is governed by surface sites which typically consist of only a few atoms. The properties and behavior of catalysts are strongly influenced by the surrounding gas atmosphere and the temperature, thus necessitating environmental techniques (e.g., ETEM) which permit ambient pressures of gaseous reactants and applied heat to be present during imaging, i.e., *in situ* under reaction conditions. An aspirational goal for *in situ* ETEM research would be to establish a direct, *operando* link between the observed structure and the activity (e.g., reaction rate) of the catalytic material. The *in situ* reactors used for ETEM catalysis research are complex, but may nonetheless be modeled

using, e.g., finite element approaches, enabling a quantitative *operando* determination of catalytic reaction rates during atomic-level structural observations.

In situ and *operando* ETEM and its related techniques are the primary characterization methods employed in the work of this thesis. A brief overview of the fundamental TEM principles related to the presented work will be given in the following section, including a short discussion of (a) aberration correction, (b) direct electron detector technology, and (c) electron energy loss spectroscopy, and (d) *in situ* and *operando* ETEM methodology. An extended discussion on electron beam effects will also be given. For detailed descriptions of the instrumentation and principles underlying TEM and its related techniques, the reader is referred to the following references: (Cowley, 1995; Spence, 2003; Egerton, 2005; Fultz & Howe, 2007; Williams & Carter, 2008; Egerton, 2011; Pennycook & Nellist, 2011; Zuo & Spence, 2017; Ross & Minor, 2019).

2.3.1. Transmission electron microscopy (TEM) fundamentals

The primary motivation for the development of electron microscopy was to overcome the resolution limits associated with visible-light microscopy (Ruska, 1985). Following the Rayleigh criterion, the smallest distance that can be resolved with a visible-light microscope is equal to approximately half of the photon wavelength, which is typically on the order of 500 nm. For electron microscopes, the resolution limit, δ, can be approximated as $\delta = 1.1\lambda/\beta$, where β is the collection semi-angle of the magnifying lens and λ is the wavelength of the incident electron radiation. The wavelength of an incident electron beam accelerated to 100 kV in a TEM is about 4 pm, which offers an almost 1000-fold increase in the wavelength-limited spatial resolution over visible-light microscopes (it should be mentioned that techniques based on super-resolved light microscopy, for which Betzig, Hell, and Moerner shared the 2014 Nobel prize in chemistry, are now capable of achieving spatial resolution up to ~10 nm (Möckl et al., 2014)). In practice, the

electron wavelength-limited resolution has not been reached due to several factors, including imperfections in the electron optics (discussed in Section 2.3.2) and/or external interference from acoustic, electromagnetic, or mechanical noise (Smith, 1997).

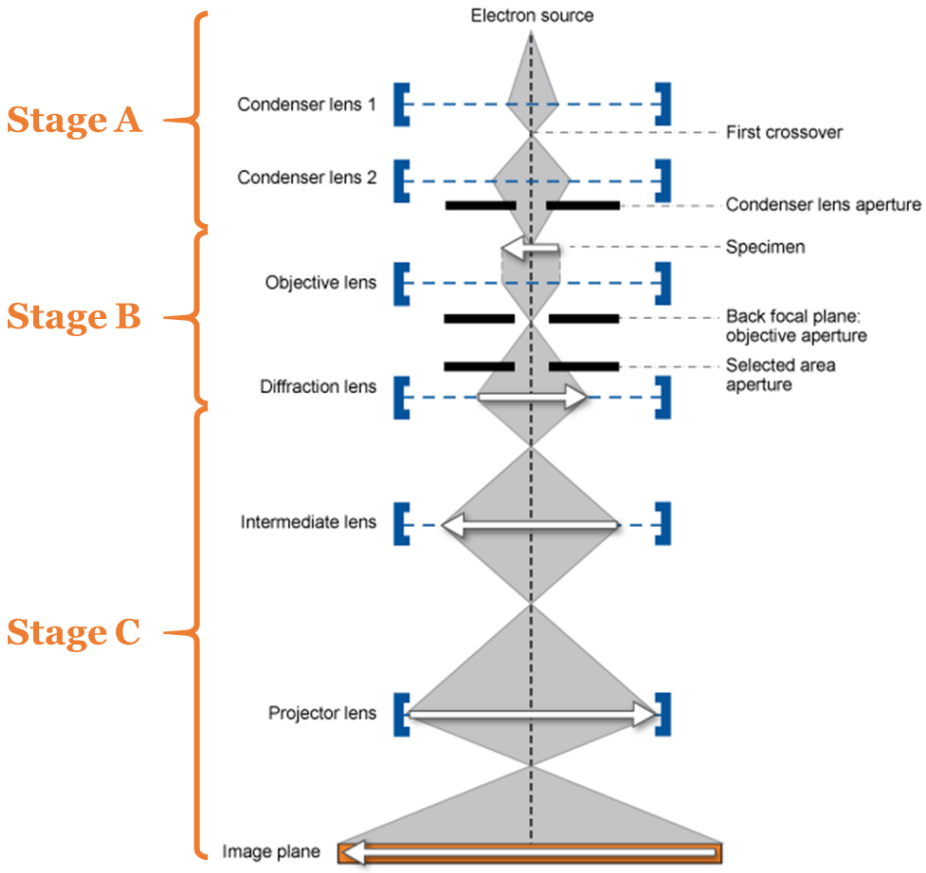

Figure 2.3. Schematic diagram showing the basic operating principles of a TEM. Image adapted from MyScope online education portal (https://myscope.training).

A schematic diagram portraying the basic operating principles of a TEM is given in **Figure 2.3**. It should be briefly noted that this diagram describes the operating principles for so-called conventional TEM, wherein a nearly parallel, broad beam of electron illumination is used, and an image is formed from the transmitted electrons that pass through an objective lens placed after the specimen. Pennycook and Nellist (Pennycook & Nellist, 2011) provide a detailed discussion on the operating principles for the closely related technique of scanning TEM (STEM), wherein the pre-specimen

objective lens is used to form a focused electron probe that is scanned over the sample to produce an image point-by-point. Conventional TEM was the primary operating mode used in the current work and will therefore be discussed exclusively.

The overall action of the TEM can be divided into three primary stages. The first stage, stage A, consists of an electron source and condenser lenses. This system of illumination is responsible for forming the incident beam of electrons. In stage B, the incident beam of electrons interacts with specimen, generating the signals that are used for imaging and spectroscopy. The electrons then pass through an objective lens, forming the primary image. Finally, in stage C, the primary image is highly magnified by a series of intermediate and projector lenses. The magnified image is ultimately transferred to the image plane, which typically consists of a fluorescent screen or a digital detector.

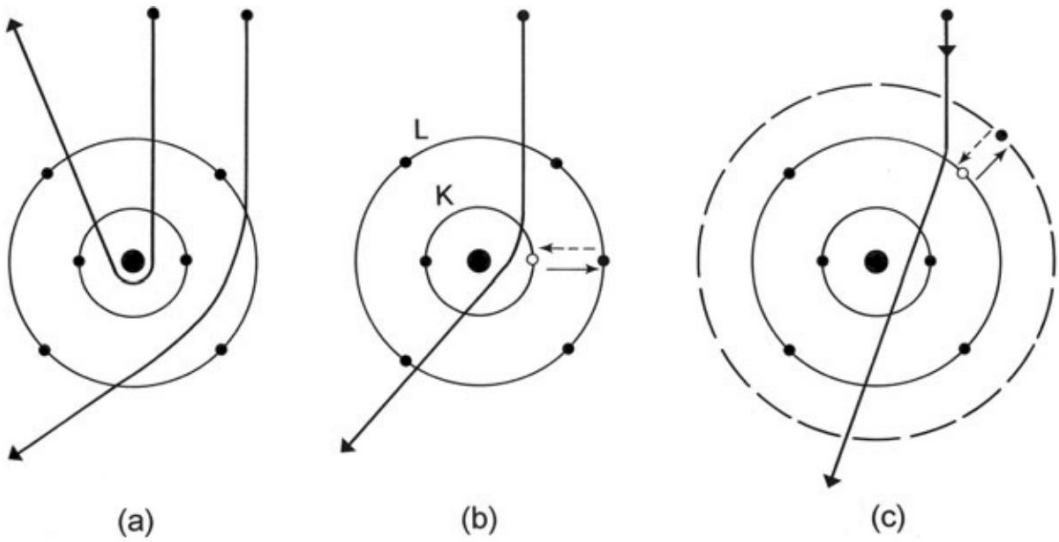

Figure 2.4. Classical view of electron scattering between an incident electron and a C atom. (a) Elastic scattering arises from the Coulombic interaction between the incident electron and atomic nucleus. Inelastic scattering arises from Coulombic interaction between the (b) inner-shell or (c) outer-shell atomic electrons, leading to excitation (solid arrows) to higher energy states, followed by de-excitation (broken arrows) leading to photon emission. Figure from (Egerton, 2011).

Electron-specimen interactions are the source of information about the sample and form the basis of TEM imaging and its associated techniques. As an incident electron passes through the specimen, it interacts with the atomic nuclei and bound electrons in the specimen through electrostatic Coulombic forces. As a result of these interactions the incident electron will scatter, which results in a change to the incident electron trajectory and in some cases may result in significant energy transfer to the specimen. Energy deposition from the beam into the sample may introduce irreversible radiation damage or other electron beam-induced changes that can adversely affect the examination of the specimen. In particular, such electron beam effects must be considered in order to properly interpret dynamic structural changes observed during *in situ* and *operando* TEM. These effects are discussed below in Section 2.3.6.

Electron scattering can be broadly distinguished into two categories: elastic and inelastic. **Figure 2.4** illustrates a subset of elastic and inelastic scattering events that may occur when an incident electron interacts with an isolated C atom (Egerton, 2011). Elastic scattering arises from interactions between the incident electron and the screened potential of the massive atomic nucleus. Such scattering typically results in the incident electrons being deflected through relatively large angles (e.g., > 15 mrad), and is generally responsible for electron diffraction and phase contrast. On the other hand, inelastic scattering arises from interactions between the incident electron and the atomic electrons that surround the nucleus. Considering the similarity in mass between the incident and atomic electrons, inelastic scattering typically involves considerable transfer of 10 – 1,000 eV of energy from the fast electron to the specimen. A simplified view of the inelastic scattering process considers that the incident electron experiences a Coulombic repulsion with the atomic electron, which excites the atomic electron into a higher energy state (which may involve atom ionization, plasmon excitation, exciton excitation, etc.). The

difference in energy between the initial and final electronic states is unique to specific elements, providing the basis for elemental and chemical analysis through electron energy-loss spectroscopy (EELS) and energy-dispersive X-ray spectroscopy (EDX).

Contrast in the TEM image can arise from changes in the amplitude and/or phase of the electron beam as it passes through the specimen. Phase contrast imaging was principally employed in the current work and will be discussed briefly. Phase contrast in an image arises when two or more beams (transmitted and/or scattered) are refocused to interfere with one another. Under ideal imaging conditions, the interference fringes present in the pattern may be interpreted in terms of the atomic structure of the imaged material. In general, however, the contrast of the interference pattern is notoriously sensitive to a multitude of instrumental and sample parameters, including lens aberrations, specimen thickness, crystal orientation, objective lens defocus, etc. Thus, phase contrast image interpretation often necessitates image simulations to reliably extract information about the structure of the imaged material (discussed in Section 2.4.1).

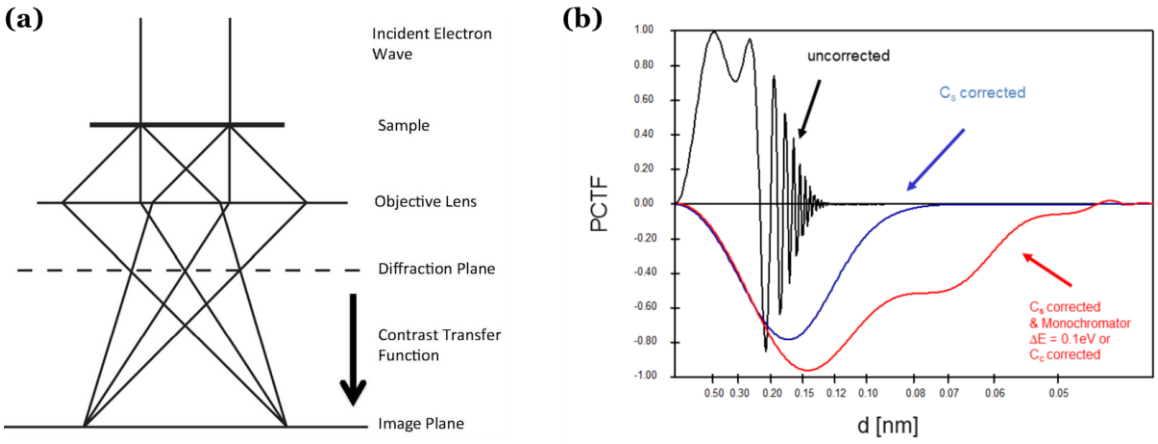

Figure 2.5. (a) Schematic ray diagram illustrating the principles of phase contrast imaging in a TEM. Image obtained from the Wikipedia commons. **(b)** Phase contrast transfer functions (PCTFs) of an uncorrected (black), a C_s-corrected (blue), and a dual C_s/C_c-corrected TEM operated at 300 kV. Figure from (Taheri et al., 2016).

A simplified schematic ray diagram illustrating the principles of phase-contrast imaging in a TEM is shown in **Figure 2.5a**. As can be seen in the figure, in this mode, the transmitted and diffracted beams exiting the sample pass through the objective lens, which refocuses them to form a magnified image at the image plane. In an ideal TEM, a point in the specimen would be mapped to a point on the image plane. Unfortunately, however, due to unavoidable aberrations present in circularly symmetric electromagnetic lenses, in addition to other sources of non-ideality, including the finite focal spread (i.e., temporal coherence) and beam divergence (i.e., spatial coherence) of the illumination, points in the specimen are mapped to extended regions on the image plane. Moreover, the diffracted beams passing through the objective lens can suffer from complicated phase modulations that are strongly dependent on the scattering angle, as well as the defocus and other aberrations of the lens. Understanding the effect these lens-dependent modulations have on the *phase contrast* in the image is required to interpret the high resolution TEM (HRTEM) image in terms of the atomic structure of the material.

Ignoring specimen effects as well as inelastic scattering (which can be neglected for suitably thin specimens), the complex process of optical transfer through the objective lens and ultimately to the image plane can be understood in terms of a phase contrast transfer function (PCTF). A detailed discussion of transfer function theory is beyond the scope of the present thesis but may be found in the following references: (Smith, 1997; Spence, 2003; Smith, 2008; Williams & Carter, 2008). In short, the PCTF describes the changes in image contrast that result from the phase modulations induced by the objective lens during the optical transfer process. The PCTF of a conventional, uncorrected TEM operated at the Scherzer defocus with an accelerating voltage of 300 kV is plotted as the black line in **Figure 2.5b** (Taheri et al., 2016). Note the presence of rapid phase oscillations at higher spatial frequency (i.e., smaller lattice fringe distance) beyond a broad

band of constant phase. The phase oscillations introduce contrast reversals and thus significant imaging artifacts which generally restrict the interpretable resolution limit to spatial frequencies less than the first crossover (0.25 nm for the black curve). Improvements in instrumentation, for example, spherical aberration (C_s) correction (**Figure 2.5b**, blue curve) and/or chromatic aberration (C_c) correction (**Figure 2.5b**, red curve), reduce the degree of phase oscillations imparted by the lens and further improve the interpretable resolution to beyond 1 Å.

2.3.2. Aberration correction

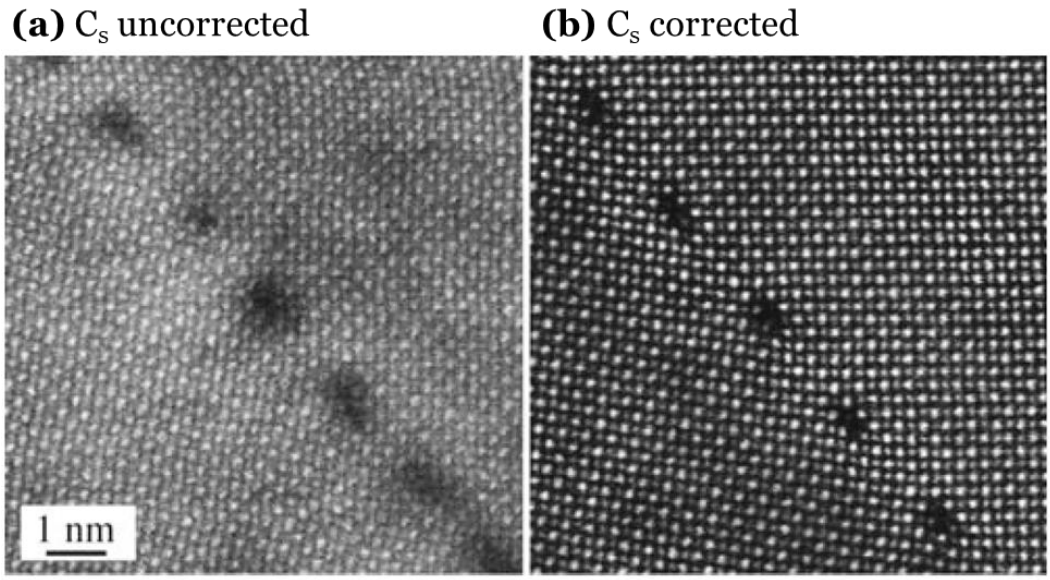

Figure 2.6. STEM image of a grain boundary in SrTiO3 (a) without C_s correction and (b) with C_s correction. Figure adapted from (Williams & Carter, 2008).

As discussed above, the presence of aberrations in the electron optical lens system induces significant phase changes to the electron beam, which lowers the resolution well below the diffraction limit and reduces the interpretability of the resultant image. The recent realization of aberration corrector systems in the late 1990's and their commercialization in the first decade of the 2000's thus introduced a remarkable transformation in the field of electron microscopy (Haider et al., 1998; Uhlemann &

Haider, 1998; Urban et al., 1999; Krivanek et al., 1999; Batson et al., 2002; Hetherington, 2004). The dramatic improvement in image contrast and resolution available with aberration correction is demonstrated in **Figure 2.6** (Williams & Carter, 2008), which shows a Z-contrast STEM image of grain boundary in $SrTiO_3$ (a) *without* C_s correction and (b) *with* C_s correction.

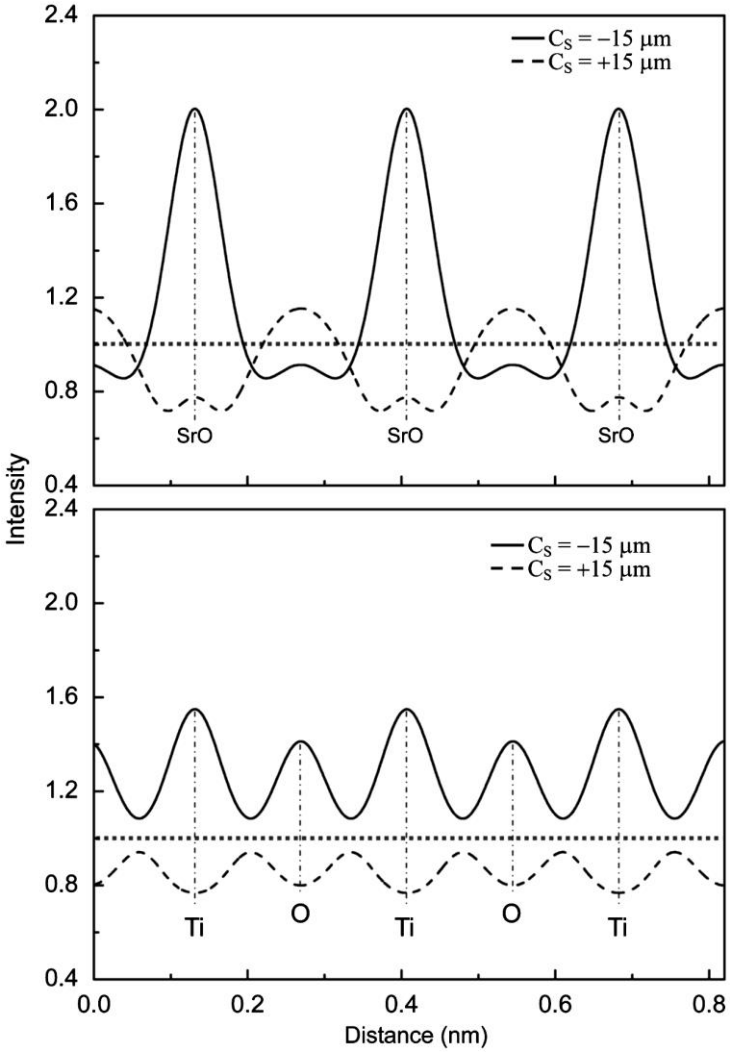

Figure 2.7. Intensity line profiles across SrO (top), and Ti and O (bottom) atomic columns from simulated images of $SrTiO_3$ with a thickness of 3.3 nm for phase contrast images with a Cs value of -15 µm (solid lines) and a Cs value of +15 µm (dashed lines). Figure from (C.L. Jia et al., 2010).

The implementation of aberration correctors into TEMs provides the operator not only with enhancements in resolution but also with additional parameters which may be tuned for certain experiments of interest. For example, Jia et al. demonstrated that tuning the spherical aberration coefficient to negative values results in an imaging modality (so called -C_s imaging, or NSCI) that yields enhanced phase contrast over traditional modes wherein the C_s value is tuned as close to zero as possible but remains small and positive (Jia et al., 2003, 2004; C.L. Jia et al., 2010). Bright-atom contrast is obtained in a slightly over-focus C_s HRTEM image, due to the constructive rather than destructive superposition of the linear and non-linear contributions to the image contrast (Jia et al., 2004). Since the contrast contributions constructively superimpose, the contrast in the image is considerably higher (e.g., > x2) than a traditional positive C_s, black-atom contrast image. As a result, weakly-scattering elements, e.g., O, become more visible.

The principle is illustrated in **Figure 2.7** (C.L. Jia et al., 2010), which plots intensity line profiles from SrO, Ti, and O columns from simulated images of $SrTiO_3$ with a C_s value of *negative* 15 μm (solid lines) and a C_s value of *positive* 15 μm (dashed lines). Note the significant improvement in visibility for the SrO columns as well as the large improvement in contrast for the weakly-scattering O columns. For this work, aberration correction was essential to resolve atomic-scale structural information at the surfaces and interfaces of CeO_2-supported catalyst nanoparticles. NCSI was used extensively for all projects, with a typical C_s value of around -15 μm. Other aberrations were tuned as close to zero as possible.

2.3.3. Indirect and direct electron detectors

For most of the 20th century, TEM images were recorded using photographic film. In the late 1980's and early 1990's, digital electron detectors were developed and commercialized, which offered significant advantages in terms of data throughput and

streamlined computerized image processing (Spence, 2003; Zuo & Spence, 2017). In particular, the development of digital electron detectors and associated in-line image processing was crucial to the implementation of commercially available aberration correctors, for which diffractograms of images are needed to measure the aberrations present in the electron beam (Krivanek & Fan, 1992; Smith, 1997; Hetherington, 2004). The first generation of digital cameras that replaced photographic film were based on an indirect exposure technique and on charge-coupled device (CCD) electronics (Spence & Zuo, 1988; Mooney et al., 1990; De Ruijter, 1995). **Figure 2.8a** illustrates a schematic diagram of the architectural principles for an indirect, CCD-based electron detector (Direct Electron, 2021). In these indirect detectors, the incoming electron signal is converted to a photon signal in a scintillator, which is transferred by a thick fiber optic coupling to a CCD, where the photon signal generates charges that are registered, read out, amplified, and digitized. A cooling layer (typically Peltier cooling to -20 – -5 °C) is also implemented in order to reduce noise in the sensor that may be associated with thermal fluctuations (also called dark current or dark noise).

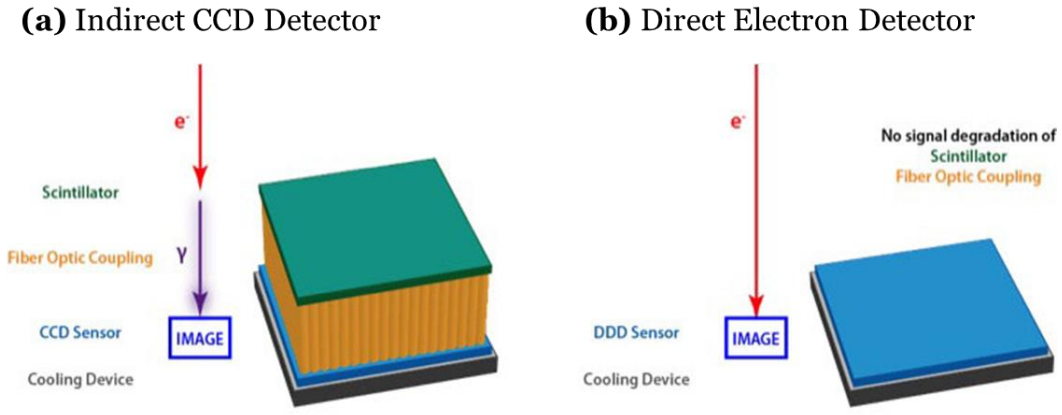

Figure 2.8. Architectural principles for TEM imaging detectors based on **(a)** charge-coupled devices (CCD) vs **(b)** direct electron detection. Figure adapted from (Direct Electron, 2021).

The scintillator-based CCD design was developed to protect the sensitive detector electronics from damage by high energy incident electrons. However, the indirect technique comes with significant drawbacks, including most notably the scattering of incident electrons in the scintillator layer, which leads to a spatial broadening of the arriving signal and a resultant loss of resolution (de Ruijter & Weiss, 1992; De Ruijter, 1995; Zuo, 1996). The characteristic broadening or blurring resulting from the detector itself can be measured and is described by a point spread function (PSF) in real space or by a related modulation transfer function (MTF) in reciprocal space. Another drawback of the indirect detection technique is that noise is introduced at each step in the sequence of signal conversion and optical transfer processes, leading to lower signal-to-noise ratio (SNR) per incident electron. The degree to which a detector introduces additional noise to a signal can be measured and is often reported in terms of a detective quantum efficiency (DQE), which is simply the squared ratio of output to input SNR (max value of DQE = 1).

Recently, the realization of highly efficient direct electron detectors has yielded significant improvements in performance. Direct electron detectors rely on a single electron-to-charge conversion by employing a thin, radiation-hardened complementary metal-oxide semiconductor (CMOS) pixel array detector design (Ruskin et al., 2013; Faruqi & McMullan, 2018). **Figure 2.8b** illustrates the architectural principles behind direct electron detector technology (Direct Electron, 2021). In this design, the scintillator and fiber optic coupling are eliminated, which improves the DQE by removing sources of noise. Thinning the sensor minimizes electron backscatter. Moreover, for CMOS-based sensors, the pixels are read out individually (compared with serially, via e.g., a shift register for slow-scan CCD detectors), greatly enhancing signal acquisition speed. Additional improvements in detector hardware and firmware have also led to the ability to perform electron counting, where individual electron arrival events are detected and

isolated to individual or even sub-pixel regions (Mooney et al., 2011; Ciston et al., 2019). The successful registration of individual electron arrival events to individual pixels has largely eliminated read-out noise and yielded improvements to detector MTF and DQE.

In this work, a CCD detector was used for the experiments reported in Chapter 4, while a direct electron detector was used for the experiments reported in Chapters 5 and 6. The direct electron detector was particularly useful for acquiring high time-resolution series of images of Pt/CeO_2 nanoparticles undergoing dynamic fluxional behavior in reactant gas atmospheres. The image time-series were typically acquired with frame rates around 20 – 40 frames per second (fps) unless otherwise specified. Image time-series were binned in time or space as desired by addition, not averaging. Time-series of images acquired on direct detectors were aligned in the Digital Micrograph (DM) software after acquisition *without interpolation* in order to preserve the original number of counts in each pixel. No imaging filter was used during the calculation of the alignment shift vectors.

2.3.4. Electron energy-loss spectroscopy (EELS)

EELS is a powerful spectroscopic technique capable of probing the physical, chemical, and optical properties of solids, liquids, and gases. When combined with a highly focused STEM probe, such information can be accessible with atomic resolution. A comprehensive handbook for EELS in the TEM has been written by Egerton (Egerton, 2011), and additional literature detailing the instrumentation, theory, and practice of EELS can be found in: (Williams & Carter, 2008; Colliex, 2019; Brydson, 2020).

In this work, EELS was implemented during *operando* TEM to quantify the composition of gas surrounding the catalyst during catalysis and to measure the reaction rate of the catalyst during atomic-resolution imaging (Crozier & Chenna, 2011; Chenna & Crozier, 2012; Miller & Crozier, 2014; Vincent et al., 2020; Vincent & Crozier, 2021). The basic principles of TEM EELS are illustrated in **Figure 2.9** (Williams & Carter, 2008).

Part (a) illustrates how the spectrometer system is interfaced to the column below the viewing screen and provides a quick reference to the location of various spectrometer components. Electrons entering the spectrometer are selected by a variable-sized entrance aperture, travel through a magnetic prism where they are deflected through ≥ 90° depending on their energy, are therefore dispersed in terms of their energy, and are finally projected onto an electron detector for digital spectral acquisition. The action of the magnetic prism, which functions similarly to a glass prism for photon radiation, is emphasized in part (b). The spectrum thus formed on the dispersion plane shows intensity as a function of energy loss. It should be briefly noted that for TEM EELS, the object of the spectrometer lens system is the back-focal plane of the projector lens.

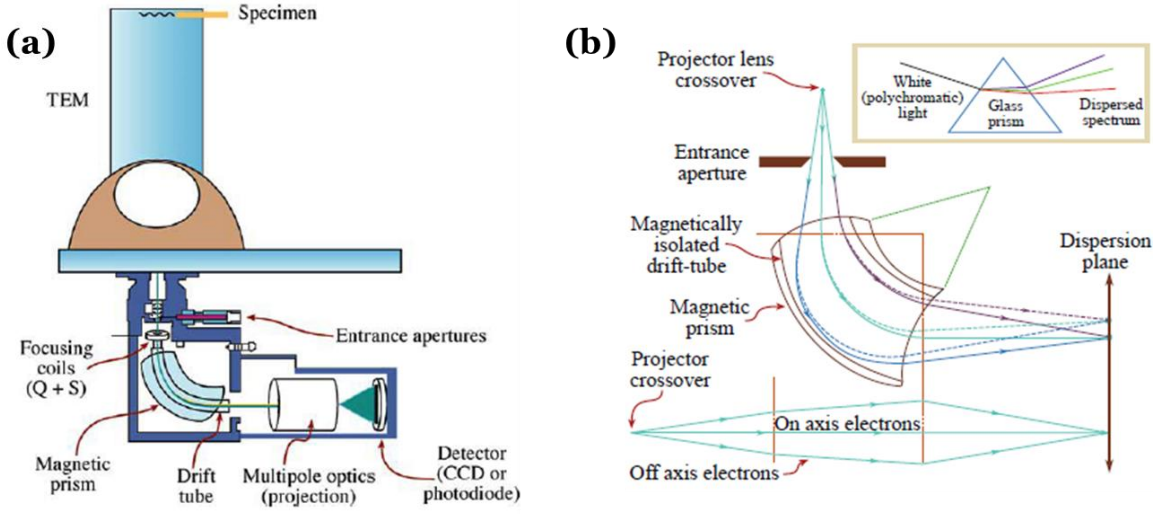

Figure 2.9. Schematic diagram illustrating **(a)** how a post-column spectrometer is interfaced to the TEM below the viewing screen, and **(b)** the action of the magnetic prism that disperses the electrons entering the spectrometer into a spectrum based on their energy, much like a glass prism that disperses photons based on their energy. Figures obtained from (Williams & Carter, 2008).

The EEL spectrum can be divided into three regions: zero-loss, low-loss, and core-loss. An example energy-loss spectrum of a Ni/NiO sample plotted on a logarithmic intensity scale is shown in **Figure 2.10a** with these regions marked (Williams & Carter,

2008). The zero-loss peak is comprised of electrons that have lost negligible energy upon transmitting through the specimen (i.e., predominately elastically scattered electrons) and is the most intense feature in the energy-loss spectrum. The low-loss region (also called the valence-loss) usually lies within ~50 eV of the zero-loss peak, and it generally contains information about inelastic scattering events that occurred between the incident electron beam and the outer shell (i.e., valence shell) electrons bound to atoms in the specimen (e.g., optical responses, plasmonic responses, heavy element M and N shell excitation, etc.). Recent developments in TEM monochromation have improved the available energy resolution to the order of 10 meV, opening up analysis for electron-beam induced vibrational excitations that lie in the ultra-low loss regime around ≤ 500 meV (Krivanek et al., 2014; Venkatraman et al., 2019). The core-loss region begins beyond ~50 eV and generally contains information about inelastic events that occurred between the incident electron beam and the core-level electrons deeply bound to atoms in the specimen.

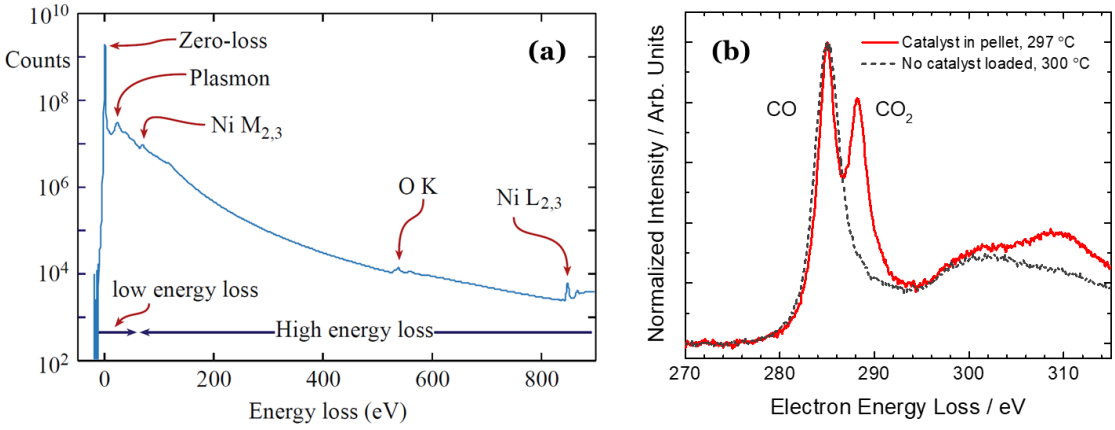

Figure 2.10. (a) Electron energy-loss spectrum of a Ni/NiO sample displayed on a logarithmic intensity scale over a broad range of energy-loss. Figure from (Williams & Carter, 2008). **(b)** Core-loss *in situ* EEL spectra of the gas surrounding the *operando* ETEM reactor during conditions of catalysis when *no* catalyst is loaded in the reactor (dashed gray line) and when ~180 μg of catalyst *is* loaded (solid red line). Figure from (Vincent & Crozier, 2021).

In this work, *in situ* core-loss EELS was performed on the gas surrounding the catalyst during CO oxidation in order to quantify the gas composition and to determine the reactant conversion. For CO oxidation, the quantification is relatively straightforward as the CO and CO_2 signals can be easily differentiated. **Figure 2.10b** (Vincent & Crozier, 2021) displays an *in situ* core-loss EEL spectrum centered on the C K-edge taken from the gas atmosphere in the *operando* ETEM reactor for a temperature of ~300 °C when *no* catalyst is loaded in the reactor (dashed gray line) and when ~180 μg of catalyst *is* loaded in the reactor (solid red line). As seen in the solid red curve, the π* peaks corresponding to CO and CO_2 are clearly distinguishable and well-separated by 3.3 eV loss. The π* peaks arise from the excitation of a C 1s electron to the unoccupied anti-bonding π* orbital. As discussed extensively in (Crozier & Chenna, 2011; Chenna & Crozier, 2012; Miller & Crozier, 2014), the ratio of CO to CO_2 can be determined by fitting the experimental energy loss spectra to a linear combination of reference spectra acquired individually from CO and from CO_2. It is critical that the reference spectra be acquired under identical spectroscopic conditions as the experimental spectra. For these measurements, the microscope was operated in broad-beam TEM mode and core-loss spectra of the gas were collected in diffraction mode, using a spectrometer entrance aperture of 2 mm, a camera length of 245, a dispersion 0.05 eV/pixel, and an acquisition time of 5 seconds. Given the 1:1 stoichiometry of C in the CO oxidation reaction, the *in situ* CO conversion can be calculated as the fractional amount of CO_2 to CO and CO_2. The catalytic reaction rate may be estimated by multiplying the conversion by the inlet flowrate of reactant.

2.3.5. *In situ* and *operando* environmental electron microscopy (ETEM)

Aberration-corrected *in situ* and *operando* ETEM is a powerful characterization tool capable of providing atomic-level information from high surface area catalysts under reaction conditions. A literature review covering seminal *in situ* and *operando* ETEM

research applied to heterogeneous catalysis is given in Chapter 1, Section 1.2. In this thesis, both *in situ* and *operando* ETEM are employed to investigate the atomic-scale dynamic fluxional behavior of CeO_2-supported Pt nanoparticle catalysts when exposed to reactant gas atmospheres and heated to catalytically-relevant elevated temperatures (Chapters 4 and 5) or when imaged during simultaneous measurements of the catalytic reaction rate (Chapter 4). All *in situ* and *operando* ETEM experiments were conducted at 300 kV in a differentially-pumped, aberration-corrected Thermo Fisher Titan ETEM equipped with a Gatan Imaging Filter for EELS.

A conceptual overview of the *operando* ETEM technique as implemented in a differentially-pumped ETEM is given in **Figure 2.11** (adapted from Miller et al., 2015). An *operando* pellet reactor approach was implemented to increase the mass of catalyst in the microscope and facilitate the determination of chemical kinetics during atomic-resolution imaging (Chenna & Crozier, 2012; Miller et al., 2015; Langdon et al., 2019). An overview of the *operando* ETEM pellet reactor geometry is given in the middle of **Figure 2.11**. In this approach, a Gatan 628 furnace-style Ta hot stage is used for heating. The Ta is inactive. The furnace is loaded with a porous glass fiber pellet and an inert Ta metal TEM grid. Catalyst particles are dispersed on the TEM grid for imaging. Catalyst is also loaded into the porous glass fiber pellet. A detailed description of the *operando* pellet fabrication process is given in the Appendix, Section A.1.

When heated in reactant gases, the relatively large mass of catalyst on the pellet facilitates the production of detectable conversions (for this work, m_{cat} = 180 ± 5 μg). Since the fiber pellet is annular in shape, having a 1 mm wide hole at its center, the electron beam can pass through unobstructed for spectroscopy and imaging. The TEM grid is visible in the region containing the hole, and it is conducting, so it provides a stable platform for atomic-resolution imaging.

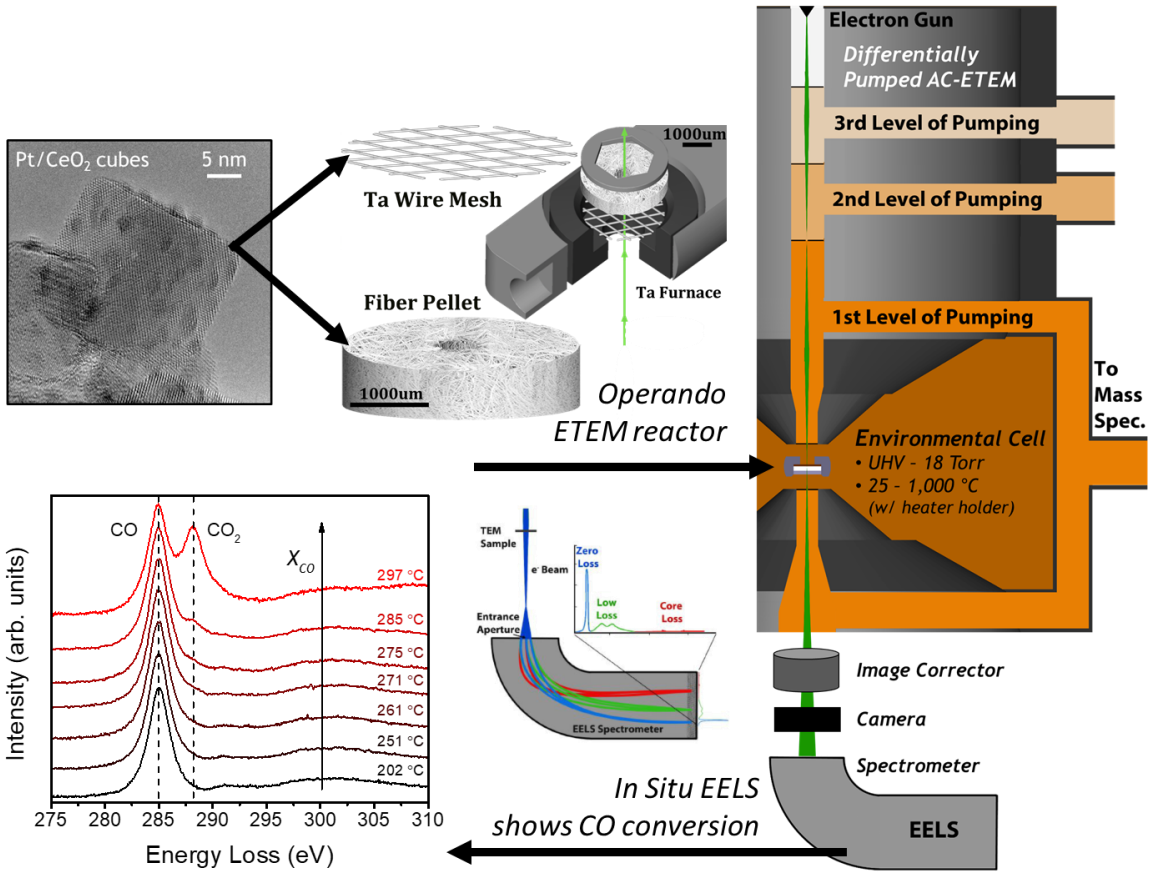

Figure 2.11. Schematic of aberration-corrected *operando* ETEM experimental methodology. Figures for reactor and differentially-pumped ETEM adapted from (Miller et al., 2015).

In situ ETEM experiments were also conducted in an image-corrected differentially-pumped ETEM, often using a DENSsolutions Wildfire micro electromechanical system (MEMS)-based SiN_x chip heating holder. The as-received MEMS chips were ion-milled in a Thermo Fisher Helios Dual Beam FIB SEM machine with a patterned array of roughly ~800 nm circular holes separated by ~1,400 nm from center to center, to provide regions for the catalyst to be imaged without interference from the SiN_x membranes. The chip was briefly plasma cleaned in an O_2 environment for 3 seconds prior to loading the sample in order to improve the dispersion of the powder on the chip. Catalyst powder was dispersed in ultra-pure H_2O and then drop cast onto the already plasma-cleaned and milled chip, which was then loaded into a DENSsolutions

Wildfire heating holder. Extreme caution must be exercised when preparing a MEMS-based SiN_x chip sample so as to avoid over-loading the chip with catalyst particles. An optical microscope with 40x magnification or better was found to be helpful in evaluating the amount of powder loaded onto the chip during preparation. Additional care must be taken to properly ground the electrical leads that provide heating to the holder in order to avoid ground loops or other electrical instabilities that can interfere with high-resolution TEM imaging. Further methodological details on *in situ* and *operando* ETEM experiments will be provided in the associated results chapters where necessary.

2.3.6. Electron beam-induced dynamic changes to the specimen structure

Dynamic structural changes observed during *in situ* and *operando* ETEM experiments can be attributed to thermally-activated processes or to electron beam-induced displacements. Understanding which of these mechanisms dominates under experimental conditions is necessary to attribute observed fluxional behavior to catalytic materials functionality instead of the incident electron beam. Knowledge of the dominant mechanism can be obtained by comparing the relative rates of thermally-activated and electron beam-induced atomic displacement events. In general, the rate of any atomic displacement event will depend on the activation energy, E_a, needed to move the atom through an energetic saddle point to a new spatial position. The kinetics of thermally-activated displacement events can be modeled with an Arrhenius equation, which has an exponential dependence on the activation energy:

Eq. 2.1 $$N_{th} = A \exp\left(-\frac{E_a}{k_B T}\right)$$

Here, N_{th} is the number of thermally-activated displacement events per second per atomic site, A is the attempt frequency, T is the absolute temperature in Kelvin, and k_B is the Boltzmann constant (8.6173×10^{-5} eV K^{-1}). The attempt frequency can be estimated as 10^{13}

s^{-1} (Lawrence, 2019). **Figure 2.12** below plots the thermally-activated Pt atom displacement rate as a function of E_a for temperatures of 20 °C (green solid line), 200 °C (olive dashed line), and 400 °C (cyan dashed line).

The electron beam may induce atomic displacements by transferring momentum through ionization damage (i.e., radiolysis) and from direct collisions with atomic nuclei (i.e., knock-on damage). The kinetics of these displacement events depend on the corresponding damage cross sections, σ_D, and on the incident electron flux, Φ^{e^-} (Egerton et al., 2004; Egerton, 2013, 2019):

Eq. 2.2 $$R = \Phi^{e^-}\sigma_D$$

Here R is the rate of a beam-induced displacement event, with units of events per second per atomic site. The incident electron flux Φ^{e^-} is a controlled parameter that is known experimentally. Often it was set to 600 – 5,000 $e^-/Å^2/s$ in the experiments reported in this thesis. The following calculations will therefore be performed with a value of 5,000 $e^-/Å^2/s$ to provide an upper bound on the displacement rate. The cross sections for both types of damage can be calculated from first principles, enabling the rates of electron beam-induced atom displacement to be derived as a function of activation energy. The following derivation and discussion will focus on Pt atoms. Rates of thermal and electron beam-induced displacements for O and Ce atoms are presented in the Appendix, in Section A.2

Knock-on displacement damage kinetics

Knock-on displacement damage arises from energy transfer during elastic scattering processes (Egerton, 2019). Due to the large difference in mass between electrons and atomic nuclei (e.g., $\frac{M_{atom}}{m_e} > 10^4 - 10^6$), only a fraction of the incident electron energy may be transferred to the scattering atom. Assuming the mass of the atom

is initially at rest, relativistic kinematics yields an expression for the maximum energy transferred, E_{max} (Egerton, 2019):

Eq. 2.3 $$E_{max} = 2E_0(E_0 + 2m_0c^2)/Mc^2$$

Here, E_0 is the kinetic energy of the incident electron (300 keV in this work), m_0 is the rest mass of the incident electron, c is the speed of light in vacuum, and M is the mass of the scattering atom. For a Pt atom, algebraic substitution yields that E_{max} = 4.4 eV. Similar calculations yield a value of E_{max} = 6.1 eV for a Ce atom and a value of E_{max} = 53.1 eV for an O atom.

During elastic scattering, the condition of maximum energy transfer corresponds to a direct collision between the incident electron and the scattering atom, resulting in complete back-scatter. In general, however, the incident electron will be deflected through a smaller angle and an energy $E < E_{max}$ will be transferred to the scattering atom. It can be shown that an electron that undergoes elastic scattering through an angle θ transfers an energy E to the atomic nucleus equal to (Egerton, 2019):

Eq. 2.4 $$E = E_{max} \sin^2\left(\frac{\theta}{2}\right)$$

The maximum energy transfer is obtained during a back-scattering event corresponding to θ = 180°. Typical values of elastic energy transfer as a function of scattering angle are tabulated below in **Table 2.1** for O, Ce, and Pt atoms. As an aside, note that at E_0 = 300 kV, the Bragg scattering angles for lattice planes with d_{hkl} > 0.7 Å are all less than 1° (17.45 mrad), which corresponds to small energy transfer on the order of ~1 meV.

Table 2.1. Energy transferred during elastic scattering by O, Ce, and Pt atoms as a function of electron scattering angle $\boldsymbol{\theta}$.

Scattering Angle	O atom	Ce atom	Pt atom
1°	4 meV	0.5 meV	0.3 meV
5°	100 meV	11 meV	8 meV
90°	26.6 eV	3.0 eV	2.2 eV
180°	53.1 eV	6.1 eV	4.4 eV

The differential cross section for elastic scattering of high energy electrons by atomic nuclei can be approximated by the relativistic Rutherford scattering cross section formula (Egerton, 2013). Strictly speaking, for electron scattering at large angles from heavy elements like Pt, the Mott scattering cross section should be used, which accounts for the incident electron spin (Reimer & Lödding, 1984; Reimer, 1998). Nonetheless, the Rutherford scattering cross section is used in this analysis due to it being far simpler to calculate. Calculations by Reimer and Lödding show that for Au (Z = 79, close to Pt for which Z = 78) the ratio of the Mott to Rutherford cross sections approaches a factor of approximately two at high accelerating voltage (e.g., ~100 kV) (Reimer & Lödding, 1984). The choice to implement the simpler Rutherford cross section should thus have a minor impact on the conclusions reached by the following analysis. However, it should be noted that the difference between the Mott and Rutherford scattering cross sections becomes more pronounced at lower accelerating voltages (e.g., ≤ 80 kV), and that such simplifying approximations may no longer be valid under such conditions.

The relativistic Rutherford differential scattering cross section is given by the following equation, written here with respect to scattering angle, θ, after integrating over the azimuthal angle (Egerton, 2013):

Eq. 2.5 $$\frac{d\sigma}{d\theta} = \left[\frac{e^2 Z}{(8\pi\varepsilon_0 E_0)}\right]^2 \left[\frac{E_0 + m_0 c^2}{E_0 + 2m_0 c^2}\right]^2 \left[\frac{2\pi \sin\theta}{\sin^4\frac{\theta}{2}}\right]$$

The differential scattering cross section must be integrated over a range of angles (θ_{min}, θ_{max}) that corresponds to scattering events which could transfer sufficient energy E to the atomic nuclei in order to activate a displacement event. The maximum transferrable energy is E_{max} as determined by **Eq. 2.4** above. Thus θ_{max} = π. The minimum transferrable energy can be left as an open variable in the integration, allowing the scattering cross section to be expressed in terms of a displacement activation energy E_a. Such arbitrary transfers of energy simply result from scattering through angles given by manipulation of **Eq. 2.4**. Thus, $\theta_{min} = \arcsin\left[2\left(\frac{E_a}{E_{max}}\right)^{0.5}\right]$. Analytical integration and algebraic substitution yields a knock-on damage scattering cross section for energy transfer in the range of E_a to E_{max} by 300 kV electrons:

Eq. 2.6 $$\sigma_D = (0.2659 \times 10^{-28}\, m^2) \times Z^2 \left[\frac{E_{max}}{E_a} - 1\right]$$

The knock-on damage cross section σ_D for a displacement event requiring an energy E_a can thus be calculated for any given atom with atomic number Z and maximum elastically transferred energy E_{max}. Following **Eq. 2.2**, the knock-on displacement rate can be estimated simply as the product of this cross section and the incident electron dose rate. The rate of knock-on displacement events has been calculated for Pt under the experimental conditions relevant to this work and is plotted as a function of activation energy as the solid blue line in **Figure 2.12** (The rate of knock-on displacements is also plotted as a function of activation energy for O and Ce atoms in **Figure A.1** and **Figure A.2**, respectively).

Radiolytic displacement damage kinetics

The electron beam may induce radiolytic displacements due to ionization processes resulting from inelastic scattering (Egerton, 2019). Following Hobbs, the scattering cross section for radiolytic displacement events requiring a minimum energy E_a can be estimated as follows (Hobbs, 1984, p. 422):

Eq. 2.7 $$\sigma_D^* = 7 \times 10^6 \, \xi \, \left(\frac{Z}{E_a}\right) (barns = 10^{-28} \, m^2)$$

Here ξ is an efficiency factor that varies by material and decreases for materials with higher electronic conductivities. In SiO_2, the value of ξ is reported to be = 10^{-4} (Hobbs, 1984). CeO_2 has an electronic conductivity that is orders of magnitude higher than SiO_2. Thus, for O and Ce atoms in CeO_2, an efficiency factor of ξ = 10^{-5} can be chosen as a conservative upper bound, following (Lawrence, 2019) In metals, the ionized center can be delocalized by conduction band electrons in approximately 1 fs, which is 10^2 – 10^3 x faster than the mechanical relaxation time of the atomic nucleus (i.e., the phonon period) (Egerton, 2019). Radiolysis is thus not prevalent in metals and therefore no radiolytic displacement rate was calculated for Pt. The rate of radiolytic displacement due to an incident electron flux of 5,000 e-/Å^2/sec is plotted as the red line as a function of activation energy for O and Ce atoms in **Figure A.1** and **Figure A.2**, respectively.

The rates of thermally-activated and beam-induced displacements to Pt atoms are summarized in **Figure 2.12.** The thermal displacement rate is a strong function of activation energy, with displacement events having E_a lower than approximately 0.75 eV showing more than one occurrence per second at room temperature. The rate of knock-on damage is a weaker function of activation energy and begins to give rise to more than one displacement event per second for sites with E_a lower than approximately 0.3 eV. However, at this activation energy, the thermal displacement rate is many orders of

magnitude larger than the knock-on damage rate. At room temperature, displacement events due to electron bombardment dominate those due to thermal fluctuations for events with activation energies E_a < 0.77 eV. At higher temperatures, e.g., 300 °C, thermally-activated displacement dominates dynamic motion for events with even larger activation energies up to ~1.5 eV.

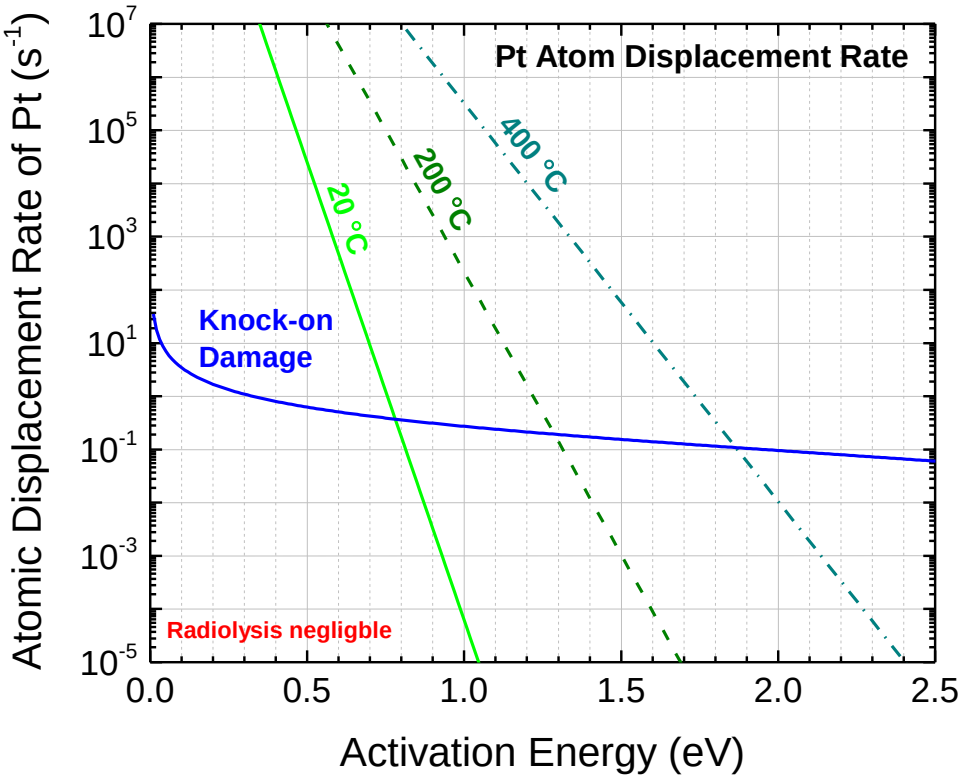

Figure 2.12. Thermally-activated and electron beam-induced Pt atom displacement rate (displacement per atom per second) as a function of displacement activation energy. Knock-on damage rate shown for an incident electron flux of 5,000 e-/Å^2/sec. Radiolysis is considered negligible (< 10^{-5} event/site/sec) and thus not shown.

Insight can be gained into the prevalence of electron beam effects on the *in situ* and *operando* TEM observations made in this thesis by examining the activation energy required for Pt adatom self-diffusion. Experimental measurements for the activation energy of adatom self-diffusion on Pt (111), (110), and (100) single crystal surfaces were taken from (Kyuno et al., 1998; Linderoth et al., 1997; Kellogg & Feibelman, 1990), and

reported to be 0.26, 0.81, and 0.47 eV, respectively. For these activation energies, the knock-on displacement rate is on the order of ~1 site/sec. At and above 200 °C, the thermal displacement rate is larger than the knock-on rate by orders of magnitude. Thus, for *in situ* and *operando* work at elevated temperatures, dynamic changes to the Pt atomic structure may be attributed to thermal processes rather than to the electron beam.

At room temperature, the knock-on rate for diffusion on Pt (110) (activation energy of 0.81 eV) is comparable to the thermal rate. However, it should be mentioned that the *in situ* and *operando* TEM observations made in this thesis were often done in the presence of strongly adsorbing gases such as CO. The presence of such gases may increase the adatom diffusion rate through the formation of adatom-adsorbate complexes, which may have a lower diffusion activation energy. For example, *in situ* scanning tunneling microscopy (STM) measurements and DFT calculations performed by Horch, Helveg, Nørskov, et al. show that dissociatively adsorbed H atoms on Pt *decrease* the activation barrier for Pt diffusion across Pt (110), which leads to a factor of 500 enhancement in the Pt adatom diffusion rate (Horch et al., 1999). Controlled experiments for Pt in the presence of CO were not found at the time of writing, however, the activation energies reported for Pt self-diffusion in ultra-high vacuum (UHV) conditions may be regarded as upper bounds compared to that in the presence of strongly adsorbing CO gas. These upper bounds demonstrate that dynamic structural changes induced by the electron beam may be largely neglected compared to changes from thermal fluctuations at temperatures above 20 °C.

2.4. Computational methods

2.4.1. Multislice TEM image simulation

As discussed above, simulations are often necessary to interpret phase contrast HRTEM images. A comprehensive yet accessible introduction to the history and theory of

image simulation in TEM has been written by Kirkland (Kirkland, 2010). In this thesis, multislice TEM image simulations were used for interpreting experimental micrographs (Chapters 4 and 5) and also primarily to generate a large and flexible image dataset used for training and testing a convolutional neural network for image denoising (Chapter 6).

Introduced by Cowley and Moodie in 1957 (Cowley & Moodie, 1957), the multislice method is a simple and powerful approach that has triumphed in popularity over others (e.g., Bloch wave-based methods) due to its notable advantages, which include faster computational speed (N^3 for Bloch wave vs. $N \times \log_2 N$ for multislice) and the ability to simulate structures with defects. A schematic diagram illustrating the overall approach of the multislice method is given in **Figure 2.13** (adapted from Kirkland, 2010). As shown in parts (a1) through (a3), in this method the specimen is segmented into thin two-dimensional slices along the electron beam direction. The incident electron beam is sequentially transmitted through a slice and then propagated to the next slice. The specimen slices are thin enough (usually 1 atom thick) so that each slice can be treated as a weak phase object, which simply introduces a local phase shift in the electron wave due to the projected electrostatic atomic potential in the slice. The free-space propagation of the outgoing wavefront to the subsequent slice is treated by Fresnel diffraction, as shown in **Figure 2.13b** (Kirkland, 2010). The transfer of the exit surface wavefunction leaving the last slice through the optical system of the TEM and the detection of the image by an electron sensor can also be easily simulated. This functionality in particular is useful for discriminating the image features that are due to the specimen from those that are undesirable artifacts due to lens aberrations. It can also be useful for determining the best imaging conditions for a particular experiment.

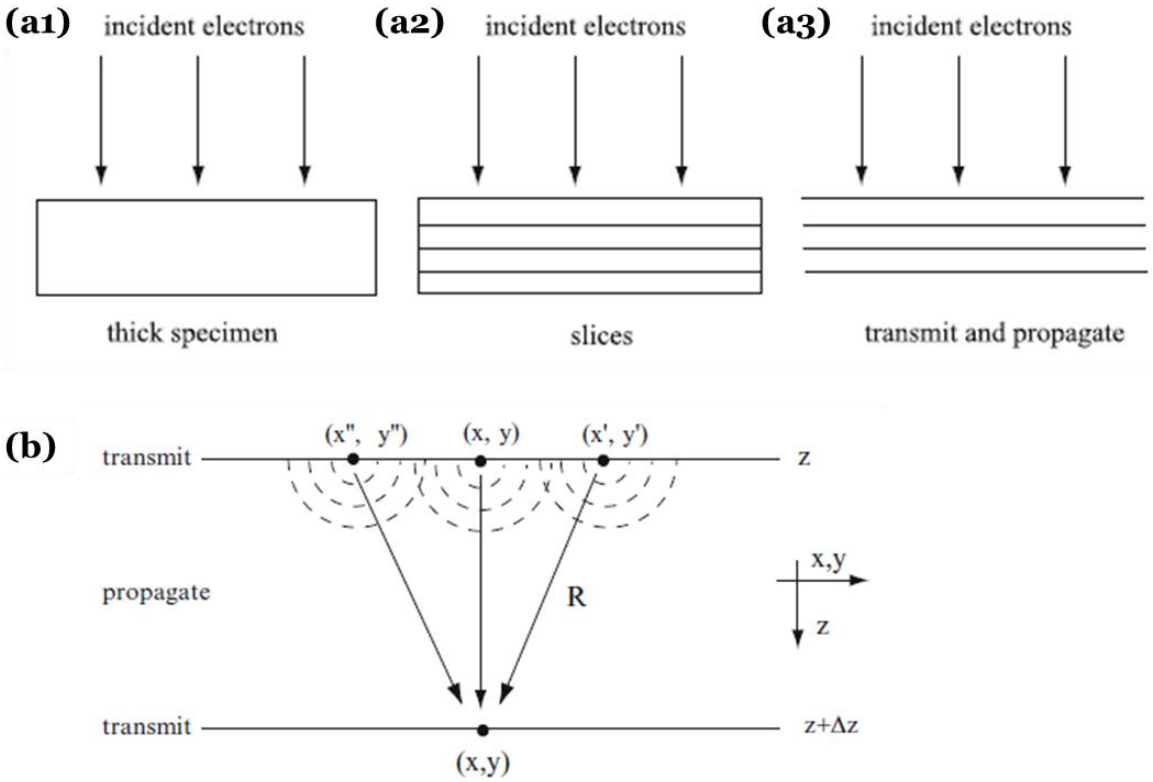

Figure 2.13. (a) Schematic diagram illustrating the overall principle of the multislice method, wherein (a1) a thick specimen is decomposed into (a2) many atomically thin slices, and finally (a3) the electron-specimen interaction is calculated by sequentially transmitting and propagating the electron beam through all the slices. **(b)** Free-space propagation between slices is treated with Fresnel diffraction. Each point in the outgoing wavefront at slice *z* emits a spherical wave, all of which recombine at every point at the next slice. Figures from (Kirkland, 2010).

2.4.2. Finite element modeling of the *operando* ETEM reactor

As discussed previously in Section 2.3.5, the *operando* ETEM reactor differs greatly from reactor architectures typically employed in chemical reaction engineering (e.g., the bench-top packed bed plug flow reactor discussed in Section 2.2). To determine quantitative chemical kinetics for gas-phase catalysis, it is necessary to develop a reliable chemical engineering model to describe catalysis as well as heat and mass transport processes within the ETEM cell. In Chapter 3, a finite element model combining fluid dynamics, heat transfer, multi-component mass transport, and chemical reaction engineering is developed to determine the gas and temperature profiles present during

catalysis in an *operando* experiment performed in an open cell ETEM. Additionally, the model provides a framework for relating the *in situ* conversion measured with EELS to the chemical reaction rate of the catalyst that is imaged during an experiment.

The finite element method is a common numerical approach for solving complex partial differential equations (PDEs) in arbitrary geometries of interest. The method involves discretizing the entire system of interest into many smaller, simpler regions known as finite elements; numerical solutions to the PDEs are approximated over these much smaller elements and ultimately stitched together to form an approximate solution to the entire system, subject to the initial/boundary conditions and a specified tolerance of error. Further details on the method are beyond the scope of this thesis but may found readily in the following references: (Zienkiewicz, 2000; Tabatabaian & Tabatabaian, 2014; Peksen, 2018). In this work, simulations were conducted with commercial program COMSOL® Multiphysics. In Chapter 3, the model was developed and applied to a Ru/SiO_2 catalyst performing CO oxidation. In Chapter 4 it was applied to a Pt/CeO_2 catalyst performing CO oxidation. A description of the modeling decisions and governing partial differential equations and boundary conditions will be given in Chapter 3, Section 3.2.1.

2.4.3. Deep convolutional neural networks for image denoising

Denoising is a fundamental challenge in atomic-resolution TEM imaging. Even with a perfect electron detector, Poisson noise degrades the information content of the image, lowering the sensitivity for atomic column detection and limiting the precision for determining the atomic column occupancy. Deep convolutional neural networks (CNNs) based on machine learning techniques achieve state-of-the-art denoising performance on natural images and are an emerging tool in various fields of scientific imaging (Liu & Liu, 2019; Tian et al., 2019). In Chapter 6, a supervised deep CNN is developed to denoise atomic-resolution TEM images of nanoparticles acquired in applications where the image

signal is severely limited by Poisson shot noise (Vincent et al., 2021). CNNs are a variety of artificial neural network that are characterized by performing convolutional operations in one or more of their layers. The convolutional operation provides the network with a way to learn about the spatial distribution of the input data, which makes CNNs particularly adept at tasks involving image data, including, e.g., classification, segmentation, and denoising. Describing the theoretical principles and the practical aspects of deep CNNs is beyond the scope of the present work, although the necessary basic elements relevant to the work performed in Chapter 6 will be elaborated below. For an introduction to the quickly evolving field of deep learning-based CNNs, especially as it is applied to image denoising, the reader is referred to the following references: (Goodfellow et al., 2016; Liu & Liu, 2019; Tian et al., 2019).

A schematic overview of the deep CNN training, application, and evaluation process is provided in **Figure 2.14** (Vincent et al., 2021). Before being applied to the real data, the network must learn how to perform the denoising task, which is done by training and evaluating on a specific set of training data (**Figure 2.14**, top). In this thesis, the network has been trained on a large dataset of noisy images produced through multislice TEM image simulation. During the course of this thesis, alternative so-called unsupervised methods, which train directly on the noisy experimental data itself and do not require simulations, were also explored (Sheth et al., 2020; Mohan, Manzorro, et al., 2020); however, these techniques will not be described here for brevity.

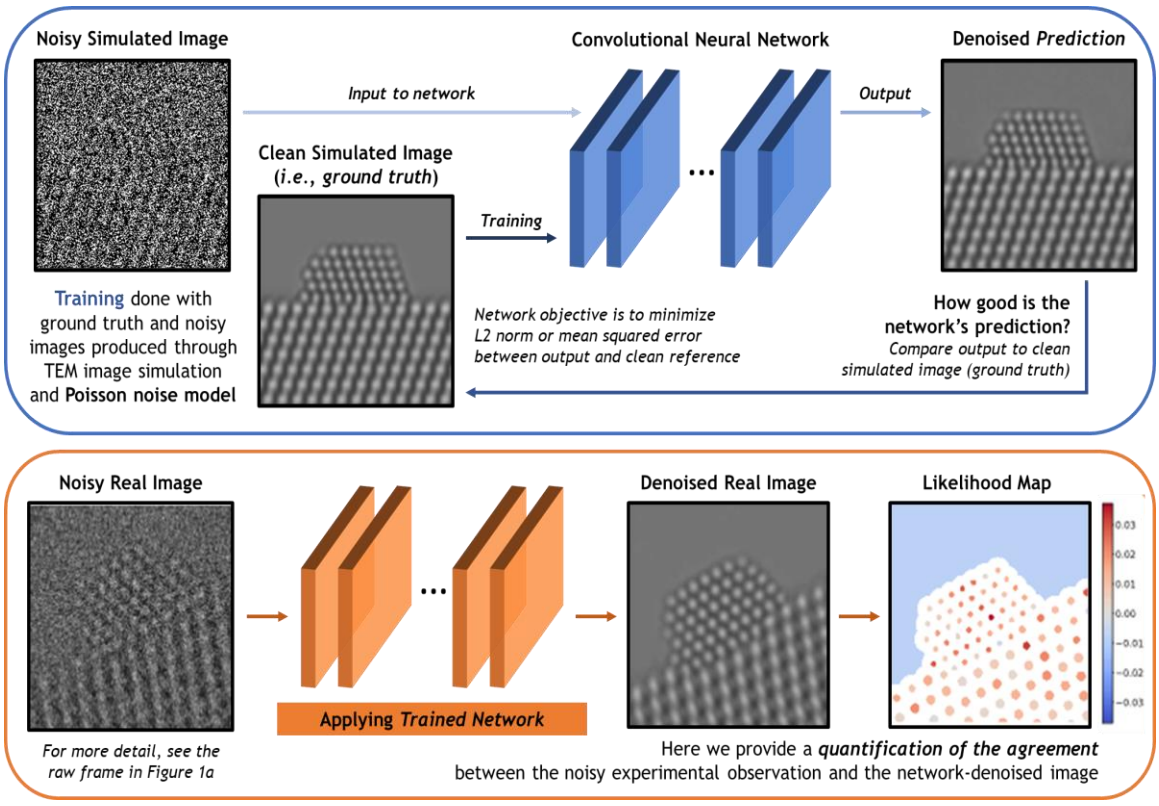

Figure 2.14. Schematic overview of the deep convolutional neural network training, application, and evaluation process. Figure from (Vincent et al., 2021).

The network training process involves (1) denoising a noisy image, (2) comparing the denoised output to the clean ground truth through a quantitative loss function, and (3) adjusting the parameters of the network iteratively to achieve better performance. For each noisy image, the network produces a prediction of the underlying signal, effectively denoising the image. The denoised prediction is compared to the original clean simulation by computing the L2 norm, or mean squared error (MSE), between the two images, as is standard in the denoising literature. Better denoising performance is achieved by iteratively adjusting the parameters within the network, in order to minimize the MSE difference between the denoised output and the original simulation. Here the parameters are adjusted via back-propagation using the stochastic gradient descent algorithm (Goodfellow et al., 2016). After successfully training the network, it may be applied to real

data (**Figure 2.14**, bottom). Given the high level of noise present in the raw data, caution must be exercised when analyzing the network-denoised output. As will be shown, an approach has been established for quantifying the agreement between the network output and the noisy input, which takes the form of a likelihood map (see Chapter 6).

The performance of the network, in terms of MSE, is conveniently represented by a related quantity known as the peak signal-to-noise ratio, or PSNR, which can be calculated from the MSE by the following equation:

Eq. 2.8 $$PSNR = 10 \times \log_{10}(\frac{MAX_I^2}{MSE})$$

Here, MAX_I is the maximum possible intensity value of the clean ground truth image. The PSNR is essentially a decibel-scale quantity that is inversely proportional to MSE: a very noisy image will have a low PSNR. The PSNR for the noisy images in this work is ~3 dB.

2.4.3.1. Baseline methods for evaluating denoising performance

A number of other methods, including other trained denoising neural networks that are typically applied to natural images, were also applied both to the simulated and the real data in order to establish a baseline for evaluating the performance of the proposed network. A brief overview of the methods will be given here. The performances of the methods were compared quantitatively in terms of PSNR and structural similarity (SSIM) (Wang et al., 2004).

(a) **Adaptive Wiener Filter (WF):** An adaptive low-pass Wiener filter was applied to perform smoothing. The mean and variance of each pixel were estimated from a local circular neighborhood with a radius equal to 13 pixels.

(b) **Low-pass Filter (LPF):** A linear low-pass filter with cut-off spatial frequency of 1.35 $Å^{-1}$ was applied to preserve information within the ETEM instrumental resolution while discarding high-frequency noise.

(c) Variance Stabilizing Transformation (VST) + Non-local Means (NLM) or Block-matching and 3D Filtering (BM3D): NLM and BM3D are commonly used denoising routines for natural images with additive Gaussian noise (Buades et al., 2005; Makitalo & Foi, 2013). Here, a nonlinear VST was used to convert the Poisson denoising problem into a Gaussian denoising problem (Zhang et al., 2019). After applying an Anscombe transformation, BM3D or NLM was applied to the image, and finally use the inverse transformation was used to recover the denoised image.

(d) Poisson Unbiased Risk Estimator + Linear Expansion of Thresholds (PURE-LET): PURE-LET is a transform-domain thresholding algorithm adapted to mixed Poisson-Gaussian noise (Luisier et al., 2011). The method requires the input image to have dimensions of the form (2n, 2n). To apply this method here, 128 × 128 pixel-sized overlapping patches were extracted from the image of interest, denoised individually, and finally stitched back together by averaging the overlapping pixels.

(e) Blind-spot Denoising: A blind-spot network based on U-net, as developed by Laine et al. (Laine et al., 2019), was trained. Here, training was done using 600 × 600 pixel-sized patches from the images of interest. The Adam optimizer was used with a starting learning rate of 1 × 10-4, which was reduced by a factor of two every 2,000 epochs. Overall, the training proceeded for a total of 5,000 epochs.

(f) Denoising Convolutional Neural Network (DnCNN): Following the protocol outlined in the Section 2.3, we trained the DnCNN model as described previously by Zhang and coworkers (Zhang et al., 2017).

(g) Small U-Net from Dynamically Unfolding Recurrent Restorer (DURR): Following the protocol outlined in the Section 2.3, we trained a U-Net architecture implemented in the DURR denoiser proposed by Zhang and coworkers (Zhang et al., 2018).

Aside from these methods, standard filtering techniques including Gaussian blurring, median filtering, and Fourier transform (FT) spot-mask filtering were applied using routines built-in to the ImageJ analysis software (Schneider et al., 2012). Where relevant, additional details will be given to aid in understanding.

3. Chemical Kinetics for Operando Electron Microscopy: 3D Modeling of Gas and Temperature Distributions during Catalytic Reactions

3.1. Motivation

In situ environmental transmission electron microscopy (ETEM) is a powerful tool for observing structural modifications taking place in heterogeneous catalysts under reaction conditions (Jinschek, 2014; Crozier & Hansen, 2015; Taheri et al., 2016). An *in situ* TEM experiment will almost always show atomic level changes in the catalyst structure upon exposure to reaction conditions, but it may not always be clear how such changes relate to catalytic functionality – unless the concentration of catalytic product species is measured simultaneously in the microscope. To address this limitation and elucidate catalytic structure-activity relationships, it is necessary to develop *operando* methods which will ideally provide quantitative data on chemical kinetics of product formation, *i.e.*, the activity and selectivity of the catalyst, simultaneously with atomic-resolution structural information.

Developing quantitative *operando* TEM methods is the primary motivation of the current Chapter. The ability to correlate changes in reaction kinetics with changes in catalyst structure is critical to determine the active structural motif in the electron microscope. To move from *in situ* to *operando* approaches, it is necessary to understand the chemical engineering aspects of the electron microscope reactor so that quantitative chemical kinetics can be determined. For an open-cell environmental TEM, modified specimen preparation methods have been developed which greatly increase the mass of catalyst in the microscope and thus enable quantitative determination of the gas phase products of a catalytic reaction while providing a stable platform for atomic-resolution imaging (Chenna & Crozier, 2012; Miller et al., 2015). Extended details on this method are given in Chapter 2, Section 2.3.5. In short, catalyst particles are dispersed on a porous

glass fiber pellet and an inert metal grid. Both the pellet and the grid are loaded into a standard furnace-style heating holder. The much larger mass of catalyst on the pellet produces detectable catalytic conversions, and catalyst particles on the metal grid are imaged. The composition of product gases in the ETEM can be monitored with residual gas analysis (RGA) and electron energy-loss spectroscopy (EELS) (Crozier & Chenna, 2011; Miller & Crozier, 2014).

To determine chemical kinetic parameters (e.g., steady-state reaction rates and activation energies) from catalytic conversion data, it is necessary to establish an appropriate reactor model for the system. This requires understanding the spatial distribution of reactant and product gases in the cell as well as temperature profiles during catalysis. The *operando* pellet reactor geometry differs greatly from reactor architectures typically employed in chemical reaction engineering, making it necessary to develop heat and mass transport models for the ETEM cell. Mortensen et al. have conducted computational fluid dynamics (CFD) simulations to investigate the temperature distribution in a furnace-type holder as a function of gas pressure and composition in an ETEM (Mortensen et al., 2015). Their model gives a good description of the temperature variation in the sample for single gases of different pressures and thermal conductivity, but it does not address the issues of catalysis or multi-component mass transport, which are essential to determining chemical kinetics.

In this work, mass transport, heat transfer and chemical conversion processes relevant to running an *operando* catalysis experiment in an open cell ETEM are explored. As an exemplary case study, the model is applied to a SiO_2-supported Ru catalyst performing CO oxidation ($CO + \frac{1}{2}O_2 \rightarrow CO_2$). Simulations were conducted with the commercial program COMSOL Multiphysics®. The Computational Fluid Dynamics, Heat Transfer, and Chemical Reaction Engineering modules were used to simulate the gas and

temperature profiles during catalysis. The model was initially developed by then-undergraduate student Jayse Langdon as part of an Honors project carried out in 2016 – 2017 under the supervision of then-PhD student Ben Miller. The experimental gas composition measurements used to benchmark the model were acquired by Ben Miller in 2014 (Miller & Crozier, 2014). The project was finished as part of this thesis, with help from undergraduate student Jarod Vance, who I supervised between 2019 and 2020.

3.2. Experimental

3.2.1. Finite element simulation of *operando* ETEM reactor

A finite element multiphysics model of the *operando* ETEM reactor combining fluid dynamics, heat transfer, multi-component mass transport, and chemical reaction engineering was developed to determine the gas and temperature profiles during catalysis. An overview of the model geometry and finite element mesh is given in **Figure 3.1**. Detailed information on the governing equations and boundary conditions describing the treatment of mass transport, heat transfer, and catalytic reactions are given below in Sections 3.2.1.1 - 3.2.1.4 and in (Vincent et al., 2020). For this work, steady-state simulations were performed with a reactant gas inflow of 1 SCCM of stoichiometric CO and O_2, which leads to a chamber pressure of ~2.2 – 2.4 Torr. The furnace temperature was set in the range of 25 – 340 °C. These conditions correspond to those where experimental *operando* data was acquired of Ru/SiO_2 performing CO oxidation (Miller & Crozier, 2014), which serves as a basis for evaluating the validity of the simulations.

3.2.1.1. Geometry of the model

Dimensions for most microscope components were derived from manufacturer blueprints for the FEI Tecnai ETEM, which is similar to the Titan instrument. The dimensions of the *operando* pellet are based on those used in our lab (Miller et al., 2015).

The diameter of the pellet is 3 mm and the radius of the center hole is 0.5 mm. The model geometry is shown in the top half of **Figure 3.1** (Vincent et al., 2020), which displays (a) the environmental cell and (b) the *operando* pellet reactor. Note that the model has mirror symmetry, so only half of the chamber needs to be solved. A defined pressure and composition of reactant gas flows into the cell from the inlet on the left. The inlet extends approximately one meter out of the cell so the composition in the cell does not impact the composition at the inlet (see Appendix, **Figure B.1**). Differential pumping apertures in the pole pieces serve as outlets. The *operando* pellet reactor and furnace holder reside between the pole pieces. The temperature and/or composition may be determined at any element in the model or integrated over domains. The gas composition measured experimentally is replicated as an integral of the composition along the path labeled "EELS Line". The pressure immediately beyond the differential pumping apertures is on the order of 2×10^{-3} Torr (Mølgaard Mortensen et al., 2015), while the pressure inside the cell is typically around 1,000 times higher. Therefore, it is sufficient to calculate the composition along the line marked in **Figure 3.1b**, rather than an extended path that traverses beyond the differential pumping aperture outlets. The composition and temperature at the grid are found through a surface integral on the plane labeled "TEM Grid," and the composition and temperature in the pellet are calculated as integrals over its volume.

The finite element mesh for this model is displayed in the bottom half of **Figure 3.1**, which shows (c) the full view of the cell and (d) and enhanced view of the *operando* pellet reactor. Small elements are used in the confined regions around the pellet reactor and differential pumping aperture outlets, while larger elements are used in the spacious cell and inlet. The mesh is comprised of approximately 205,000 elements. An analysis of the mesh quality shows that an increased number of elements does not greatly alter the solution but does unacceptably extend the computation time (Vincent et al., 2020).

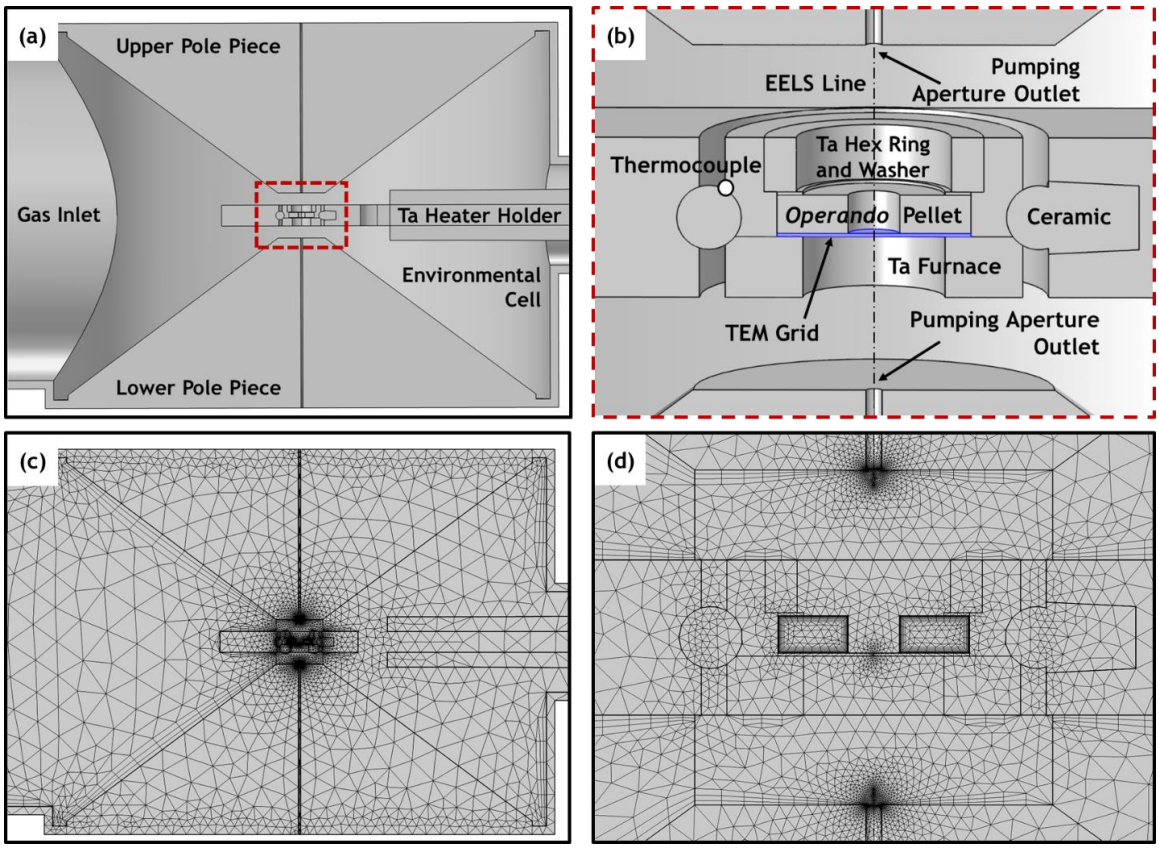

Figure 3.1. Environmental cell model geometry and finite element mesh (a, c) in full view, and (b, d) in an enhanced view focused on the *operando* pellet reactor. The TEM grid domain is colored blue for clarity. Figure from (Vincent et al., 2020).

The components labeled in **Figure 3.1** are listed in **Table 3.1**, along with the materials with which they are modeled. As will be shown, the gas and temperature distributions are largely uniform within the cell except for the small region localized to the furnace reactor and its immediate (< 3 mm) surroundings. Thus, including additional components found outside of this region (such as a cold trap, RGA sniffer tube, and objective aperture barrel), will unlikely impact the steady-state gas and temperature distributions, so these elements are excluded from the model for simplicity. Additionally, this line of reasoning is supported by results from previously published studies (see e.g., (Mølgaard Mortensen et al., 2015)). Materials properties have been imported from the COMSOL® library where appropriate (e.g., 304 steel). In other cases, properties are

retrieved from references cited throughout the text. Materials properties relevant to heat and mass transport are given throughout the text and summarized in **Table 3.2**.

Table 3.1. Model components and properties.

Component	**Material**
Gas inlet	Gas (varies)
Environmental cell	Gas (varies)
Pole pieces	304 steel
Chamber surface	304 steel
Heater holder body	Brass
Heater holder furnace, washer, and hex nut	Tantalum
Ceramic bridges	Zirconia
Operando pellet	Glass, porous
TEM grid	Tantalum, porous
Differential pumping aperture outlets	--
Thermocouple	--
EELS Line	--

Table 3.2. Modeled material properties relevant to heat and mass transport.

Material	Thermal Conductivity ($W\ m^{-1}\ K^{-1}$)	Heat Capacity ($J\ kg^{-1}\ K^{-1}$)	Emiss-ivity	Viscosity ($kg\ m\ s^{-1}$)	Density ($kg\ m^{-3}$)	Diffusivity ($cm^2\ s^{-1}$)
Steel	44.5	475	0.3	N/A, solid	7,850	N/A, solid
Tantalum	57.5	140	0.05	N/A, solid	16,700	N/A, solid
Zirconia	2	500	~0	N/A, solid	5,700	N/A, solid
Brass	120	377	0.05	N/A, solid	8,500	N/A, solid
Glass	1.2	730	0.9	N/A, solid	2,210	N/A, solid
CO	Eq. B.14	Eq. B.11	N/A, gas	Eq. B.4	Ideal gas law	Eq. B.7
O_2	Eq. B.15	Eq. B.12	N/A, gas	Eq. B.5	Ideal gas law	Eq. B.8
CO_2	Eq. B.16	Eq. B.13	N/A, gas	Eq. B.6	Ideal gas law	Eq. B.9

3.2.1.2. Treatment of mass transport

For multi-component gas mixtures, mass transport can occur by bulk convection and by inter-species diffusion. Bulk convection is modeled here with the Navier-Stokes equation. The gas is considered laminar, compressible, Newtonian, and unaffected by gravitational forces. A dimensionless number analysis supports these simplifications (Appendix Section B.2). With these considerations, the form of the Navier-Stokes equation solved becomes (Bird et al., 2006):

Eq. 3.1 $$\boldsymbol{\rho}\frac{\boldsymbol{\delta u}}{\boldsymbol{\delta t}} + \boldsymbol{\rho}(\boldsymbol{u}\cdot\boldsymbol{\nabla u}) = \boldsymbol{\nabla}\cdot[-\boldsymbol{p}\mathbf{I} + \boldsymbol{\mu}(\boldsymbol{\nabla u} + (\boldsymbol{\nabla u})^{\mathbf{T}}) - \frac{\mathbf{2}}{\mathbf{3}}\boldsymbol{\mu}(\boldsymbol{\nabla}\cdot\boldsymbol{u})\mathbf{I}]$$

This equation is solved simultaneously along with the equation of continuity (Bird et al., 2006):

Eq. 3.2 $$\frac{\delta\rho}{\delta t} + \nabla\cdot(\rho\boldsymbol{u}) = 0$$

Here, ρ is the fluid density, $\boldsymbol{u}$ is the velocity vector, t is time, ∇ is the del operator, p is the pressure, $\boldsymbol{I}$ is the identity matrix, μ is the dynamic viscosity, and T is the transposition operation. Only steady-state solutions were computed, so the time derivatives were set to zero. The density of the gas was modeled with the ideal gas law (De Nevers, 2005). Polynomial expressions for the viscosity of CO, O_2, and CO_2 were determined from published data (Laesecke et al., 1990; Vesovic et al., 1990; AIChE, 2005) and are provided in Appendix Section 0. The viscosity of mixtures of these gases were computed by Wilke's method (Wilke, 1950). Additional information related to the modeling of convection is omitted here for brevity but given in detail in (Vincent et al., 2020).

Inter-species diffusion is described with a Maxwell-Stefan approach (Krishna & Wesselingh, 1997; Bird & Klingenberg, 2013). Expressions for the binary diffusivities of CO, O_2, and CO_2 are found in the low-pressure limit from the literature (Marrero & Mason, 1972) and provided in Appendix Section 0. A simplification is implemented that averages the binary diffusivities against the local composition to produce a mixture-averaged diffusion coefficient for each component i, D_i^m. This mixture-averaged form is appropriate for gases of similar molecular weights (e.g., CO, O_2, and CO_2) and simplifies mass flux calculations by eliminating parameters that are difficult to compute (Kee et al., 2003; Torstensson, 2014).

With these simplifications, the overall mass transport equations may be written as:

Eq. 3.3 $$\nabla \cdot \boldsymbol{j_i} + \rho(\boldsymbol{u} \cdot \nabla)\omega_i = R_i$$

Eq. 3.4 $$\boldsymbol{N_i} = \boldsymbol{j_i} + \rho \boldsymbol{u} \omega_i$$

With supporting equations:

Eq. 3.5 $$\boldsymbol{j_i} = -\left(\rho D_i^m \nabla \omega_i + \rho \omega_i D_i^m \frac{\nabla \mathrm{M_n}}{M_n}\right)$$

Eq. 3.6 $$M_n = \left(\sum_i \frac{\omega_i}{M_i}\right)^{-1}$$

Here, the symbols used in **Eq. 3.1** and **Eq. 3.2** retain their same meaning. In **Eq. 3.3** and **Eq. 3.4**, $\boldsymbol{j_i}$ is the mass diffusion flux vector of component i, ω_i is the mass fraction of species i, R_i is the rate of consumption or disappearance of species i due to a reaction, and $\boldsymbol{N_i}$ is the overall mass flux vector for component i. In **Eq. 3.5**, D_i^m is the mixture-averaged diffusion coefficient for component i, and M_n is the mass-averaged molar mass, which is computed in **Eq. 3.6** from the molar masses of each component i, M_i.

In the *operando* pellet where diffusion is obstructed by the pellet's pore network, the diffusion coefficient is reduced with a Knudsen term as described in **Eq. 3.7** and **Eq. 3.8** below:

Eq. 3.7 $$D_i^K = \frac{\lambda}{3}\sqrt{\frac{8RT}{\pi M_i}}$$

Eq. 3.8 $$D_i^{mK} = \left(\frac{1}{D_i^m} + \frac{1}{D_i^K}\right)^{-1}$$

In **Eq. 3.7**, D_i^K is the Knudsen diffusion coefficient for component i, λ is the molecular mean free path, R is the gas constant, and T is the local temperature. The mean free path in the pellet was set to the pore diameter of 2.7 μm published by the manufacturer (Whatman®, Grade GF/D). In **Eq. 3.8**, the Knudsen-corrected, mixture-averaged diffusivity D_i^{mK} is calculated by a parallel resistance treatment.

In addition, the pellet's porosity, ε, and tortuosity, τ, further attenuate the gas diffusivities in the pellet. This attenuation is applied to the binary diffusivities before any further calculations are done and is described by **Eq. 3.9** below:

Eq. 3.9 $$D_{e,ik} = \frac{\varepsilon}{\tau} D_{ik}$$

Here, $D_{e,ik}$ is the effective binary diffusivity for components i and k. As mentioned, the porosity has been evaluated as $\varepsilon = 0.7$. There are several methods for estimating tortuosity from porosity; here the Bruggeman method is chosen (Tjaden et al., 2016), yielding a value of $\tau = \varepsilon^{-1/2} = \sim 1.2$.

With the considerations for diffusion through the pore network implemented, the diffusive flux vector for species i in the pellet becomes slightly modified from **Eq. 3.5** to **Eq. 3.10** below:

Eq. 3.10 $$\boldsymbol{j_i} = -\left(\rho D_{e_i}^{mK} \nabla \omega_i + \rho \omega_i D_{e_i}^{mK} \frac{\nabla \mathrm{M_n}}{M_n}\right)$$

Here, $D_{e_i}^{mK}$ represents the effective mixture-averaged diffusion coefficient of component i after correcting for Knudsen resistance to diffusion.

3.2.1.3. Treatment of heat transfer

Heat transfer considerations include radiation, convection, and conduction. Radiation is treated with the Stefan-Boltzmann law (Bird et al., 2006). Convection is largely negligible given the low pressures/flow rates and small geometries present in the cell. Conduction through solids is modeled with Fourier's law (Bird et al., 2006). Thermo-physical properties for solid densities, heat capacities, and thermal conductivities have been gathered from tabulated sources, as referenced, or imported from the COMSOL® material library.

Conduction through gases is modeled by Fourier's law with a slight modification to the thermal conductivity of the gas. For macroscopic heat transfer, a gas's thermal conductivity is typically independent of pressure or of geometry. Given the low pressures and confined spaces present in the ETEM reactor, the thermal conductivity may become dependent on these factors, as the mean free path between molecular collisions can become comparable to the wall distance that separates the surfaces transferring heat

(usually, the molecular mean free path is many times smaller). In this case, gas-wall collisions may occur as frequently as gas-gas collisions, which effectively reduces the conductivity of the gas (C. C. Minter, 1963). In the reactor, the effect is relevant around the furnace and the pole pieces, where the wall separation distances are smallest.

A theoretical description of the pressure-distance dependence has not been found, so an empirical fit was employed, given by:

Eq. 3.11 $$k_i = k_{0,i} * \left(1 - \exp\left(\frac{-w_d}{\lambda * \alpha}\right)\right)$$

Here, k_i is the adjusted thermal conductivity for component i, $k_{o,i}$ is the unadjusted conductivity, w_d is the distance to the nearest wall, λ is the mean free path, and α is a fitting parameter. The mean free path was evaluated by the kinetic theory of gases (Weston, 1985). The adjustment was implemented in two regions: (1) between the furnace and the pole pieces, and (2) between the furnace and the holder body. By inspection, one can see that the unadjusted conductivities are recovered in the limits of large w_d (*i.e.,* unconfined spaces) or small λ (*i.e.,* high pressure).

The impact of the adjustment can be seen by examining **Figure 3.2**, which displays the power required to maintain a temperature of 400 °C in CO pressures ranging from 10^{-5} – 10 Torr. The experimentally required amount of power was measured and is plotted with orange circles. The flat, dashed blue line depicts the simulated heat lost when no pressure adjustment is implemented. One can see that the unadjusted case shows no pressure dependence on power loss and thus disagrees with the experimental measurements. When **Eq. 3.11** is implemented (blue circles), a good fit to the experimental behavior is obtained. The vacuum simulation agrees very well with the experimental heat loss in vacuum (10^{-5} Torr). Overall, these results are taken as evidence of a sufficiently descriptive heat transfer model.

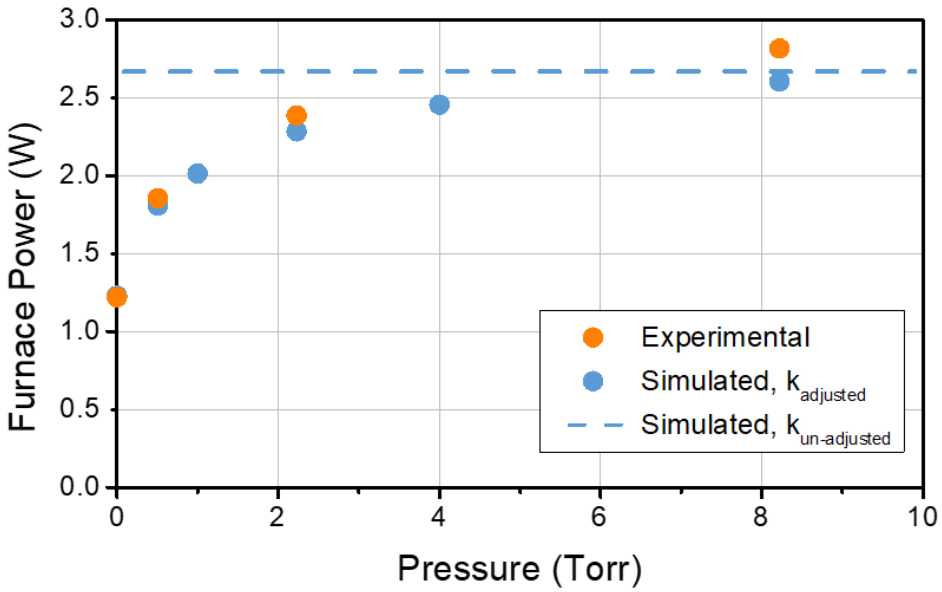

Figure 3.2. Furnace power versus pressure of CO. Power shown is that required to maintain the furnace at 400 °C. Simulated data is given with (blue circles) and without (dashed line) a pressure-dependent adjustment to the thermal conductivity, showing the adjustment provides a good fit to the experimental data (orange circles). Figure from (Vincent et al., 2020).

With these considerations, the general energy balance and the equation for heat conduction, respectively, are given by **Eq. 3.12** and **Eq. 3.13** below:

Eq. 3.12 $$\rho C_p \boldsymbol{u} \cdot \nabla T + \nabla \cdot \mathbf{q} = Q$$

Eq. 3.13 $$\mathbf{q} = -k \nabla T$$

Here, C_p is the heat capacity, $\mathbf{q}$ is the conductive heat flux vector, and Q is a volumetric heat source. The furnace is treated as a volumetric heat source. Enthalpic heat from the exothermic reaction is also treated as a volumetric heat source. The pole pieces are modeled as water cooled by setting their outer surfaces to 25 °C. The gas flowing into the cell is set to an initial temperature of 25 °C. Gases are considered to be ideal, with their heat capacity, enthalpy, and entropy taken as functions of temperature from ideal gas models (McBride et al., 2002). Polynomial expressions for the heat capacities and unadjusted thermal conductivities of CO, O_2, and CO_2 are found as a function of

temperature in the low-pressure limit in the literature (Millat & Wakeham, 1989; Vesovic et al., 1990; Laesecke et al., 1990), and are provided in Appendix Section 0.

3.2.1.4. Treatment of chemical reactions and catalysis

The model can be applied to any catalyst or reaction of interest provided the catalytic properties of the material and the reaction are known. In this Chapter, a system consisting of a Ru/SiO_2 catalyst performing CO oxidation ($CO + ½O_2 \rightarrow CO_2$, and ΔH_{rxn} = -283.0 kJ/mol) was chosen to develop the computational methodology. In Chapter 4, the model is then applied to a Pt/CeO_2 catalyst also performing CO oxidation. The reaction is known to proceed with a negligible rate in regions of the cell where there is no catalyst, so the reaction is significant only in the *operando* pellet (see, e.g., **Figure 2.10b**). For simplicity, the reaction is modeled as irreversible. For Ru/SiO_2, reaction rates for each species were given by the following elementary reaction equation:

Eq. 3.14 $$r_i = v_i A\sqrt{T}e^{-\frac{E_a}{RT}} * [CO][O_2]^{\frac{1}{2}}$$

Here r_i is the rate of reaction of species i, v_i is the stoichiometric coefficient of species i, A is a pre-exponential factor, T is the temperature, E_a is the activation energy, R is the gas constant, $[CO]$ is the concentration of CO, and $[O_2]$ is the concentration of O_2. The spatial distribution of catalyst in the pellet was modeled with an egg-shell profile (see Appendix Section B.4, the profile used in the results below corresponds to that shown in **Figure B.2b**). For the Ru/SiO2 catalyst, the total mass of catalyst was not known precisely (the mass of catalyst in the reactor is on the order of 100 μg, while the mass of the pellet is ~3000 μg), so in this work the value of A was adjusted until a match with experimental data was achieved for conversions measured at 340 °C (here, $A = 7*10^{12}$ s^{-1}). The E_a of CO oxidation over Ru/SiO_2 has been measured, and the reported mean of 90 kJ mol^{-1} was

chosen (Assmann et al., 2004). For the Pt/CeO_2 catalyst, a value of 74 kJ mol^{-1} was obtained from the bench top plug flow reactor experiments (as discussed in Section 2.2).

3.2.2. Discussion on effect of higher operating temperature (i.e., T > 340 °C)

It is worthwhile to briefly discuss the impact of higher operating temperature on the gas and temperature distributions in the cell and reactor. In general, to apply *operando* ETEM to a catalyst of interest, the reactor temperature may need to exceed 340 °C (the highest temperature explored here). The effect of higher temperature can be understood by considering the dominant modes of mass and heat transport. As will be shown, given the broad uniformity of low-magnitude velocities throughout the cell, mass transport is dominated by diffusion and heat transfer by conduction. Increasing the temperature will not change the dominant mode of mass transport, but it may make it more efficient, as the diffusivities which describe the intermixing of gas species become larger at higher temperatures (see, e.g., **Eq. B.7** – **Eq. B.9**). In this sense, the distribution of gas products in the cell and reactor could become more uniform for catalysts with higher light-off temperatures. For heat transfer, as the furnace temperature increases above 400 °C, radiation becomes more important and eventually dominates since the radiative heat flux scales by $\boldsymbol{q} \propto T^4$. The impact of radiation is complicated and competitive. On one hand, radiation from the inner walls of the furnace through the glass pellet could lead to a more uniform temperature distribution between the pellet and the furnace. On the other hand, radiation away from the TEM grid may lead to the evolution of a temperature discrepancy between the grid and the furnace thermocouple. This second mechanism was identified by Mortensen and colleagues, who showed that a temperature difference of ~5 °C evolved for furnace temperatures up to 700 °C (Mortensen et al., 2015). The softening point of borosilicate glass is approximately 800 °C, so it is advised to operate the reactor below 700 °C to avoid damage to the glass fiber pellet-loaded furnace holder. The magnitude of

this temperature difference is on the same order of that reported in **Figure 3.5**, and therefore, for specimen temperatures up to 700 °C, the temperature distribution in the reactor is unlikely to change by a significant amount compared with that presented below.

3.3. Results and discussion

3.3.1. Velocity and pressure profiles

A view of the velocity field and pressure profiles around the *operando* pellet reactor are shown in **Figure 3.3**. Data from a temperature setpoint of 100 °C are shown at the top half of the figure, while data from 300 °C are shown at the bottom for comparison. The plots of the velocity fields contain overlaid quiver plots to show the bulk flow velocity vectors within the fluid regions of the cell; the velocity vectors are plotted for magnitudes greater than 3 m s^{-1} and their lengths are displayed on a natural log scale. As seen in **Figure 3.3a and Figure 3.3c**, the bulk fluid velocity is low everywhere in the cell except for in the immediate vicinity of the differential pumping aperture outlets. While the gas there accelerates rapidly from the cell- averaged speed of ~0.2 m s^{-1} up to ~100 m s^{-1}, the velocity field only extends ~1 mm into the chamber and does not produce appreciable flow near the heater holder or *operando* pellet surfaces. The velocity fields at 100 °C and 300 °C differ by little. The gradient at 300 °C is slightly more confined to the aperture outlets due to the lower average cell pressure. The broad uniformity of low-magnitude velocities throughout the cell suggests that convective heat transfer and mass transport are limited (see dimensionless number analysis presented in Appendix, Section B.2).

The pressure profiles shown in **Figure 3.3b and Figure 3.3d** follow a trend similar to the velocity distributions. Far from the pumping aperture outlets, the pressure in the cell is uniform. Changes in pressure are only seen to occur in the immediate vicinity of the outlets, where a pressure drop forms to drive the bulk flow of gas out of the cell.

From these results, one can justifiably believe that the steady-state pressure measured along the inlet line matches the pressure around the catalyst. This is a particularly useful finding for those interested in detecting *operando* conversions by accounting for changes in total cell pressure (Van Spronsen et al., 2017). For the CO oxidation reaction, $CO + \frac{1}{2}O_2 \rightarrow CO_2$, the pressure in the cell decreases as 1½ mol of reactants are converted to 1 mol of products. The effect is visible as the pressure in the cell drops 0.2 Torr from the conversion of CO and O_2 to CO_2 when the furnace is heated from 100 °C (**Figure 3.3b**) to 300 °C (**Figure 3.3d**). Finally, it is noted that the velocity and pressure distributions simulated here match well with those reported by Mortensen et al. (Mortensen et al., 2015).

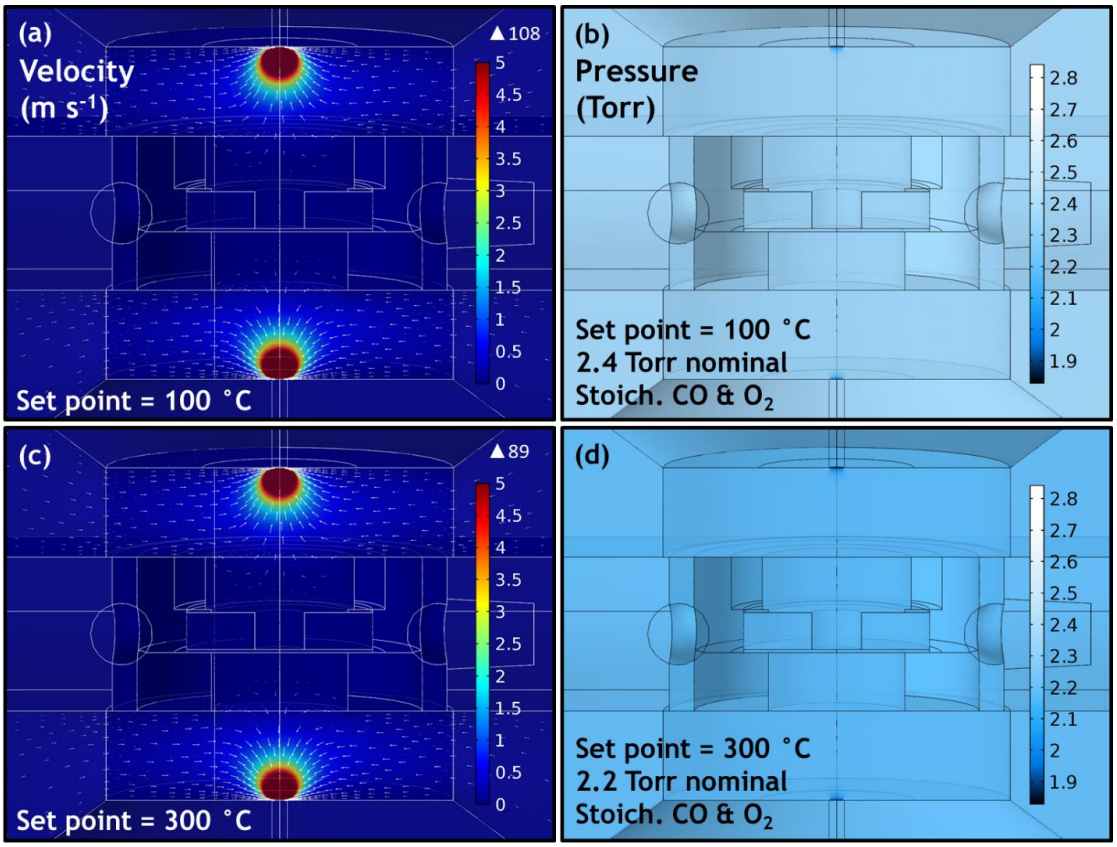

Figure 3.3. Velocity and pressure distributions near the reactor and differential pumping aperture outlets for a furnace set point of **(a, b)** 100 °C and **(c, d)** 300 °C. The velocity and pressure are both uniform away from the outlets, so those regions are not shown. The velocity vectors in **(a)** and **(c)** are plotted for magnitudes greater than 3 m s^{-1} and their lengths are displayed on a natural log scale. Figure from (Vincent et al., 2020).

3.3.2. Temperature distribution

Figure 3.4 displays the temperature distribution around the *operando* pellet reactor for four furnace thermocouple set points: (a) 100 °C, (b) 190 °C, (c) 230 °C, and (d) 300 °C. The elevated temperature is localized to the reactor and the gas surrounding it, so the discussion is focused on this region. For each condition, the apparent temperature of the reactor matches remarkably well with the furnace set point. The temperature distributions are also largely uniform throughout the reactor. The temperature rapidly decreases outside this region to 25 °C at the surface of the water-cooled pole pieces. The thermal gradient at higher temperatures shows similar behavior.

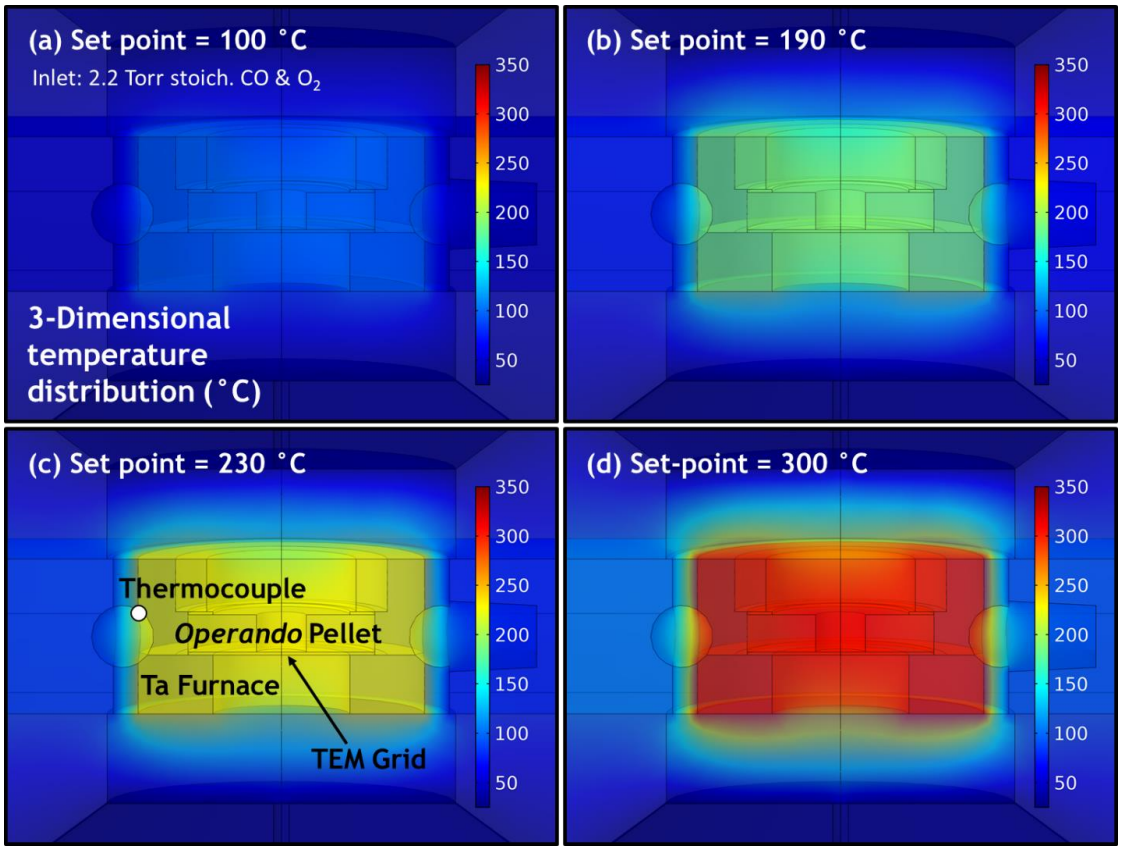

Figure 3.4. Three-dimensional temperature distributions in and around the reactor during catalysis for thermocouple set points of: **(a)** 100 °C, **(b)** 190 °C, **(c)** 230 °C, and **(d)** 300 °C. At each condition the temperature distribution appears largely uniform and matches well with the furnace thermocouple set point. Figure from (Vincent et al., 2020).

The high degree of thermal uniformity in the *operando* pellet reactor is an important and encouraging result that suggests that the furnace temperature set point matches the temperature at the TEM grid and the *operando* pellet. A quantitative comparison of the temperature difference at these locations vs. the temperature set point is shown in **Figure 3.5**. The temperature of the thermocouple is described by a point value at that location, while the TEM grid and *operando* pellet temperatures are defined by averages over the respective surface and volume domains. A positive value signifies that the location is hotter than the temperature set point. At 25 °C all the temperatures overlap. For furnace set points below ~220 °C, the temperature of the grid and pellet are lower than the set point by 0.5 – 1 °C. This slight gradient drives the flow of heat to them from the hotter furnace. The smaller thermal conductivity of the glass pellet causes the average pellet temperature to be slightly (~0.5 °C) lower than the highly conductive tantalum TEM grid. The inflection point observed in the curves at ~190 °C indicates the ignition of the exothermic catalytic reaction. At set points above ~250 °C, the contribution from the heat of the reaction exceeds the heat lost to the surrounding gas, and the pellet/grid become ~1 °C hotter than the furnace itself. The temperature difference at the thermocouple is virtually 0 °C for all set points. It is worth noting that an absence of a temperature difference at the thermocouple matches the simulations done by Mortensen and coworkers (Mortensen et al., 2015). Overall, for the conditions simulated here, the TEM grid temperature does not differ from the intended furnace set point by more than 1.5 °C. This data suggests that the furnace thermocouple is a reliable probe of the temperature of the catalyst imaged on the TEM grid – even at temperatures where the catalyst is active.

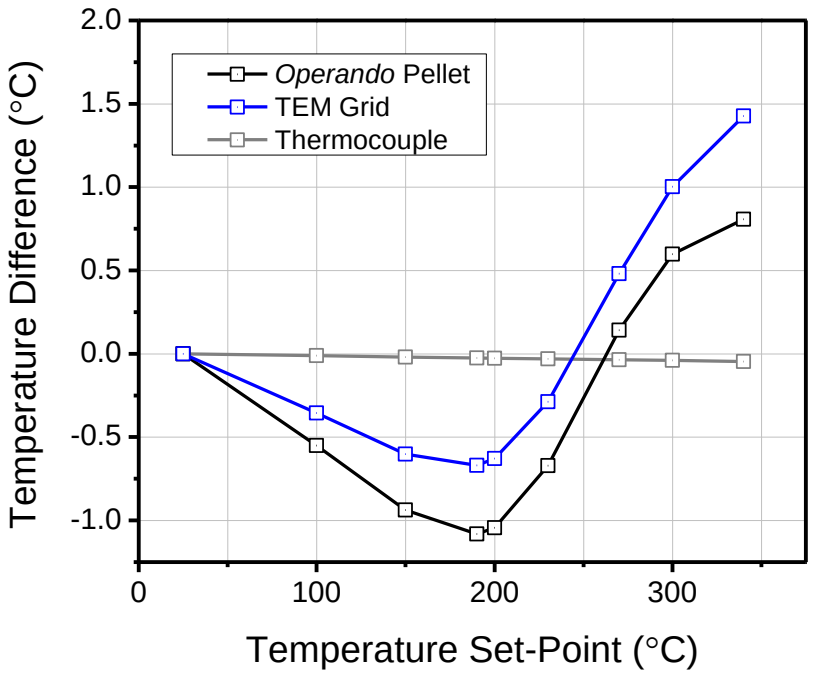

Figure 3.5. Quantitative comparison of temperature set point vs. the simulated temperature at the furnace thermocouple (gray line), TEM grid (blue), and *operando* pellet (black). A positive value signifies that the location is hotter than the temperature set point. The inflection point at ~190 °C signifies the ignition of the catalytic reaction. Figure from (Vincent et al., 2020).

3.3.3. Distribution of catalytically-produced CO_2

The steady-state 3-dimensional mole fraction of catalytically produced CO_2 is shown in **Figure 3.6** for thermocouple set points of (a) 100 °C, (b) 190 °C, (c) 230 °C, and (d) 300 °C. Here, the mole fraction of species *i* is defined in a standard way as the number of moles of that species divided by the total number of moles of all species (see, for example, **Eq. B.21**). The gas composition is homogeneous in the cell except for the region in and around the *operando* pellet reactor, so the results and discussion presented below focus on this region. The inset of each figure displays the simulated CO conversion, X_{CO}, at each temperature. Here, X_{CO} is defined as:

Eq. 3.15 $$X_{CO} = \frac{\dot{n}_{CO,in} - \dot{n}_{CO,out}}{\dot{n}_{CO,in}}$$

Where $\dot{n}_{CO,in}$ is the molar flow rate (mol/s) of CO into the ETEM chamber, which is calculated by taking a surface integral of the molar flux of CO across the inlet surface into the ETEM. The variable $\dot{n}_{CO,out}$ is the molar flow rate of CO out of the ETEM, which is calculated by taking a surface integral of the molar flux of CO across the differential pumping aperture outlet surfaces.

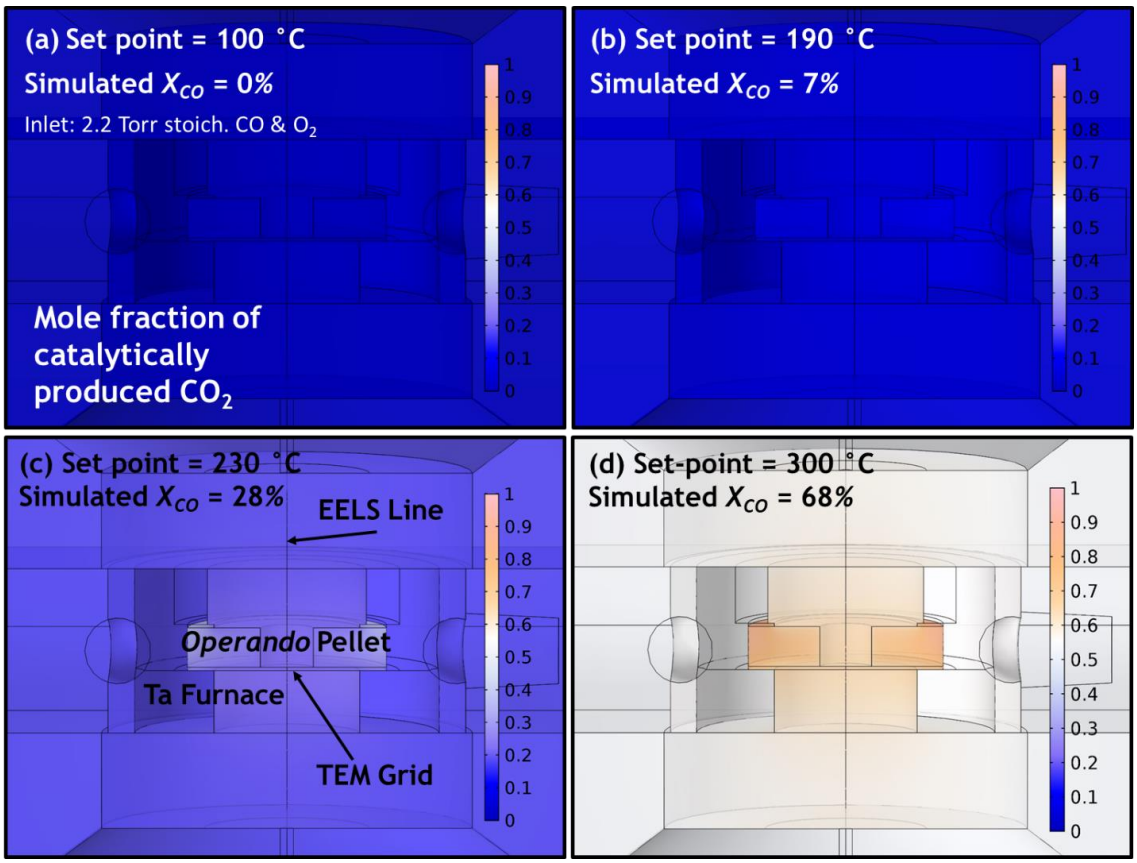

Figure 3.6. Mole fraction of catalytically produced CO_2 in and around the *operando* pellet reactor for furnace set points of: **(a)** 100 °C, **(b)** 190 °C, **(c)** 230 °C, and **(d)** 300 °C. The simulated CO conversion is given in the inset of each figure. Figure from (Vincent et al., 2020).

Below the catalyst's light off point, very little CO_2 is produced, as observed in **Figure 3.6a**, which shows that the CO_2 mole fraction at 100 °C is approximately 0 everywhere. As the temperature ramps up, the catalyst becomes active and the amount of CO_2 produced increases. The CO_2 produced from the reaction distributes mostly

homogeneously throughout the cell and the reactor. **Figure 3.6b** shows the largely uniform CO_2 mole fraction at 190 °C, a condition of 7% conversion. As the conversion increases, a slight enrichment of product gas develops in the *operando* pellet, in particular at the top outermost region of the pellet, which is enclosed by the impermeable surfaces of the Ta furnace and washer. The bottom layer of the pellet is exposed to the TEM grid, which has been modeled as porous and thus accessible for CO_2 diffusion. **Figure 3.6c** and **Figure 3.6d** present the 3D mole fraction of CO_2 at 230 °C and 300 °C, where the simulated conversions of CO are 28% and 68%, respectively. Even at such high catalytic conversions, the gas in and around the reactor exhibits a well-mixed composition.

A deeper understanding of the compositional variation throughout the reactor is developed by comparing the average CO_2 mole fraction quantified at three domains of interest across a range of temperatures. **Figure 3.7a** displays the CO_2 mole fraction averaged over the *operando* pellet (black line), at the TEM grid (blue line), and along the EELS line (red line), for furnace temperature set points spanning 100 – 340 °C. Experimental measurements of the CO_2 composition along the EELS line (red boxes) are also plotted from nominally identical conditions across the same range of temperatures. The experimental data (Miller & Crozier, 2014) agree well with the simulated EELS measurements.

The high degree of agreement between the experimentally acquired and computationally modeled CO_2 compositions across a broad range of temperatures is taken as evidence that the model faithfully captures the relevant heat transport and chemical reaction physics. The catalyst begins lighting off at 190 °C. At each location, the CO_2 composition curve displays a sigmoidal shape. The average CO_2 mole fraction in the *operando* pellet is higher than that along the EELS line, though this is expected given the 3-dimensional distributions shown in **Figure 3.6**. The difference between the average

CO_2 mole fraction in the pellet and that along the EELS line grows as the conversion increases, reaching a maximum of 0.15 at 300 °C, where the CO_2 mole fractions in the pellet and along the EELS line are 0.75 and 0.60, respectively. The difference between the pellet and EELS line drops to 0.03 when the activity is lower at 190 °C. The percentage difference between the pellet and the EELS line is appreciably more constant across the same temperature range, as shown by the orange boxes in **Figure 3.7b**. At 190 °C the percent difference is 27%, and at 300 °C the percent difference is 20%.

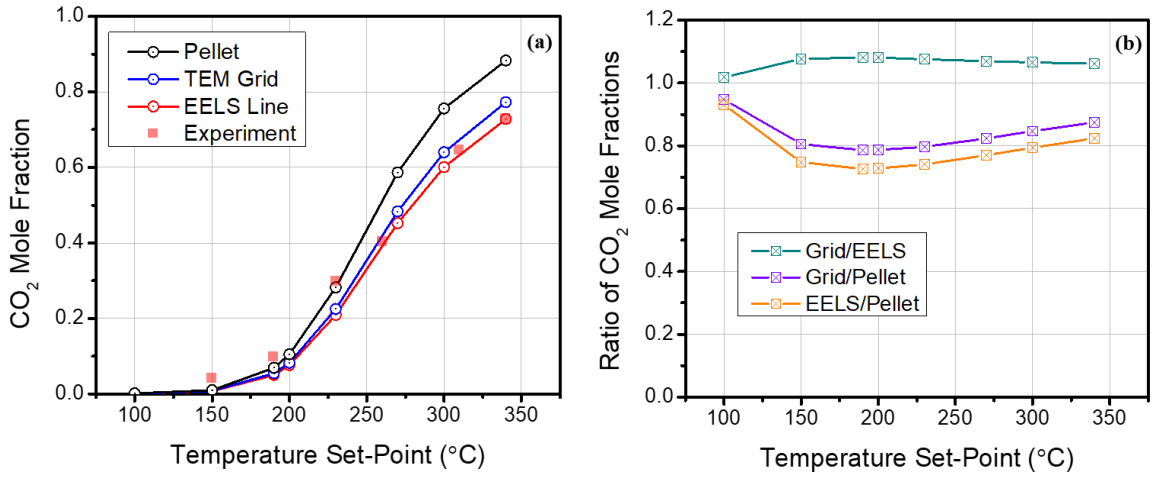

Figure 3.7. (a) Quantitative comparison of the CO_2 mole fraction across a range of temperatures in the *operando* pellet (black circles), at the TEM grid (blue circles), and along the EELS center line (red circles). The composition measured experimentally (red boxes) agrees very well with the values simulated along the EELS center line. **(b)** Ratio of CO_2 mole fraction between the grid and the EELS line (green boxes), the grid and the pellet (purple boxes), and the EELS line and the pellet (orange boxes). Figure from (Vincent et al., 2020).

While the difference in composition between the EELS line and the pellet can be appreciable, the difference between the EELS measurement and the composition at the TEM grid is rather small for all conditions. The composition at the TEM grid is important since the grid supports the catalyst that is actually imaged during an *operando* TEM experiment. In most cases here, the mole fraction difference is between 0.01 – 0.04, which is on the same order as the precision of the experimental gas quantification procedure

(Miller & Crozier, 2014). As seen by the green line in **Figure 3.7b**, the fractional variation over the entire temperature range is 3 – 8%. Consequently, one can practically assume that the gas composition measured with EELS matches that surrounding the catalyst on the grid. This is an important result because it demonstrates that EELS can reliably probe the local gas composition around the imaged catalyst.

3.3.4. Reactant conversion analysis

Two important performance characteristics for studying catalytic reaction chemistry are the conversion of reactants and the rate of reaction. Here we show that EELS can be used to estimate both the CO conversion, X_{CO}, and the reaction rate, r_{CO}. Recall from **Eq. 3.15** that the CO conversion can be calculated from the integrated flux of CO across the gas inlet and pumping aperture outlet surfaces of the ETEM cell. The CO conversion obtained in this way is regarded as the true conversion in the chemical reaction engineering sense, and it is tabulated in the second column of **Table 3.3** for reactor temperatures spanning 150 – 340 °C. The CO conversion can also be expressed in terms of the CO_2 mole fraction at the outlet surfaces. A derivation starting from **Eq. 3.15** is provided in Appendix Section B.5, and it results in the following expression for a stoichiometric mixture of reactants:

Eq. 3.16 $$X_{CO} = \frac{y_{CO_2}}{(1-y_{CO_2})\times\frac{2}{3} + y_{CO_2}}$$

Here, y_{CO2} is the CO_2 mole fraction of the gas leaving the ETEM reactor through the pumping aperture outlets. It is not feasible to measure the composition across this exit surface experimentally. However, given the large degree of gas-phase homogeneity, an estimate may be made from the CO_2 mole fraction measurement obtained by EELS. The third column of **Table 3.3** shows the estimated CO conversion obtained in this way, *i.e.*,

by calculating X_{CO} in **Eq. 3.16** from the CO_2 mole fraction along the EELS line. Estimates of X_{CO} are shown for furnace temperature set points spanning 150 – 340 °C.

The CO conversion values calculated from the CO flow in and out of the ETEM cell differ little compared to those estimated from the gas composition along the EELS line. The relative difference for each temperature is provided alongside the conversions in **Table 3.3**. At 190 °C, the calculated and estimated CO conversions are 7.1% and 7.4%, respectively, which corresponds to an absolute difference of 0.003 and a relative difference of 4.2%. When the catalyst is more active at 270 °C, the calculated and estimated conversions are 54.0% and 55.3%, respectively, which corresponds to an absolute difference of 0.013 and a relative difference of 2.4%. The conversion estimated from EELS is consistently higher by a slight amount, due to the enrichment of CO_2 along the EELS line relative to the composition at the outlet (see, *e.g.*, **Figure 3.6c** or **Figure 3.6d**, particularly the region along the EELS line in the vicinity of the pellet). Overall, though, the resulting impact on estimating the CO conversion is small, amounting to a relative difference around 2 – 9% for the conditions explored here. As a result, these findings show that EELS can be used to estimate the catalytic conversion during an open-cell *operando* TEM experiment. Moreover, the model developed here may be used to provide a correction factor to obtain the true conversion if desired. These simulations along with experimental measurements show that the gas is well-mixed in differentially pumped cells (Miller et al., 2015). This relative homogeneity for the differentially pumped cell combined with the *operando* pellet architecture means that to a good approximation, the system behaves as continuously-stirred tank reactor (CSTR), especially at low conversions. The ability to apply a simple reactor model to the *operando* pellet reactor would greatly facilitate the evaluation of kinetic parameters for catalytic structure-activity relationships (*e.g.*, activation energies), which is a subject of future work for this project.

Table 3.3. Comparison of CO conversion obtained by integrating the flux of CO in and out of cell, and by estimating the outlet composition from EELS. The relative difference between the two conversion values is also given.

Temp. (°C)	X_{CO} Calculated from CO Flow Rate in and out of ETEM Cell (%)	X_{CO} Estimated from CO_2 Mole Fraction along EELS Line (%)	Relative Difference between Calculated and Estimated X_{CO} (%)
150	1.1	1.0	9.1
190	7.1	7.4	4.2
200	10.5	11.1	3.7
230	27.5	28.4	3.3
270	54.0	55.3	2.4
300	67.8	69.3	2.2
340	78.6	80.0	1.8

3.3.5. Reaction rate analysis

With an estimate of the CO conversion, one can calculate the rate of product formation, or the reaction rate, which is of principle importance to chemical kinetics. In the model, the true rate of product formation (with units of mol CO_2 per second) may be found by integrating the reaction rate throughout the domain of the pellet where the reaction occurs. For heterogeneous catalysis, the reaction rate is usually normalized to the mass of catalyst or to the surface area of the catalyst in the reactor. With an appropriate active site model, one may also normalize the rate to the number of active sites available, yielding a turnover frequency measurement. Here we have chosen to normalize to mass, with the total mass of catalyst as 200 μg, since this is the amount loaded during a typical *operando* experiment with the Ru/SiO_2 catalyst studied here. The mass-normalized rate integrated over the entire domain of the pellet, which we refer to as r_1, with units of mol

CO_2 per second per gram catalyst, is tabulated across a range of temperatures in **Table 3.4**. The CO conversion estimated from EELS is provided again for reference.

An estimate of integrated rate of product formation may be made from the conversion measurement derived from EELS and is simply related to the estimated X_{CO} and to the inlet flow rate of reactants. For reference, the inlet molar flow rate of CO into the cell, $\dot{n}_{CO,in}$, is ⅔ SCCM or 4.95×10^{-7} mol/s. The estimated rate of product formation, r_2, may be calculated and normalized to the mass of catalyst in the pellet, m_{cat}, by the equation:

Eq. 3.17 $$r_2 = \frac{X_{CO} \times \dot{n}_{CO,in}}{m_{cat}}$$

The fourth column of **Table 3.4** displays the mass-normalized rate estimated by the EELS conversion measurement. The relative difference between the rate integrated over the entire domain of the pellet (r_1) and that estimated by the EELS conversion measurement (r_2) is also given in **Table 3.4**.

It is of interest to compare the estimated – and experimentally measurable – rate of product formation to the true rate obtained through 3D integration. As seen in **Table 3.4**, in general, for reactant conversions above 5%, the EELS measurement provides an estimate of the rate of product formation that is within 10% of the true, integrated rate. Typically, the systematic error in the EELS conversion is 5 – 7% larger than the true conversion. Consequently, the error on the ratio of rates at different temperatures is generally better than 5%. Pragmatically, the inlet reactant flow rates are calibrated and known, so these findings present an important result demonstrating that one can use EELS to determine the overall steady-state reaction rate during an open-cell *operando* TEM experiment. If desired, simulations with the model developed here could be performed to obtain a correction factor that adjusts experimental measurements to the

true rate in the simulation. Finally, it is noted that the integrated reaction rate (moles of CO consumed per second) approaches the rate of CO flown into the cell. The only way this could be true is if most (≥ 80%) of the reactant gas interacts with the catalyst-loaded pellet before exiting through the pumping aperture outlets.

Table 3.4. Summary of reaction rate analysis. The rate of CO_2 formation obtained by integrating the reaction rate over the entire pellet ($\boldsymbol{r_1}$) and the rate of CO_2 formation estimated by the EELS CO conversion measurement ($\boldsymbol{r_2}$) are tabulated as a function of temperature. The ratio between the integrated and estimated rate is given ($\boldsymbol{r_2}$: $\boldsymbol{r_1}$), and the CO conversion estimated by EELS is provided again for reference. Finally, the rate of CO_2 formation obtained by integrating the reaction rate within a 50 μm thick layer at the surface along the inner hole in the pellet ($\boldsymbol{r_3}$) is given, in addition to the ratio between the surface-integrated and pellet-integrated rates ($\boldsymbol{r_3}$:$\boldsymbol{r_1}$).

Temp. (°C)	$\boldsymbol{X_{CO}}$ **Estimated from EELS (%)**	$\boldsymbol{r_1}$ **(mol CO_2 sec^{-1} g_{cat}^{-1})**	$\boldsymbol{r_2}$ **(mol CO_2 sec^{-1} g_{cat}^{-1})**	**Ratio of r_2: r_1 (%)**	$\boldsymbol{r_3}$ **(mol CO_2 sec^{-1} g_{cat}^{-1})**	**Ratio of r_3:r_1 (%)**
150	1.0	2.19×10^{-5}	2.45×10^{-5}	111.9	2.14×10^{-5}	97.7
190	7.4	1.65×10^{-4}	1.81×10^{-4}	109.7	1.66×10^{-4}	100.6
200	11.1	2.49×10^{-4}	2.71×10^{-4}	108.8	2.56×10^{-4}	102.8
230	28.4	6.49×10^{-4}	6.97×10^{-4}	107.4	7.40×10^{-4}	114.0
270	55.3	1.27×10^{-3}	1.36×10^{-3}	107.1	1.83×10^{-3}	144.1
300	69.3	1.60×10^{-3}	1.70×10^{-3}	106.3	2.80×10^{-3}	175.0
340	80.0	1.85×10^{-3}	1.96×10^{-3}	105.9	4.09×10^{-3}	221.1

The overall rate of product formation discussed above and estimated by **Eq. 3.17** is averaged over the entire pellet, in which the mass distribution and reactant concentrations vary (especially at high conversions). We can determine a local reaction rate by noting that the rate depends on local parameters (see **Eq. 3.14**). Of particular interest is the reaction rate of the catalytic particles on the TEM grid, since those are the

particles that are imaged. **Figure 3.6** shows that the gas composition on the TEM grid and on the surface along the inner hole in the pellet are almost identical. We can therefore calculate the rate at the surface along the inner hole in the pellet to determine the reaction rate of the particles on the TEM grid. We determine the reaction rate per unit mass by integrating the rate and mass around a 50 μm thick layer at the surface of the inner hole in the pellet. This reaction rate, which we refer to as r_3, is tabulated in **Table 3.4**. The ratio of the reaction rate at the surface of the pellet (r_3) to the reaction rate integrated over the whole pellet (r_1) is also displayed in the table. In general, the reaction rate averaged over the entire pellet is lower than that at the TEM grid because the concentrations of reactants in the pellet are lower than at the grid (due to mass transport limitations). The difference between the two rates increases with conversion. For conversions below 30%, the reaction rate for catalyst particles on the grid is less than 15% higher than that of the average rate in the pellet. However, at a conversion of 80%, the reaction rate on the grid is more than a factor of two higher than the rate integrated over the entire pellet. A visual representation of the behavior of the three rates r_1, r_2, and r_3 is given in **Figure 3.8**.

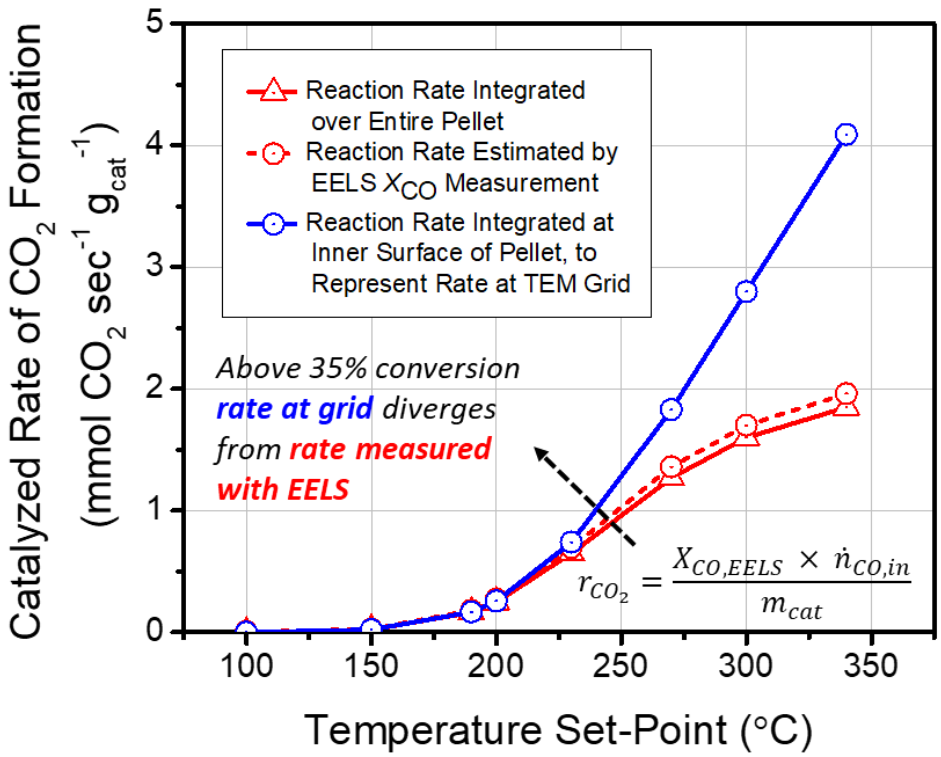

Figure 3.8. Mass-specific rate integrated throughout entire pellet (solid red line marked with triangles), mass-specific rate integrated throughout a thin 50 um layer on the inner surface of the pellet to represent the rate of catalyst on the TEM grid (solid blue line marked with circles), and mass-specific rate estimated by the EELS X_{co} simulation (dashed red line marked with circles) all plotted as a function of reactor temperature set-point. The black dashed line corresponds to a condition of 35% CO conversion.

The current model may overestimate the difference in reaction rates since we essentially assume that the pellet is sealed when it contacts the body of the hot stage, which limits mass transport and allows the CO_2 concentration to build up (see **Figure 3.6**). In practice, the pellet will not make a gas-tight seal with the body of the hot stage, and consequently the difference between the reaction rate in the pellet and at the TEM grid will be less. However, for the current reaction and catalyst, the model suggests that for conversions less than 50%, the absolute value of the reaction rate can be determined to within about 20%. The model can be used to make more accurate estimates of this

difference provided the catalyst loading is known and the order of the reaction kinetics is known. Of course, relative differences in reaction kinetics will be known more precisely.

The ability to measure the catalyzed reaction rate provides useful information for catalyst chemistry and characterization. Generally speaking, a measurement of the reaction rate allows an experimentalist to directly correlate atomic-level imaging and spectroscopy with the chemical kinetics of the same catalyst. For the ETEM reactor, at low conversions the relative homogeneity in the gas composition within the domain of the TEM pellet and grid enables reaction rates to be estimated from EELS for the catalyst particles being imaged. Even at higher conversions, the entire TEM grid used for imaging is exposed to the same reactor conditions and surface chemistry taking place at similar structures on different nanoparticles throughout the TEM sample will be identical. Essentially, for the differentially pumped ETEM reactor, the reactor conditions are fairly uniform, well defined, and measurable. The *in situ* TEM approach described here can be called *operando* because the observed nanoparticle structure can be directly linked to chemical kinetics. This *operando* capability may permit one to differentiate catalytically-relevant structures from spectator species by identifying those which emerge or correlate with the activity of the catalyst.

3.4. Summary

We have developed a finite element model combining fluid dynamics, heat transfer, multi-component mass transport, and chemical reaction engineering in order to determine the gas and temperature profiles present during catalysis in an *operando* experiment performed in an open cell ETEM. The model determines steady state solutions for an ETEM reactor with inflows of reactant gas mixtures, with product gases produced in the microscope during catalysis. Under typical *operando* TEM conditions, mass transport is dominated by diffusion, while heat transfer is dominated by conduction. For

reactor temperatures above 400 °C, radiation becomes more important and eventually dominates heat transfer.

As a case study, we have applied the model to a SiO_2-supported Ru catalyst performing CO oxidation. Steady state solutions were computed for a 3 mbar reactant gas inflow of stoichiometric CO and O_2. The simulated composition of catalytically-produced CO_2 agrees well with experimental measurements taken under nominally identical conditions across a range of temperatures spanning 25 – 350 °C. The CO_2 produced from the reaction distributes throughout the cell and the reactor, with an enrichment in the *operando* pellet. The enrichment in the *operando* pellet relative to the TEM grid ranges from 21% to 12% for CO_2 mole fractions between 5% and 73%, as measured with EELS, respectively. The gas composition at the TEM grid, which is important as the grid contains the catalyst that is imaged during an experiment, differs by less than 8% from the composition measured with EELS. For the conditions simulated here, the average temperature at the TEM grid differs from the intended furnace set point by less than 2 °C, even at temperatures where the catalyst is active. The results show that one can determine the temperature and gas composition surrounding catalytic nanoparticles imaged during an *operando* experiment in a differentially-pumped ETEM.

In general, the simulations show that the temperature and gas are relatively homogeneous within the hot zone of the holder where the catalyst is located. The uniformity of gas and temperature across the catalyst and TEM sample indicates that the system behavior around the catalyst approximates that of a continuously stirred tank reactor. The results show that EELS can be used to estimate the catalytic conversion of reactants in the ETEM cell to within 10%. A kinetic analysis shows that the rate at which reactants are consumed in the pellet approaches the rate at which reactants are flown into the ETEM cell, which demonstrates that most of the reactant gases interact with the

catalyst-loaded pellet and that there is limited gas bypass. A very important consequence of the gas-phase homogeneity is that the overall activity at all points in the TEM catalysts are similar to within 20% for conversions below 50%. Essentially, the reactor conditions are fairly uniform, well defined, and measurable for a differentially-pumped ETEM reactor. It is this characteristic that allows one to claim that this is truly *operando* TEM since the observed nanoparticle structure can be directly linked to known local reactor conditions and chemical kinetics. Overall, these findings indicate that under suitable conditions during an *operando* ETEM experiment, one can reliably evaluate the temperature and steady-state reaction rate of the catalyst that is imaged on the TEM grid.

4. Fluxional Behavior at the Atomic Level and its Impact on Activity: CO Oxidation over CeO_2-supported Pt Catalysts

4.1. Motivation

Reducible oxides (e.g., CeO_2) are widely used catalyst supports that can increase oxidation reaction rates over metal nanoparticles (e.g., Pt) by transferring their lattice oxygen to adsorbates at the metal-support interface. For CO oxidation, the interfacial oxidation process is typically described in terms of a Mars-van Krevelen mechanism (Mars & van Krevelen, 1954; Puigdollers et al., 2017), in which CeO_2 lattice oxygen is transferred to CO at the perimeter of the metal-support interface, which is also called the three-phase boundary. There is very little information about the atomic structure and structural dynamics of an active metal-support interface performing catalysis. Consequently, there are many outstanding questions regarding the atomic scale evolution of the interface, metal particle, and adjacent oxide surface during catalysis. For example, how does the metal particle and the metal-support interface behave during catalysis if oxygen vacancies are constantly being created and annihilated? Does such a process destabilize the metal particles and make coarsening more likely? Where is the likely site for molecular oxygen reduction and reincorporation into the lattice, which completes the catalytic cycle?

One may expect substantial changes in metal particle shape and bonding to occur during catalytic turnover, as the interfacial energy fluctuates from the continual creation and annihilation of oxygen vacancies. The adhesion between the metal particle and support may also weaken significantly since bridging interfacial oxygen are responsible for anchoring the metal to the support (Yasutaka Nagai et al., 2006; Shinjoh et al., 2009; Hatanaka et al., 2010; Gänzler et al., 2017, 2018). Oxygen vacancies will introduce strain in the CeO_2, which could further destabilize the system and make it more reactive (Balaji Gopal et al., 2017). Recently, there has been an emerging paradigm that has roots in

surface science (Somorjai, 1991) and chemistry (Cotton, 1975) for understanding catalytically active sites as dynamic, meta-stable, or so-called fluxional species (Zhai & Alexandrova, 2017; Sun & Sautet, 2018; Zhang et al., 2020; Lawrence et al., 2021; Li et al., 2021). In order to deepen our understanding of the factors affecting catalysis and to develop strategies for improved catalyst design, it is essential to elucidate and describe the structural meta-stability (i.e., fluxional behavior) that occurs at the atomic level during simultaneous catalytic turnover.

In this Chapter, aberration-corrected *operando* environmental transmission electron microscopy (ETEM) is employed along with finite element simulations to directly correlate atomic-resolution observations of fluxional behavior in CeO_2-supported Pt catalysts with the catalyst's turnover frequency for CO oxidation. Atomic-resolution imaging of the Pt/CeO_2 catalyst is performed during the simultaneous measurement of the catalytic CO oxidation reaction rate. Finite element simulations of the *operando* ETEM reactor are conducted to develop the chemical reaction rate analysis. Structural dynamics occurring at/near the sites that comprise the metal-support interface are correlated with the catalyst's turnover frequency for CO oxidation. Additionally, the catalyst is observed at 300 °C in an inert atmosphere of N_2 to differentiate spectator structural dynamics associated with applied heat from those associated with catalysis. Uniquely, during CO oxidation, the increasing frequency of catalytic turnover is seen to correlate with an increasing concentration of CeO_2 surface oxygen vacancies and dynamic structural behavior marking an enhanced rate of oxygen vacancy creation and annihilation; at the same time, the ~1.5 nm Pt nanoparticles become increasingly destabilized and undergo continuous and more frequent fluxional behavior. While the particular fluxional behaviors reported here are specific to the Pt/CeO_2 system and to CO oxidation, breaking and forming chemical bonds is an essential functionality for all heterogeneous catalysts, and it

may only occur if the catalytic surface undergoes substantial structural dynamics. The *operando* electron microscopy approach described here should be applicable to a large number of nanoparticle catalysts, which will enable the identification of catalytically functional surface structures and strengthen our ability to establish (dynamic) structure-activity relationships.

4.2. Experimental

4.2.1. Catalyst preparation and characterization of catalyst structure and activity

The catalyst, which consists of Pt nanoparticles supported on nanoparticles of CeO_2, was produced by standard hydrothermal and incipient wetness impregnation methods that are described previously in Chapter 2, Section 2.1.

Structural characterization was performed using X-ray diffraction (XRD) and aberration-corrected (scanning) TEM ((S)TEM). XRD patterns were collected on a Bruker D-5000 with a Cu Kα source (λ = 0.15406 nm). HRTEM images were collected on a Thermo Fisher Titan operated at 300 kV in a negative Cs imaging mode (see Chapter 2, Section 2.3.2). The STEM (a probe-corrected JEOL ARM200F) was operated at 200 kV and high angle annular dark field (HAADF) images were collected to determine the Pt nanoparticle size distribution, which allowed for an estimate to be made of the number of Pt atoms located at the interfacial perimeter. A derivation of this estimation is given in the Appendix, Section C.2.

Catalytic activities for CO oxidation were evaluated in a packed bed plug-flow reactor. Details on the experimental conditions are given in the Chapter 2, Section 2.2. Plug flow reactor experiments were performed in a RIG-150 micro-reactor from In Situ Research Instruments (ISRI). Effluent gas compositions were measured with a Varian

3900 gas chromatograph (GC) equipped with a thermal conductivity detector (TCD), as described in Chapter 2, Section 2.2.

4.2.2. Atomic-resolution *operando* environmental TEM

Atomic-resolution *operando* ETEM experiments were performed on an image-corrected Thermo Fisher Titan ETEM at 300 kV equipped with a Gatan Imaging Filter for electron energy-loss spectroscopy (EELS). An overview of the experimental *operando* ETEM methodology relevant to the work presented in this chapter is provided in Chapter 2, Section 2.3.5. After inserting the catalyst-loaded furnace reactor into the ETEM, an *in situ* reduction step was typically performed in 1 Torr of H_2 at 400 °C for 2 hours. The stage was then cooled to 120 °C and the column was briefly evacuated. As is common for CO oxidation, an oxygen rich reactant environment was used; 0.24 Torr of CO and 0.33 Torr of O_2 were admitted into the cell and the reactor was heated up to 300 °C. The pressure of gases used in the ETEM should not significantly impact the kinetic catalytic mechanism given the well-known 0^{th}-order dependence of the rate on the CO and O_2 partial pressures (Cargnello et al., 2013; Liu et al., 2014). Carrier gases were not used to increase the relative partial pressures of the reactants and to achieve high signal-to-background levels for EELS measurements.

Operando TEM images of the catalyst were acquired in the aforementioned negative C_s imaging mode (see Section 2.3.2) with an incident electron dose rate of ~1×10^3 $e^-/Å^2/s$ and an exposure time of 0.5 sec on a Gatan Ultrascan 1000 CCD detector. The use of a low electron dose rate and a CCD detector resulted in a poor signal-to-noise ratio (SNR) in the 0.5 second exposure images that were acquired (for example, see one of frames shown below in **Figure 4.2b – Figure 4.2e**). Utilizing a longer image acquisition time was impractical due to instabilities associated with drift in the furnace hot stage required for *operando* TEM. A higher dose-rate was not employed to avoid significant

radiation damage. Thus, a drift-corrected, time-averaged image method was implemented to increase the SNR available for local structural analysis under *operando* conditions. A schematic of the approach is provided in Appendix **Figure C.4**.

Previous ETEM work investigating the effect of the incident electron beam dose rate on the structure and chemistry of CeO_2 surfaces has demonstrated that electron beam effects are not significant for imaging current densities below 6 x 10^3 $e^-/Å^2/s$ (Sinclair et al., 2017). Additionally, Sinclair et al. (2017) report that no observable structural or chemical changes occur for this dose when low pressures of ambient oxygen are present. Here, oxygen is present, an electron flux below the reported critical threshold is used, and the dose rate is maintained below this level throughout the experiment. Furthermore, work by Lawrence et al. (2021) shows that, for the imaging conditions employed in the present work, the rate of electron beam-induced radiolytic or knock-on events becomes negligible compared to that of thermally-induced events (i.e., those expected to regulate catalytic processes) as the temperature of the CeO_2 rises above 150 °C, which is explored here (Lawrence et al., 2021).

In situ EELS was implemented to determine the *in situ* conversion of CO to CO_2 as discussed in Chapter 2, Section 2.3.4**.** The catalytic reaction rate was estimated from the *in situ* conversion by multiplying the conversion with the known inlet molar flow rate of reactant CO. A correction factor for calculating the true reaction rate of the catalyst supported on the TEM grid was obtained by performing finite element simulations of the ETEM reactor under conditions nominally identical to the experiment. More details on the reaction rate analysis are given in Chapter 3 and in (Vincent et al., 2020; Vincent & Crozier, 2021).

4.2.3. Finite element simulation of *operando* ETEM reactor for kinetic analysis

As discussed in Chapter 3, a finite element model of the ETEM reactor has been developed, allowing for an investigation into how the reactant conversion measured along the EELS line can be used to derive the steady-state reaction rate for the catalyst supported on the TEM grid (Vincent et al., 2020). Here we have employed the model to simulate the *operando* ETEM reactor under conditions matching the present experiment in order to evaluate the catalytic chemical reaction rate during atomic-resolution imaging to establish truly *operando* TEM. The catalytic reaction was modeled as 0^{th} order, with kinetic parameters describing the activity of the catalyst taken from the Arrhenius analysis from the plug flow reactor data (Appendix **Figure C.3**). Simulations were performed in the commercial program COMSOL Multiphysics®. More information describing the simulations is given in the Appendix, Section C.3.

4.2.4. *In situ* ETEM of Pt/CeO_2 in an inert gas atmosphere at elevated temperature

In situ ETEM experiments were conducted on the Pt/CeO_2 catalyst in an atmosphere of inert N_2 both at room temperature and at 300 °C to differentiate spectator structural dynamics associated with applied heat from those associated with CO oxidation. These experiments were conducted in an image-corrected Thermo Fisher Titan ETEM operated at 300 kV using a DENSsolutions Wildfire MEMS-based heating holder. The catalyst was imaged in 5 mTorr of N_2 gas at room temperature; then the catalyst was heated to 300 °C in N_2 and imaged again. Images were acquired with an incident electron beam dose rate of 5 x 10^3 $e^-/Å^2/s$ using a Gatan K2 IS direct detector in electron counting mode. The beam was blanked whenever images were not being acquired to further minimize electron beam-induced changes.

4.3. Results

4.3.1. Catalyst morphology and ex situ structural characterization

The catalyst's activity for CO oxidation was evaluated in a packed-bed plug-flow reactor. The light-off curves for the bare and Pt-loaded CeO_2 are shown in **Figure 4.1a**. An identical mass loading of catalyst was used for both cases. The activity of the bare CeO_2 support (blue) is demonstrably less than the Pt-loaded CeO_2 (red) and the effect of blank reactor (black) is negligible at working temperatures. No difference in the CeO_2-supported Pt catalyst's activity was detected on the temperature ramp up to full conversion (filled red triangles pointing up) in comparison to the ramp back down to room temperature (empty red triangles pointing down). An Arrhenius analysis of the light-off curves for the Pt/CeO_2 catalyst (Appendix **Figure C.3**) shows linear behavior, with an apparent activation energy of $E_{a,\,app}$ = 74 kJ mol^{-1} calculated from the linear regression, which is consistent with activation energy values reported previously (Cargnello et al., 2013).

The XRD patterns of the bare CeO_2 and Pt/CeO_2 are shown in Appendix **Figure C.1**. A simulated XRD pattern of an infinite crystal of CeO_2 (*JCPDS* No. 34-0394) matches well with the experimental XRD patterns of the catalyst, indicating that the sample is phase-pure CeO_2 (space group Fm-3m, a = 5.41 Å) with highly dispersed Pt particles.

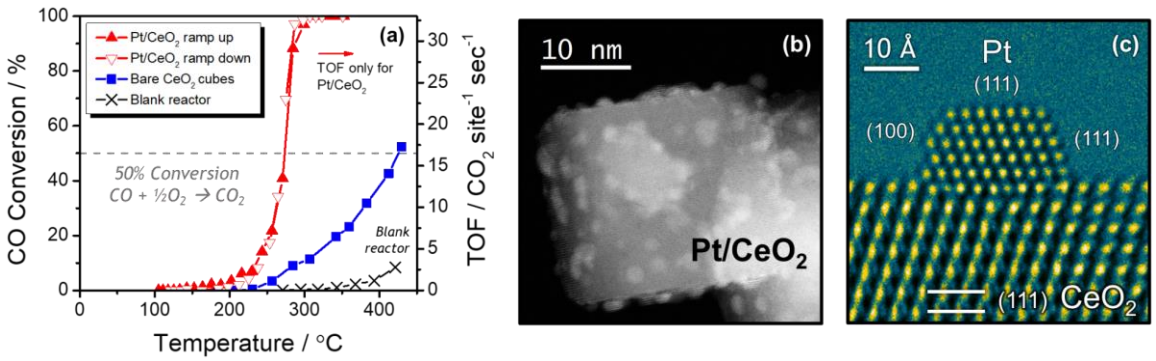

Figure 4.1. (a) Catalytic activity for CO oxidation evaluated in a packed-bed plug-flow reactor. The activity of the bare CeO_2 support is demonstrably less and the effect of blank reactor is negligible. **(b)** Z-contrast STEM image of a typical Pt-loaded CeO_2 nanoparticle showing dispersion of roughly 1.6 nm Pt nanoparticles loaded on the CeO_2 nanoparticle support. **(c)** HRTEM image of a typical Pt nanoparticle supported on a (111) surface of a CeO_2 nanoparticle, with indices of exposed Pt surfaces marked in the image.

A HAADF-STEM image of a typical Pt-loaded CeO_2 nanoparticle is shown in **Figure 4.1b**. The Pt nanoparticles are well-dispersed on the CeO_2 nanoparticle support and are around 2 nm in size. The size distribution of the Pt nanoparticles was further investigated and quantified with HAADF-STEM imaging. Details are provided in Appendix **Figure C.2**. Many different regions of the catalyst sample were imaged and the diameter sizes of 475 Pt nanoparticles were measured, revealing that the average Pt nanoparticle size was 1.6 nm. Quantifying the Pt nanoparticle size allowed for catalytic turnover frequencies (TOFs) to be determined on an interfacial perimeter-site basis. A derivation and sample calculation are provided in the Appendix, Section C.2.

Figure 4.1c displays an HRTEM image of a typical CeO_2-supported Pt nanoparticle. The Pt nanoparticles are stable and well-facetted when imaged *ex situ*, with the one shown in **Figure 4.1c** exposing nanosized (100) and (111) surfaces, which is typically observed. The Pt nanoparticles exhibit a well-defined epitaxy with the support, with virtually all nanoparticles presenting (111) surfaces to the metal-support interface, which in this case is comprised of a (111) CeO_2 surface on the support side. Well-defined

orientation relationships have been reported for CeO_2-supported Pt nanoparticles, and they can be attributed to epitaxial relationships that indicate strong structural interactions between the metal and the support (Bernal et al., 1997, 2000; Trovarelli, 2002). The Pt particles remained stable during the HRTEM observation at room temperature.

4.3.2. *In situ* ETEM imaging under CO oxidation reaction conditions

The catalyst was imaged *in situ* under CO oxidation reaction conditions. **Figure 4.2** shows an *in situ* ETEM image time-series of a typical CeO_2-supported Pt nanoparticle in 0.57 Torr of CO and O_2 at 144 °C. The Pt particle occupies a short CeO_2 (111) nanofacet and each side of the particle is in contact with a CeO_2 (111) step edge. Images of the catalyst obtained *in situ* under reaction conditions show prominent motion artifacts and features attributable to fluxional behavior. The time-series is comprised of four images in succession, each with a 0.5 sec exposure time. **Figure 4.2a** displays the time-averaged image obtained by summing together the frames over the entire [0 – 2.0] sec acquisition period. Relative to the bulk of the CeO_2 support, which appears with well-defined white atomic column contrast, the Pt NP presents white as well as black atomic column contrast.

The weak and varying Pt contrast in the 2.0 second time-averaged image of **Figure 4.2a** is not a consequence of poor microscope imaging conditions, as evidenced by comparison with the bulk CeO_2. Rather, the Pt particle is demonstrating fluxional behavior, in which the nanoparticle dynamically progresses through a series of reconfigurations over the course of the time-averaging period. Multislice TEM image simulations have been performed to investigate this effect (see Appendix **Figure C.5**). The simulations demonstrate the appearance of mixed black and white Pt atomic column contrast when the particle is aligned with the incident beam and imaged at an electron optical defocus of 2 nm. Furthermore, the simulations show that contrast reversals can occur when the Pt nanoparticle tilts by a few degrees, e.g., due to a rigid-body rotation.

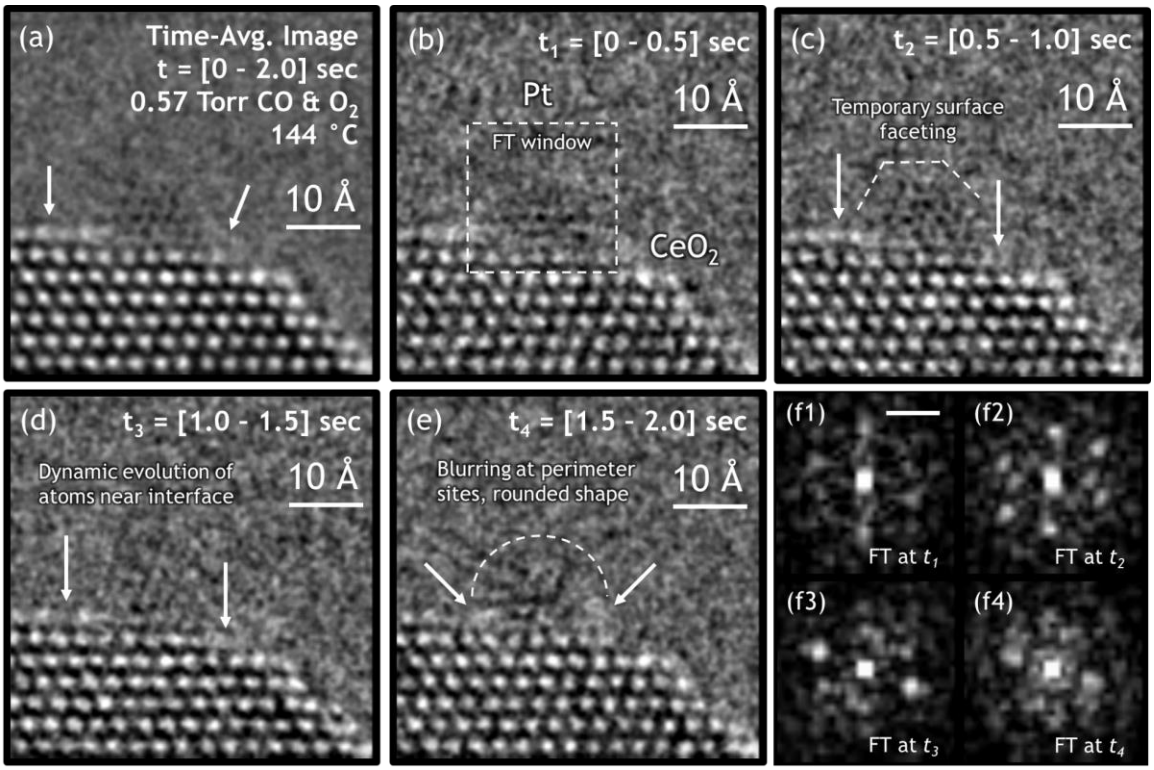

Figure 4.2. *In situ* ETEM image time-series of CeO_2-supported Pt NP at 144 °C in 0.57 Torr of CO and O_2. Part **(a)** shows the time-averaged image of the catalyst, obtained by summing together the individual 0.5 second exposure frames over the entire [0 – 2.0] second acquisition period. Parts **(b)** – **(e)** show the atomic-scale structural dynamics that evolve over 0.5 second intervals from t = 0 seconds to t = 2.0 seconds. Parts **(f1)** – **(f4)** display the FT taken at each time interval from the windowed region around the Pt NP, as denoted in **(b)**. The scale bar in **(f1)** is 5.0 nm^{-1}. Images have been processed with a bandpass filter for clarity. FTs were produced from unfiltered, windowed images that were processed with a Hanning function to remove edge artifacts caused by windowing; the modulus of the FT is shown.

For the sake of clarity in the following discussion, we define three locations of reference, namely (1) the free CeO_2 surface, which is comprised of the sites at the freely exposed CeO_2 surface around the Pt nanoparticle, (2) the three-phase boundary, which is comprised of the sites at the perimeter of the metal-support interface, and lastly (3) the buried interface, which is comprised of the sites within the metal-support interface that are not exposed to the gas phase. In the 2.0 sec time-averaged image (**Figure 4.2a**), diffuse contrast is observed at the three-phase boundary (right arrow) and along the free

CeO_2 surface on the CeO_2 (111) terrace to the left of the Pt nanoparticle (left arrow). In comparison, the sub-surface and bulk Ce sites show sharp and clearly resolved atomic columns. The diffuse contrast or local streaking/blurring observed at the CeO_2 surface and Pt/CeO_2 interface is therefore not due to drift in the hot stage or the electron optics, but instead arises from dynamic structural reconfigurations occurring at these specific sites (Lawrence et al., 2021).

An examination of the *in situ* image time-series reveals the atomic-scale structural dynamics and how they evolve over time. **Figure 4.2b – Figure 4.2e** show the four individual 0.5 second exposure frames taken over the [0 – 2.0] second acquisition period (the images have been processed with a bandpass filter for clarity). **Figure 4.2(f1) – Figure 4.2(f4)** display the Fourier transform (FT) at each time interval, taken from the windowed region around the Pt nanoparticle that is indicated by the dashed box in **Figure 4.2b**. An analysis of the major spots that appear in the FTs indicate the presence of metallic Pt (shown in Appendix **Figure C.6**). (The FTs were produced from unfiltered images that were pre-processed with a 2D Hanning function to suppress edge artifacts caused by windowing).

As seen both in the time-series images and corresponding FTs, the Pt nanoparticle undergoes a series of structural reconfigurations that involve dynamic restructuring at the Pt particle surface and at the Pt/CeO_2 interface. At the same time, certain surface and interfacial Ce sites exhibit dynamic events that occur along with those observed in the supported Pt. In **Figure 4.2c**, we observe the catalyst at a moment of relative structural stability, evidenced by the surface faceting and atomic column contrast in the Pt. In **Figure 4.2c**, the arrowed Ce atomic columns at/near the three-phase boundary appear with diffuse contrast but are clearly resolved. In the next frame, 0.5 seconds later (**Figure 4.2d**), the same arrowed Ce sites have either disappeared or substantially blurred. The Pt

has undergone a rotation or tilt, evidenced by the diagonal streaking in the Pt and by the loss of associated Bragg spots in the FT shown in **Figure 4.2(f3)**. Another 0.5 seconds later (**Figure 4.2e**), the Pt particle shows weak contrast with no evident lattice fringes. The particle has also adopted an apparently rounded shape, which is marked with a dashed line in the image. The lack of lattice fringe contrast in the Pt signifies that the supported particle is undergoing dynamic restructuring at a speed that is much faster than the frame exposure time. Interestingly, in this time interval, the Ce sites at the free CeO_2 surface and at the three-phase boundary also appear very dynamic. As seen in **Figure 4.2e**, a build-up of bright but diffuse intensity appears at the perimeter of the Pt/CeO_2 interface, which is indicated with the arrows. Neighboring Ce sites now show vacancies, so the bright and diffuse contrast at the interfacial perimeter may indicate that nearby surface atoms have migrated to the perimeter sites, where they continue to undergo rapid dynamics that cannot be resolved with the present frame rate (see, e.g. (Crozier et al., 2019)).

At this condition, the reactor temperature is below the light-off point of the catalyst, and no conversion is detected yet in the ETEM cell. While the ensemble of catalyst particles loaded in the ETEM reactor is not yet active enough to produce a measurable conversion, the Pt/CeO_2 catalyst still undergoes a variety of dynamic structural reconfigurations which constantly evolve over time. Extrapolating the reaction rates experimentally measured at higher temperatures (and presented in **Figure 4.3**) to this temperature, 144 °C, results in a turnover frequency on the order of 5×10^{-5} molecules CO $site^{-1}$ sec^{-1}, showing that continuous catalytic turnover is not occurring at an appreciable rate. As such, the dynamic structural reconfigurations observed in **Figure 4.2** are likely associated with intermediate steps in the catalytic reaction that have a lower activation energy than the rate-limiting step.

Recent density functional theory calculations indicate that abstraction of lattice oxygen by CO on CeO_2 (111) surfaces proceeds with an activation energy barrier around 0.4 eV (Salcedo & Irigoyen, 2020). On the other hand, it is generally well known that the molecular dissociation and gas phase exchange of O_2 is energetically much more challenging, with theoretical calculations and experimental isotopic oxygen exchange measurements placing the activation energy over CeO_2 around 1.1 eV (Martin & Duprez, 1996; Han et al., 2019). Hence, here we speculate that the observed fluxional behavior is associated with the energetically more facile steps of lattice oxygen abstraction by CO, and that the absence of measurable conversion is due to the lack of oxygen vacancy back-filling from molecular O_2 exchange. This fluxional behavior was not observed at room temperature in vacuum. Additional imaging experiments carried out in a N_2 atmosphere at a temperature of 300 °C show a lack of similar structural dynamics, further demonstrating that the fluxional behavior is not due simply to thermal effects (see the Appendix, Section C.7).

Finally, it is worth noting that the dynamic behavior exhibited by the CeO_2-supported Pt nanoparticle in **Figure 4.2** is typical of the many observed during the ETEM experiment. Additional images and analysis from a different particle, for example, are shown in Appendix C, **Figure C.9**. We have also carried out *in situ* TEM imaging of CeO_2-supported Pt nanoparticle catalysts in atmospheres of CO (Crozier et al., 2019), CO and O_2 (Vincent & Crozier, 2020), and CO and H_2O (Li et al., 2021), and shown that substantial fluxional behavior can occur in these reactant gases – even at room temperature. In order to identify structural dynamics unambiguously associated with catalytic chemistry, we proceed to image the catalyst under *operando* conditions and correlate the observed fluxional behavior directly with the chemical kinetics measured in the ETEM cell.

4.3.3. Detection and quantification of reaction rate in the ETEM reactor

The catalyst was heated until detectable conversions of CO into CO_2 occurred. The catalytic reaction rate in the ETEM was determined by EELS conversion measurements supported by finite element simulations. **Figure 4.3a** displays a set of background-subtracted and normalized energy-loss spectra to demonstrate the detection of catalytically-produced CO_2. When no catalyst is loaded in the reactor, the spectrum of gas around the reactor (dashed gray curve) shows a prominent C π^* peak at 285 eV, which corresponds to CO. The conversion of CO to CO_2 is observed only after Pt/CeO_2 catalyst is present (solid red curve). In this case, a second prominent peak appears at 288.3 eV which corresponds to the C π^* peak of CO_2. Both spectra were acquired under nominally identical conditions for a furnace set point of 300 °C in 0.57 Torr of CO and O_2.

The ratio of CO and CO_2 present in the spectrum can be quantified to calculate the CO conversion (Crozier & Chenna, 2011; Chenna & Crozier, 2012; Miller & Crozier, 2014). **Figure 4.3b** presents the EELS CO conversions detected during the *operando* ETEM experiment, plotted as a function of the reactor temperature (red circles). At 251 °C, the CO conversion was calculated to be 2.8 ± 3.7%, increasing at 275 °C to a value of 15.1 ± 0.5% and further at 285 °C to a value of 19.8 ± 0.3%. Finite element simulations of the ETEM reactor were performed to establish a framework for linking the CO conversion measured along the EELS line to the reaction rate of the catalyst imaged on the TEM grid. Further details on the simulations are given in Chapter 3, in Section C.3 of the Appendix**,** and in (Vincent et al., 2020). Steady-state calculations were done under conditions nominally identical to the current experiment, and the gas and temperature distributions were determined during catalysis. The simulated CO conversion measured along the EELS line in the model is plotted as the solid gray curve in **Figure 4.3b.** The simulated conversion curve shows reasonable agreement with the values measured experimentally.

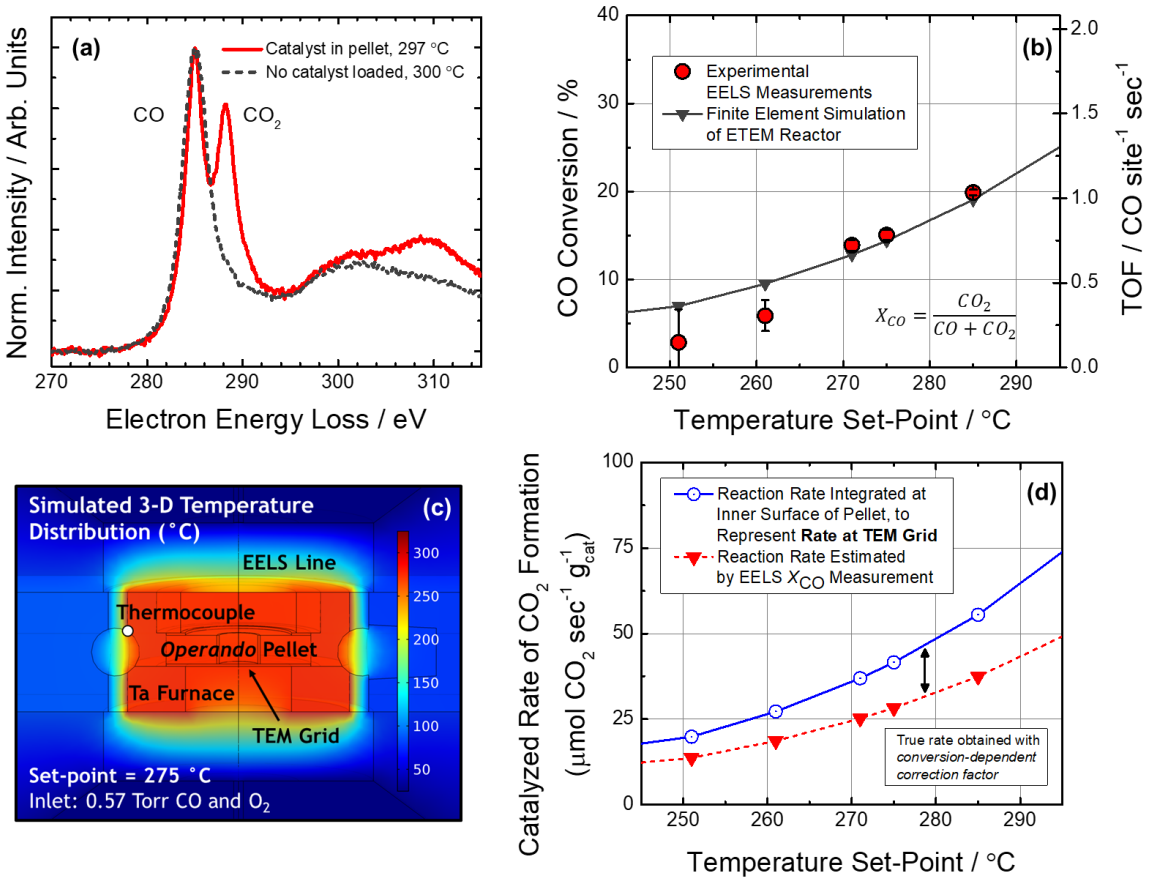

Figure 4.3. Detection and quantification of *in situ* CO conversion and catalytic reaction rate in the ETEM reactor. In **(a)** a set of background-subtracted electron energy-loss spectra taken from the gas atmosphere around the reactor demonstrates that activity is attributed to the Pt/CeO_2 catalyst, not the reactor. In **(b)** the CO conversion detected with EELS during the *operando* ETEM experiment was quantified and plotted as a function of temperature (red circles). The solid gray curve displays the CO conversion evaluated under nominally identical conditions within a finite element simulation of the ETEM reactor. In **(c)** the simulated temperature distribution in the model reactor is plotted for a furnace set point of 275 °C. Finally, in **(d)** an analysis of the catalyzed rate of product formation in the model is presented, which provides a conversion-dependent correction factor for quantitatively determining the catalytic reaction rate from the *in situ* conversion measurement.

It is important to investigate the extent of any thermal gradients that may exist within the reactor. **Figure 4.3c** shows the simulated 3-dimensional temperature distribution in the *operando* ETEM reactor for a furnace thermocouple set point of 275 °C. The temperature distribution appears largely uniform throughout the reactor, and

the temperature of the reactor matches well with the furnace set point. The temperature distribution shown in **Figure 4.3c** is representative of the behavior observed at other working temperatures. The high degree of thermal uniformity suggests that the reactor can be treated as approximately isothermal. A quantitative comparison of the temperature difference between the furnace set point and the TEM grid, reveals that the typical discrepancy between these two locations is at most 1.6 °C, supporting this assumption (not shown here; see (Vincent & Crozier, 2021) for more details).

Next we use the finite element model to determine how the EELS CO conversion measurement can be used to derive quantitative information about the reaction rate of catalyst particles on the TEM grid (r_{CO_2}, with units of mol CO_2 per second per gram catalyst). Following the analysis developed in Chapter 3, Section 3.3.5, the simulated r_{CO_2} estimated from the EELS CO conversion is plotted vs. temperature as the dashed red curve in **Figure 4.3d**. The rate estimated from the conversion should not be taken as the rate of catalyst particles on the TEM grid. Previously we have shown that the difference between the estimated rate and the true rate at the grid can vary significantly as a function of conversion and may grow beyond 200% in some cases (see, e.g., **Figure 3.8)**. This clearly demonstrates the need for and power of a model in determining quantitative chemical kinetics. As explained in the Chapter 3, Section 3.3.5 and in Vincent et al. (2020), the mass-normalized rate for the particles on the TEM grid can be simulated by integrating the mass and rate along the innermost surface of the pellet, where the composition and temperature are both nearly identical to that of the TEM grid (Vincent et al., 2020). The true simulated rate is plotted against temperature as the solid blue curve in **Figure 4.3d**. An analysis of the ratio of the two rates provides a conversion-dependent correction factor, allowing the true rate to be calculated correctly from the rate estimated through the EELS conversion measurement (see Appendix C, Table C.1).

Finally, we choose to normalize the reaction rate on an interfacial perimeter site-basis, yielding an ensemble *in situ* TOF. As discussed, a relationship has been derived to link catalyst mass with the average number of Pt perimeter sites (see Appendix, Section C.2). Thus, the corrected *in situ* reaction rate can be used to estimate an *in situ* TOF for catalyst particles on the TEM grid. This quantity is plotted along the right axis of **Figure 4.3b**. Note that the plotted TOF values were obtained after correcting the rate measured with EELS by the finite element analysis presented above. At 251 °C, the *in situ* TOF was calculated to be 0.15 CO site^{-1} sec^{-1}, increasing at 275 °C to a value of 0.80 CO site^{-1} sec^{-1} and further at 285 °C to a value of 1.05 CO site^{-1} sec^{-1}.

4.3.4. Fluxional dynamics occurring at and near the Pt/CeO_2 interface during catalysis

With a quantitative measure of the chemical reaction rate, we proceed to image the catalyst at varying degrees of activity and then correlate the measured reaction kinetics directly with atomic-resolution observations of the dynamic working catalyst structure. **Figure 4.4** displays a set of three 12.5 second time-averaged *operando* ETEM images of the same CeO_2-supported Pt nanoparticles taken at (a) 144 °C, where the TOF was determined to be 0.00 CO site^{-1} sec^{-1}, (b) at 275 °C, where the TOF was measured to be 0.80 CO site^{-1} sec^{-1}, and (c) at 285 °C, where the TOF was measured to be 1.05 CO site^{-1} sec^{-1}. The roughly 1.5 nm Pt nanoparticles are supported on small ~2 nm CeO_2 (111) nanofacets, with either side of each nanoparticle in contact with CeO_2 (111) step edges.

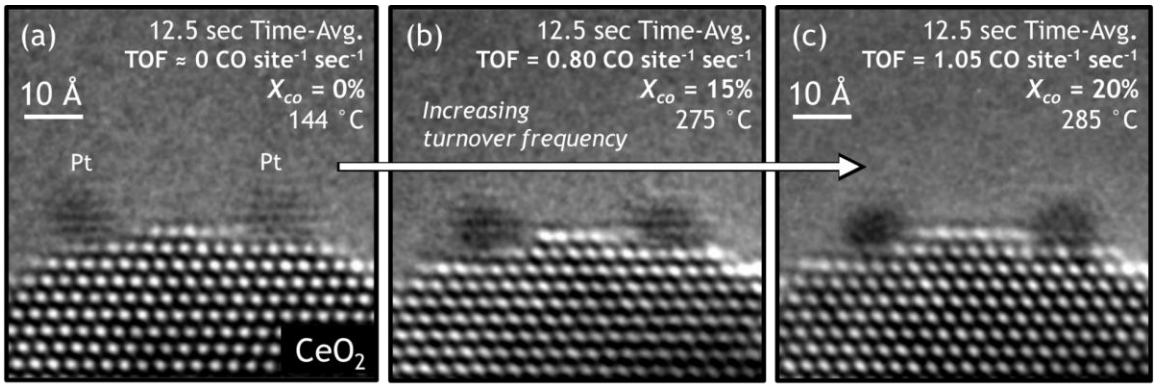

Figure 4.4. 12.5 second time-averaged *operando* TEM images showing the dynamic structural evolution of the Pt/CeO_2 interface and nearby support surface for CO conversions of **(a)** X_{co} = 0%, **(b)** X_{co} = 15%, and **(c)** X_{co} = 20%. The corresponding temperatures and perimeter-site normalized TOFs are stated in the respective figures.

The increasing frequency of catalytic turnover is seen to coincide with dynamic fluxional behavior in the working catalyst structure. The observed dynamic fluxional behaviors give rise to motion artifacts and contrast features in the time-averaged *operando* TEM images that are similar to those discussed previously in Section 4.3.2. Here we observe that the Pt nanoparticles evolve from an initially well-defined, facetted morphology, with clearly visible lattice fringe contrast (**Figure 4.4a**), to darker patches of nearly uniform contrast, now exhibiting an apparently rounded morphology, with lattice fringes that are greatly diminished in visibility (**Figure 4.4c**). Additionally, the Ce sites on the free CeO_2 surface neighboring the metal-support interface become increasingly more blurred with larger catalytic turnover. Finally, in addition to a pronounced blurring at higher turnover, the top layer of Ce that neighbors the Pt/CeO_2 interface also displays an outward surface relaxation which grows larger with increasing activity. The outward surface relaxation is difficult to see by eye in the image but is easily measurable in intensity line profiles taken at each condition (discussed below and presented in Appendix C, **Figure C.12** and **Table C.2**).

A quantitative analysis of the *operando* ETEM images was performed in order to establish correlations between these fluxional dynamics and the catalyst's turnover frequency for CO oxidation. To describe the degree of structural dynamics taking place in the Pt nanoparticles, we quantify the Pt lattice fringe visibility (**Figure 4.5**) through FT analysis. Windowed regions centered on the left and right Pt NPs were extracted from the time-averaged *operando* ETEM images at each condition, then filtered with a Hanning function, and finally transformed into Fourier space. The left and right Pt NP FT window are shown, at 144 °C for example, in the left-most side of **Figure 4.5**. **Figure 4.5(a1)-(a3)** and **Figure 4.5(b1)-(b3)** show the modulus of the FTs taken from the right and left Pt NP, respectively, at conditions corresponding, respectively, to catalytic TOFs of 0.00, 0.80, and 1.05 CO site^{-1} sec^{-1}.

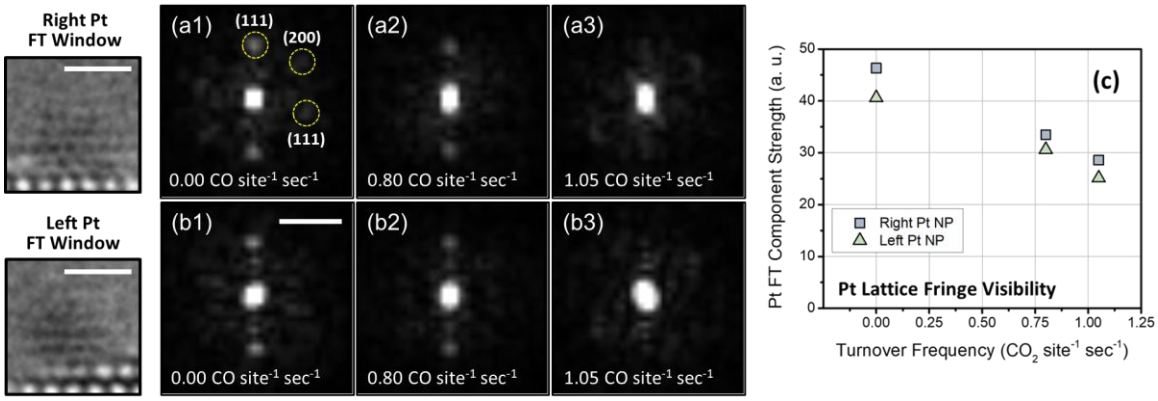

Figure 4.5. Quantification of Pt nanoparticle (NP) fringe visibility and correlation with turnover frequency for CO oxidation. The fringe visibility is determined through FT analysis of windowed regions centered on the Pt NPs shown, e.g., at left. Scale bars in images correspond to 1 nm. Parts **(a1)** – **(a3)** show the modulus of the FTs after applying a Hanning filter to the windowed images of the right Pt NP at conditions corresponding to TOFs of 0.00, 0.80, and 1.05 CO site^{-1} sec^{-1}, respectively. Parts **(b1)** – **(b3)** show the modulus of the FTs taken from the left Pt NP at the same respective conditions. The scale bar in **(b1)** corresponds to 5.0 nm^{-1}. In **(c)**, the Pt fringe visibility is quantified and plotted as a function of catalytic turnover frequency.

The Pt fringe visibility clearly decreases with increasing catalytic turnover. In **Figure 4.5(a1)**, labels are given to Bragg spots corresponding to various low-index Pt fringes. The Pt lattice fringe visibility can be quantified by summing the magnitude of the Bragg spots corresponding to Pt (here we sum the FT modulus within the regions defined by the dashed yellow circles as shown in **Figure 4.5(a1)**; the image intensities were normalized prior to summation). We call this quantity the Pt FT component strength and plot it for the left and right Pt NP as a function of catalytic turnover frequency in **Figure 4.5c**. The component strength of the left (green triangles) and right (blue squares) Pt NP are similar at each temperature. As the turnover frequency for CO oxidation increases, the visibility of fringes in either NP decreases. The component strengths of the left and right NP are 40.6 and 46.3, respectively, at 144 °C when the TOF is 0.00 CO site^{-1} sec^{-1}. At 275 °C, the TOF increases to 0.80 CO site^{-1} sec^{-1} and the left and right Pt NP component energies drop to 30.6 and 33.4, respectively. At 285 °C, where the TOF has increased to 1.05 CO site^{-1} sec^{-1}, the left and right Pt NP component energies decrease again to 25.1 and 28.6, respectively. As seen in the time-averaged *operando* TEM images (**Figure 4.3c**) and in the associated FTs (**Figure 4.5(a3)** and **Figure 4.5(b3)**), at this condition, the lattice fringes are diffuse in either Pt NP and Bragg spots are significantly weaker.

Next we focus on the fluxional behavior and structural dynamics occurring on the free (111) CeO_2 surface that connects the two Pt particles. Enhanced views of the connecting terrace are given in **Figure 4.6** for TOFs of (a1) 0.00 CO site^{-1} sec^{-1}, (a2) 0.80 CO site^{-1} sec^{-1}, and (a3) 1.05 CO site^{-1} sec^{-1}. The surface Ce sites neighboring the metal-support interface become increasingly blurred with higher catalytic turnover. As can be seen in **Figure 4.6(a1)**, the free CeO_2 surface sites neighboring the Pt/CeO_2 interface already shown a visible degree of blurred intensity at a TOF of 0.00 CO site^{-1} sec^{-1}. However, when the TOF increases to 1.05 CO site^{-1} sec^{-1}, the blurring of the surface Ce

becomes further pronounced to the point that the top layer appears as a nearly continuous band of intensity running parallel to the (111) CeO_2 support surface (**Figure 4.6 (a3)**). A similar blurring of the free surface Ce sites located at the opposite sides of the Pt nanoparticles can be observed in **Figure 4.4c**. The blurring does not appear within the CeO_2 bulk, indicating that the contrast change in the image is a consequence of fluxional changes in the CeO_2 surface near the metal-support interface.

The degree of blurring can be quantified and correlated with TOF by computing the average free surface Ce atomic column contrast at each condition. Here, the atomic column contrast is calculated by analyzing 100 pm wide intensity line profiles taken over the region that contains the surface Ce cation columns. A description of the approach along with the intensity line profiles used in the analysis is given in Appendix C, **Figure C.10**. The average surface Ce atomic column contrast is plotted as a function of catalytic turnover frequency in **Figure 4.6b**; error bars are given as the standard deviation relative to the mean measurement.

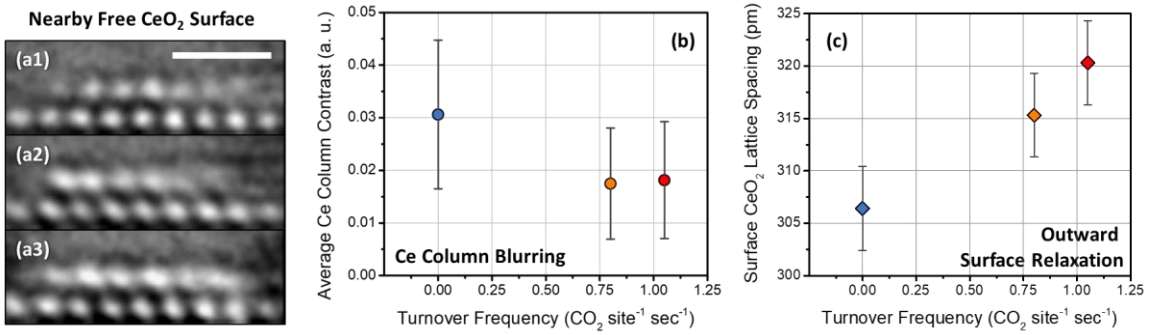

Figure 4.6. Quantification of fluxional behavior taking place on the free CeO_2 (111) surface neighboring the Pt nanoparticles and correlation with TOF for CO oxidation. Enhanced views of the nearby free CeO_2 (111) surface are shown for TOFs of **(a1)** 0.00 CO site^{-1} sec^{-1}, **(a2)** 0.80 CO site^{-1} sec^{-1}, and **(a3)** 1.05 CO site^{-1} sec^{-1}. The scale bar in **(a1)** corresponds to 1 nm. Part **(b)** displays the average surface Ce atomic column contrast plotted against catalytic TOF; error bars are given as the standard deviation relative to the mean measurement. In **(c)**, the separation distance between the surface and subsurface CeO_2 (111) planes is correlated with TOF. Error bars are derived from the standard deviation about the mean lattice spacing measured in the subsurface and bulk CeO_2.

The contrast measurements plotted in **Figure 4.6b** show unambiguously that the fluxional behavior giving rise to the Ce column blurring becomes more pronounced at higher catalytic turnover. At 144 °C when the TOF is 0.00 CO site^{-1} sec^{-1}, the average surface Ce contrast is 0.031. At 275 °C, the TOF has increased to 0.80 CO site^{-1} sec^{-1}, and the average contrast has decreased to a value of 0.017. At 285 °C the TOF has again increased to 1.05 CO site^{-1} sec^{-1}, although the average measured contrast remains more or less the same at a value of 0.018. Upon further investigation, it became clear that the contrast measurement at 275 °C was biased toward lower values due to the fact that the support particle had tilted, leading to an enhanced streaking in the direction of the measurement. An examination of intensity line profiles taken from the bulk of the CeO_2 show an analogous reduction in contrast (Appendix **Figure C.10b**). As the catalyst was heated up to 285 °C, the crystal tilted back to roughly the same orientation, evidenced by the recovered contrast from columns in the bulk of the nanoparticle as seen in Appendix **Figure C.10b**. Since the CeO_2 support has returned to roughly the same [110] zone axis orientation at 285 °C, comparing the quantified contrast of the columns at 144 °C vs 285 °C can provide insight into the evolution of blurring that occurs at individual surface Ce sites near the metal-support interface. Appendix **Figure C.11** presents the quantified contrast of individual surface Ce columns at a TOF of 1.05 CO site^{-1} sec^{-1} plotted against the quantified contrast of the same column when the TOF was measured to be 0.00 CO site^{-1} sec^{-1}. The plot demonstrates that while on average the contrast decreases with increasing turnover, one column (located in the middle of the surface row) actually shows a slight increase in contrast, which indicates that redistributions of cation column occupancy along the surface are occurring as well as the dynamic behavior.

In addition to a pronounced blurring at higher turnover, the top layer of Ce that neighbors the Pt/CeO_2 interface also displays an outward surface relaxation which grows

larger with increasing activity. The outward CeO_2 (111) surface relaxation was quantified by measuring the lattice plane separation distance from intensity line profiles taken from the interior of the CeO_2 support toward the catalyst surface (see Appendix C, **Figure C.12)**. The distance measured between the surface and subsurface CeO_2 (111) lattice planes is plotted as a function of catalytic turnover frequency in **Figure 4.6c**. The error bars are derived from the standard deviation about the mean lattice spacings measured in the subsurface and bulk at that condition (here, we briefly note that the average of the sub-surface and bulk lattice plane separation distances was measured to be 310 ± 4 pm, which agrees with the accepted CeO_2 (111) Miller plane spacing of 312 pm).

Examining the surface lattice spacing plotted against catalytic turnover frequency illustrates the emergence of an outward surface relaxation that grows linearly with increasing activity. At 144 °C where the TOF is 0.00 CO $site^{-1}$ sec^{-1}, the surface CeO_2 (111) lattice plane distance is 306 ± 4 pm. At 275 °C, where the TOF has increased to 0.80 CO $site^{-1}$ sec^{-1}, the surface CeO_2 (111) lattice plane has relaxed outward by 9 pm to a value of 315 ± 3 pm. At 285 °C, the TOF has increased to 1.05 CO $site^{-1}$ sec^{-1}, and the surface CeO_2 (111) lattice plane has relaxed by another 5 pm to a value of 320 ± 5 pm. The surface lattice plane separation was also measured in an inert atmosphere of N_2 at room temperature and at working temperature; no such expansion was detected upon heating the catalyst up to 300 °C, as shown in Appendix **Figure C.8**.

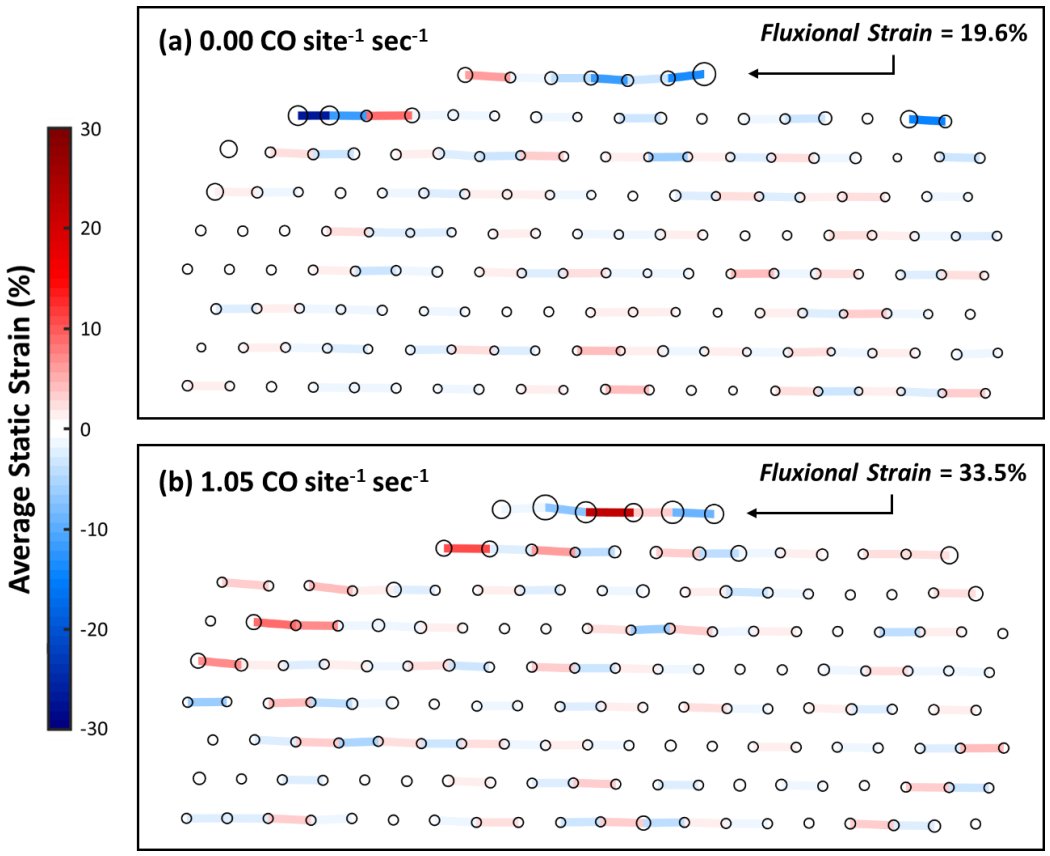

Figure 4.7. Static and fluxional strain in CeO_2 support at TOFs of **(a)** 0.00 CO site^{-1} sec^{-1} and **(b)** 1.05 CO site^{-1} sec^{-1}. The circles signify the Ce atomic column position determined by Gaussian peak fitting and are drawn proportional in size to the standard deviation of the fitted Gaussian. The strain between sites is represented with a colored bar; red and blue correspond to tensile and compressive strain, respectively. The free CeO_2 (111) surface terrace between the supported Pt particles is marked with a black arrow.

Considering the substantial fluxional behavior as well as the outward CeO_2 support surface relaxation observed to occur during catalysis, one may suspect significant local lattice strain to be present. We have measured the strain in the CeO_2 by fitting 2D elliptical Gaussians to the Ce columns in the time averaged image (Levin et al., 2020), in order to determine their position; then we have calculated the difference in each columns' position with respect to the bulk terminated lattice, in a standard way. We call this quantity the *average static strain* since it is measured from the time-averaged images, which are the sum of image signals recorded over a total time period of 12.5 s. The in-plane component

of the average static strain is plotted in **Figure 4.7** for TOFs of (a) 0.00 CO site^{-1} sec^{-1} and (b) 1.05 CO site^{-1} sec^{-1} (strain analysis for data corresponding a TOF of 0.85 CO site^{-1} sec^{-1} was not performed due to the aforementioned crystal tilt at this condition). In the figure, the fitted positions of Ce atomic columns are represented by circles. The in-plane component of the average static strain shows spatial variation between tensile and compressive across the CeO_2 surface terrace, with a magnitude in the range of 15 – 20%.

While the static strain at the surface is large, it does not appear to show any clear correlation with the TOF. We believe this is because the average static strain may not give an accurate representation of the dynamic bond distortion that may be present on the surface at any given time due to fluxional behavior. For example, if during an image exposure time, t, a cation spends a time $t/2$ at distance $+d$ away from its bulk terminated position and a time $t/2$ at a distance $-d$, then the average cation displacement over the observation time would be zero. To address this deficiency, we define a *fluxional strain* quantity that is proportional to the width of the atomic column in the time-averaged image. The fluxional strain, ε_{flux}, can then be taken as the difference in the standard deviation of the Gaussian fitted to the particular Ce cation column of interest, σ_{local}, and in the bulk, σ_{bulk}, and is defined in a manner similar to the static strain:

Eq. 4.1 $$\varepsilon_{flux} = \frac{(\sigma_{local} - \sigma_{bulk})}{\sigma_{bulk}}$$

The local magnitude of the fluxional strain is visually represented in **Figure 4.7** by the size of the circles, which are proportional in dimension to the standard deviation of the Gaussian fitted to the Ce atomic columns. Note that the widths of the atomic columns in the bulk of the CeO_2 do not vary significantly with increasing turnover frequency. The columns at the surface, however, grow wider with increasing turnover, as can be seen by examining the circles drawn at the top of the figures in the arrowed locations, which correspond to the atomic columns located at the free CeO_2 (111) surface terrace. The

average fluxional strain across the surface terrace is around 19% at 144 °C when the conversion is zero. However, as the conversion increases, the fluxional strain also increases and is around 33% at 285 °C when the conversion is 15%. This is a large degree of strain, and the resultant high surface energy will make the catalyst surface extremely reactive.

4.3.5. Dynamic structural response of Pt/CeO_2 nanoparticles at elevated temperatures in the absence of reactant gas

The analysis of the time-averaged *operando* TEM images shows that the turnover frequency for CO oxidation is correlated with structural dynamics taking place in the Pt nanoparticles and at/near the three-phase boundary (TPB). However, as the catalyst must be heated in order to be activated, it may be reasoned that the dynamics are driven by the elevated temperature of the catalyst and not the catalytic chemistry. We have therefore performed *in situ* TEM imaging experiments in inert N_2 gas at elevated temperatures, in order to investigate what may be called spectator fluxional behavior attributed only to the presence of applied heat and not to catalytic surface chemistry. A detailed analysis is given in Appendix C, Section C.7. A brief discussion with exemplary evidence for a lack of thermal effects on the observed fluxionality will be given below.

Figure 4.8 presents 0.5 s exposure *in situ* ETEM images of the same CeO_2-supported Pt nanoparticle in 5 mTorr of inert N_2 gas at (a) 20 °C and (b) 300 °C. Note that 300 °C is nearly the highest temperature explored in the *operando* experiment (i.e., 297 °C). Compared to the observations made *in situ* under reaction conditions (e.g., **Figure 4.2**) or the case in which the catalyst is exposed to reactant gases and/or actively producing CO_2 (e.g., **Figure 4.4b/c**), the catalyst exhibits a significantly different and more attenuated dynamic structural response as the temperature is elevated from 20 °C to 300 °C in an atmosphere of inert N_2. For instance, the Pt nanoparticles were observed

to undergo fluxional dynamics that resulted in a loss of Pt lattice fringe visibility. As can be seen in **Figure 4.8**, at room temperature the Pt nanoparticle is well-oriented into a [110] zone axis. Clear atomic-column contrast is visible in the Pt as well as at the interfacial sites that bridge the right side of the Pt/CeO_2 perimeter (white arrows). The left side of the three-phase boundary yields contrast that is challenging to interpret due to thickness/tilt issues as well as the apparent overlap of the Pt and CeO_2 lattices. Nevertheless, the sharp visibility of the arrowed interfacial sites and Pt atomic columns indicates that the Pt nanoparticle, three-phase boundary, and nearby free CeO_2 surface exhibit general structural stability (fluxional dynamics, in comparison, would give rise to distinct motion artifacts, such as blurring or a localized loss of contrast).

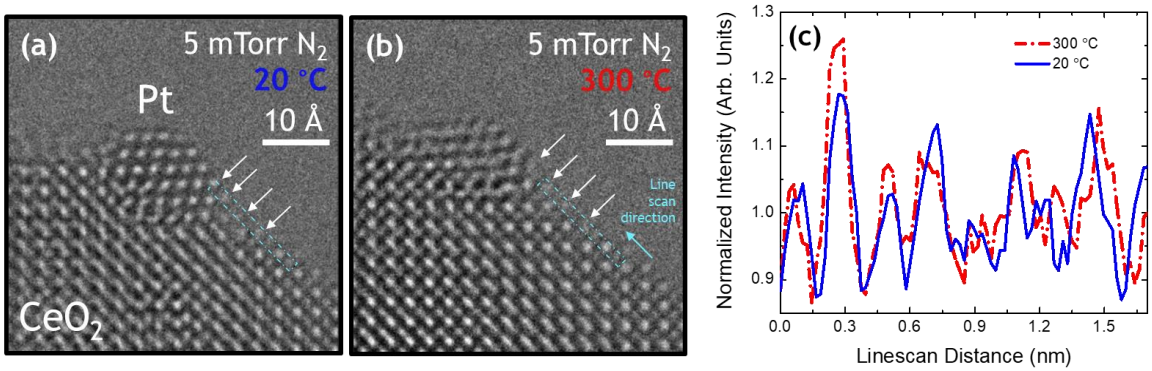

Figure 4.8. Half-second exposure *in situ* ETEM images of the same nanoparticle of a Pt/CeO_2 catalyst in 5 mTorr N_2 at **(a)** 20 °C and **(b)** 300 °C. Clearly resolved atomic columns bridging the Pt/CeO_2 three-phase boundary (TPB) are indicated with white arrows. In **(c)** a 1.2 Å wide integrated intensity line profile taken across the TPB from the region and along the direction indicated in the images shows that the atomic column contrast at 20 °C differs little from that observed when the catalyst is heated up to 300 °C. These results suggest that both the loss of Pt fringe visibility and the evolution of Ce column blurring observed during catalysis are not attributed strictly to thermal effects, but instead to dynamic chemical/structural processes resulting from catalytic turnover.

A 0.5 s exposure *in situ* ETEM image of the same Pt nanoparticle at an elevated temperature of 300 °C is shown in **Figure 4.8b**. At this elevated temperature, the Pt nanoparticle has now tilted into an oblique orientation near the [100] zone axis.

Regardless of the static restructuring that may have occurred (presumably to lower the overall system energy at this higher temperature), the primary observation of importance for the present study is the lack of blurring and/or localized motion artifacts associated with fluxional dynamics. In this case, multiple Pt lattice fringes remain sharply resolved in the nanoparticle and atomic columns can even be seen on the Pt surface. Images acquired at different times during the observation also show well-resolved Pt lattice fringes and sharp atomic columns (see, e.g., **Figure C.7**). This suggests that the loss of Pt lattice fringe visibility observed under *operando* conditions is attributed to structural dynamics driven by catalytic surface chemistry.

A close inspection of the images reveals that the particle occasionally undergoes rigid-body rotations of a few degrees (compare, e.g., **Figure 4.8b** with **Figure C.7b**). Notably, such behavior was also seen to occur at room temperature (compare, e.g., **Figure 4.8a** with **Figure C.7a**). This type of slow rotational behavior is completely different than the rapid dynamic structural fluctuations that we have observed during the experiments reported above (e.g., **Figure 4.2/Figure 4.4**) or during *in situ* TEM imaging experiments that we have performed of CeO_2-supported Pt nanoparticles exposed to CO (Crozier et al., 2019), CO and O_2 (Vincent & Crozier, 2020), and CO and H_2O (Li et al., 2021).

4.4. Discussion

The observations and measurements clearly show significant dynamic changes in the metal particles, the metal/ceramic interface, and the nearby support surfaces under reaction conditions and during catalysis. The rate of structural dynamics at or near the three-phase boundary correlates with the TOF and thus provides insights into the atomic level materials processes taking place during a Mars van Krevelen catalytic reaction. Interestingly, the structural changes are observed to some degree even when the TOF is zero. However, as we will discuss below, it would be an oversimplification to conclude that

these are spectator processes, since they are associated with necessary intermediate reactions steps even when the rate limiting step is not completed. Moreover, the catalyst changes form as the TOF increases due to the substantial increases in fluxional behavior. The fact that the changes become more pronounced when catalysis is detected suggests that they are integral to the functioning of the Mars van Krevelen mechanism in this case. The various dynamic processes are interconnected, but it is helpful to initially discuss them separately.

The most obvious change observed in our experiments is the emergence of structural dynamics taking place in the Pt particle under reaction conditions. Significant fluxional behavior of the Pt nanoparticles takes place even at 144 °C, which is below the light-off temperature for the catalyst. We also observed similar behavior in recent *in situ* TEM on the water gas shift reaction at 200 °C (Li et al., 2021) and we have even observed significant fluxional behavior in Pt particles supported on CeO_2 at room temperature in atmospheres containing CO (Crozier et al., 2019) (but not in N_2, e.g., see **Figure 4.8/Figure C.7**). It is clear that this behavior is not directly associated with the rate limiting step for CO oxidation, but one may conclude that the equilibrium shape of 1 – 2 nm Pt nanoparticles supported on CeO_2 is not easily well-defined in a CO atmosphere.

Under equilibrium conditions, a supported nanoparticle will adopt the so-called Winterbottom shape (Winterbottom, 1967) which minimizes the sum of the surface and interfacial energies. For an FCC metal like Pt, the (111) surface has the lowest energy in vacuum (McCrum et al., 2017) and the coherent interfaces associated with strong bonding (e.g., the one shown in **Figure 4.1**) are also low energy. In this case, the strong interfacial bond between Pt and CeO_2 is associated with bridging oxygen giving rise to Pt – O – Ce linkages (Yasutaka Nagai et al., 2006; Shinjoh et al., 2009; Hatanaka et al., 2010; Gänzler et al., 2017, 2018). For these metallic systems, the Winterbottom shape often gives rise to

a truncated Wulff shape (the equilibrium shape of an unsupported particle). In the presence of gas adsorbates, the surface energies may change, causing the equilibrium particle shape to change (Hansen et al., 2002; Zhu et al., 2020). As is well known, CO binds very strongly to Pt with an average chemisorption energy of about 1.3 – 1.5 eV (Podkolzin et al., 2000; Lu et al., 2020). It is important to recognize that the formation of this strong Pt-CO bond will also weaken the Pt bond with its nearest neighbors. Under reaction conditions, most surface Pt atoms will be bonded to CO (Podkolzin et al., 2000; Lu et al., 2020), so there will be a substantial bond weakening between the surface and the subsurface Pt atoms.

Examination of the Ce cations at the Pt perimeter sites in **Figure 4.4a** shows that oxygen vacancy creation and annihilation is taking place due to interaction with CO adsorbed on the Pt. For 2 nm Pt particles, assuming a simplified hemispherical cuboctahedral shape, approximately 35% of the Pt atoms are located at the Pt/CeO_2 interface and about 40% of those atoms occupy the perimeter sites. Oxygen vacancy creation at these perimeter sites removes bridging oxygen and weakens the bonding between the Pt nanoparticle and support. The fluxional behavior in the surface Ce cations suggests that there is constant competition between vacancy annihilation, which repairs the Pt-O-Ce bond, and vacancy creation, which is due to reaction with CO. We can get additional temporal insights by considering the image exposure time. Over a 0.5 sec exposure at 144 °C (see **Figure 4.2b - Figure 4.2e**), the significant blurring of the perimeter Ce cations indicates that many vacancies are created and annihilated due to interactions with CO.

At this temperature, no CO_2 is detected, so the carbonaceous intermediates may remain bound to the catalyst's surface (indeed, several authors report that CO_2 adsorbed on *reduced* CeO_{2-x} binds with an adsorption energy in excess of 1 eV, as discussed by D. R.

Mullins in (Mullins, 2015)). Ionic oxygen transport is also small at 144 °C, so there is a limited availability of lattice oxygen to backfill the surface and interfacial vacancies. Thus, much of the vacancy creation/annihilation will be associated with forward and reverse reactions between surface lattice O and CO, *i.e.* this intermediate step may be highly reversible. The continuous disruption of the Pt-O-Ce interfacial bond and the changes in adsorbate configuration on the Pt surface disrupt the Winterbottom shape and leads to the observed dynamic behavior.

As carbon species spillover onto the adjacent CeO_2 surface, additional CO will adsorb onto the vacant surface sites on Pt. This dynamic bonding and debonding of adsorbates on the metal surface leads to distortions and strains, driving surface diffusion. In recent work, we correlated *in situ* TEM and *in situ* synchrotron observations. The synchrotron analysis showed that, even when rapid fluxional behavior is occurring, the average Pt coordination and bond lengths are consistent with the Pt FCC crystal structure (Li et al., 2021). This shows that the nanoparticle is not forming an amorphous structure, but rather it is transforming rapidly between metastable configurations. At present, our temporal resolution and signal-to-noise preclude a detailed identification of the structure of these metastable phases. However, the analysis of the visibility of the Bragg beams in the diffractograms shows that the rate of reconfiguration increases with conversion. This is consistent with more frequent formation and breaking of surface and interfacial chemical bonds associated with high catalytic TOF.

As the temperature and conversion increase, there is a substantial increase in the fluxional behavior on the CeO_2 surface. While the highest vacancy creation/annihilation activity takes place at the perimeter sites, the fluxional behavior extends over the entire 20 Å nanofacet between the two Pt particles shown in **Figure 4.6c**. The outward relaxation of the surface layer is also consistent with a high concentration of oxygen

vacancies. No lattice expansion was detected in the Ce lattice plane second from the surface, and by the third lattice plane down, no evidence is seen for any Ce cation blurring. This localized surface fluxional behavior indicates that most of the oxygen vacancy creation and annihilation as well as oxygen diffusion takes place on the top CeO_2 (111) lattice plane. At present it is not possible to conclude whether the vacancies are localized to the surface or to the subsurface O layer of the CeO_2 (111) lattice plane. Negligible oxygen transport from the bulk should take place at these temperatures since the activation energy for undoped CeO_2 is known to lie in the range 0.9 – 2.3 eV (Wu et al., 2010; Kamiya et al., 2000). At conditions of detectable conversion, however, at least some of the oxygen vacancies must be annihilated *via* reduction of molecular oxygen, in order to replenish the supply of oxygen required for steady state oxidation of CO.

One may ask *where is the likely site for molecular oxygen reduction?* It could take place at the oxygen vacancies created at the perimeter sites after CO_2 desorbs. Alternatively, it could take place on the nearby free CeO_2 terrace and then diffuse to the perimeter sites. As shown in **Figure 4.7**, the average static surface strain is high on the free CeO_2 surface, and the fluxional strain on the surface terrace reaches around 30% when the conversion is 15% – this is a very large strain and the associated high surface energy will make the terrace more reactive making direct oxygen reduction feasible. At present we are not able to differentiate definitively between either the perimeter or the terrace mechanism, though it may be worth speculating on the likelihood of each. We do not have atomic resolution surface spectroscopy to determine the nature of the carbon species created as oxygen vacancies are created and annihilated. However, carbonates are known to form during CO oxidation on CeO_2 (Wu et al., 2012; Mullins, 2015), so a possible reversible reaction that may occur at the interface is:

$$2(Pt - O - Ce) + CO_{ad} \leftrightarrow 2(Pt - \square - Ce) + ((CO_3)^{-2})_{ad}$$

The perimeter environment may be rather crowded with a high concentration of CO on the Pt sites and a high concentration of carbonates on the CeO_2 sites. Backfilling of the interfacial oxygen vacancies by direct adsorption of molecular oxygen may be subject to significant steric hinderance. It may be easier to annihilate the interfacial oxygen vacancy by diffusion of lattice surface oxygen along the nearby CeO_2. During catalysis, oxygen reduction almost certainly takes place on the highly reduced nearby CeO_2 terrace and that lattice oxygen migrates to the perimeter sites for reaction with CO.

These experiments provide an atomic level view of the structural dynamics associated with the three-phase boundary of the catalyst during Mars-van Krevelen oxidation. The localized structural changes that are observed are directly associated with catalytic functionality. Many of the steps for converting reactants into products involve forming and breaking chemical bonds with the atoms forming the catalyst surface. This bonding and debonding not only changes the adsorbates but may locally destabilize the catalyst surface and interface structures, resulting in large local surface strains, surface atom migration, and the creation and annihilation of point defects. The particular fluxional behaviors reported here are specific to the catalytic system and CO oxidation. However, breaking and forming chemical bonds is an essential functionality for all heterogeneous catalysts, and it can only occur if the catalytic surface undergoes substantial structural dynamics. While the electron transfer occurring at an active site happens on the femto-second time scale, the subsequent nuclear rearrangements may alter or completely destroy the active site due to the thermodynamic and kinetic factors driving structural change. The question of how to explore structure-reactivity relations then becomes more complex: in at least some nanoparticle catalysts, it may be more appropriate to carefully consider the atomic-level *structural dynamics* that may be integral to the catalytic cycle and reactivity. The importance of adsorbate-induced structural changes has long been

recognized in the surface science community (Somorjai, 1991). Now, however, the picometer precision of advanced *operando* TEM can reveal the local, atomic-level details of these structural dynamics for actively working technical catalysts.

4.5. Summary

In summary, we have employed aberration-corrected *operando* TEM to visualize the atomic-scale dynamic structural (i.e., fluxional) behavior occurring at and near Pt/CeO_2 metal-support interfaces during oxygen transfer, with a focus on CO oxidation. Finite element modeling is performed to develop a reaction rate analysis wherein the atomic-resolution structural observations are directly correlated with the catalyst's turnover frequency for CO oxidation. We show that the increasing frequency of catalytic turnover correlates with dynamic fluxional behavior that (a) destabilizes the supported Pt particle, (b) marks an enhanced rate of oxygen vacancy creation and annihilation, and (c) leads to increased strain and reduction in the surface of the CeO_2 support. These results unambiguously demonstrate that there is a dynamic transformation in the chemical environment around the metal-support interface during catalysis. The results also show that the equilibrium shape of 1 – 2 nm Pt nanoparticles supported on CeO_2 is not well-defined in a CO oxidation atmosphere, especially at high catalytic turnover, where the larger concentration and faster cycling of oxygen vacancies contributes to the destabilization of the supported Pt nanoparticle. Overall, the results implicate the interfacial Pt-O-Ce bonds anchoring the Pt to the support as being involved also in the catalytically-driven oxygen transfer process, and they suggest that molecular oxygen reduction takes place on the highly reduced nearby CeO_2 surface before migrating to the metal-support interfacial perimeter for reaction with CO. This study highlights the importance of characterizing the structural dynamics that take place during catalysis in order to elucidate the relationship between a catalyst's structure and its functionality.

5. Visualization of Atomic-scale Fluxional Behavior in Pt/CeO_2 Catalysts using Time-Resolved AC-ETEM coupled with Direct Electron Detectors

5.1. Motivation

In the previous chapter, a slow and inefficient indirect CCD detector was used to record images of Pt/CeO_2 catalysts under conditions of increasing catalytic conversion. Due to the poor detective quantum efficiency of the detector, it was necessary to sum together multiple images taken over a timescale spanning ~10 seconds in order to provide an adequate SNR for structural analysis. The relatively long time-averaging period prevented a detailed investigation into the dynamic structural evolution of the catalyst under reaction conditions. This dynamic structural meta-stability (i.e., the so-called fluxionality) of the catalytic material is now thought to play a critical role in determining the properties of the catalyst (Zhang et al., 2020), and thus underscores the need for temporally-resolved *in situ* catalyst characterization aimed at elucidating dynamical atomic-level behavior. An ultimate goal for heterogenous catalysis research would be to describe the atomic-level structure of a catalytic material *in real time* and to relate this structure to the catalytic functionality of interest. Acquiring atomic-resolution *in situ/operando* datasets with a temporal resolution that is at least as fast or faster than the catalytic turnover frequency is a pre-requisite to meeting this grand scientific challenge.

Recent advances in direct electron detector technology now enable atomically-resolved, shot noise-limited *in situ* ETEM image time-series to be acquired with a temporal resolution on the order of milliseconds (Faruqi & McMullan, 2018; Ciston et al., 2019). As many catalysts exhibit chemical reaction turnover frequencies on the order of $10^0 – 10^2$ sec^{-1}, the emerging opportunity to visualize atomic-level fluxional behavior with high temporal resolution holds much promise for understanding the chemical transformation processes that take place on catalyst surfaces. At present, atomic-level

information acquired with high temporal resolution (e.g., < 100 ms) is lacking on the fluxional behavior exhibited by many industrially relevant catalysts upon exposure to reactant gases or subjection to reaction conditions. In order to ultimately establish improved design principles for catalysts used in these applications, high quality experimental observations and descriptions of catalysts undergoing atomic-level fluxional behavior are required.

The purpose of this chapter is to apply aberration-corrected ETEM coupled with a fast direct electron detector to visualize and characterize fluxional behavior at catalyst surfaces with high spatiotemporal resolution. The work in this Chapter focuses on CeO_2-supported Pt nanoparticles due to their role in automotive exhaust and clean energy conversion catalysis. We have investigated the dynamic structural response of Pt/CeO_2 catalysts exposed to inert N_2 gas, as well as to CO oxidation ($CO + ½O_2 \rightarrow CO_2$) reactant gases and to water-gas shift ($H_2O + CO \rightarrow H_2 + CO_2$) reaction conditions (i.e., reactant gases and an elevated temperature of 200 °C). The results of this work provide insight into the atomic-level dynamic structural reconfigurations that occur on reducible oxide-supported metal nanoclusters.

The research performed in this Chapter was performed in part in collaboration with Dr.'s Wei-Chang David Yang, Canhui Wang, and Renu Sharma at the National Institutes of Standards and Technology (NIST) in Gaithersburg, MD and with Prof. Anatoly Frenkel and Dr. Yuanyuan Li of Brookhaven National Laboratory in Upton, NY. The experiments were performed by me, at NIST, due to the availability of an aberration-corrected ETEM coupled with a direct detector. Dr. Sharma provided me with access to the equipment and helpful guidance, while Dr.'s Yang and Wang provided me with training on the equipment, especially the direct electron detector, as well as useful feedback during the experimentation. Prof. Frenkel and Dr. Li contributed helpful insight

during discussions and also provided a powder sample of CeO_2-supported Pt nanoparticles that was used during the WGS experiments. Access to this second sample also allowed multiple catalyst formulations to be examined *in situ* and for the behavior to be compared against one another. Finally, the image simulations presented in Section 5.3.1.3 were conducted as part of a Barret Honors Thesis by undergraduate student Claire Block, who worked under my supervision from 2019 - 2021. My contributions to the work include performing the *in situ* TEM experiments, analyzing the image data, supervising Claire, and assisting with the image simulations as needed.

5.2. Experimental

5.2.1. Catalyst preparation and ex situ characterization

For the investigations performed at room temperature in N_2 and in CO oxidation reactant gas atmospheres (Section 5.3.1 below), CeO_2-supported Pt catalyst was synthesized following the standard hydrothermal and incipient wetness impregnation methods described in Chapter 2, Section 2.1. For the investigations performed at elevated temperatures in pure CO and in water-gas shift (WGS) reaction gas atmospheres (Section 5.3.2 below), CeO_2-supported Pt catalyst was obtained from collaborators who followed synthesis procedures that have been outlined in (Li et al., 2021). In brief, 0.5 g of CeO_2 nanopowder (< 25 nm) was dispersed in a solution consisting of 2.0 g of urea and 8 mL of ultrapure water. While stirring, 3.3 g of a solution (approximately 1 wt% Pt) of chloroplatinic acid hydrate in water was added to the dispersion. The mixture was sealed in a vial and stirred for 24 hours in an oil bath at 95 °C. Afterward, the postdeposition sample was separated and washed by 3 cycles of centrifuging/redispersing in water to remove the residual ions from the precursors. The sample was then dried overnight at 60 °C before being crushed into a powder and calcined at 500 °C (10 °C/min heating

ramp). Access to these two samples allowed the dynamic structural response of two Pt/CeO_2 catalyst formulations to be investigated and compared.

5.2.2. Time-resolved aberration-corrected *in situ* TEM

Atomic-resolution *in situ* TEM image time-series of the CeO_2-supported Pt nanoparticles were acquired to investigate fluxional behavior occurring in reactant gases and under reaction conditions. Time-resolved series of images were collected on an aberration-corrected FEI Titan ETEM operated at 300 kV following the procedures outlined in Chapter 2, Section 2.3.5. *In situ* TEM specimens were prepared by dispersing the individual powders of Pt/CeO_2 catalyst onto a windowed MEMS-based SiN_x chip, which was loaded into a DENSsolutions Wildfire heating holder. For the work performed at room temperature in N_2 and in CO oxidation reactant gas atmospheres (Section 5.3.1 below), the holder was inserted into the ETEM after aligning the instrument and 0.5 mTorr of N_2 gas was introduced into the environmental cell. The catalyst was imaged at room temperature using an incident electron flux of 5×10^3 $e^-/Å^2/s$. Time-resolved series of 1.0 second images were acquired using a Gatan K2 IS direct electron detector operated in electron counting mode at an image acquisition frame rate of 40 frames per second (fps), resulting in a temporal resolution of 25 milliseconds (ms) per frame. After imaging in N2, the ETEM column was briefly evacuated and then 10 mTorr of CO and O_2 gas in a stoichiometric mixture (i.e., $CO:O_2$ = 2:1) was introduced into the environmental cell. Time-resolved series of images were again acquired at 40 fps with the same nominal dose rate in electron counting mode. Image time-series alignment was performed post-acquisition without interpolation. The experimental image dataset collected for this work in N_2 also supplied the basis of the real noisy data used for denoising in Chapter 6.

For the work performed at elevated temperature in a pure CO atmosphere and in WGS reaction conditions (Section 5.3.2 below), after loading the sample into the ETEM,

0.24 mbar of CO gas was introduced into the environmental cell and the catalyst was reduced in situ at 300 °C for 2 hours. The catalyst was subsequently cooled to 200 °C and imaged under the same pressure of CO gas. To produce a WGS reaction environment, at 200 °C, water vapor was introduced to the cell with a H_2O:CO reactant gas ratio of 2:1, resulting in a total cell pressure of 0.73 mbar. Images were acquired at 20 fps with an incident electron dose rate of 600 $e^-/Å^2/s$ and a total exposure time of 6 s, also in electron counting mode. The time-resolved images were temporally binned by summing to various desired time resolutions (e.g., 0.15 s, 1.5 s, and 6.0 s), producing so-called time-averaged images with an increased signal-to-noise ratio.

5.3. Results and discussion

5.3.1. Dynamic structural response in N_2 and in CO oxidation reactant gases

5.3.1.1. Average structure in 1.0 second exposure time-averaged images

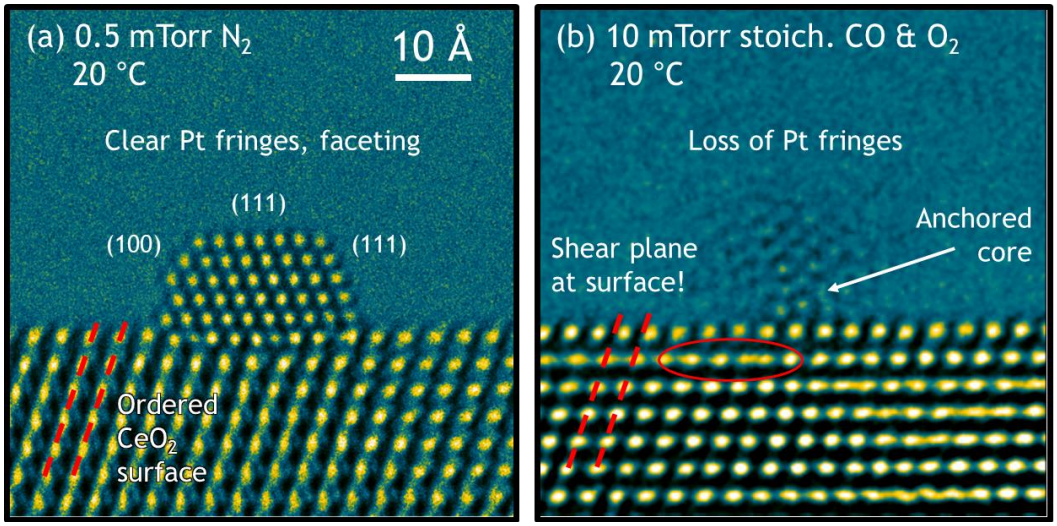

Figure 5.1. Time-averaged 1.0 sec *in situ* ETEM images of the same 2.5 nm Pt nanoparticle supported on a CeO_2 (111) surface at room temperature in **(a)** 0.5 mTorr of N_2 and (b) 10 mTorr of stoichiometric CO and O_2 gas (i.e., $CO:O_2$ = 2:1).

Figure 5.1 shows *in situ* HRTEM images of a Pt nanoparticle roughly 2.5 nm in size supported on the (111) surface of a CeO_2 nanoparticle, imaged at room temperature in (a) 0.5 mTorr of N_2 gas and (b) 10 mTorr of stoichiometric CO and O_2 (i.e., $CO:O_2$ = 2:1). The images are 1.0 second time averages comprised of 40 aligned frames each taken with an exposure time of 25 ms. The appearance and behavior of the particle and the support differs significantly in the two different gas atmospheres. In the N_2 atmosphere (**Figure 5.1a**), the Pt nanoparticle is generally stable over the 1.0 second image acquisition period, as evidenced by the highly visible Pt lattice fringes and clearly resolved atomic columns. The particle also exhibits clear surface faceting. In this case, the supported Pt particle is to seen expose (111) surfaces predominately, along with another smaller, 4 to 5 atom-wide (100) surface nanofacet (the facets are labeled in the figure). The predominance of exposed (111) surfaces is expected considering that Pt is a face centered cubic metal in which the (111) plane is close packed and thus lowest in energy. DFT calculations by (Singh-Miller & Marzari, 2009) place the surface energy in vacuum around 1.49 J/m^2. For Pt, (100) is the next lowest in energy (1.81 J/m^2), while (110) is highest in energy (1.85 J/m^2), which is in fact not seen in this case. The agreement between the observed Pt surface structure and the Pt surface energy ordering suggests that the nanoparticle has adopted a Winterbottom configuration, which is the minimum energy shape for a crystalline nanoparticle in contact with an interface (Winterbottom, 1967; Marks & Peng, 2016).

In N_2 (**Figure 5.1a**), the Pt nanoparticle displays an epitaxial, well-defined interfacial relationship with the CeO_2 support. During this experiment, both the Pt nanoparticle and the CeO_2 support have been imaged in a (110) zone axis. The Pt nanoparticle is supported on a flat (111) CeO_2 surface, with (111) Pt lattice planes meeting the (111) CeO_2 surface at the interface. The epitaxy at the interface appears twinned as opposed to parallel in this orientation, with the nearly vertical (111) planes in the Pt related

by a mirror plane operation to the other nearly vertical (111) planes in the CeO_2 (it should be mentioned that the twinned and parallel epitaxy are structurally identical and only differ in appearance due to the projected viewing orientation, as discussed by Bernal et al. in the literature (Bernal et al., 1995, 1997, 2000)). The atomic column contrast at the metal-support interface is complex and exhibits varying bright and faint intensity that suggests some degree of compositional intermixing. At least three misfit dislocations are visible along the interfacial atomic layer to accommodate the unmatched lattice parameters between Pt (a = 3.923 Å) and CeO_2 (a = 5.411 Å).

Away from the interface, the CeO_2 support appears well-ordered and crystalline. Overall, the Winterbottom shape of the particle and the well-defined epitaxy at the interface lends evidence to conclude that the supported particle has achieved a deep low-energy configuration in the potential energy landscape; the stability of the system over 1.0 sec indicates that in a N_2 atmosphere at 20 °C there is an absence of energetic perturbations with sufficient energy to promote the entire supported particle system above the kinetic barriers that may separate it from another structural configuration (i.e., an absence of significant fluxional behavior for the entire particle). It should be briefly mentioned that dynamic fluxional behavior may still occur at low-coordination sites on the Pt nanoparticle surface (e.g., corner/edge sites) where the kinetic barriers for structural reconfiguration may be low relative to the thermal energy available at room temperature (presented in **Figure 5.2** and discussed further in Section 5.3.1.2 below). A detailed analysis of the rate of atomic displacements induced by the electron beam suggests that the self-diffusion of Pt atoms at these sites is dominated by thermal effects and not the incident beam (see Chapter 2, Section 2.3.6).

After the gas atmosphere is switched to 10 mTorr of stoichiometric CO and O_2 (**Figure 5.1b**), the catalyst exhibits considerably different behavior. The Pt nanoparticle

adopts a more rounded, disordered shape that appears 20 – 30% larger. The lattice fringes that were clearly visible in the Pt nanoparticle have now largely disappeared, with the Pt showing a quasi-amorphous pattern of contrast that does not communicate the presence of any persistent long-range structural ordering. This indicates that the particle is more disordered in the reactant gas atmosphere and/or that dynamic restructuring of the entire particle is occurring on the sub-second time scale. The buried core of the Pt cluster (arrowed in **Figure 5.1b**) appears stabilized and thus more clearly resolved, perhaps due to anchoring Pt-O-Ce linkages at the center of the Pt/CeO_2 interface. The contrast along the outer perimeter of the metal-support interface appears substantially weaker, which suggests that the edge of the supported particle has de-wetted and/or is dynamically restructuring, likely due to a destabilization of the local bonding environment. Oxide-supported metal nanoparticles are known to gain thermodynamic stability and sintering resistance through interfacial anchoring with highly coherent hetero-epitaxy (Ta et al., 2012; Liu et al., 2015, 2016). Thus, the dynamic behavior of the particle in CO and O_2 gas is remarkable given the strong interfacial hetero-epitaxy observed in N_2.

Under the CO and O_2 gas atmosphere, changes in structural behavior are also observed away from the interface in the CeO_2 support. The most apparent change in the CeO_2 is the streaking of the Ce cation columns at many distinct locations throughout the support (e.g., the region indicated with the red circle in **Figure 5.1b**). Another subtler structural transformation involves the emergence of a crystallographic shear plane at the top layer of the CeO_2 support. The crystallographic shear is evidenced by the fact that the surface Ce cations are displaced laterally by close to half a repeat distance with respect to the subsurface and bulk positions. The dashed red lines placed in **Figure 5.1b** provide a guide to the eye in ascertaining the shear plane (note that the dashed red lines in **Figure 5.1a** coincide with both the bulk and the surface Ce cation columns, indicating the absence

of a shear plane defect in N_2). It is perhaps likely that the apparent Ce cation column streaking throughout the support may simply be due to viewing local regions of surface crystallographic shear head-on in the projected dimension, which would give rise to an almost continuous band of intensity, as observed in many places in the image (e.g., the red circle in **Figure 5.1b**). The crystallographic shear planes signify substantial disruptions to the CeO_2 lattice under these conditions. Non-stochiometric oxides are known to form stable crystallographic shear planes in order to accommodate the elimination of complete rows of oxygen vacancies (Magnéli, 1951; Anderson & Hyde, 1967; Gai & Boyes, 2003). Thus, one may conclude that upon exposure to the CO oxidation reaction gas atmosphere, an increased number of oxygen vacancy point defects have been introduced into the CeO_2, which were then at least partially eliminated by the formation of extended crystallographic shear plane defects. A subject of ongoing research could address the role, if any, of the crystallographic shear planes on the catalytic activity of the Pt/CeO_2 system for CO oxidation. For now, we turn our attention to the dynamic fluxional behavior observed to occur in the supported Pt nanoparticle during time-resolved *in situ* ETEM imaging.

5.3.1.2. Fluxional behavior of Pt revealed with time-resolved *in situ* imaging

Figure 5.2 presents two examples of dynamic structural behavior seen to occur on the Pt nanoparticle surface during time-resolved *in situ* ETEM imaging at room temperature in 0.5 mTorr of N_2 gas. As discussed above, under these conditions, the overall particle exhibits marked stability, as evidenced by its clearly resolved atomic structure in the 1.0 second time-averaged image. However, a thorough examination of the time-resolved series of images suggests that subtle, atomic-level dynamic reconfigurations may still take place, especially at the weakly-coordinated and/or high energy corner and edge sites on the Pt nanoparticle surface. **Figure 5.2(a1)** and **Figure 5.2(a2)** display two 25 millisecond (ms) exposure *in situ* ETEM images taken 100 ms apart. In **Figure**

5.2(a1), the arrowed sites located along the short (100) Pt surface nanofacet appear to be absent from the nanoparticle structure. In **Figure 5.2(a2)**, the atomic columns become visible and can be discerned clearly as part of the nanoparticle structure.

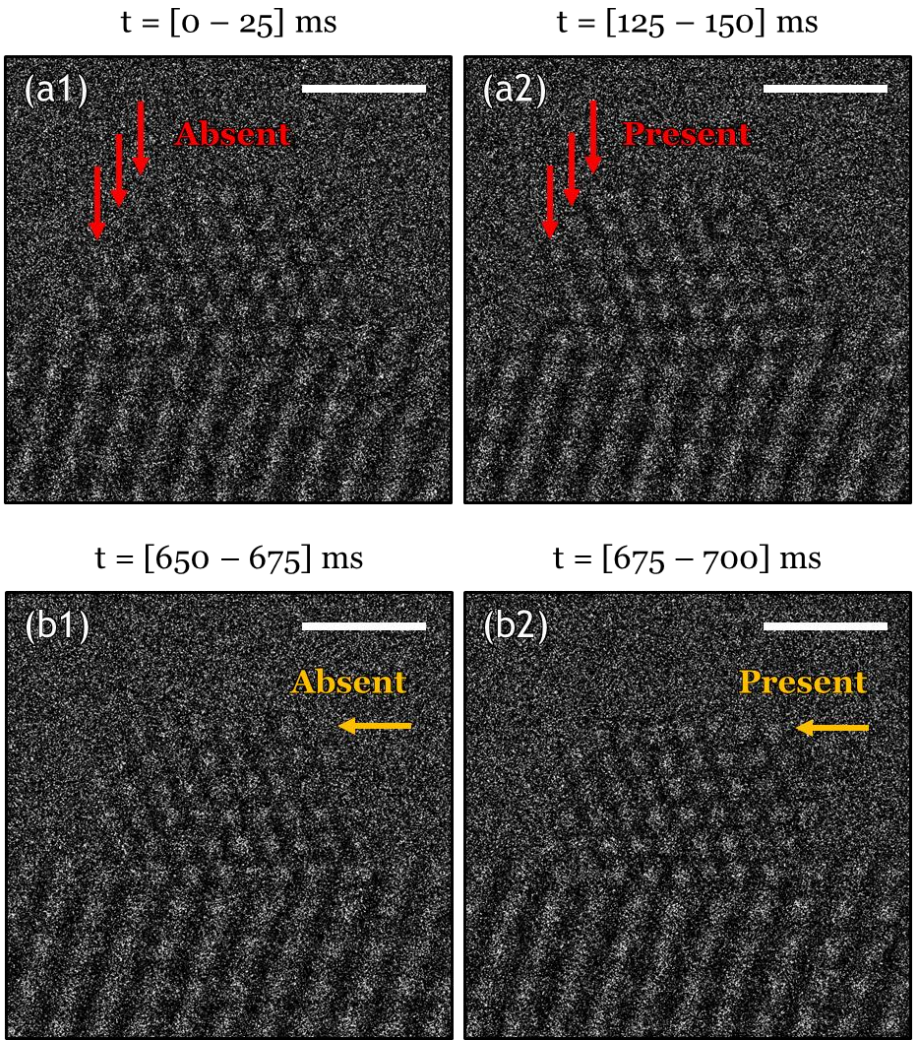

Figure 5.2. Two examples of dynamic structural behavior on a CeO_2-supported Pt nanoparticle at 20 °C in 0.5 mTorr of N_2 gas. In **(a1)** and **(a2)**, three Pt atomic columns located on the short (100) nanofacet appear absent during observation from [0 – 25] ms, and then appear during observation from [125 – 150] ms. In **(b1)** and **(b2)**, a Pt column at the corner site of two connected (111) nanofacets is absent during observation from [650 – 675] ms, and then appears 25 ms later during observation from [675 – 700] ms. Each figure corresponds to a 25 ms exposure *in situ* ETEM image (time provided in the label at top). All scale bars correspond to 1 nm.

Figure 5.2(b1) and **Figure 5.2(b2)** present two 25 ms exposure images taken in succession. In **Figure 5.2(b1)**, the arrowed site located at the corner of two connected (111) surface facets appears absent from the nanoparticle structure. In **Figure 5.2(b2)**, 25 ms later, a clearly resolved and sharp atomic column appears present at the corner site. The extent to which these observed intensity variations correspond to true alterations in the supported Pt nanoparticle surface structure or instead to Poisson noise fluctuations is the focus of ongoing analysis. The prevalence of the noise in the experimental time-series also motivated the development of the deep learning-based noise reduction techniques reported in Chapter 6. A visual analysis of the remaining frames of the image time-series recorded in N_2 reveal a lack of apparent dynamic reconfigurations on the (111) terrace sites.

Figure 5.3 presents a 400 ms portion of the time-series acquired after switching the gas atmosphere to 10 mTorr of CO and O_2. The displayed frames have been averaged in time to increase the signal-to-noise ratio in each image, resulting in a temporal resolution of 100 ms. An examination of the time-series reveals that the entire supported Pt nanoparticle undergoes a sequence of structural reconfigurations which occur in concert with dynamic behavior at certain interfacial Ce sites. During the observation from [500 – 600] ms (**Figure 5.3a**), the particle occupies a meta-stable structural configuration, evidenced by the relative stability over this image acquisition time period which gives rise to the clear visibility of multiple Pt atomic columns. In the next 100 ms, the particle starts to lose stability, evidenced by the loss of lattice fringe visibility; however, the particle remains anchored at the buried core of the metal-support interface, as implied by the resolved atomic columns within the white circle marked in **Figure 5.3b**.

The Pt nanoparticle becomes highly fluxional over the next 100 ms (**Figure 5.3c**) and appears almost invisible due to rapid dynamic restructuring. The absence of any lattice fringes in the image implies that the nanoparticle is continuously reconfiguring over

the course of the 100 ms image acquisition period. Interestingly, the interfacial Ce atomic columns at the metal-support perimeter (i.e., sites within white circle of **Figure 5.3c**) are both blurred and slightly bent while the Pt nanoparticle undergoes this rapid reconfiguration, likely pointing to their involvement in the dynamic processes that have destabilized the supported nanoparticle. After another 100 ms (**Figure 5.3d**), the supported particle regains some degree of stability, with the (111) Pt lattice fringes returning to visibility; the interfacial Ce atomic columns become sharper as well.

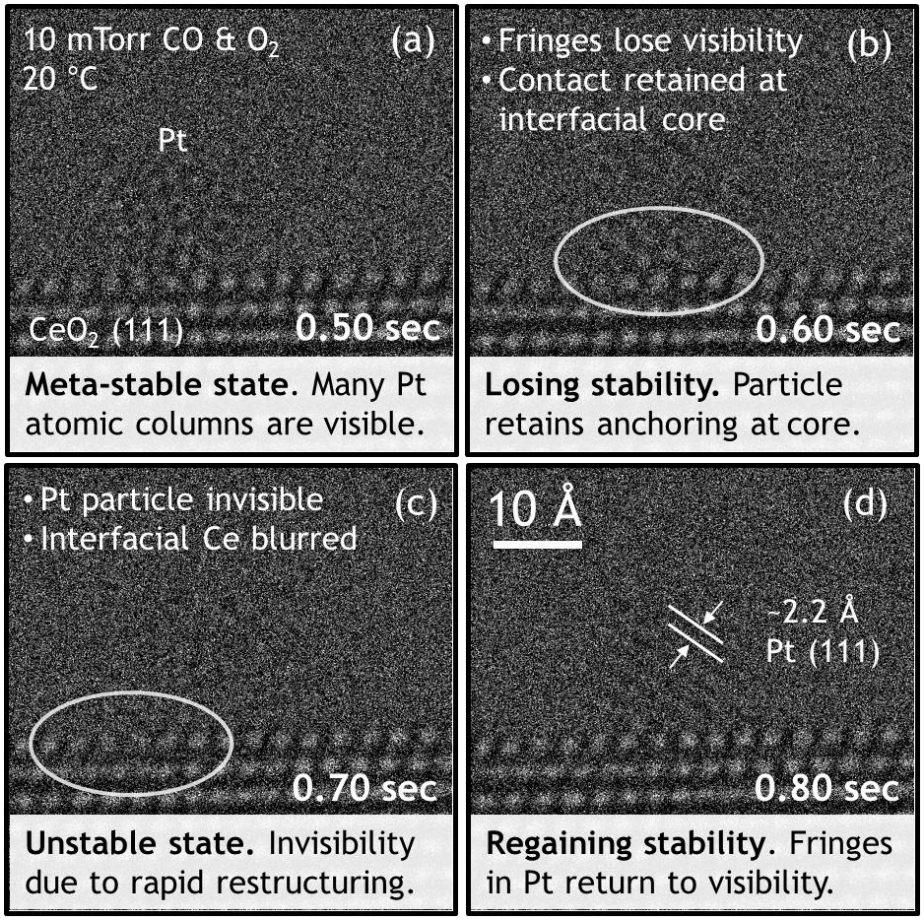

Figure 5.3. Time-resolved series of images showing fluxional behavior of a Pt nanoparticle on a (111) CeO_2 surface at room temperature in a 10 mTorr atmosphere of stoichiometric CO and O_2. **(a)** – **(d)** present 100 ms time-averaged images from a longer 1.0 sec time-series.

The highly fluxional behavior observed in the time-resolved series of images demonstrates that the equilibrium shape of a 1 – 2 nm CeO_2-supported Pt nanoparticle is not well-defined in an atmosphere of CO and O_2 gas, even at room temperature. This meta-stability implies that the potential energy landscape for structural reconfigurations has become sufficiently flat under these conditions, such that one or more of the available energetic perturbations (e.g., phonons, gas adsorption/desorption, chemical bond transformation, etc.) are capable of promoting the system over at least some of the kinetic barriers that separate geometrically distinct but energetically comparable structural configurations. The particle shape and structure are observed to change rapidly over 100 ms intervals, presumably due to many Pt atomic sites changing configuration/position on even faster timescales. An analysis of the rate of Pt atom displacements due to the electron beam under these conditions vs. those due to thermal activation (see Chapter 2, Section 2.3.6), indicates that Pt atom displacements occurring at such timescales are dominated by thermally-controlled processes (see Chapter 2, **Figure 2.12**). We have made observations of similarly sized CeO_2-supported Pt nanoparticles exposed to only CO gas both at room temperature (Crozier et al., 2019) and at an elevated temperature of 200 °C (see (Li et al., 2021) and/or **Figure 5.6** below). In these cases, the Pt nanoparticle displays qualitatively similar fluxional behavior both at room temperature and at 200 °C, as well as in a CO/O_2 atmosphere and in a CO atmosphere. Altogether, this suggests that the presence of CO gas and the resulting CO–Pt/CeO_2 gas-solid interactions are the primary driving force for dynamic structural change. Two hypotheses about this driving force would include: (1) abstraction of lattice oxygen by CO at the metal-support interface reduces the adhesion of the Pt nanoparticle to the CeO_2 substrate, leading to the destabilization of the supported particle; as well as (2) that the strong adsorption of CO onto Pt, with an average chemisorption energy of ~1.3 eV (Podkolzin et al., 2000; Lu et

al., 2020), weakens the Pt-Pt bond, allowing the Pt cluster to become more mobile (Elsen et al., 2015; Michalka et al., 2016). The exact origin is an interesting matter of future research; some suggestions for possible lines of inquiry are given in Chapter 7.

5.3.1.3. Preliminary attempt to model supported Pt structural dynamics occurring in CO and O_2 reactant gases

Among various types of fluxional behavior, the structural reconfigurations in CO and O_2 appear to include bulk rigid-body-like rotations, which produce dynamic contrast features and fluctuating Pt lattice fringe visibility in the nanoparticle at different instances in time. In some frames of the image time-series (e.g., **Figure 5.3c**), Pt lattice fringes are not clearly visible in any region of the nanoparticle. The very small size of the nanoparticle (i.e., ~ 20 Å) implies that the associated reciprocal lattice rods are quite large and extensive in diffraction space (Williams & Carter, 2008). Consequently, it is expected that regardless of the orientation of the nanoparticle, at least one of the rods should intersect with the Ewald sphere and satisfy the diffraction condition, giving rise to visible lattice fringes. The lattice fringe invisibility is not a consequence of drift in the specimen hot stage or electron optics, since lattice fringes are visible in the CeO_2 in the same frames of the time-series.

One explanation for the fluctuating lattice fringe visibility in the small Pt nanoparticle is as follows: over the course of the image acquisition time period, the supported particle structure may occupy a number of distinct meta-stable crystalline structural configurations, for example, by rotating into different orientations on the CeO_2 support surface relative to the incident electron beam. Each of these structures contributes to the overall image signal (the constituent contributions from each structure can be thought of as being summed to form the overall image signal). In regions where the constituent image contributions contain lattice fringes with similar intensity, the lattice fringes will remain visible in the summed image. However, in regions where the

constituent image contributions contain lattice fringes with dissimilar intensity (e.g., dark during one part of the image acquisition time period and bright during another), the lattice fringes will appear washed out and potentially invisible in the acquired noisy image.

Following this line of reasoning, an attempt was made to interpret the experimental image contrast using a simulation-based approach, wherein the supported Pt nanoparticle is modeled as undergoing structural reconfigurations that *only* include bulk rigid-body-like rotations. Details on the methodology are reported in (Block, 2021). An overview of the approach is shown in **Figure 5.4**. Atomic-scale models of CeO_2-supported Pt particles undergoing bulk rigid-body-like rotations are generated (**Figure 5.4(a1) - Figure 5.4(a3)**), TEM images of these models are simulated (**Figure 5.4(b1) - Figure 5.4(b3)**), and finally the simulations are averaged to approximate the effect of the nanoparticle undergoing the constituent configurations over the course of the image acquisition (**Figure 5.4c**). Poisson noise may also be added to better replicate the experimental observation (**Figure 5.4d**). Note that after adding Poisson noise, the region arrowed in **Figure 5.4d** shows relatively weak, nearly invisible lattice fringe contrast, while the region in the center of the particle retains clearly visible Pt lattice fringes.

The atomic-scale structural models portrayed in **Figure 5.4(a1) - Figure 5.4(a3)** involve twinned Pt nanoparticles. A close examination of the experimental time-series acquired in CO and O_2 shows evidence for a five-fold symmetric twinned Pt structure (see Appendix, **Figure D.1**). Some caution is warranted in decisvely concluding that the Pt structure is twinned, as it is well known that single crystal structures can produce deceiving fringe contrast when tilted into oblique orientations, due to, e.g., Moire pattern effects (Tsen et al., 2003). However, an investigation of the image contrast produced by single crystal Pt tilted into various orientations yielded no sign of five-fold symmetry (Block, 2021). The twinned Pt structure was thus kept for this work.

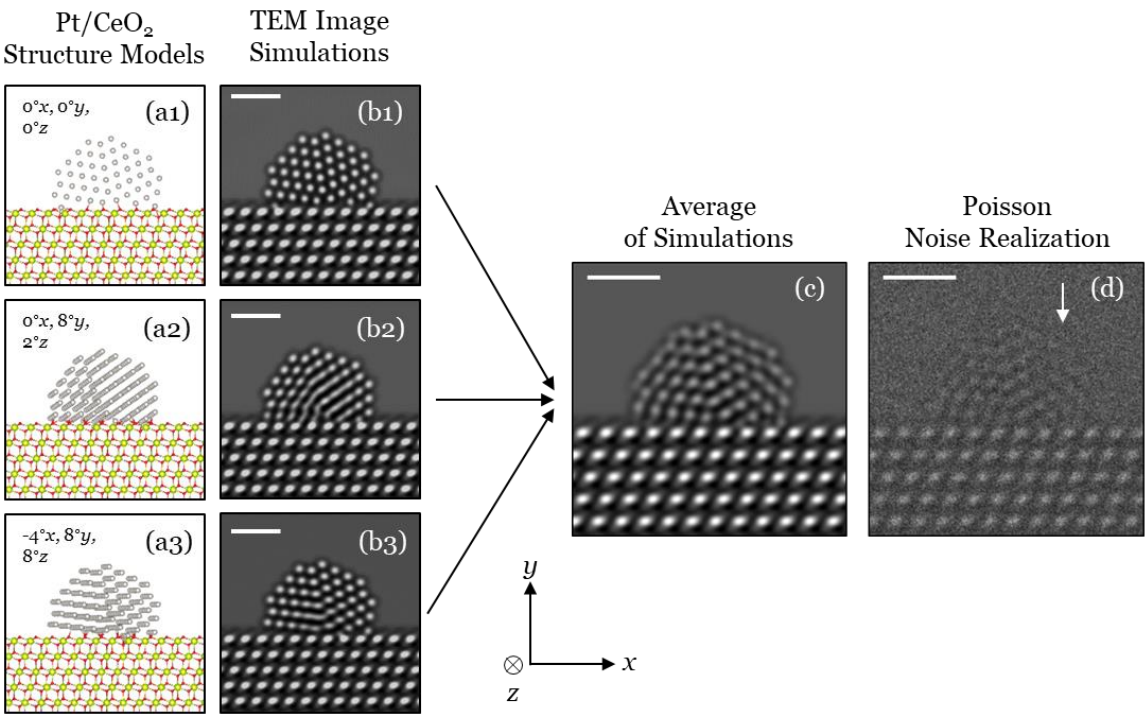

Figure 5.4. Overview of simulation-based approach for modeling dynamic reconfigurations of the supported Pt. **(a1)** – **(a3)** Three structural models of CeO_2-supported multiply-twinned Pt nanoparticles; the notation in the upper left of the figure inset provides the orientation of the Pt nanoparticle relative to the (110) zone axis. A tilt of 8° x corresponds to a rigid-body rotation of the Pt nanoparticle by 8° about the *x* axis, with respect to the principle tilt axes illustrated in the bottom middle of the figure. Pt atoms are shown as gray, Ce atoms as yellow-green, and O atoms as red; the CeO_2 support is also in a (110) zone axis and the nanoparticle sits on a (111) CeO_2 surface. **(b1)** – **(b3)** TEM image simulations of the Pt/CeO_2 structures. **(c)** Average of the three simulated images. Note the reduction in lattice fringe visibility in the Pt but not in the CeO_2. **(d)** Poisson noise realization of the average simulation. White arrow indicates region with nearly invisible Pt lattice fringes due to washing out of contrast. All scale bars correspond to 1 nm.

A multiply twinned Pt nanoparticle 270 atoms in size was generated using the WulffPack Python package (Rahm & Erhart, 2020). Surface energies were gathered from (Singh-Miller & Marzari, 2009) and a default twin energy ratio of 0.04 was used. The twinned nanoparticle was then attached to a CeO_2 (111) surface slab model using the Pymatgen Python package (Ong et al., 2013). Pymatgen was also used to rotate the supported Pt nanoparticle into various desired orientations. The Pt nanoparticles were

rotated in 2° increments about each principal axis up to ±10°. Increments of 2° were chosen, since rotations smaller than this produced insubstantial changes in the resultant image contrast. The particles were not rotated beyond ±10° because it was deemed unlikely that they had rotated farther based on inspection of the experimental time-series. TEM images of the atomic-scale structural models were simulated using the Dr. Probe multislice simulation package (Barthel, 2018). Simulated time-averaged images were generated by averaging multiple simulations together; Poisson noise was added after scaling the vacuum intensity of the simulation to that of the experiment. All model and image generation codes are provided on the Crozier Group GitHub page (https://github.com/Crozier-Research-Group/), and a few documented examples of relevant scripts have been given in the Appendix, Section D.4.

During this study, two sequential 150 ms periods of the experimental image time-series were investigated which offered strong contrast potentially favorable to interpretation. One such experimental 150 ms time-averaged *in situ* ETEM image from the time-series acquired in CO and O_2 is shown in **Figure 5.5a**. Several prominent contrast features are visible in the Pt nanoparticle, as denoted by the annotations labeled A – D. For example, at point A, strong atomic column-like contrast is visible, whereas 1 nm away at point B, less distinct nearly uniform contrast appears. Arrow C points to a Pt lattice fringe where at least 3 Pt atomic columns are clearly visible. Arrow D points to a region where upwardly diagonal streaking lattice fringes are visible. Using this arrangement of unique contrast features as a guide, one can attempt to replicate the observation by averaging simulations of variously tilted Pt/CeO_2 structures. **Figure 5.5b** presents a simulated time-average that represents the best-achieved qualitative match to the experimental observation (the models and images for this simulated time-average have been presented in **Figure 5.4(a1)-(a3)** and **Figure 5.4(b1)-(b3)**, respectively).

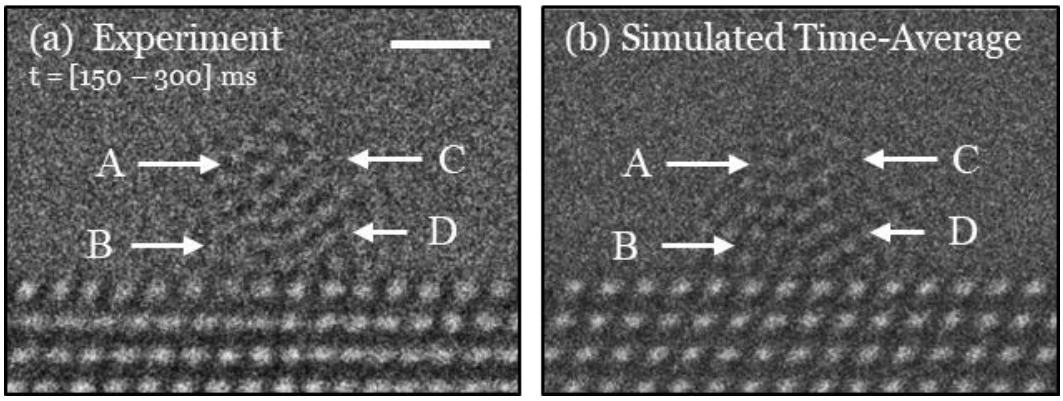

Figure 5.5. (a) Experimental 150 ms time-averaged *in situ* ETEM image extracted from time-series of Pt/CeO_2 particle in CO and O_2. Scale bar corresponds to 1 nm. **(b)** Simulated time-average showing contrast features similar to that observed experimentally. Lettering A, B, C, and D mark regions with prominent contrast features; see text for more details. The simulated time-average is comprised of three images generated from the models displayed in Figure 5.4(a1)-(a3).

The simulated time-averaged image presents a decent qualitative agreement with the experimental observation. In particular, the contrast around point A and in the center of the particle appear compellingly similar in both images. The contrast around point D also appears in qualitatively good agreement, although it is noticed that the lattice fringes are oriented more vertically in the experimental image. Points B and C present the biggest mis-match between simulation and experiment: at point C, the simulated time-average shows more diffuse contrast than the experiment; at point B, the simulated time-average shows clearly resolved atomic columns, which are not observed experimentally. The next sequential 150 ms of the experimental *in situ* TEM image time-series was also modeled in the same manner. The results are presented in the Appendix (Section D.2, see **Figure D.2** and **Figure D.3**), which show comparable behavior to that presented in **Figure 5.5**; namely, that contrast in some regions of the supported Pt nanoparticle, particularly the center, provide excellent qualitative agreement between simulation and experiment, while other regions, especially the surface and near the Pt/CeO_2 interface, do not.

Despite the incomplete correspondence, the decent qualitative agreement achieved by this preliminary attempt offers a few valuable insights for future efforts involving more sophisticated approaches. First, the overall resemblance between the experimentally observed contrast and the simulated time-average suggest that CeO_2-supported Pt nanoparticle does indeed adopt a multiply-twinned morphology in the CO and O_2 atmosphere. A speculative hypothesis for it doing so would be that the introduction of the twinned structure (and the associated planar defects in the particle) lowers the overall system energy by allowing the particle to form a hemispherical shape that reduces the surface area in contact with the CO gas. Further research is needed to investigate this hypothesis. Secondly, the results suggest that the experimentally observed fluxional behavior involves rigid-body-like rotations of the Pt through angles of at least up to 10°.

The discrepancy between the generally good contrast match in the nanoparticle bulk and the typically poor match at the surface/interface demonstrate the limitations of the simplified approach undertaken here. In this work, only bulk-terminated structures were considered. A more sophisticated treatment would ideally include energetics calculations that permit the modeled structure to relax prior to image simulation. Additionally, in this work the simulated time-averages were generated manually based upon visual inspection of the contrast features identified in the experimental data. With the implementation of high-throughput computing, a promising alternative approach would be to quantitatively compare the experimental image with an arbitrarily large database of simulations, using, e.g., a numerical measure of distance such as the structural similarity index measure or SSIM (Wang et al., 2004).

5.3.2. Dynamic behavior at elevated temperature in an atmosphere of pure CO and under water-gas shift (WGS) reaction conditions

The fluxional behavior of CeO_2-supported Pt nanoparticles was investigated at 200 °C under conditions relevant to WGS. **Figure 5.6** presents *in situ* ETEM images of a typical particle observed during the experiment in (a) 0.24 mbar of pure CO and (b) 0.73 mbar of CO:H_2O in a 2:1 ratio. In CO, the Pt nanoparticle exhibits substantial fluxional behavior, evidenced by the fluctuating contrast throughout the image time-series comprised of 1.5 sec summed images in **Figure 5.6(a1) – Figure 5.6(a4)**. Over a 6.0 sec time-averaged observation, the particle appears poorly ordered and hemispherical in shape (**Figure 5.6(a5)**). The apparent structure of the supported nanoparticle is again not well-defined. There appears to be a stabilized cluster of atoms anchored to the support in the core of the nanoparticle. The diffuse and varying contrast over time at the nanoparticle surface suggest that significant Pt surface diffusion may be taking place. The adsorption of CO onto Au nanoparticles is known to promote Au diffusion (McKenna & Shluger, 2007), and a similar process may occur in this system. It is worth noting that the behavior of the particle observed with an electron flux of 600 $e^-/Å^2/s$ at 200 °C in pure CO appears qualitatively similar to that observed an electron flux of 5,000 $e^-/Å^2/s$ at room temperature in CO and O_2 (see, e.g., **Figure 5.2b** and **Figure 5.3**), which further supports the working hypothesis that the dynamics are driven by the CO gas atmosphere and not the electron beam.

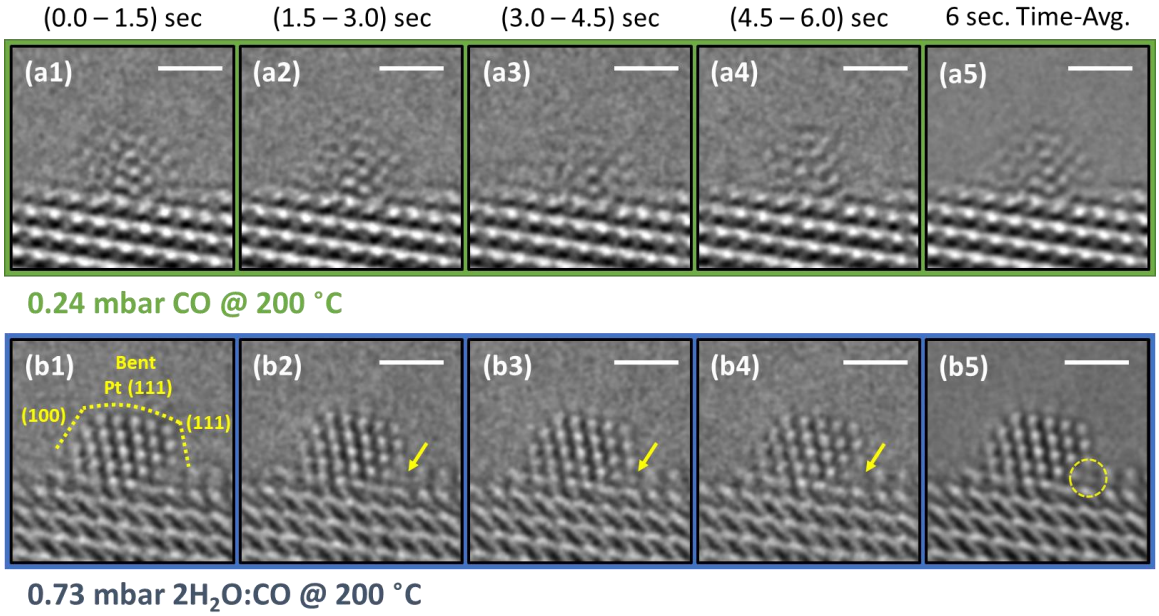

Figure 5.6. (a1) – (a5) Images of a CeO_2-supported Pt catalyst at 200 °C in 0.24 mbar of CO gas. **(b1) – (b5)** Images of the same catalyst at 200 °C in 0.73 mbar of $2H_2O$:CO, corresponding to the water-gas shift reaction conditions. Sequential 1.5 sec intervals from the 6.0 sec image time-series are shown from each condition in **(a1)** – **(a4)** and **(b1) – (b4)**. A time-average over the entire 6.0 sec image acquisition period is shown for each condition in **(a5)** and **(b5)**. The same Pt nanoparticle is shown in all frames. All scale bars correspond to 1.0 nm. Figure from (Li et al., 2021).

Upon introduction of water (**Figure 5.6b**), the fluxional behavior of the Pt particle is attenuated significantly. In the WGS atmosphere, the same supported Pt nanoparticle now exhibits a higher degree of stability and ordering, evidenced by the clearly resolved bulk and surface atomic columns as well as the emergence of surface faceting, all of which remain generally visible throughout the image time series (**Figure 5.6(b1) – Figure 5.6(b4)**). In this case the particle presents (111) and (100) surface facets, and the morphology appears generally consistent with that expected for equilibrium supported Winterbottom shape. However, a distortion in the interplanar spacing is observed to result in the bending of the lattice planes, as indicated in **Figure 5.6(b1)**, which gives the particle a slightly rounded shape like that observed in the pure CO atmosphere. At present it remains unclear as to why the particle has stabilized in the presence of water.

While the supported particle appears generally much more stabilized/localized, dynamic fluxional behavior is observed to occur at sites on the Pt nanoparticle surface and at the Pt/CeO_2 interface. Careful inspection of the top (111) Pt surface throughout the image time-series (**Figure 5.6(b1) – Figure 5.6(b4)**) reveals the continual rearrangement of the surface atomic columns on the ~1 sec or faster time scale. At the perimeter sites (e.g., site indicated with yellow arrow), the Pt atomic columns are seen to disappear (**Figure 5.6(b2)**) and reappear (**Figure 5.6(b3)**) in sequential 1.5 sec time intervals. These observations suggest that the atoms located at different sites within the nanocluster dynamically and heterogeneously change under *in situ* conditions. The behavior exhibited by the Pt nanoparticle shown in **Figure 5.6** is representative of the many observed during the ETEM experiment. Additional images from a different particle are shown in Appendix **Figure D.4**. By correlating these *in situ* TEM observations with other multimodal *in situ* characterization of the same catalyst (including diffuse reflectance infrared spectroscopy (DRIFTS), X-ray absorption spectroscopy (XAS), and photoelectron spectroscopy (XPS)), it was possible to deduce how the heterogeneous dynamic behavior impacts the mechanism of the WGS reaction (Li et al., 2021), a full discussion of which is beyond the scope of this Chapter. However, the results presented herein nonetheless demonstrate the power of *in situ* AC-ETEM coupled with fast direct electron detectors for elucidating dynamic structural behavior of nanoparticle catalysts.

5.4. Summary

Due to its intimate connection with reactivity, the dynamic structural meta-stability (i.e., fluxionality) exhibited by catalysts is becoming an increasingly important focus of fundamental heterogenous catalysis research. However, at present there is a lack of atomic-level information on the fluxional behavior exhibited by many catalysts under conditions relevant to their use. In this Chapter, aberration-corrected *in situ* ETEM

coupled with a fast direct electron detector was applied to CeO_2-supported 1 – 2 nm Pt nanoparticle catalysts to visualize and characterize fluxional behavior with high spatiotemporal resolution. Time-resolved atomic-resolution *in situ* observations of Pt/CeO_2 are made (a) at 20 °C in 0.5 mTorr of N_2 and in 10 mTorr of a 1:2 ratio of CO and O_2 and (b) at 200 °C in 0.24 mbar of CO and in 0.74 mbar of a 1:2 ratio of H_2O and CO.

In the N_2 atmosphere at room temperature, Pt nanoparticles exhibit clear surface faceting, a morphology consistent with the equilibrium Winterbottom shape, an epitaxial relationship with the underlying support, and are generally stable, except for possible changes in atomic column occupancy at the weakly-coordinated and/or high energy sites on the nanoparticle surface. In CO and O_2, even at room temperature, the same supported Pt nanoparticle becomes highly fluxional, undergoing continuous structural reconfigurations between meta-stable states on the time scale of ~50 ms or faster. Evidence is also seen for the emergence of multiple nanoscale crystallographic shear planes in the CeO_2 support, which indicates that a high concentration of CeO_2 lattice oxygen vacancies are present. Consequently, it implies that the observed Pt nanoparticle dynamics could be driven at least in part by oxygen vacancy effects in the underlying reducible oxide support. A preliminary attempt to model the complex fluxional behavior of the supported Pt nanoparticle as comprised of only bulk rigid-body-like rotations yields decent qualitative agreement with the experiment and may provide a promising starting point for more sophisticated approaches.

CeO_2-supported Pt particles observed at 200 °C in an atmosphere of pure CO show similar qualitative behavior to those observed at room temperature in CO and O_2, which suggests that in this case the CO–Pt/CeO_2 gas-solid interactions are the primary driving force for the observed fluxional behavior. Interestingly, upon introduction of water, the same particles exhibit a much higher degree of stability and ordering, evidenced by the

appearance of well-defined surface faceting and a shape that is consistent with the equilibrium Winterbottom shape. Sites located at the Pt surface and at the Pt/CeO_2 interface continue to exhibit fluxional behavior that causes them to disappear and re-appear in subsequent ~1.0 sec periods of the observation.

Overall, the results of this work provide insight into the atomic-level dynamic structural reconfigurations that can occur in reducible oxide-supported metal nanoparticle catalysts under conditions relevant to the CO oxidation and water-gas shift reactions.

6. Developing and Evaluating Deep Neural Network-based Denoising for Nanoparticle TEM Images with Ultra-low Signal-to-noise

6.1. Motivation

As demonstrated in the previous chapter, direct electron detectors now enable atomically-resolved ETEM image time series of catalytic nanoparticles to be acquired with a temporal resolution on the order of milliseconds (ms). Although there is potentially much to be gained from applying these new detectors to catalytic nanomaterials characterization, acquiring *in situ* ETEM image time series with very high temporal resolution produces datasets that can be severely degraded by shot noise (Lawrence et al., 2020). Cutting edge sensors offer detective quantum efficiencies (DQEs) approaching the theoretical maximum of unity, largely by eliminating readout noise and by employing electron counting to improve the modulation transfer function (Ruskin et al., 2013; Faruqi & McMullan, 2018). Even so, especially at high frame rates, where the average dose is < 1 e- per pixel per frame, the information content of the image signal remains limited by Poisson shot noise associated with the electron emission and scattering processes.

Following Poisson statistics, counted images with an average dose < 1 e^- per pixel per frame have signal-to-noise ratios (SNR) on the order of or less than unity, and consequently, ascertaining the structure in the image signal becomes a major obstacle. The SNR can be improved by counting for longer or increasing the beam current, but this is not always possible. By carefully selecting and summing frames in a time-series, precise information on metastable states can be obtained with improved SNR. Averaging consecutive frames may reveal fluxional behavior provided the lifetime of each metastable state is longer than the averaging time. However, information on short-lived intermediate states, *which may ultimately underpin the material's overall functionality*, may no longer be precisely determined with degraded temporal resolution.

One approach to address this SNR challenge is to develop denoising techniques which effectively estimate and partially restore some of the information missing from the experimental image. There is a pressing need for sophisticated noise reduction techniques that preserve the temporal resolution of the image series and facilitate the retrieval of structural features at the catalyst surface. The details and effectiveness of such approaches to atomic resolution electron microscopy images have not been well explored. The aim of this Chapter is to develop and evaluate deep learning methods for denoising images of nanoparticle surfaces recorded from AC-ETEM. While our primary motivation is catalysis, the approaches described here may be applicable to a wider range of atomic resolution imaging applications that are characterized by ultra-low SNR.

Convolutional neural networks (CNNs) achieve state-of-the-art denoising performance on natural images (Liu & Liu, 2019; Tian et al., 2019; Zhang et al., 2017) and are an emerging tool in various fields of scientific imaging, for example, in fluorescence light microscopy (Zhang et al., 2019; Belthangady & Royer, 2019) and in medical diagnostics (Yang et al., 2017; Jifara et al., 2019). In electron microscopy, deep CNNs are rapidly being developed for denoising in a variety of applications, including structural biology (Buchholz et al., 2019; Bepler et al., 2020), semiconductor metrology (Chaudhary et al., 2019; Giannatou et al., 2019), and drift correction (Vasudevan & Jesse, 2019), among others (Ede & Beanland, 2019; Lin et al., 2021; Spurgeon et al., 2021), as highlighted in a recent review (Ede, 2020).

To our knowledge, deep neural networks have not yet been developed to denoise atomic-resolution TEM images of nanoparticles with an emphasis on atomic scale surface structure. As the potentially fluctuating atomic-scale structure at the catalyst surface is of principal scientific interest in this application, it is critical to establish methods for evaluating the agreement between the noisy observation and the structure that appears in

the network-denoised image. As far as we are aware, such analysis is not found in the previous literature on CNNs for electron-micrograph denoising. Moreover, the mechanisms by which trained networks successfully denoise is often treated as a "black box". Revealing and studying these mechanisms is, however, a key step towards further improving this methodology and understanding its potential and limitations.

In this Chapter, a supervised deep CNN is developed to denoise atomic-resolution TEM images of nanoparticles acquired in applications where the image signal is severely limited by shot noise. The network was trained on a dataset of simulated images produced through multislice calculations and then applied to experimentally acquired images of a Pt/CeO_2 catalyst. Extensive analysis is done to characterize the network's ability to recover the exact atomic-scale structure at the Pt nanoparticle surface. An approach is established to assess the agreement between the noisy observation and the atomic structure in the network-denoised image, without access to ground-truth reference images. Finally, the mechanisms used by the network to denoise experimental images is investigated and visualization of these mechanisms is presented in the form of equivalent linear filters, which reveal how the network adapts to non-periodic surface defects.

The work in this Chapter was performed in collaboration with data scientists specializing in machine learning methods through an NSF *Harnessing the Data Revolution* (HDR) program. Prof. Carlos Fernandez-Granda and Sreyas Mohan of NYU were responsible for designing and training the CNNs and for evaluating the performance of the CNNs and baseline denoising methods, in conjunction with Prof. David Matteson and Binh Tang of Cornell, who helped to determine metrics for quantitatively evaluating the denoising performance in terms of surface atomic structure. Additionally, Dr. Ramon Manzorro of ASU designed the structures in the dataset and assisted with the image simulations. My primary contributions include acquiring and processing the experimental

data, generating the training and test datasets of simulated images, and providing detailed visual inspection and quantitative evaluation of the network's performance.

6.2. Experimental

6.2.1. Experimental data acquisition

Atomic-resolution TEM image time-series of CeO_2-supported Pt nanoparticles acquired as described in Chapter 5, Section 5.2.2 provided experimental data for testing and developing the network. Images were taken at a speed of 40 frames per second (fps) and an incident electron beam dose rate of 5,000 $e^-/Å^2/s$ was used. For the pixel size employed during the experiment (i.e., 0.061 Å /pixel), these conditions resulted in an average dose of 0.45 e^-/pixel/frame.

6.2.2. Atomic model generation and TEM image simulation

A crucial step to achieve effective denoising performance with the supervised deep convolutional neural network is to carefully design the training dataset. A large and flexible dataset of 17,955 multislice simulations was generated from 855 atomic-scale structural models of Pt/CeO_2 systems (see **Figure 6.1**). Each model was simulated under 21 different defocus conditions, resulting in a total of 855 × 21 = 17,955 total images. A wide range of structural configurations and imaging conditions were pursued (a) to encompass potential variations that could occur experimentally and (b) to explore the effect of training and testing the network on various subsets of images under different conditions. Each atomic-scale structure model represents Pt nanoparticles of various size, shape, and atomic structure (e.g., small, medium, or large size, with either faceted or defected surfaces, or some combination of both), supported on CeO_2, which itself may present either a faceted surface or one characterized by surface defects. Extended details on the modeled structures are given Appendix Section E.1. The models consist of Pt

nanoparticles that oriented in a [110] zone axis and that are supported on a CeO_2 (111) surface which is itself oriented in the [110] zone axis. This crystallographic configuration corresponds to that often observed experimentally and is thus the focus of the work.

The models have been constructed with Rhodius (Bernal et al., 1998). The faceting and shape of the Pt nanoparticle was informed by surface energies reported by McCrum et al (McCrum et al., 2017). A Wulff construction based on these values was built in the MPInterfaces Python package (Mathew et al., 2016) and iteratively adjusted in size until a qualitative match in dimension was achieved with the experimentally-observed shape. Each model consists of a supercell having *x* and *y* dimensions of 5 nm x 5 nm. The support thickness was varied between 3 nm and 6 nm in 1 nm increments, so the supercell's *z* dimension varies depending on the thickness of the particular model. The orientation of the structure with respect to the incident electron beam was also systematically varied from 0° to 4° about the *x* and *y* axes independently in increments of 1°. Thus, variations from 0° in *x* and 0° in *y*, to 4° in *x* and 0° in *y*, or 0° in *x* and 4° in *y* were considered.

Simulated HRTEM images were generated using the multi-slice method as implemented in the Dr. Probe software package (Barthel, 2018). All of the simulations were performed using an accelerating voltage of 300 kV, a beam convergence angle of 0.2 mrad and a focal spread of 4 nm. A slice thickness of 0.167 Å was used. Following the experimental conditions, the third-order spherical aberration coefficient (Cs) was set to be -13 μm. The fifth-order spherical aberration coefficient (C5) was set to be 5 mm. All other aberrations (e.g., 2-fold and 3-fold astigmatism, coma, star aberration, etc.) were approximated to be 0 nm. To explore the effect of defocus on the training and testing of the network, the defocus value (C1) was varied from 0 nm to 20 nm in increments of 1 nm. Image calculations were computed using a non-linear model including partial temporal and spatial coherence (Barthel, 2018). An isotropic vibration of 50 pm was applied during

the image calculation. To make the process of computing nearly 18,000 image simulations tractable, the calculations were performed in a parallel fashion on a CPU supercomputing cluster (Agave cluster at ASU). All model generation and image simulation Python codes are on the Crozier Research Group GitHub page (https://github.com/Crozier-Research-Group), and a few examples have been provided in the Appendix, Section D.4.

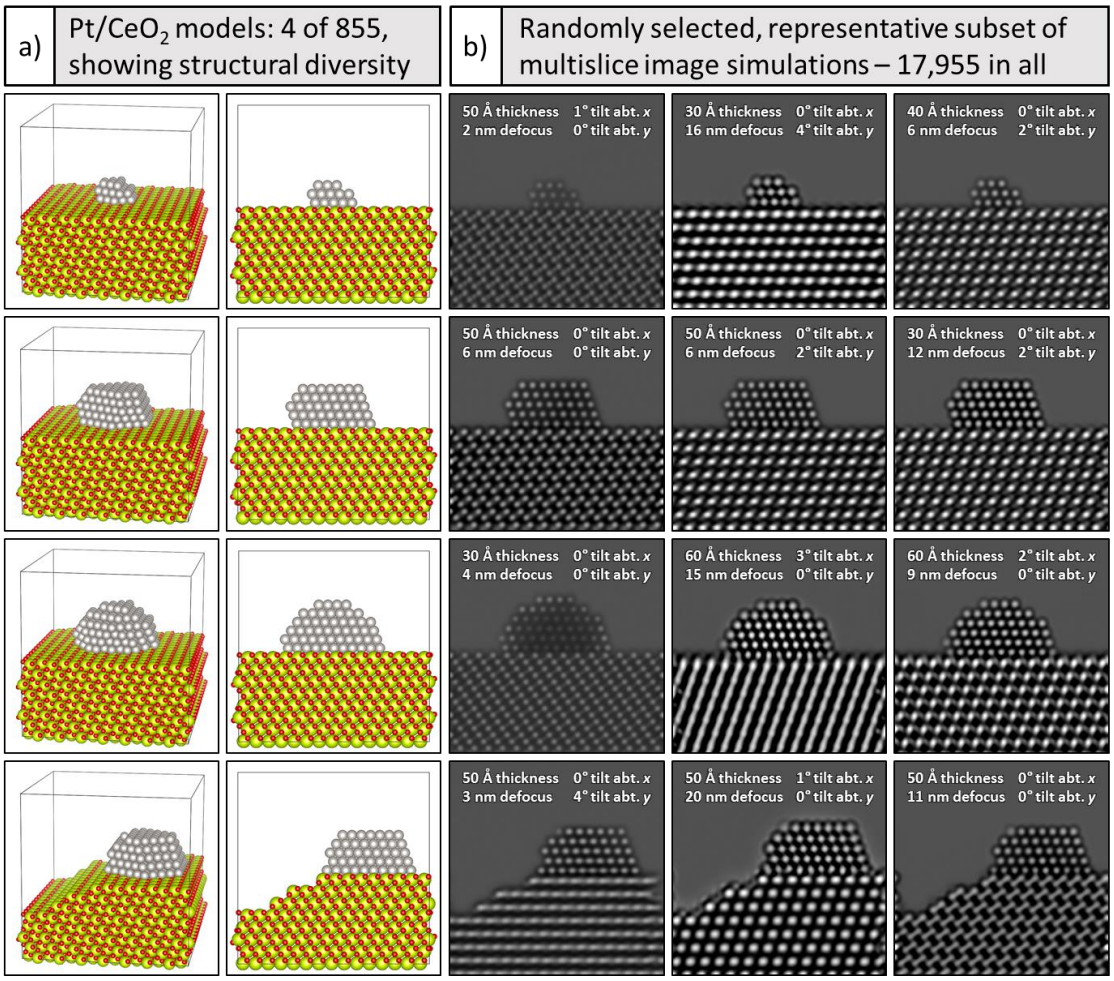

Figure 6.1. Under (a) four (of 855) models are shown in a tilted view to emphasize the 3D structure (far left) and in a projected view along the electron beam direction (second column). Pt atoms are shown in gray, O atoms in red, and Ce atoms in yellow-green. A simulated image of every structure was generated for defocus values spanning 0 – 20 nm, resulting in 17,955 total images. Beneath (b), a representative subset of simulated images from each model is shown, with imaging conditions given in the figure inset. Figure from (Vincent et al., 2021).

To exemplify the variation incorporated into the overall dataset, **Figure 6.1a** depicts a representative subset of four Pt/CeO_2 atomic structural models, along with (**Figure 6.1b**) three randomly selected multislice TEM image simulations generated from each model. The structural models are shown in two perspectives: a tilted view to emphasize 3D structure (first column), and a projected view along the electron beam direction (second column). Note the variation in Pt particle size, shape, and surface defect structure, as well as the changes to the CeO_2 support surface character, with the bottom model displaying a Pt particle having a single atom surface site supported on a CeO_2 surface having multiple step-edge defects. Simulations randomly selected from each model and shown in **Figure 6.1b** demonstrate the large variety of signal contrast and specimen structure available for training and testing the neural network.

6.2.3. Convolutional neural network training and testing

The networks were trained and evaluated on various subsets of simulated images before being applied to the real data. Noisy data for training and evaluating the network were generated from clean simulated images by artificially corrupting the clean simulations with Poisson shot noise. We have verified that the noise in the experimental counted TEM image time-series follows a Poisson distribution (see Appendix, Section E.2 and **Figure E.6**), which is expected given the physical origin of the shot noise in the electron counted image acquisition process.

To evaluate the so-called generalization ability of the network, we divided the simulated dataset into various subsets, systematically trained the network on one of the subsets, and then evaluated its performance on the rest. In these cases, the number of images in each training subset was set equal to establish a fair assessment. The subsets were classified based on (1) the character of the atomic column contrast, (2) the structure/size of the supported Pt nanoparticle, and (3) the non-periodic defects present

in the Pt surface. The atomic column contrast was classified into three divisions: black, intermediate, or white, largely based on the Pt and Ce atomic column intensities relative to the vacuum intensity as shown in Appendix **Figure E.4**). The nanoparticle structures were classified into four categories, "PtNp1" through "PtNp4", each with different size and shape, in accordance with the models displayed in Appendix **Figure E.1.** Finally, the defects were divided into five categories: "D0", "D1", "D2", "Dh", and "Ds", in accordance with the models presented in Appendix **Figure E.2.**

As will be shown, standard CNN architectures used for denoising natural images do not perform well on atomic-resolution HRTEM images. We propose a network architecture is a modified version of U-Net (Ronneberger et al., 2015) with six scales to achieve a large field of view (roughly 900 x 900 pixels). The network consists of 6 down-blocks and 6 up-blocks. A down-block consists of a max-pooling layer, which reduces the spatial dimension by half, followed by a convolutional-block (conv-block). Similarly, an up-block consists of bilinear up-sampling, which enlarges the size of the feature map by a factor of two, followed by a conv-block. Each conv-block itself consists of conv-BN-ReLU-conv-BN-ReLU, where conv represents a convolutional layer, BN represents a batch normalization process (Ioffe & Szegedy, 2015), and ReLU represents a non-linear activation by a rectified linear unit. In our final model, we use 128 base channels in each layer of conv-block. An extended discussion of the network architecture is given in (Mohan, Manzorro, et al., 2020; Vincent et al., 2021).

The network was trained on 400 x 400 pixel sized patches extracted from the training images and augmented with horizontal flipping, vertical flipping, random rotations between -45° and +45°, as well as random resizing by a factor of 0.955 – 1.055. Periodically during training, the network is evaluated on a validation set of images not included in the training set. Typically, around 5,500 simulated images were used to train

the network, with 550 other images randomly selected for validation and testing. The models were trained using the Adam optimizer (Kingma & Ba, 2015), with a default starting learning rate of 1×10^{-3}, which was reduced by a factor of two each time the PSNR of the validation dataset plateaued. Training was terminated via early stopping, based on validation PSNR (Goodfellow et al., 2016). A number of other methods (described in Chapter 2, Section 2.4.3.1), were also applied to both the simulated and the real data in order to establish a baseline for evaluating the performance of the proposed network.

6.3. Results and discussion

6.3.1. Need for improved denoising methods and overview of CNN-based denoiser

A single 25 ms exposure counted frame of a Pt/CeO_2 particle is presented in **Figure 6.2(a1 and a2)**. The Pt particle is in a [110] zone axis on a [111] CeO_2 surface that is itself in a [110] zone axis orientation. Even though a relatively high dose rate of 5×10^3 $e^-/Å^2/s$ was used to acquire the image series, for time-resolved frame rates on the order of ms, many of the counts are 0. In the present case, the average electron dose counted in the vacuum region of the image is 0.45 e^-/pixel/frame. Following Poisson statistics, wherein the variance of the signal is equal to the mean value, and assuming the intensity in the vacuum region is uniform, the signal-to-noise ratio (SNR) of the incident beam is only $SNR = \frac{0.45}{\sqrt{0.45}} = \sqrt{0.45} = 0.67 < 1$. Hence, the image is severely degraded by shot noise. The impact of shot noise is emphasized by magnifying the region marked by the dashed white box, which is presented in **Figure 6.2(a2)**. Here, the quality of the signal is appreciably low, and the Pt atomic columns at the nanoparticle surface are hardly discernible.

One common approach to improving the SNR of time-resolved image series involves aligning and then summing together non-overlapping groups of sequential

frames, yielding a so-called time-averaged or summed image. **Figure 6.2(b1)** presents a 1.000 sec time-averaged image produced from adding together 40 sequential 0.025 sec frames. The pronounced improvement in SNR, which has increased by a factor of $\sqrt{40} = 6.32$ to $SNR = 4.24$, is readily evident, as seen by the well-defined and bright atomic columns that appear in **Figure 6.2(b2)**.

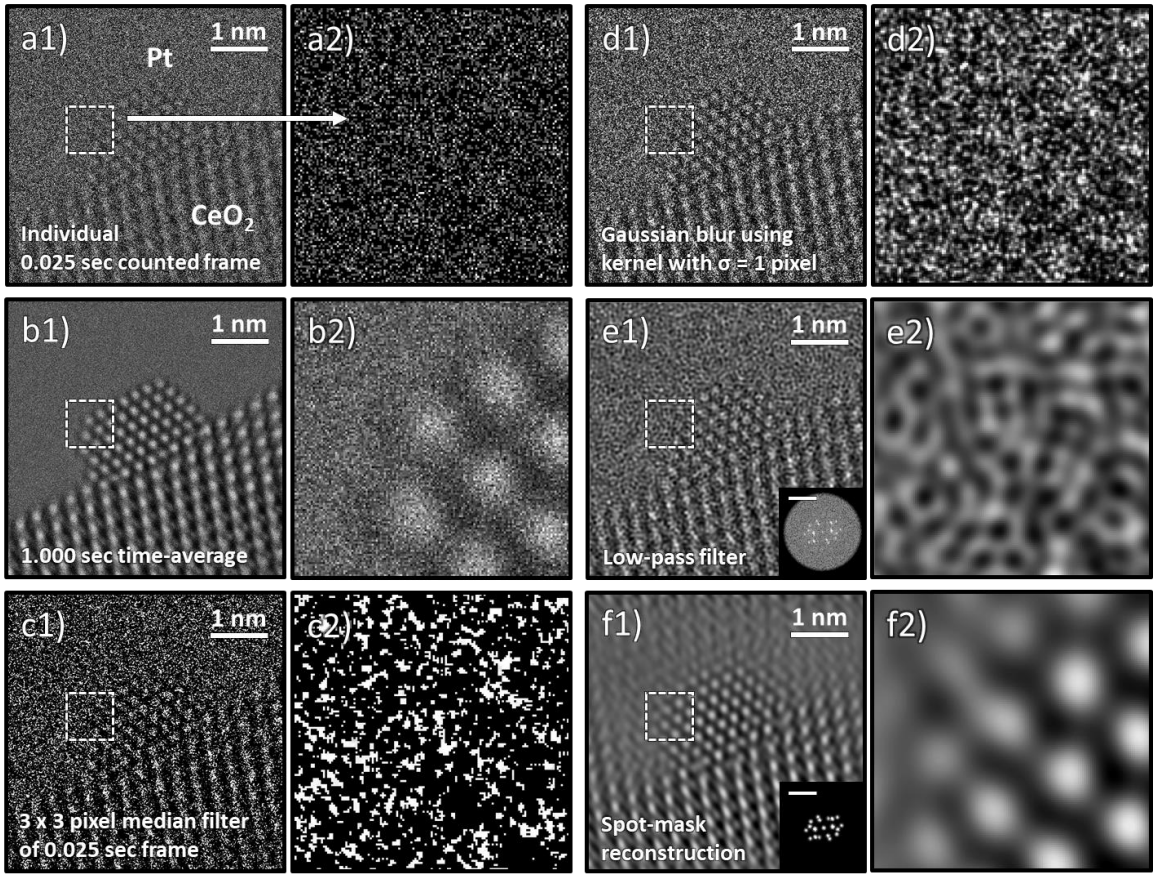

Figure 6.2. Comparison of typical processing techniques applied to an ultra-low SNR experimental TEM image of a CeO_2-supported Pt nanoparticle. In **(a1)** an individual 0.025 sec counted frame is shown along with **(a2)** a zoom-in image taken from the region designated by the dashed box. In **(b)** a 1.000 sec time-averaged image is shown; **(c)** displays the result of filtering the frame with a 3 × 3 pixel median filter; **(d)** displays the result of filtering the frame with a Gaussian blur with standard deviation equal to 1 pixel; **(e)** shows a Fourier reconstruction of the individual frame after applying a low-pass filter up to the 0.74 Å information limit, with the FT given in the inset along with a 1 $Å^{-1}$ scale bar; and **(f)** displays another Fourier reconstruction acquired through masking the Bragg beams in the diffractogram, as shown in the figure inset.

Increasing the SNR without time-averaging can be accomplished by applying linear or non-linear filters that act on variously sized and/or distributed domains in real or frequency space to remove sharp features arising from high noise content. The result of applying a non-linear median filter with a 3 × 3 pixel-sized kernel to the noisy single frame is presented in **Figure 6.2c**. The application of a linear Gaussian blur with a kernel that has a standard deviation equal to 1 pixel yields the filtered image presented in **Figure 6.2d**. Applying kernels of these size and character produced the best improvement in image quality for each filter. Although the filtered images appear smoother and offer an enhanced visualization of the atomic columns in comparison to the raw image, the action of the filters also introduces artifacts to the signal, which can complicate a precise analysis of the atomic column position and/or intensity.

Working in reciprocal space through the application of a Fourier transform (FT) allows one to consider spatial frequency filters that exclude components attributable to noise, with a subsequent reconstruction of the image using the desired domains from the filtered FT. **Figure 6.2(e1)** presents a Fourier reconstruction of the individual frame after applying a linear low-pass filter that excludes components with spatial frequencies beyond the instrument's 1.35 $Å^{-1}$ information limit. After eliminating the high frequency information corresponding to noise, the contrast in the image exhibits an unusual texture that hinders feature identification, as seen in **Figure 6.2(e2)**. **Figure 6.2f** displays another Fourier reconstruction produced here by spot-masking the regions corresponding to Bragg beams in the FT, as presented in the figure inset. Although this reconstructed image offers an improved SNR compared to the raw frame and even to the other filtering techniques, the procedure introduces severe ringing lattice-fringe artefacts into the vacuum region and at the nanoparticle surface, making it unacceptable for use on defects.

There is a pressing need for improved denoising techniques that both preserve the high time resolution of the original data and also facilitate the retrieval of non-periodic structural features, e.g., nanoparticle surfaces and atomic-level defects. Toward this end, we develop a deep CNN that is trained on a big dataset of simulated TEM images before being applied to real data. A schematic overview of the proposed deep CNN training, application, and evaluation process was provided earlier in Chapter 2, **Figure 2.14**. During training (**Figure 2.14,** top), a large dataset of noisy simulated images is given to the network. For each noisy image, the network produces a prediction of the underlying signal, effectively denoising the image. Better denoising performance is achieved by iteratively adjusting the parameters within the network in order to minimize the mean squared error (MSE) difference between the denoised output and the original simulation. After successfully training the network, it may be applied to real data (**Figure 2.14,** bottom). The denoised experimental frame produced by the network presents a significant improvement in SNR without temporal averaging and without making sacrifices to study non-periodic structural features. However, given the high level of noise present in the raw data, caution must nonetheless be exercised when performing analysis on the network denoised output. As will be shown in Section 6.3.4, we have established an approach for quantifying the degree of agreement between the network output and the noisy raw input, which takes the form of a statistical likelihood map.

6.3.2. Performance of network on validation dataset of simulated images

Before applying the trained network to real data, it is important to assess the network's performance on noisy simulated data that it has not seen. **Figure 6.3** presents a representative comparison of the surveyed methods against our proposed network on an image randomly selected from the validation dataset. A similar comparison for another randomly selected image is given in Appendix **Figure E.7**. The aggregate performance, in

terms of PSNR and structural similarity (SSIM, (Wang et al., 2004)), for each denoising approach over all images in the validation dataset is summarized in **Table 6.1**. The noisy simulated image shown in **Figure 6.3a**, along with the zoom-in image taken from the boxed region along the Pt nanoparticle surface, illustrates the severity of the signal degradation that has occurred due to shot noise. The same noisy image was processed using the denoising methods described in Chapter 2, Section 2.4.3.1. The results are presented from **Figure 6.3b** to **Figure 6.3i** in order of increasing performance in terms of PSNR. The original ground truth simulated image is presented in **Figure 6.3j**.

In general, the proposed deep CNN denoising architecture outperforms the baseline methods by a large margin, achieving a PSNR of 42.87 ± 1.45 dB and a SSIM of 0.99 ± 0.01. The starting PSNR of the noisy simulation is about 3 dB. As seen in **Figure 6.3i**, the proposed network produces an estimated image that closely resembles the ground truth simulation. In addition to recovering the overall shape of the Pt nanoparticle, the aperiodic structures of the Pt surface and the Pt/CeO_2 interface, as well as the subtle contrast variations that are present in the CeO_2, have all been accurately denoised by the proposed architecture. The next best performance is attained by the other two simulation-based denoising (SBD) neural networks (e.g., **Figure 6.3g/h**), which reach PSNR and SSIM values around 30.6 dB and 0.93, respectively. However, in the images denoised through these inferior networks, the contrast around aperiodic sites or abruptly terminating surfaces are typically distorted. Moreover, significant artifacts often appear in these images, including phantom atomic column-like contrast in the vacuum, or unrealistic structures characterized by missing columns in unphysical sites, e.g., the bulk.

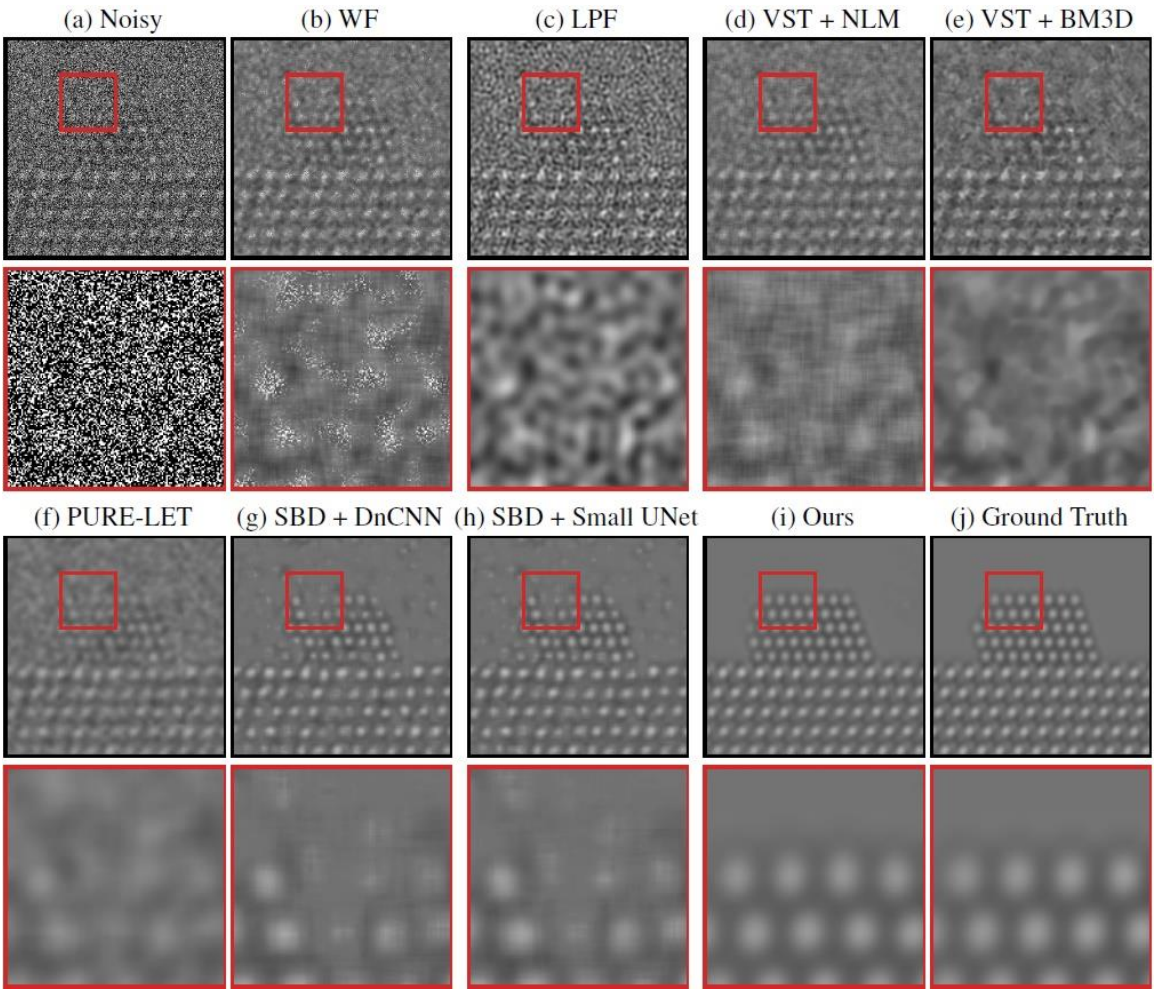

Figure 6.3. Comparison of the network's performance on multislice simulations against other baseline denoising methods, including other neural networks. See Chapter 2, Section 2.4.3.1 for an explanation of the methods. In brief, part **(a)** displays a noisy simulated image, along with a zoom-in on the region indicated by the red box in the figure inset. The clean simulated image is shown as a ground truth reference in **(j)**. The proposed network produces denoised images of high quality, recovering precisely the structure of the nanoparticle, even at the surface, with comparatively few artifacts, as shown in **(i)**.

A number of decisive factors contribute to the performance of the network. First is the size of the network's receptive field. The receptive field is the region of the noisy image that the network can see while estimating the intensity of a particular denoised output pixel. The baseline networks included in the performance comparison, which are the present state-of-the-art in denoising natural images, employ receptive fields either 41 × 41

pixels (in the case of DnCNN, **Figure 6.3g**) or 45 × 45 pixels (in the case of the small UNet, **Figure 6.3h**). Given the fact that the real space pixel size of the data is 6.1 pm, these receptive fields amount to regions around 0.26 nm × 0.26 nm in size. As shown in Appendix **Figure E.8**, with a limited receptive field of such size, it is challenging to see the structure of the atomic columns in the ground truth simulation. Once shot noise has been added to reduce the PSNR to 3 dB, differentiating regions containing structure from those which contain only vacuum becomes virtually impossible by eye.

Table 6.1. Summary of denoising performance on simulated images in terms of mean peak signal-to-noise ratio (PSNR) and structural similarity (SSIM), along with the standard deviation, for each of the surveyed methods aggregated over all of the images in the validation dataset.

Denoising Method	**PSNR (dB)**	**SSIM (arb. units)**
Raw	3.56 ± 0.03	0.00 ± 0.00
Adaptive Wiener Filter (WF)	21.59 ± 0.07	0.44 ± 0.03
Low-pass Filter (LPF)	22.42 ± 1.08	0.63 ± 0.02
VST + NLM	26.55 ± 0.16	0.73 ± 0.01
VST + BM3D	22.57 ± 0.15	0.80 ± 0.01
PURE-LET	28.36 ± 0.88	0.93 ± 0.01
SBD + DnCNN	30.47 ± 0.64	0.93 ± 0.01
SBD + Small UNet	30.87 ± 0.56	0.93 ± 0.01
Ours	42.87 ± 1.45	0.99 ± 0.01

Increasing the receptive field is critical to achieving better performance. Appendix **Figure E.9** shows that expanding the receptive field by a factor of 25 to a region around 200 × 200 pixels (i.e., 1.22 nm × 1.22 nm) allows the network to sense the local structure around the pixel to be denoised. With a receptive field of this size, different structures (e.g., vacuum, Pt surface, CeO_2 bulk, surface corner site) remain discernible even after adding noise. This suggests that increasing the receptive field contributes to the network's ability

to detect subtle contrast variations as well as aperiodic defects. The receptive field of the proposed network is roughly 900 x 900 pixels (i.e., 5.49 nm × 5.49 nm, **Figure 6.3i**).

The network's performance is also influenced by the nature of the images contained in the training dataset. Here we have discovered that the geometry of the image (i.e., the scaling and orientation) as well as the character of the atomic column contrast (i.e., the focusing condition) appear to have the largest impact. In Appendix **Figure E.10** we demonstrate that the denoising performance measured in terms of PSNR degrades significantly when the network is evaluated on simulated images that have been scaled or rotated in a manner that was missing from the images in the training dataset. Note that the performance remains roughly constant across various values of pixel size and orientation *when these pixel sizes and orientations are present in the training dataset*. These results indicate that augmenting the training data with random resizing/rotations can ensure that robust performance is obtained when the network is applied to real data, which may differ slightly in exact scaling or orientation from the images in the training dataset. Practically, the results also imply that networks must be carefully trained to denoise images taken at the particular image magnification of interest.

We have also investigated the generalizability of the network to unseen supported nanoparticle structures, non-periodic surface defects, and atomic column contrast conditions (i.e., defocus). As shown in Appendix **Figure E.11** the network generalizes well to new (a) nanoparticle structures of various shape/size and (b) atomic-level Pt surface defects, with a good and consistent PSNR denoising performance above 34 dB for all of the categories explored here. The network is also generally robust to ± 5 nm variations in defocus. The largest degradation in performance (PSNR = 28 dB) is observed when the network is trained on images with black-column contrast and tested on images with white-

column contrast. A general conclusion would be to train the network using images simulated at a defocus close to the data that is to be denoised.

6.3.3. Evaluating the network's ability to accurately predict surface structure

Understanding the atomic-scale structure of the catalyst surface is of principal scientific interest. Here, we perform a detailed evaluation of the network's ability to produce denoised images that accurately recover the atomic-level structure of the Pt nanoparticle surface. The analysis was conducted over a set of 308 new simulated images that were specifically generated for the surface evaluation. A series of 44 Pt/CeO_2 structural models were created with many different types of atomic-level surface defects, including, e.g., the removal of an atom from a column, the removal of two atoms, the removal of all but one atom, the addition of an atom at a new site, etc., to emulate atomic-level reconfigurations that could be observed experimentally. Nine of the models are shown in Appendix **Figure E.12** to provide an overview of the type of structures that were considered. Images were simulated under defocus values ranging from 6 nm to 10 nm, all with a tilt of 3° in x and -1° in y and a support thickness of 40 Å. Note that these images were never seen by the network during training.

A ground truth simulated image from the surface evaluation dataset is shown in **Figure 6.4(a1)**. A so-called blob detection algorithm based on the Laplacian of Gaussian approach was implemented to locate and identify the Pt atomic columns in the image (Kong et al., 2013). The atomic columns at the nanoparticle surface were distinguished from those in the bulk, which was done by computing a Graham scan on the identified structure (Graham, 1972). **Figure 6.4(a2)** shows a binary image depicting the Pt atomic columns identified in the ground truth simulated image. The set of atomic columns located at the surface have been highlighted with a green line.

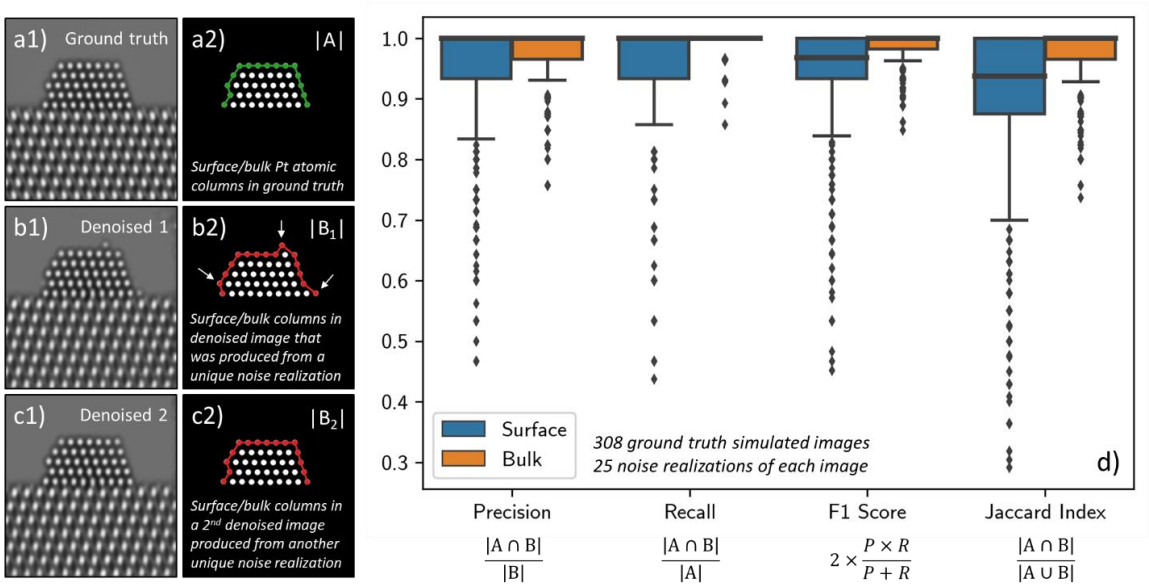

Figure 6.4. (a1) A representative ground truth simulation from the structure evaluation data set ($n_{ground\ truth}$ = 308). **(a2)** The set of Pt columns identified in the ground truth image (i.e., $|A|$) are shown, with those at the surface highlighted by a green line. **(b1)** and **(c1)** Two denoised images produced by the network from two unique noise realizations of the same simulation. **(b2)** and **(c2)** The set of Pt columns identified in the denoised images (i.e., $|B|$) are shown, with those at the surface highlighted now by a red line. **(d)** Box plot distributions of each metric for surface (blue boxes) and bulk (orange boxes). Outliers in the distributions are marked by small diamonds.

Evaluating the network's ability to recover surface structure can be accomplished by examining how this set changes after denoising. **Figure 6.4(b1)** displays a denoised image produced by the network from a unique noise realization of the ground truth simulation. While the network denoises with outstanding performance and recovers the overall shape of the specimen, note the appearance of the three spurious Pt surface atomic columns that do not appear in the ground truth. The Pt atomic columns identified in this denoised image are pictured in **Figure 6.4(b2)**, where those located at the surface are highlighted now by a red line. The spurious Pt surface atomic columns have been marked with white arrows. Based on inspection of the noisy data, we believe that the particular distribution of intensity present in the noise realization can lead the network to produce denoised estimates with spurious surface atoms, perhaps due to the random clustering of

intensity in a manner that appears to resemble an atom (see, e.g., Appendix, **Figure E.13**). **Figure 6.4(c1)** displays a denoised image produced by the same network from a *second* unique noise realization. Note that in this case the Pt surface structure has been *recovered exactly*. The Pt atomic columns identified in this denoised image are pictured in **Figure 6.4(c2)** and are equivalent to those identified in the original simulation.

To quantify the network's performance in recovering the Pt atomic structure, we compute four metrics that are commonly employed in the field of machine learning: precision, recall, F1 score, and Jaccard index. These metrics are defined by the following equations:

Eq. 6.1 $Precision = \frac{|A \cap B|}{|B|}$ *A higher precision corresponds to less false positives, i.e., spurious atoms.*

Eq. 6.2 $Recall = \frac{|A \cap B|}{|A|}$ *A higher recall corresponds to fewer false negatives, i.e., columns originally in the ground truth image that are no longer present.*

Eq. 6.3 $F1\ Score = 2 \times \frac{Precision \times Recall}{Precision + Recall}$ *The F1 score is the geometric mean of the recall and precision. Can be used to determine how often combinations of errors occur.*

Eq. 6.4 $Jaccard\ Index = \frac{|A \cap B|}{|A \cup B|}$ *The Jaccard index gauges the degree of exact similarity between the ground truth and denoised image (ideal value of 1 occurs when they are identical in structure).*

These metrics were calculated for both the surface and the bulk structure; when the metrics were calculated for the surface structure, $|A|$ represents the set of Pt atomic columns identified at the surface in the ground truth simulation, and $|B|$ represents the columns identified at the surface in the denoised image. Similarly, when the metrics were

calculated for the bulk structure (i.e., everything other than the surface), $|A|$ and $|B|$ represent the bulk atomic columns in the ground truth and denoised images, respectively. To attain an accurate representation of the network's performance, 25 noise realizations of each ground truth simulation were sampled and then denoised, resulting in an evaluation over 7,700 total images.

Figure 6.4d displays box plot distributions of the four metrics computed over all 7,700 images for the surface (blue boxes) and the bulk (orange boxes). Box plots, or box-and-whisker plots, are useful for graphically visualizing distributions of data on the basis of the quartiles that exist within the distribution. The quartiles are a set of three numerical values that divide the number of data points in the distribution into four roughly equally-sized parts; e.g., the 2nd quartile is the median or mid-point of the dataset when the values are ordered from smallest to largest, the 1st quartile lies halfway between the smallest value and the median, and the 3rd quartile lies halfway between the median and the largest value. In the box-and-whisker plot, the box is drawn from the 1st quartile (Q_1) to the 3rd quartile (Q_3) with the median value represented by a line within this box. Whiskers, which are lines extending beyond the edges of the box, can be useful for describing the behavior of the data that falls in the upper or lower quartile of the distribution. Here we choose to follow a standard practice for drawing the whiskers: a distance equal to 1.5x the interquartile range (defined by $Q_3 - Q_1$) is drawn from each edge of the box; on the top of the box, for example, the largest value above Q3 that lies within this distance is defined as the edge of the top whisker; similarly, the smallest value below Q1 that lies within this distance is defined as the edge of the bottom whisker. Values beyond the edge of the whiskers are considered outliers; here, they are drawn as small solid diamonds. As seen in **Figure 6.4d**, the box plots for the bulk are all narrow and have median values of 1.0, which is

expected given that the network was not seen to produce images characterized by unphysical bulk structures, such as, e.g., missing interior atomic columns.

The distributions for the surface are slightly more varied and reveal detailed information about the performance of the network. First, consider the distribution for the precision (left-most box plot in **Figure 6.4d**). The precision, or the positive predictive value, measures the fraction of real surface columns over all of the surface columns identified in the denoised image. Effectively, a lower precision value indicates that there are more false positives (i.e., spurious surface columns) in the denoised output. As a reference, consider a ground truth simulation in which there are originally 15 atomic columns present at the surface (e.g., **Figure 6.4(a1)**). The addition of one spurious surface column would result in a precision value of 0.93, while the addition of three columns would yield a precision value of 0.80. As seen in **Figure 6.4d**, the median precision value is 1.0 and the first quartile lies nearby at 0.93. Thus, the precision distribution shows the network frequently produces denoised images that do not contain spurious columns; occasionally it will include one, and rarely it will add two or more.

In addition to including spurious atomic columns, the network may fail to recover the full structure, resulting in a column being omitted from the denoised image. The prevalence of this is captured by the recall, which measures the fraction of real columns over all of the columns identified in the *clean ground truth image*. Effectively, a lower recall value indicates that there are more false negatives in the network denoised output, which means that columns which were originally present in the ground truth image are no longer present in the network denoised output. As presented in **Figure 6.4d**, the median recall value is also 1.0, with a distribution that is similar to – but narrower than – the precision. These values again indicate an impressive performance by the network.

Interestingly, the slightly smaller distribution suggests that the network may tend to include spurious atomic columns more often than it fails to sense real atomic columns.

Taking the harmonic mean of the precision and recall yields the F1 score, which accounts both for false positives as well as false negatives. Here, the median value of the F1 score distribution is around 0.96, and the first quartile lies around 0.93. Given that the median precision and recall are both 1.0, it is not surprising that the F1 score distribution is also narrow and clustered around high values (i.e., greater than 0.90). Note that the harmonic mean of 1.0 (the median precision/recall) and 0.93 (the first quartile of both distributions) equals 0.96, which is the median F1 score. Thus, the F1 score reveals that while the network may occasionally include a spurious column or fail to include a real one, combinations of these errors occur less frequently.

Finally, we have computed the Jaccard index to gauge the exact degree of similarity between the surface structure in the clean and denoised images. As defined above, the Jaccard index equals the fraction of true positives (i.e., real columns) over the union of surface columns identified in both the clean and the denoised images. The ideal value of 1.0 occurs only when the exact atomic structure is recovered. In general, for the images in the surface evaluation dataset, the addition of a spurious atomic column would give a Jaccard index of 0.87, while the omission of a real column would give a value of 0.93. The distribution plotted in **Figure 6.4d** shows that the median Jaccard index value is 0.93 and that the first quartile lies at 0.87. Observe that the third quartile lies at 1.0, signaling that the network will achieve a perfect performance in recovering the precise atomic structure at the surface at least 25% of the time, *despite the extreme degree of signal degradation that has occurred due to shot noise*. The location of the first quartile at 0.87 indicates that at least 66% of the errors involve the addition or omission of only one atomic column. The remaining errors, which represent at most 25% of the total data, involve the

addition and/or omission of more than one atomic column. Further studies implementing this approach could be done in the future to assess the effect that varying the noise level has on the network's ability to predict the atomic level surface structure exactly.

6.3.4. Quantifying agreement between the noisy observation and the network-denoised output

When applying the trained network to real data, the atomic structure in the network denoised output cannot be compared to a clean ground truth image, since none is available. Establishing a tool to assess the likelihood of an atomic column's appearance in the network-denoised image would thus be of great utility. Here, we develop a statistical analysis based on the log-likelihood ratio test that makes it possible to hypothetically evaluate whether an atomic column in the denoised image is (1) likely to represent a true atomic column in the structure or (2) likely to be an artifact introduced by the denoising neural network. Additionally, a graphical visualization of the log-likelihood ratio is created in the form of a likelihood map. The log-likelihood ratio method requires only the network denoised image and the noisy input and is therefore extensible to real experimental data, where no clean ground truth references exist.

We validate the analysis on a large dataset of simulations, for which the true structures are known. **Figure 6.5** depicts a representative (a) noisy and (b) denoised image from the simulated dataset discussed in the prior section. To compute the log-likelihood ratio and generate the likelihood map, the following procedure is implemented: first, an atomic column in the denoised image is located, e.g., through blob detection (here, we focus on the Pt columns, although the method is generalizable to any area of interest so long as it can be identified in the denoised image). As a simplifying assumption, we model the intensity of the atomic column as a constant value, which is obtained by averaging over all the denoised pixels in the region R identified by the blob detection

algorithm. In Appendix **Figure E.14** we show that for these imaging conditions this is a good assumption, provided that the region R is restricted to a limited area (e.g., radius < 0.75 Å) within the atomic column where the intensity is largely invariant.

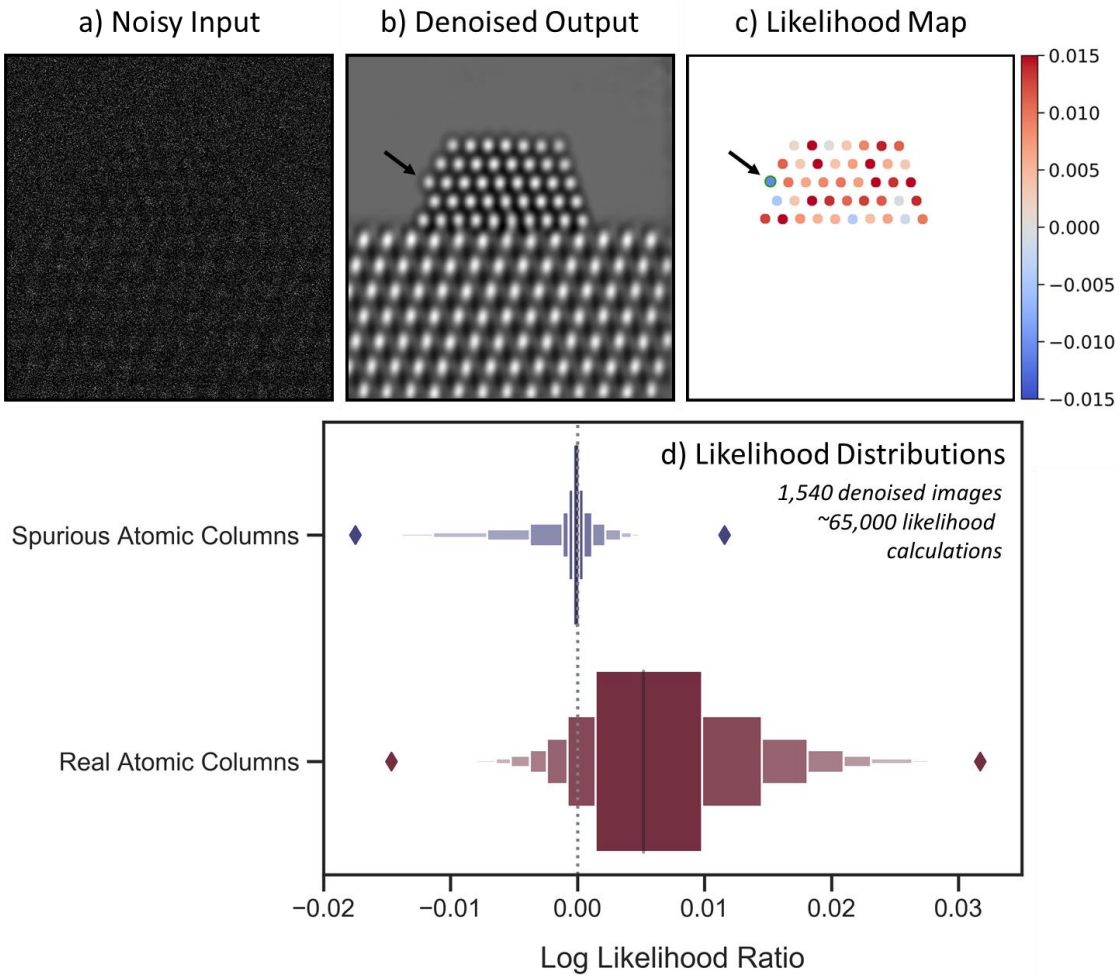

Figure 6.5. Likelihood analysis to quantify agreement between noisy data and denoised output. In **(a)** a representative noisy simulated image is shown along with **(b)** a denoised image output by the network. Part **(c)** depicts an atomic-level likelihood map, which visualizes the extent to which the atomic structure identified in the denoised image is consistent with the noisy observation. After denoising, a spurious atomic column appears at the arrowed site, which shows a large negative value in the likelihood map, indicating that the presence of an atomic column at this location is not likely. The likelihood analysis has been performed over 1,540 denoised images, yielding the distributions given by the letter-value plots for spurious (blue, top) and real (red, bottom) columns in part **(d)**. The diamonds mark the extrema of the two distributions.

Second, we compute the statistical likelihood, L, of observing the noisy data in R of the input, assuming the true signal in this region is the constant value calculated from the denoised output. We know that the observed signal is governed only by shot noise, which can be modeled with a Poisson distribution. And furthermore, we assume that every pixel is mutually independent, so that the overall likelihood in R is simply the product of the individual probabilities for each pixel i in R. Mathematically, the likelihood calculation is then defined by the following equation:

Eq. 6.5 $$L(R) = \prod_{i \in R} p_\lambda(x_i)$$

Where x_i is the intensity of the ith noisy pixel in R, and p_λ is a Poisson probability mass function characterized by a mean of λ, which is equal to the constant value calculated from the denoised output. Here, a higher likelihood value would indicate a better level of agreement between the denoised output and the noisy data. To assess instead whether the column is an artifact of the denoising network, we also compute the likelihood of observing the noisy data in R with the true signal now represented by the constant value of the vacuum (i.e., λ = 0.45).

Comparing the relative magnitude of these two likelihood values allows one to consider the whether the atomic column is likely to be real or spurious. How consistent either hypothesis is with the noisy observation can be tested by taking the natural log of the likelihood ratio (also known as a log-likelihood ratio test). Considering, e.g., the noisy and denoised images of **Figure 6.5a and Figure 6.5b**, the results of this test are conveniently visualized for every atomic column detected in the denoised image through the likelihood map that is presented in **Figure 6.5c**. Positive (red) log-likelihood ratio values indicate the detected column is more consistent with the noisy data than is the presence of vacuum. Conversely, sites with negative (blue) values are less consistent with the data and may therefore be spurious additions. A spurious atomic column appears in

this denoised image at the corner site marked by the black arrow on the left side of particle. The likelihood map displays a relatively large negative value of -0.012 at this site, signaling that the atomic column is inconsistent with the noisy data and likely to be spurious.

It should be discussed that the likelihood map shows a handful of sites that correspond to real atomic columns, but which nonetheless have negative log-likelihood ratio values, including, e.g., in the bulk of the nanoparticle. First, we point out that the likelihood map does not provide an absolute validation of the structure present in the denoised image but rather offers a visualization of the statistical agreement between this structure and the noisy input. In this case, the observed image has been so degraded by shot noise (vacuum SNR = 0.67) that, inevitably, a few real atomic columns will be observed to have average noisy intensities that are more consistent with the vacuum level. The sensitivity of the log-likelihood ratio in response to the overall SNR has not been investigated and could be the subject of future work. As a second point, the appearance of real atomic columns with negative log-likelihood ratio is in some way a testament to the network's ability to infer the presence of structure in spite of a SNR so low that the data appears more consistent with vacuum. This point is explored further in Section 6.3.5. It is also worth pointing out that in a time series of images, one would be able to look at the variation in the likelihood map for different frames to facilitate a more correct interpretation.

Regardless of these nuances, some useful heuristics may still be established that allow one to use the likelihood map to quickly assess the atomic structure that appears in the denoised image. **Figure 6.5d** presents letter value or so-called boxen plots of ~65,000 log-likelihood ratio values calculated over 1,540 denoised images (5 unique noise realizations of 308 ground truth images), providing insight into how the distribution of values derived from spurious atomic columns (top) compares with that derived from real

atomic columns (bottom). A dashed vertical line is provided at 0.0 for reference. The spurious column distribution shows a slightly negative median and is clustered around 0.0 while being skewed toward negative values. The positive tail diminishes rapidly and becomes marginal for values above 0.0045. On the other hand, the real atomic column distribution has a positive median of 0.0052 and is skewed toward the right. Many values are seen exceed 0.010, which virtually never occurs for spurious atomic columns. The negative tail becomes negligible for values below -0.0060. These distributions reveal two simple guidelines: (1) sites with log-likelihood ratio values ≥ 0.0050 can be treated as real structure with a high degree of certainty, and (2) sites with log-likelihood ratios ≤ -0.0060 (e.g., the spurious column arrowed in **Figure 6.5c**) are almost certainly artificial. A site with a value in between is not as easily distinguishable but nonetheless still has a quantitative statistical measure of agreement given by its log-likelihood ratio. In practice, additional information (e.g., knowledge of the material) can also be leveraged to support an assessment of the predicted structure.

6.3.5. Performance on experimental data and visualizing the network's effective filter

The trained network was applied to the experimentally acquired TEM image dataset. Several other denoising techniques were applied to the same data to establish a baseline for evaluating the performance of the proposed network. **Figure 6.6** presents a summary of the results. A single 25 ms exposure *in situ* TEM image of a CeO_2-supported Pt nanoparticle in 5 mTorr N_2 gas is shown in **Figure 6.6a**. A zoom-in image is shown from the region marked by the red box at the Pt surface, to demonstrate the severity of the shot noise and the lack of clarity about the underlying image signal. Each baseline method was applied to the same noisy image, producing the denoised outputs shown from **Figure 6.6b** to **Figure 6.6g**. Details on all the methods are given in Section 2.4.3.1. The denoised

image produced by the proposed network is shown in **Figure 6.6h**. Although a clean reference image is not available experimentally, a relatively high SNR image has been prepared by time-averaging the experimental data over 40 frames for 1.0 sec total, as shown in **Figure 6.6i**. Finally, **Figure 6.6h** displays the likelihood map for interpreting the structure that appears in the proposed network's output.

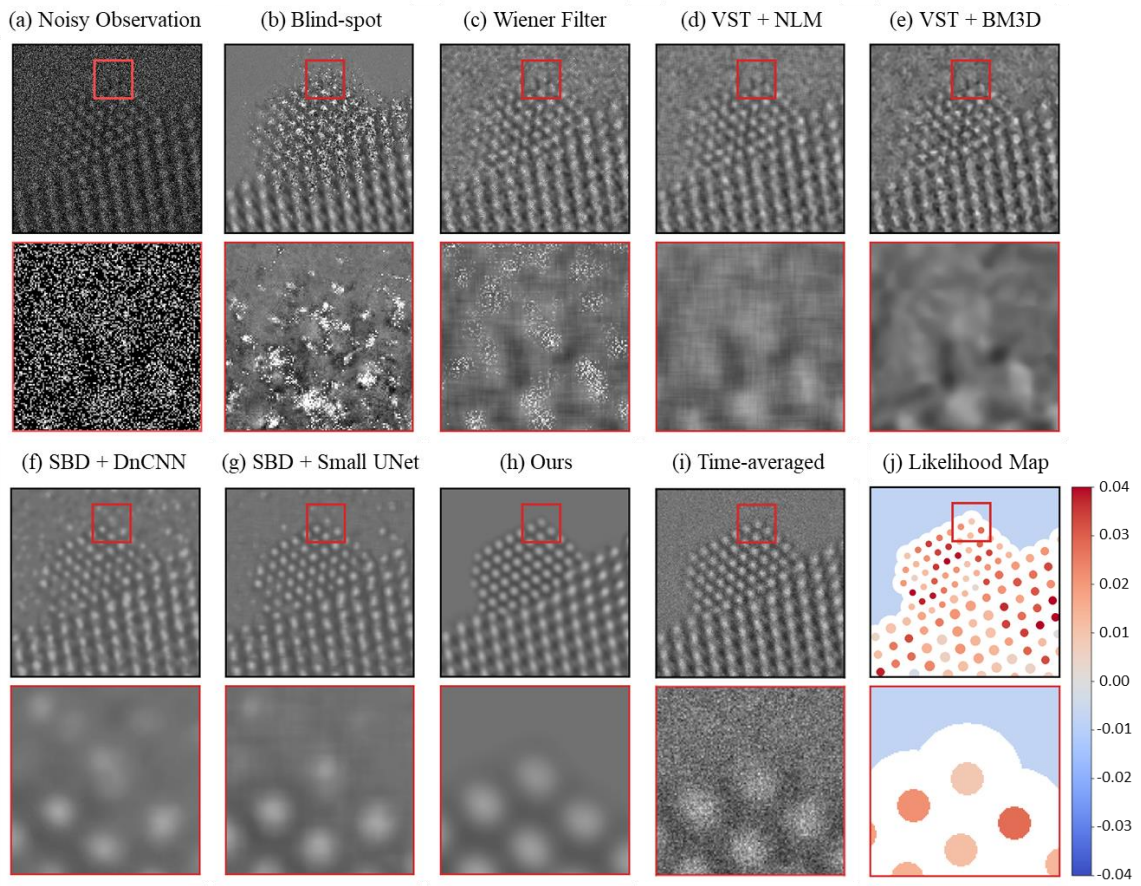

Figure 6.6. Evaluating the performance of the proposed network on experimental 25 ms exposure *in situ* TEM images, in comparison to current state-of-the-art methodologies. A raw 25 ms frame of a CeO_2-supported Pt nanoparticle in 5 mTorr N_2 gas is shown in **(a)** along with a zoom-in image from the region marked by the red box. Denoised estimates of the same raw frame from the baseline methods are presented in **(b)** through **(g)**, while **(h)** displays the denoised estimate from the proposed network. Part **(i)** presents a time-average over 40 raw frames, or 1.0 sec total, to serve as a relatively high SNR reference image. Finally, part **(j)** shows the likelihood map of the proposed network's output to quantify the agreement with the noisy observation.

As seen in comparing the time-averaged image against the denoised estimates generated by the various methods, the proposed network architecture produces denoised images of superior quality. In particular, the proposed network is the only method that recovers a physically sensible atomic structure at the Pt surface, with the denoised zoom-in of **Figure 6.6h** strongly resembling the time-averaged zoom-in of **Figure 6.6i**. The DnCNN (**Figure 6.6f**) and small UNet (**Figure 6.6g**) denoising networks achieve the next-best overall performance. However, the images output by these architectures tend to exhibit unphysical structures characterized by, e.g., warped contrast around corner sites, not to mention that they also show unusual atomic column-like intensity in the vacuum and at the Pt surface, likely due to localized noise fluctuations. The remaining methods yield images of relatively similar inferior quality. A remarkable exception worth mentioning is the blind-spot network (**Figure 6.6b**). This self-supervised deep learning method, which was trained only on the raw experimental data and not on the simulations, outputs an image with arguably worse noise content in the image center around the Pt nanoparticle and Pt/CeO_2 interface; interestingly, in other regions (e.g., the vacuum and the CeO_2 bulk), the denoised estimate matches the time-averaged image contrast with exceptional similarity. We are presently investigating alternative blind-spot architectures for improved performance (Sheth et al., 2020), but this is beyond the scope of the current thesis. Another series of denoised images generated from another experimental frame is shown in Appendix **Figure E.15**.

The denoising mechanisms used by CNNs are often treated as a "black box", with little offered to interpret how they work. Recent work shows that computing the gradient of the network's output with respect to its input at a specific pixel of interest can offer an interpretable visualization of the network's equivalent linear filter at that pixel (Mohan, Kadkhodaie, et al., 2020). In this section, we investigate the filtering strategies used by the

network to denoise real data and show how they adapt to the presence of atomic-level defects at the catalyst surface.

Consider the denoised experimental frame shown in **Figure 6.7a**. Three pixels in the image have been marked by (small) red squares. One pixel is in the vacuum, one is in an atomic column at the Pt nanoparticle surface, and the last is in an atomic column in the CeO_2 bulk. The effective receptive field around each pixel is marked by a larger red box; these regions are plotted in **Figure 6.7(b1)**, **Figure 6.7(c1)**, and **Figure 6.7(d1)**, respectively, with the pixels of interest again marked by a small red square. It is noted that while the true receptive fields around each pixel are about 800 x 800 pixels in size, most of the information in the gradient is concentrated around the central 300 x 300 pixels, so for plotting purposes we choose to focus on this region. We wish to investigate the mechanism by which the network denoises these particular pixels. **Figure 6.7(b2)**, **Figure 6.7(c2)**, and **Figure 6.7(d2)** display the field of view around each pixel in the noisy experimental data. These windowed images are effectively what the network senses when denoising each pixel. In **Figure 6.7(b3)**, **Figure 6.7(c3)**, and **Figure 6.7(d3)** the Jacobian of the network at each pixel is plotted, which gives a local linear approximation of the function used by the network to map the noisy input to a denoised output. We call this visualization the network's effective filter, as it shows which regions of the input have the most impact on the denoised estimate.

Interestingly, the effective filter shows considerable variation at different locations in the image. For the pixel in the vacuum, **Figure 6.7(b3)** shows the gradient at this location is mostly uniform with a magnitude close to 0.0. The largely uniform gradient suggests the network senses a lack of structure in the vacuum and has incorporated this information into its denoising strategy. Compare this with the gradient plotted in **Figure 6.7(d3)** for the pixel on an atomic column in the CeO_2 bulk. Here, the gradient shows a

clear periodicity, with a symmetric pattern that mirrors the local structure of the bulk material. The symmetry reveals that the network has learned to recognize an uninterrupted continuation of structure at this location. Note that the magnitude of the gradient in the region around the central pixel is comparable to that of the surrounding atomic column-like regions. The mostly equal weighting of local and non-local periodic information implies that the network considers the central atomic column to be similar to those surrounding it.

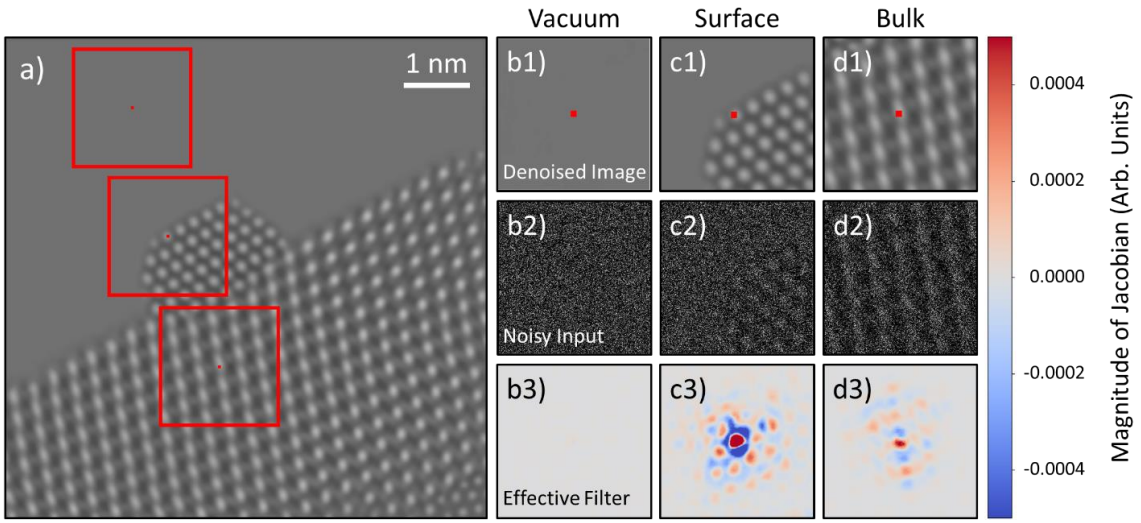

Figure 6.7. A denoised experimental image is shown in **(a)**. Three regions of the image in the vacuum, catalyst surface, and bulk have been highlighted by red boxes and are depicted in **(b1)**, **(c1)**, and **(d1)**, respectively. The central pixel in each windowed region is marked with a red box. The noisy input within the network's receptive field around each pixel is displayed in **(b2)**, **(c2)**, and **(d2)**. In **(b3)**, **(c3)**, and **(d3)** the Jacobian of the network at each pixel is plotted, which provides an interpretable visualization of the regions of the noisy input that have the most impact on the denoised estimate.

The network's denoising strategy adapts in response to non-periodic structural features at the Pt nanoparticle surface. As seen in **Figure 6.7(c3)**, at the surface the network gives substantially more weight to information that is in the immediate proximity of the pixel to be denoised. Strongly weighting the intensity within an atomic column-sized

region may be what enables the network to recover the non-periodic atomic features at the catalyst surface. In unfavorable cases, the same strategy could lead to artifacts if the noisy input contains a randomly bright clustering of intensity that resembles an atomic column. As in the CeO_2 bulk, periodicity is seen in the gradient at the Pt surface, although now the separation distance between the atomic column-like regions has changed to match the periodicity of the projected Pt lattice. Notably, the spatial distribution of the filter is also now less symmetric, with the magnitude of the gradient diminishing to zero more rapidly in the regions that contain vacuum. Hence, the asymmetry reflects the termination of the nanoparticle structure and suggests that the network has learned to identify the presence of the catalyst surface.

6.4. Summary

A supervised deep convolutional neural network has been developed to denoise atomic-resolution TEM images of nanoparticles acquired during applications wherein the image signal is severely limited by Poisson shot noise. Multislice image simulations were leveraged to generate a large dataset images for training and testing the network. The proposed network outperforms existing methods, including other convolutional neural networks, by a PSNR of 12.0 dB, achieving a PSNR of about 43 dB on a test set of simulated images (the typical starting PSNR of the data explored in this work is only 3 dB). We show that the network is generally robust to ± 5 nm variations in defocus, although we suggest training the network using images at a defocus similar to the data that is to be denoised. The network's ability to correctly predict the atomic-scale structure of the nanoparticle surface was assessed by comparing the atomic columns originally present in clean simulations against those that appear in denoised images. We have also developed an approach based on the log-likelihood ratio test that provides a quantitative measure of the agreement between the noisy observation and the atomic-level structure present in the

denoised image. The proposed assessment method requires only the network-denoised image and the noisy input and is therefore extensible to real experimental data, where no ground truth reference images exist. The network was applied to an experimentally acquired TEM image dataset of a CeO_2-supported Pt nanoparticle. We have conducted a gradient-based analysis to investigate the mechanisms used by the network to denoise experimental images. Here, this shows the network both (a) exploits information on the surrounding structure and (b) adapts its filtering approach when it encounters non-periodic terminations or atomic-level defects at the nanoparticle surface. The approaches described here may be applicable to a wide range of atomic resolution imaging applications that are characterized by ultra-low SNR, including the investigation of dynamic processes with time-resolved *in situ* microscopy or the study of beam sensitive systems.

7. Conclusions and Future Work

Conclusions

In this thesis, multiple computational and experimental methodologies were developed and applied to visualize the structural behavior occurring at the surfaces and interfaces of CeO_2-supported Pt catalysts under reaction conditions (*in situ*) or during catalysis (*operando*). The overarching objectives of this work were to establish quantitative *operando* TEM methodologies and to obtain fundamental, atomic-level information on the complex structural behavior that regulates oxygen transfer reactions over CeO_2-supported Pt catalysts, which are of critical importance to clean energy conversion and environmental remediation applications.

To accomplish the first objective, a detailed finite element model of the *operando* ETEM reactor was developed, allowing the gas and temperature profiles to be determined during experimental conditions of catalysis. Under typical *operando* TEM conditions, mass transport is dominated by diffusion, while heat transfer is dominated by conduction. For reactor temperatures above 400 °C, radiation becomes more important and eventually dominates heat transfer. The model was benchmarked against experimental *operando* ETEM data obtained from a Ru/SiO_2 catalyst performing CO oxidation. It was shown that the simulated composition of catalytically-produced CO_2 agrees well with experimental measurements taken under nominally identical conditions across a range of temperatures spanning 25 – 350 °C. In general, the simulations show that the temperature and gas are relatively homogeneous within the hot zone of the holder where the catalyst is located. The uniformity of gas and temperature across the catalyst and TEM sample indicates that the system behavior around the catalyst approximates that of a continuously stirred tank reactor (CSTR). The results show that EELS can be used to estimate the catalytic conversion of reactants in the ETEM cell to within 10%. Most importantly, the model

provides a foundation for chemical kinetic analysis, allowing the conversion measured with EELS to be related to the reaction rate of the catalyst that is imaged on the TEM grid. As a result, this work produced a truly *operando* TEM methodology, since the nanoparticle structure observed during an experiment can be directly linked to known local reactor conditions and quantitative chemical kinetics.

The ability to directly link atomic-level structural imaging with quantitative chemical kinetics of the same catalyst was leveraged to investigate structure-activity relationships for CO oxidation at the surfaces and interfaces of Pt/CeO_2 catalysts. Aberration-corrected *operando* TEM coupled with finite element modeling of the ETEM reactor was employed to visualize the atomic-scale dynamic structural behavior occurring at increasing rates of catalytic turnover. The results show that the activity of the catalyst correlates with dynamic structural behavior that (a) destabilizes the supported Pt particle, (b) marks an enhanced rate of oxygen vacancy creation and annihilation, and (c) leads to increased strain and reduction in the surface of the CeO_2 support. Additionally, the results implicate the interfacial Pt-O-Ce bonds anchoring the Pt to the support as being involved also in the catalytically-driven oxygen transfer process, and they suggest that molecular oxygen reduction takes place on the reduced nearby CeO_2 surface before migrating to the metal-support interfacial perimeter for reaction with CO. Overall, this study highlights the importance of characterizing the structural dynamics that take place during catalysis in order to elucidate the relationship between a catalyst's structure and its functionality.

An important result revealed during preliminary *operando* experiments was that the equilibrium shape of 1 – 2 nm Pt nanoparticles supported on CeO_2 is not well-defined in a CO oxidation atmosphere, especially at high catalytic turnover, where the larger concentration and faster cycling of oxygen vacancies is thought to contribute to the destabilization of the supported Pt nanoparticle. To further investigate this structural

meta-stability (i.e., fluxionality), time-resolved *in situ* AC-ETEM was employed to visualize the catalyst's dynamical behavior with high spatiotemporal resolution. In an inert N_2 atmosphere, the Pt nanoparticles are generally stable, exhibiting surface faceting and a morphology consistent with the equilibrium Winterbottom shape. In CO and O_2, even at room temperature, the same supported Pt nanoparticle becomes highly fluxional, undergoing continuous structural reconfigurations between meta-stable states on the time scale of ~50 ms or faster. Evidence is also seen for the emergence of multiple nanoscale crystallographic shear planes in the CeO_2 support, which indicates that a high concentration of CeO_2 lattice oxygen vacancies are present. CeO_2-supported Pt particles observed at 200 °C in an atmosphere of pure CO show similar qualitative behavior to those observed at room temperature in CO and O_2, which suggests that in this case the CO–Pt/CeO_2 gas-solid interactions are the primary driving force for the observed fluxional behavior. Interestingly, upon introduction of water, the same particles exhibit a much higher degree of stability and ordering, evidenced by the appearance of well-defined surface faceting and a shape that is consistent with the equilibrium Winterbottom shape. Overall, the results of this work provide insight into the atomic-level dynamic structural reconfigurations that can occur in reducible oxide-supported metal nanoparticle catalysts under conditions relevant to the CO oxidation and WGS reactions.

Acquiring *in situ* TEM image time series with high temporal resolution produces datasets that can be severely degraded by shot noise, and consequently, ascertaining the underlying structure in the image can become a major obstacle to scientific analysis. One approach to address this issue is to develop denoising techniques that can estimate the information missing from the experimental image. To this end, in this work deep learning-based convolution neural networks for denoising ultra-low SNR images of nanoparticle surfaces were developed and critically evaluated. The network was trained and tested on

multislice image simulations before being applied to experimental data. The proposed network, which employs a large field of view encompassing 800 x 800 pixels, vastly outperforms existing methods. We show that the network is generally robust to ± 5 nm variations in defocus. An approach was developed based on the log-likelihood ratio test to quantify the agreement between the noisy observation and the atomic-level structure present in the denoised image. The method requires only the network-denoised image and the noisy input, and it is therefore extensible to real experimental data, where no ground truth reference images exist. Finally, a gradient-based analysis was performed to investigate the mechanisms used by the network to denoise experimental images. This shows the network both (a) exploits information on the surrounding structure and (b) adapts its filtering approach when it encounters non-periodic terminations or atomic-level defects at the nanoparticle surface.

Future Work

While this research program has provided valuable tools for *in situ* and *operando* investigations of high surface area supported nanoparticle catalysts, as well as specific insight into the (dynamic) structure-activity relationships underlying CeO_2-supported Pt catalysts, important questions still remain unanswered. Future areas of study could include, for example:

1. **Time-resolved observations of supported metal catalysts under *operando* conditions and correlation of fluxional behavior with activity/selectivity**

In this work, the reported *operando* experiments (Chapter 4) were performed on an aberration-corrected ETEM (AC-ETEM) equipped with a slow scan CCD camera. While this work initially informed us of the fluxional behavior that working Pt/CeO_2 catalysts can exhibit during CO oxidation, as well as to how the fluxionality impacts the activity of the catalyst, the poor time resolution available (i.e., 0.5 sec) precluded a detailed

investigation into the catalyst's dynamic structural evolution. Performing *operando* experiments on an AC-ETEM coupled to a high-speed, high-sensitivity direct electron detector would provide considerable advantages to understanding the (dynamic) structure-activity relationships regulating the chemical transformation pathways on catalyst surfaces. Time-resolved information can be particularly valuable here, as catalytically-relevant structures could be identified by mapping surface and interfacial motifs that appear in concert and by correlating the frequency of the structural dynamics with the turnover frequency of the catalyst. Additionally, employing this instrumentation would also make it more feasible to conduct experiments at lower incident electron dose rates. Potential time-resolved *operando* experiments to perform could involve different catalysts and/or different reactions than that explored here (i.e., largely Pt/CeO_2 catalysts for CO oxidation and the WGS reaction). One logical next step would include Pt/CeO_2 catalysts for the preferential oxidation of CO in a H_2 rich stream (PROX reaction), which is industrially important for purifying H_2 for use in many applications. In this case, it could be particularly interesting to compare two similar catalysts that exhibit different selectivity for CO/H_2 oxidation.

2. ***In situ* characterization of fluxional behavior exhibited by CeO_2-supported Pt particles of varying size under variable pressures of reactant gases**

The fluxional behavior exhibited by CeO_2-supported Pt nanoparticles could be better understood by investigating how the dynamic structural response is regulated by the nanoparticle size and by the ambient pressure of reactant gases. As the nanoparticle size approaches ~1 nm, the presence of edge and corner defects comes to dominate the fraction of exposed surface sites; on the other hand, for nanoparticles larger than ~7 nm, edges and corners comprise a minority of the surface sites available as terrace sites become dominant. The availability of different surface adsorption sites may impact the fluxional

behavior of the particle. Additionally, the adsorbate coverage on the surface is expected to change with pressure, which may also significantly influence the dynamic response of the particle. Controlled experiments to characterize the fluxionality of small (i.e., ~1 – 2 nm) and large (i.e., ~6 – 8 nm) nanoparticles under increasing pressures of reactant gas (e.g., 10^{-8}, 10^{-6}, 10^{-4}, 10^{-2}, and 1 mbar of CO) would provide valuable insight into the chemical and structural factors that impact the metastability of catalytic Pt/CeO_2 nanoparticles.

3. Estimation of fluxional structures by high-throughput image simulations coupled to first-principles energetics calculations and machine learning

An aspirational goal in employing time-resolved *in situ* TEM to characterize fluxional behavior would be to describe the 3D atomic-level structural evolution of the catalyst as a function of time. One approach for doing so could involve a combination of high-throughput image simulations coupled to first principles energetics calculations (e.g., *ab initio* molecular dynamics) and deep convolutional neural networks (CNNs). Deep CNNs trained for so-called semantic segmentation are capable of assigning each pixel in an image to a class label, which, e.g., could be the elemental identity and occupancy of an imaged atomic column. A more sophisticated and refined class label would include the occupancy of an atomic column imaged at a specific crystallographic orientation, under a particular defocus, or in the presence of certain aberrations, for example. Applying deep CNNs trained for such a task to experimental data would thus provide a description of the identity and occupancy of the atomic columns in the experimental image and potentially information on the imaging conditions. Such information could be used to generate a 3D atomic-scale structural model, potentially automatically with the use of scripting. TEM images of these structures under different orientations, tilt, defocus, and in the presence of various aberrations can be simulated rapidly using high-throughput methods on e.g. a supercomputer.

Each image from this set of simulations could then be compared to the experimental observation using an appropriate quantitative metric. One could then investigate the structures associated with the simulations that best match the experimental observation. In principle, such a process could be carried out for each frame of a time-resolved series of images. Energetics calculations could be employed both to (a) relax the structures prior to simulation and/or (b) determine the relative energy associated with the candidate structures, which might be useful for filtering out structures unlikely to exist from those that are more likely to exist. While it would require considerable effort involving collaborations among many different experts, this approach could offer an enormous impact to heterogenous catalysis research by providing a transformational approach to describing the atomic-scale dynamic structural evolution of supported nanoparticle catalysts.

REFERENCES

AICHE (2005). *DIPPR Project 801, full version: evaluated standard thermophysical property values*. Provo: BYU DIPPR, Thermophysical Properties Laboratory.

AJAYAN, P. M. & MARKS, L. D. (1988). Quasimelting and phases of small particles. *Physical Review Letters* **60**, 585–587.

ANDERSON, J. S. & HYDE, B. G. (1967). On the possible role of dislocations in generating ordered and disordered shear structures. *Journal of Physics and Chemistry of Solids* **28**, 1393–1408.

ANEGGI, E., BOARO, M., COLUSSI, S., DE LEITENBURG, C. & TROVARELLI, A. (2016). Ceria-Based Materials in Catalysis: Historical Perspective and Future Trends. *Handbook on the Physics and Chemistry of Rare Earths* **50**, 209–242.

ASSMANN, J., NARKHEDE, V., KHODEIR, L., LÖFFLER, E., HINRICHSEN, O., BIRKNER, A., OVER, H. & MUHLER, M. (2004). On the Nature of the Active State of Supported Ruthenium Catalysts Used for the Oxidation of Carbon Monoxide: Steady-State and Transient Kinetics Combined with in Situ Infrared Spectroscopy †. *The Journal of Physical Chemistry B* **108**, 14634–14642.

AVANESIAN, T., DAI, S., KALE, M. J., GRAHAM, G. W., PAN, X. & CHRISTOPHER, P. (2017). Quantitative and Atomic-Scale View of CO-Induced Pt Nanoparticle Surface Reconstruction at Saturation Coverage via DFT Calculations Coupled with *in Situ* TEM and IR. *Journal of the American Chemical Society* **139**, 4551–4558.

BALAJI GOPAL, C., GARCÍA-MELCHOR, M., LEE, S. C., SHI, Y., SHAVORSKIY, A., MONTI, M., GUAN, Z., SINCLAIR, R., BLUHM, H., VOJVODIC, A. & CHUEH, W. C. (2017). Equilibrium oxygen storage capacity of ultrathin CeO 2-δ depends non-monotonically on large biaxial strain. *Nature Communications* **8**, 15360.

BAÑARES, M. A. (2005). Operando methodology: Combination of in situ spectroscopy and simultaneous activity measurements under catalytic reaction conditions. *Catalysis Today* **100**, 71–77.

BANHART, F. (2008). *In-situ Electron Microscopy At High Resolution*. Singapore, SINGAPORE: World Scientific Publishing Company http://ebookcentral.proquest.com/lib/asulib-ebooks/detail.action?docID=1193637.

BARTHEL, J. (2018). Dr. Probe: A software for high-resolution STEM image simulation. *Ultramicroscopy* **193**, 1–11.

BASU, S., DEVI, P. S. & MAITI, H. S. (2004). Synthesis and properties of nanocrystalline ceria powders. *Journal of Materials Research* **19**, 3162–3171.

BATSON, P. E., DELLBY, N. & KRIVANEK, O. L. (2002). Sub-ångstrom resolution using aberration corrected electron optics. *Nature* **418**, 617–620.

BAXTER, E. T., HA, M.-A., CASS, A. C., ALEXANDROVA, A. N. & ANDERSON, S. L. (2017). Ethylene Dehydrogenation on Pt4,7,8 Clusters on Al2O3: Strong Cluster Size Dependence Linked to Preferred Catalyst Morphologies. *ACS Catalysis* **7**, 3322–3335.

BELKACEM, A., FRIEND, C., ZHU, Y., BARE, S. R., GLOTZER, S., PETFORD-LONG, A., ROSS, F. M., SCHLÖGL, R., SETHIAN, J., STACH, E. A., CROZIER, P., JENKS, C., NUZZO, R., OGILVIE, J., FENTER, P., HESS, W., NEATON, J., DE LA CRUZ, M. O., SETTERSTEN, T., GARRETT, B., HORTON, L., KERCH, H., KRAUSE, J., LEE, P., MARACAS, G., MCLEAN, G., MIRANDA, R., HAINES, J., RUNKLES, K., SUMMERS, M., HADLEY, C. & EDGAR, J. (2016). *Basic Research Needs for Innovation and Discovery of Transformative Experimental Tools*. http://www.osti.gov/servlets/purl/1616508/ (Accessed May 9, 2021).

BELL, A. T. (2003). The Impact of Nanoscience on Heterogeneous Catalysis. *Science* **299**, 1688–1691.

BELTHANGADY, C. & ROYER, L. A. (2019). Applications, promises, and pitfalls of deep learning for fluorescence image reconstruction. *Nature Methods* **16**, 1215–1225.

BEPLER, T., KELLEY, K., NOBLE, A. J. & BERGER, B. (2020). Topaz-Denoise: general deep denoising models for cryoEM and cryoET. *Nature Communications* **11**, 5208.

BERNAL, S., BAKER, R. T., BURROWS, A., CALVINO, J. J., KIELY, C. J., LOPEZ-CARTES, C., PEREZ-OMIL, J. A. & RODRIGUEZ-IZQUIERDO, J. M. (2000). Structure of highly dispersed metals and oxides: exploring the capabilities of high-resolution electron microscopy. *Surf. Interface Anal.* 11.

BERNAL, S., BOTANA, F. J., CALVINO, J. J., CIFREDO, G. A., PE´REZ-OMIL, J. A. & PINTADO, J. M. (1995). HREM study of the behaviour of a Rh/CeO2 catalyst under high temperature reducing and oxidizing conditions. *Catalysis Today* **23**, 219–250.

BERNAL, S., BOTANA, F. J., CALVINO, J. J., LÓPEZ-CARTES, C., PÉREZ-OMIL, J. A. & RODRÍGUEZ-IZQUIERDO, J. M. (1998). The interpretation of HREM images of supported metal catalysts using image simulation: profile view images. *Ultramicroscopy* **72**, 135–164.

BERNAL, S., CALVINO, J. J., GATICA, J. M., LARESE, C., LÓPEZ-CARTES, C. & PÉREZ-OMIL, J. A. (1997). Nanostructural evolution of a Pt/CeO2 catalyst reduced at increasing temperatures (473-1223 K): A HREM study. *Journal of Catalysis* **169**, 510–515.

BEUSCH, H., FIEGUTH, P. & WICKE, E. (1972). Thermisch und kinetisch verursachte Instabilitäten im Reaktionsverhalten einzelner Katalysatorkörner. *Chemie Ingenieur Technik* **44**, 445–451.

BIRD, R. B. & KLINGENBERG, D. J. (2013). Multicomponent diffusion—A brief review. *Advances in Water Resources* **62**, 238–242.

BIRD, R. B., STEWART, W. E. & LIGHTFOOT, E. N. (2006). *Transport Phenomena*. 2nd ed. John Wiley & Sons http://doi.wiley.com/10.1002/aic.690070245.

BLENNOW, P., CHEN, W., LUNDBERG, M. & MENON, M. (2009). Characterization of Ce0.9Gd0.1O1.95 powders synthesized by spray drying. *Ceramics International* **35**, 2959–2963.

BLOCK, C. (2021). 'TEM Image Simulations of Structural Dynamics on CeO2-supported Pt Catalysts'. Text, Arizona State University.

BOYES, E. D. & GAI, P. L. (1997). Environmental high resolution electron microscopy and applications to chemical science. *Ultramicroscopy* **67**, 219–232.

BRYDSON, R. (2020). *Electron Energy Loss Spectroscopy*. CRC Press https://books.google.com/books?id=umIPEAAAQBAJ.

BUADES, A., COLL, B. & MOREL, J.- (2005). A non-local algorithm for image denoising. In *2005 IEEE Computer Society Conference on Computer Vision and Pattern Recognition (CVPR'05)*vol. 2, pp. 60–65 vol. 2.

BUCHHOLZ, T., JORDAN, M., PIGINO, G. & JUG, F. (2019). Cryo-CARE: Content-Aware Image Restoration for Cryo-Transmission Electron Microscopy Data. In *2019 IEEE 16th International Symposium on Biomedical Imaging (ISBI 2019)*, pp. 502–506.

BUNLUESIN, T., CORDATOS, H. & GORTE, R. J. (1995). Study of CO oxidation kinetics on Rh/Ceria. *Journal of Catalysis* **157**, 222–226.

C. C. MINTER (1963). *Effect of pressure on the thermal conductivity of a gas*. U. S. Naval Research Laboratory.

CARGNELLO, M., DOAN-NGUYEN, V. V. T., GORDON, T. R., DIAZ, R. E., STACH, E. A., GORTE, R. J., FORNASIERO, P. & MURRAY, C. B. (2013). Control of Metal Nanocrystal Size Reveals Metal-Support Interface Role for Ceria Catalysts. *Science* **341**, 771–773.

CHAUDHARY, N., SAVARI, S. A. & YEDDULAPALLI, S. S. (2019). Line roughness estimation and Poisson denoising in scanning electron microscope images using deep learning. *Journal of Micro/Nanolithography, MEMS, and MOEMS* **18**, 024001.

CHEE, S. W., ARCE-RAMOS, J. M., LI, W., GENEST, A. & MIRSAIDOV, U. (2020). Structural changes in noble metal nanoparticles during CO oxidation and their impact on catalyst activity. *Nature Communications* **11**.

CHEE, S. W., LUNKENBEIN, T., SCHLÖGL, R. & CUENYA, B. R. (2021). In situ and operando electron microscopy in heterogeneous catalysis—insights into multi-scale chemical dynamics. *Journal of Physics: Condensed Matter* **33**, 153001.

CHEN, W., LI, F. & YU, J. (2006). Combustion synthesis and characterization of nanocrystalline CeO2-based powders via ethylene glycol–nitrate process. *Materials Letters* **60**, 57–62.

CHENNA, S., BANERJEE, R. & CROZIER, P. A. (2011). Atomic-Scale Observation of the Ni Activation Process for Partial Oxidation of Methane Using In Situ Environmental TEM. *ChemCatChem* **3**, 1051–1059.

CHENNA, S. & CROZIER, P. A. (2012). Operando Transmission Electron Microscopy: A Technique for Detection of Catalysis Using Electron Energy-Loss Spectroscopy in the Transmission Electron Microscope. *ACS Catalysis* **2**, 2395–2402.

CHEULA, R., MAESTRI, M. & MPOURMPAKIS, G. (2020). Modeling Morphology and Catalytic Activity of Nanoparticle Ensembles Under Reaction Conditions. *ACS Catalysis* **10**, 6149–6158.

CISTON, J., JOHNSON, I. J., DRANEY, B. R., ERCIUS, P., FONG, E., GOLDSCHMIDT, A., JOSEPH, J. M., LEE, J. R., MUELLER, A., OPHUS, C., SELVARAJAN, A., SKINNER, D. E., STEZELBERGER, T., TINDALL, C. S., MINOR, A. M. & DENES, P. (2019). The 4D Camera: Very High Speed Electron Counting for 4D-STEM. *Microscopy and Microanalysis* **25**, 1930–1931.

COLLIEX, C. (2019). Chapter Three - Electron energy loss spectroscopy in the electron microscope. In *Advances in Imaging and Electron Physics*vol. 211, *Advances in Imaging and Electron Physics*, Hawkes, P. W. & Hÿtch, M. (Eds.), pp. 187–304. Elsevier https://www.sciencedirect.com/science/article/pii/S1076567019300278 (Accessed June 8, 2021).

COQ, B. & FIGUERAS, F. (1998). Structure–activity relationships in catalysis by metals: some aspects of particle size, bimetallic and supports effects. *Coordination Chemistry Reviews* **178–180**, 1753–1783.

COTTON, F. A. (1975). Fluxionality in organometallics and metal carbonyls. *Journal of Organometallic Chemistry* **100**, 29–41.

COWLEY, J. M. (1995). *Diffraction physics*. 3. rev. ed., 1. impr. Amsterdam: Elsevier.

COWLEY, J. M. & MOODIE, A. F. (1957). The scattering of electrons by atoms and crystals. I. A new theoretical approach. *Acta Crystallographica* **10**, 609–619.

CRACIUN, R., SHERECK, B. & GORTE, R. J. (1998). Kinetic studies of methane steam reforming on ceria-supported Pd. *Catalysis Letters* **51**, 149–153.

CREEMER, J. F., HELVEG, S., HOVELING, G. H., ULLMANN, S., MOLENBROEK, A. M., SARRO, P. M. & ZANDBERGEN, H. W. (2008). Atomic-scale electron microscopy at ambient pressure. *Ultramicroscopy* **108**, 993–998.

CREEMER, J. F., SANTAGATA, F., MORANA, B., MELE, L., ALAN, T., IERVOLINO, E., PANDRAUD, G. & SARRO, P. M. (2011). An all-in-one nanoreactor for high-resolution microscopy on nanomaterials at high pressures. In *2011 IEEE 24th International Conference on Micro Electro Mechanical Systems*, pp. 1103–1106.

CROZIER, P. A. & CHENNA, S. (2011). In situ analysis of gas composition by electron energy-loss spectroscopy for environmental transmission electron microscopy. *Ultramicroscopy* **111**, 177–185.

CROZIER, P. A. & HANSEN, T. W. (2015). in situ and operando transmission electron microscopy of catalytic materials. *MRS Bulletin* **40**, 38–45.

CROZIER, P. A., LAWRENCE, E. L., VINCENT, J. L. & LEVIN, B. D. A. (2019). Dynamic Restructuring during Processing: Approaches to Higher Temporal Resolution. *Microscopy and Microanalysis* **25**, 1464–1465.

DAI, S., YOU, Y., ZHANG, S., CAI, W., XU, M., XIE, L., WU, R., GRAHAM, G. W. & PAN, X. (2017). In situ atomic-scale observation of oxygen-driven core-shell formation in Pt3Co nanoparticles. *Nature Communications* **8**, 204.

DE NEVERS, N. (2005). *Fluid mechanics for chemical engineers*. 3rd ed. Boston: McGraw-Hill Higher Education.

DE RUIJTER, W. J. (1995). Imaging properties and applications of slow-scan charge-coupled device cameras suitable for electron microscopy. *Micron* **26**, 247–275.

DEMOULIN, O., NAVEZ, M., M. GAIGNEAUX, E., RUIZ, P., MAMEDE, A.-S., GRANGER, P. & PAYEN, E. (2003). Operando resonance Raman spectroscopic characterisation of the oxidation state of palladium in Pd/γ-Al 2 O 3 catalysts during the combustion of methane. *Physical Chemistry Chemical Physics* **5**, 4394–4401.

DETTMER-WILDE, K. & ENGEWALD, W. (2014). *Practical Gas Chromatography*. 1st ed. Berlin, Heidelberg: Springer.

VAN DILLEN, A. J., TERÖRDE, R. J. A. M., LENSVELD, D. J., GEUS, J. W. & DE JONG, K. P. (2003). Synthesis of supported catalysts by impregnation and drying using aqueous chelated metal complexes. *Journal of Catalysis* **216**, 257–264.

DING, K., GULEC, A., JOHNSON, A. M., SCHWEITZER, N. M., STUCKY, G. D., MARKS, L. D. & STAIR, P. C. (2015). Identification of active sites in CO oxidation and water-gas shift over supported Pt catalysts. *Science* **350**, 189–192.

DIRECT ELECTRON (2021). Direct Detection Cameras. *Direct Electron*. https://www.directelectron.com/de-series/ (Accessed April 18, 2021).

DOORNKAMP, C. & PONEC, V. (2000). The universal character of the Mars and Van Krevelen mechanism. *Journal of Molecular Catalysis A: Chemical* **162**, 19–32.

DUPRAT, F. (2002). Light-off curve of catalytic reaction and kinetics. *Chemical Engineering Science* 11.

EDE, J. M. (2020). Review: Deep Learning in Electron Microscopy. *Machine Learning: Science and Technology*. http://iopscience.iop.org/article/10.1088/2632-2153/abd614 (Accessed January 14, 2021).

EDE, J. M. & BEANLAND, R. (2019). Improving electron micrograph signal-to-noise with an atrous convolutional encoder-decoder. *Ultramicroscopy* **202**, 18–25.

EGERTON, R. (2011). *Electron energy-loss spectroscopy in the electron microscope*. Third. Springer.

EGERTON, R. F. (2005). *Physical Principles of Electron Microscopy*. Springer.

EGERTON, R. F. (2013). Beam-Induced Motion of Adatoms in the Transmission Electron Microscope. *Microscopy and Microanalysis* **19**, 479–486.

——— (2019). Radiation damage to organic and inorganic specimens in the TEM. *Micron* **119**, 72–87.

EGERTON, R. F., LI, P. & MALAC, M. (2004). Radiation damage in the TEM and SEM. *Micron* **35**, 399–409.

ELECTRON MICROSCOPY SCIENCES (2021). EMS-Core Sampling Tool. https://www.emsdiasum.com/microscopy/products/preparation/punch.aspx (Accessed April 21, 2021).

ELSEN, A., JUNG, U., VILA, F., LI, Y., SAFONOVA, O. V., THOMAS, R., TROMP, M., REHR, J. J., NUZZO, R. G. & FRENKEL, A. I. (2015). Intracluster Atomic and Electronic Structural Heterogeneities in Supported Nanoscale Metal Catalysts. *The Journal of Physical Chemistry C* **119**, 25615–25627.

ERTL, G. (2001). Heterogeneous catalysis on the atomic scale. *The Chemical Record* **1**, 33–45.

——— (2007). Reactions at Surfaces: From Atoms to Complexity.

ERTL, G., KNZINGER, H. & WEITKAMP, J. (eds.) (1997). *Handbook of Heterogeneous Catalysis*. Weinheim, Germany: Wiley-VCH Verlag GmbH http://doi.wiley.com/10.1002/9783527619474.fmatter (Accessed August 31, 2020).

FAJRINA, N. & TAHIR, M. (2019). A critical review in strategies to improve photocatalytic water splitting towards hydrogen production. *International Journal of Hydrogen Energy* **44**, 540–577.

FARIA, M. V., VARELLA, R. A., DUARTE, G. O., FARIAS, T. L. & BAPTISTA, P. C. (2018). Engine cold start analysis using naturalistic driving data: City level impacts on local pollutants emissions and energy consumption. *Science of the Total Environment* **630**, 544–559.

FARUQI, A. R. & MCMULLAN, G. (2018). Direct imaging detectors for electron microscopy. *Nuclear Instruments and Methods in Physics Research Section A: Accelerators, Spectrometers, Detectors and Associated Equipment* **878**, 180–190.

FOGLER, H. (2017). *Essentials of Chemical Reaction Engineering, 2nd Edition*. 1st edition. Pearson.

FRIEND, C. M. & XU, B. (2017). Heterogeneous Catalysis: A Central Science for a Sustainable Future. *Accounts of Chemical Research* **50**, 517–521.

FULTZ, B. & HOWE, J. M. (2007). *Transmission Electron Microscopy and Diffractometry of Materials*. Third. http://resolver.caltech.edu/CaltechAUTHORS:20121025-210157406.

GAI, P. L. (1997). *In-situ microscopy in materials research : leading international research in electron and scanning probe microscopies*. Boston: Kluwer Academic Publishers.

GAI, P. L. & BOYES, E. D. (2003). *Electron Microscopy in Heterogeneous Catalysis*. CRC Press.

GANDHI, H. S., GRAHAM, G. W. & MCCABE, R. W. (2003). Automotive exhaust catalysis. *Journal of Catalysis* **216**, 433–442.

GÄNZLER, A. M., CASAPU, M., MAURER, F., STÖRMER, H., GERTHSEN, D., FERRÉ, G., VERNOUX, P., BORNMANN, B., FRAHM, R., MURZIN, V., NACHTEGAAL, M., VOTSMEIER, M. & GRUNWALDT, J.-D. (2018). Tuning the Pt/CeO2 Interface by in Situ Variation of the Pt Particle Size. *ACS Catalysis* **8**, 4800–4811.

GÄNZLER, A. M., CASAPU, M., VERNOUX, P., LORIDANT, S., CADETE SANTOS AIRES, F. J., EPICIER, T., BETZ, B., HOYER, R. & GRUNWALDT, J. D. (2017). Tuning the Structure of Platinum Particles on Ceria In Situ for Enhancing the Catalytic Performance of Exhaust Gas Catalysts. *Angewandte Chemie - International Edition* **56**, 13078–13082.

GIANNATOU, E., PAPAVIEROS, G., CONSTANTOUDIS, V., PAPAGEORGIOU, H. & GOGOLIDES, E. (2019). Deep learning denoising of SEM images towards noise-reduced LER measurements. *Microelectronic Engineering* **216**, 111051.

GOODFELLOW, I., BENGIO, Y. & COURVILLE, A. (2016). *Deep Learning*. MIT Press.

GORTE, R. J. (2010). Ceria in catalysis: From automotive applications to the water-gas shift reaction. *AIChE Journal* **56**, 1126–35.

GRAHAM, R. L. (1972). An efficient algorith for determining the convex hull of a finite planar set. *Information Processing Letters* **1**, 132–133.

GRAND VIEW RESEARCH (2019). *Catalyst Market Size, Share, & Trends: Industry Growth Report 2019-2025*. San Francisco, California, United States.

GUERRERO-PÉREZ, M. O. & BAÑARES, M. A. (2006). From conventional in situ to operando studies in Raman spectroscopy. *Catalysis Today* **113**, 48–57.

HAIDER, M., ROSE, H., UHLEMANN, S., SCHWAN, E., KABIUS, B. & URBAN, K. (1998). A spherical-aberration-corrected 200kV transmission electron microscope. *Ultramicroscopy* **75**, 53–60.

HÄKKINEN, H., ABBET, S., SANCHEZ, A., HEIZ, U. & LANDMAN, U. (2003). Structural, Electronic, and Impurity-Doping Effects in Nanoscale Chemistry: Supported Gold Nanoclusters. *Angewandte Chemie International Edition* **42**, 1297–1300.

HAN, J., CHEN, D. & ZHU, J. (2019). Isotopic Oxygen Exchange between CeO 2 and O 2 : A Heteroexchange Mechanism. *ChemistrySelect* **4**, 13280–13283.

HANSEN, P. L., WAGNER, J. B., HELVEG, S., ROSTRUP-NIELSEN, J. R., CLAUSEN, B. S. & TOPSØE, H. (2002). Atom-resolved imaging of dynamic shape changes in supported copper nanocrystals. *Science* **295**, 2053–2055.

HANSEN, T. W. & WAGNER, J. B. (2016). *Controlled Atmosphere Transmission Electron Microscopy: Principles and practice*. 1st ed. Springer International Publishing.

HATANAKA, M., TAKAHASHI, N., TANABE, T., NAGAI, Y., DOHMAE, K., AOKI, Y., YOSHIDA, T. & SHINJOH, H. (2010). Ideal Pt loading for a Pt/CeO2-based catalyst stabilized by a Pt-O-Ce bond. *Applied Catalysis B: Environmental* **99**, 336–342.

HE, B., ZHANG, Y., LIU, X. & CHEN, L. (2020). In-situ Transmission Electron Microscope Techniques for Heterogeneous Catalysis. *ChemCatChem* **12**, 1853–1872.

HECK, R. M. & FARRAUTO, R. J. (2001). Automobile exhaust catalysts. *Applied Catalysis A: General* **221**, 443–457.

HETHERINGTON, C. (2004). Aberration correction for TEM. *Materials Today* **7**, 50–55.

HOBBS, L. W. (1984). Radiation Effects in Analysis by TEM. In *Quantitative Electron Microscopy, Proceedings of the Twenty Fifth Scottish Universities Summer School in Physics*. Edinburgh: SUSSP Publications.

HONKALA, K., HELLMAN, A., REMEDIAKIS, I. N., LOGADOTTIR, A., CARLSSON, A., DAHL, S., CHRISTENSEN, C. H. & NØRSKOV, J. K. (2005). Ammonia Synthesis from First-Principles Calculations. *Science* **307**, 555–558.

HORCH, S., LORENSEN, H. T., HELVEG, S., LÆGSGAARD, E., STENSGAARD, I., JACOBSEN, K. W., NØRSKOV, J. K. & BESENBACHER, F. (1999). Enhancement of surface self-diffusion of platinum atoms by adsorbed hydrogen. *Nature* **398**, 134–136.

HSIEH, C.-T., GU, J.-L., TZOU, D.-Y., CHU, Y.-C. & CHEN, Y.-C. (2013). Microwave deposition of Pt catalysts on carbon nanotubes with different oxidation levels for formic acid oxidation. *International Journal of Hydrogen Energy* **38**, 10345–10353.

HUSSEIN, L. (2012). 'Decorated Nanostructured Carbon Materials for Abiotic and Enzymatic Biofuel Cell Applications'. PhD, Universität Freiburg.

IMBIHL, R. & ERTL, G. (1995). Oscillatory Kinetics in Heterogeneous Catalysis. *Chemical Reviews* **95**, 697–733.

INSTRUMENTATION TOOLS (2018). Chromatograph Sample Valves. *Instrumentation Tools*. https://instrumentationtools.com/chromatograph-sample-valves/ (Accessed April 15, 2021).

IOFFE, S. & SZEGEDY, C. (2015). Batch Normalization: Accelerating Deep Network Training by Reducing Internal Covariate Shift. *arXiv:1502.03167 [cs]*. http://arxiv.org/abs/1502.03167 (Accessed January 2, 2021).

JIA, AI-PING, JIANG, S.-Y., LU, J.-Q. & LUO, M.-F. (2010). Study of Catalytic Activity at the CuO–CeO ₂ Interface for CO Oxidation. *The Journal of Physical Chemistry C* **114**, 21605–21610.

JIA, C.L., HOUBEN, L., THUST, A. & BARTHEL, J. (2010). On the benefit of the negative-spherical-aberration imaging technique for quantitative HRTEM. *Ultramicroscopy* **110**, 500–505.

JIA, C. L., LENTZEN, M. & URBAN, K. (2003). Atomic-Resolution Imaging of Oxygen in Perovskite Ceramics. *Science* **299**, 870–873.

JIA, C., LENTZEN, M. & URBAN, K. (2004). High-Resolution Transmission Electron Microscopy Using Negative Spherical Aberration. *Microscopy and Microanalysis*.

JIFARA, W., JIANG, F., RHO, S., CHENG, M. & LIU, S. (2019). Medical image denoising using convolutional neural network: a residual learning approach. *The Journal of Supercomputing* **75**, 704–718.

JINSCHEK, J. R. (2014). Advances in the environmental transmission electron microscope (ETEM) for nanoscale in situ studies of gas–solid interactions. *Chem. Commun.* **50**, 2696–2706.

JUNGJOHANN, K. & CARTER, C. B. (2016). In Situ and Operando. In *Transmission Electron Microscopy: Diffraction, Imaging, and Spectrometry*, Carter, C. B. & Williams, D. B. (Eds.), pp. 17–80. Cham: Springer International Publishing https://doi.org/10.1007/978-3-319-26651-0_2.

KAMIYA, M., SHIMADA, E., IKUMA, Y., KOMATSU, M. & HANEDA, H. (2000). Intrinsic and Extrinsic Oxygen Diffusion and Surface Exchange Reaction in Cerium Oxide. *Journal of The Electrochemical Society* **147**, 1222.

KAŠPAR, J., FORNASIERO, P. & GRAZIANI, M. (1999). Use of CeO2-based oxides in the three-way catalysis. *Catalysis Today* **50**, 285–298.

KEE, R. J., COLTRIN, M. E. & GLARBORG, P. (2003). *Chemically reacting flow: theory and practice*. Hoboken: Wiley-Interscience.

KELLOGG, G. L. & FEIBELMAN, P. J. (1990). Surface self-diffusion on Pt(001) by an atomic exchange mechanism. *Physical Review Letters* **64**, 3143–3146.

KINGMA, D. P. & BA, J. (2015). Adam: A Method for Stochastic Optimization. *ICLR*.

KIRKLAND, E. J. (2010). *Advanced Computing in Electron Microscopy*. Boston, MA: Springer US http://link.springer.com/10.1007/978-1-4419-6533-2 (Accessed August 31, 2020).

KONG, H., AKAKIN, H. C. & SARMA, S. E. (2013). A Generalized Laplacian of Gaussian Filter for Blob Detection and Its Applications. *IEEE Transactions on Cybernetics* **43**, 1719–1733.

KOPELENT, R., VAN BOKHOVEN, J. A., SZLACHETKO, J., EDEBELI, J., PAUN, C., NACHTEGAAL, M. & SAFONOVA, O. V (2015). Catalytically Active and Spectator Ce3+ in Ceria-Supported Metal Catalysts. *Angewandte Chemie - International Edition* **54**, 8728–8731.

KOZLOV, S. M. & NEYMAN, K. M. (2016). Effects of electron transfer in model catalysts composed of Pt nanoparticles on CeO2(111) surface. *Journal of Catalysis* **344**, 507–514.

KRISHNA, R. & WESSELINGH, J. A. (1997). The Maxwell-Stefan approach to mass transfer. *Chemical Engineering Science* **52**, 861–911.

KRIVANEK, O. L., DELLBY, N. & LUPINI, A. R. (1999). Towards sub-Å electron beams. *Ultramicroscopy* **78**, 1–11.

KRIVANEK, O. L. & FAN, G. Y. (1992). Application of Slow-Scan Charge-Coupled Device (CCD) Cameras to On-Line Microscope Control. *Scanning Microscopy* **1992**, 11.

KRIVANEK, O. L., LOVEJOY, T. C., DELLBY, N., AOKI, T., CARPENTER, R. W., REZ, P., SOIGNARD, E., ZHU, J., BATSON, P. E., LAGOS, M. J., EGERTON, R. F. & CROZIER, P. A. (2014). Vibrational spectroscopy in the electron microscope. *Nature* **514**, 209–212.

KRÖGER, F. A. & VINK, H. J. (1956). Relations between the Concentrations of Imperfections in Crystalline Solids. In *Solid State Physics*vol. 3, Seitz, F. & Turnbull, D. (Eds.), pp. 307–435. Academic Press https://www.sciencedirect.com/science/article/pii/S0081194708601356 (Accessed May 9, 2021).

KWON, O., SENGODAN, S., KIM, K., KIM, GIHYEON, JEONG, H. Y., SHIN, J., JU, Y.-W., HAN, J. W. & KIM, GUNTAE (2017). Exsolution trends and co-segregation aspects of self-grown catalyst nanoparticles in perovskites. *Nature Communications* **8**, 15967.

KYUNO, K., GÖLZHÄUSER, A. & EHRLICH, G. (1998). Growth and the diffusion of platinum atoms and dimers on Pt(111). *Surface Science* **397**, 191–196.

LABERTY-ROBERT, C., LONG, J. W., LUCAS, E. M., PETTIGREW, K. A., STROUD, R. M., DOESCHER, M. S. & ROLISON, D. R. (2006). Sol–Gel-Derived Ceria Nanoarchitectures: Synthesis, Characterization, and Electrical Properties. *Chemistry of Materials* **18**, 50–58.

LAESECKE, A., KRAUSS, R., STEPHAN, K. & WAGNER, W. (1990). Transport Properties of Fluid Oxygen. *Journal of Physical and Chemical Reference Data* **19**, 1089.

LAINE, S., KARRAS, T., LEHTINEN, J. & AILA, T. (2019). High-Quality Self-Supervised Deep Image Denoising. *Advances in Neural Information Processing Systems* **32**, 6970–6980.

LANGDON, J. T., VINCENT, J. L. & CROZIER, P. A. (2019). Finite Element Modeling of Gas and Temperature Distributions during Catalytic Reactions in an Environmental

Transmission Electron Microscope. *Microscopy and Microanalysis* **25**, 2014–2015.

LAWRENCE, E. L. (2019). 'Atomic-Level Analysis of Oxygen Exchange Reactions on Ceria-based Catalysts'. PhD Thesis, Arizona State University.

LAWRENCE, E. L. & CROZIER, P. A. (2018). Oxygen Transfer at Metal-Reducible Oxide Nanocatalyst Interfaces: Contrasting Carbon Growth from Ethane and Ethylene. *ACS Applied Nano Materials* **1**, 1360–1369.

LAWRENCE, E. L., LEVIN, B. D. A., BOLAND, T., CHANG, S. L. Y. & CROZIER, P. A. (2021). Atomic Scale Characterization of Fluxional Cation Behavior on Nanoparticle Surfaces: Probing Oxygen Vacancy Creation/Annihilation at Surface Sites. *ACS Nano*.

LAWRENCE, E. L., LEVIN, B. D. A., MILLER, B. K. & CROZIER, P. A. (2020). Approaches to Exploring Spatio-Temporal Surface Dynamics in Nanoparticles with In Situ Transmission Electron Microscopy. *Microscopy and Microanalysis* **26**, 86–94.

LEVIN, B. D. A., LAWRENCE, E. L. & CROZIER, P. A. (2020). Tracking the picoscale spatial motion of atomic columns during dynamic structural change. *Ultramicroscopy* **213**, 112978.

LI, P., CHEN, X., LI, Y. & SCHWANK, J. W. (2019). A review on oxygen storage capacity of CeO2-based materials: Influence factors, measurement techniques, and applications in reactions related to catalytic automotive emissions control. *Catalysis Today* **327**, 90–115.

LI, Y., KOTTWITZ, M., VINCENT, J. L., ENRIGHT, M. J., LIU, Z., ZHANG, L., HUANG, J., SENANAYAKE, S. D., YANG, W.-C. D., CROZIER, P. A., NUZZO, R. G. & FRENKEL, A. I. (2021). Dynamic structure of active sites in ceria-supported Pt catalysts for the water gas shift reaction. *Nature Communications* **12**, 914.

LI, Y., ZAKHAROV, D., ZHAO, S., TAPPERO, R., JUNG, U., ELSEN, A., BAUMANN, P., NUZZO, R. G., STACH, E. A. & FRENKEL, A. I. (2015). Complex structural dynamics of nanocatalysts revealed in Operando conditions by correlated imaging and spectroscopy probes. *Nature Communications* **6**, 1–6.

LIN, R., ZHANG, R., WANG, C., YANG, X.-Q. & XIN, H. L. (2021). TEMImageNet training library and AtomSegNet deep-learning models for high-precision atom segmentation, localization, denoising, and deblurring of atomic-resolution images. *Scientific Reports* **11**, 5386.

LINDEROTH, T. R., HORCH, S., LÆGSGAARD, E., STENSGAARD, I. & BESENBACHER, F. (1997). Surface Diffusion of Pt on Pt(110): Arrhenius Behavior of Long Jumps. *Physical Review Letters* **78**, 4978–4981.

LIU, B. & LIU, J. (2019). Overview of Image Denoising Based on Deep Learning. *Journal of Physics: Conference Series* **1176**, 022010.

LIU, H. H., WANG, Y., JIA, A. P., WANG, S. Y., LUO, M. F. & LU, J. Q. (2014). Oxygen vacancy promoted CO oxidation over Pt/CeO2 catalysts: A reaction at Pt-CeO2 interface. *Applied Surface Science* **314**, 725–734.

LIU, J. J. (2011). Advanced Electron Microscopy of Metal-Support Interactions in Supported Metal Catalysts. *ChemCatChem* **3**, 934–948.

LIU, J., QIAO, B., SONG, Y., HUANG, Y. & LIU, J. (JIMMY) (2015). Hetero-epitaxially anchoring Au nanoparticles onto ZnO nanowires for CO oxidation. *Chemical Communications* **51**, 15332–15335.

———— (2016). Synthesis of Anchored Bimetallic Catalysts via Epitaxy. *Catalysts* **6**, 88.

LIU, P., QIN, R., FU, G. & ZHENG, N. (2017). Surface Coordination Chemistry of Metal Nanomaterials. *Journal of the American Chemical Society* **139**, 2122–2131.

LIU, R.-J., CROZIER, P. A., SMITH, C. M., HUCUL, D. A., BLACKSON, J. & SALAITA, G. (2005). Metal sintering mechanisms and regeneration of palladium/alumina hydrogenation catalysts. *Applied Catalysis A: General* **282**, 111–121.

LOGADÓTTIR, Á. & NØRSKOV, J. K. (2003). Ammonia synthesis over a Ru(0001) surface studied by density functional calculations. *Journal of Catalysis* **220**, 273–279.

LU, Y., THOMPSON, C., KUNWAR, D., DATYE, A. K. & KARIM, A. M. (2020). Origin of the High CO Oxidation Activity on CeO2 Supported Pt Nanoparticles: Weaker Binding of CO or Facile Oxygen Transfer from the Support? *ChemCatChem* **12**, 1726–1733.

LUISIER, F., BLU, T. & UNSER, M. (2011). Image Denoising in Mixed Poisson–Gaussian Noise. *IEEE Transactions on Image Processing* **20**, 696–708.

MAGNÉLI, A. (1951). Diffraction effects in X-ray Fourier syntheses due to non-observed `weak reflexions'. *Acta Crystallographica* **4**, 447–450.

MAI, H.-X., SUN, L.-D., ZHANG, Y.-W., SI, R., FENG, W., ZHANG, H.-P., LIU, H.-C. & YAN, C.-H. (2005). Shape-Selective Synthesis and Oxygen Storage Behavior of Ceria Nanopolyhedra, Nanorods, and Nanocubes. *The Journal of Physical Chemistry B* **109**, 24380–24385.

MAKITALO, M. & FOI, A. (2013). Optimal Inversion of the Generalized Anscombe Transformation for Poisson-Gaussian Noise. *IEEE Transactions on Image Processing* **22**, 91–103.

MARKS, L. D. & PENG, L. (2016). Nanoparticle shape, thermodynamics and kinetics. *Journal of Physics: Condensed Matter* **28**, 053001.

MARRERO, T. R. & MASON, E. A. (1972). Gaseous Diffusion Coefficients. *Journal of Physical and Chemical Reference Data* **1**, 3.

MARS, P. & VAN KREVELEN, D. W. (1954). Oxidations carried out by means of vanadium oxide catalysts. *Chemical Engineering Science* **3**, 41–59.

MARTIN, D. & DUPREZ, D. (1996). Mobility of surface species on oxides. 1. isotopic exchange of 18O2 with 16O of SiO2, AI2O3, ZrO2, MgO, CeO2, and CeO2-Al2O3. activation by noble metals. correlation with oxide basicity. *Journal of Physical Chemistry* **100**, 9429–9438.

MATHEW, K., SINGH, A. K., GABRIEL, J. J., CHOUDHARY, K., SINNOTT, S. B., DAVYDOV, A. V., TAVAZZA, F. & HENNIG, R. G. (2016). MPInterfaces: A Materials Project based Python tool for high-throughput computational screening of interfacial systems. *Computational Materials Science* **122**, 183–190.

MCBRIDE, B., ZEHE, M. & GORDON, S. (2002). NASA Glenn Coefficients for Calculating Thermodynamic Properties of Individual Species. *NASA Center for Aerospace Information*.

MCCRUM, I. T., HICKNER, M. A. & JANIK, M. J. (2017). First-Principles Calculation of Pt Surface Energies in an Electrochemical Environment: Thermodynamic Driving Forces for Surface Faceting and Nanoparticle Reconstruction. *Langmuir* **33**, 7043–7052.

MCKENNA, K. P. & SHLUGER, A. L. (2007). Shaping the Morphology of Gold Nanoparticles by CO Adsorption. *The Journal of Physical Chemistry C* **111**, 18848–18852.

MEHRABADI, B. A. T., ESKANDARI, S., KHAN, U., WHITE, R. D. & REGALBUTO, J. R. (2017). A Review of Preparation Methods for Supported Metal Catalysts Song, C. (Ed.). *Advances in Catalysis* **61**, 1–35.

METCALF, I. S. (2011). *Chemical Reaction Engineering: A First Course*. Oxford University Press.

MICHALKA, J. R., LATHAM, A. P. & GEZELTER, J. D. (2016). CO-Induced Restructuring on Stepped Pt Surfaces: A Molecular Dynamics Study. *The Journal of Physical Chemistry C* **120**, 18180–18190.

MILLAT, J. & WAKEHAM, W. A. (1989). The Thermal Conductivity of Nitrogen and Carbon Monoxide in the Limit of Zero Density. *Journal of Physical and Chemical Reference Data* **18**, 565.

MILLER, B. K., BARKER, T. M. & CROZIER, P. A. (2015). Novel sample preparation for operando TEM of catalysts. *Ultramicroscopy* **156**, 18–22.

MILLER, B. K. & CROZIER, P. A. (2014). Analysis of Catalytic Gas Products Using Electron Energy-Loss Spectroscopy and Residual Gas Analysis for Operando Transmission Electron Microscopy. *Microscopy and Microanalysis* **20**, 815–824.

———— (2021). Linking Changes in Reaction Kinetics and Atomic-Level Surface Structures on a Supported Ru Catalyst for CO Oxidation. *ACS Catalysis* 1456–1463.

MÖCKL, L., LAMB, D. C. & BRÄUCHLE, C. (2014). Super-resolved Fluorescence Microscopy: Nobel Prize in Chemistry 2014 for Eric Betzig, Stefan Hell, and William E. Moerner. *Angewandte Chemie International Edition* **53**, 13972–13977.

MOGENSEN, M. (2000). Physical, chemical and electrochemical properties of pure and doped ceria. *Solid State Ionics* **129**, 63–94.

MOHAN, S., KADKHODAIE, Z., SIMONCELLI, E. P. & FERNANDEZ-GRANDA, C. (2020). Robust and interpretable blind image denoising via bias-free convolutional neural networks. *arXiv:1906.05478 [cs, eess, stat]*. http://arxiv.org/abs/1906.05478 (Accessed January 14, 2021).

MOHAN, S., MANZORRO, R., VINCENT, J. L., TANG, B., SHETH, D. Y., SIMONCELLI, E. P., MATTESON, D. S., CROZIER, P. A. & FERNANDEZ-GRANDA, C. (2020). Deep Denoising For Scientific Discovery: A Case Study In Electron Microscopy. *arXiv:2010.12970 [cs, eess]*. http://arxiv.org/abs/2010.12970 (Accessed April 21, 2021).

MØLGAARD MORTENSEN, P., WILLUM HANSEN, T., BIRKEDAL WAGNER, J. & DEGN JENSEN, A. (2015). Modeling of temperature profiles in an environmental transmission electron microscope using computational fluid dynamics. *Ultramicroscopy* **152**, 1–9.

MONTINI, T., MELCHIONNA, M., MONAI, M. & FORNASIERO, P. (2016). Fundamentals and Catalytic Applications of CeO2-Based Materials. *Chemical Reviews* **116**, 5987–6041.

MOONEY, P., CONTARATO, D., DENES, P., GUBBENS, A., LEE, B., LENT, M. & AGARD, D. (2011). A High-Speed Electron-Counting Direct Detection Camera for TEM. *Microscopy and Microanalysis* **17**, 1004–1005.

MOONEY, P., FAN, G. Y., MEYER, C. E., TRUONG, K. V., BUI, D. B. & KRIVANEK, O. L. (1990). Slow-Scan CCD Camera for Transmission Electron Microscopy. *Proc. 12th Int. Congr. for Electron Microscopy* **1**.

MORRIS, V. N., FARRELL, R. A., SEXTON, A. M. & MORRIS, M. A. (2006). Lattice Constant Dependence on Particle Size for Ceria prepared from a Citrate Sol-Gel. *Journal of Physics: Conference Series* **26**, 119–122.

MULLINS, D. R. (2015). The surface chemistry of cerium oxide. *Surface Science Reports* **70**, 42.

MULLINS, D. R. & ZHANG, K. Z. (2002). Metal – support interactions between Pt and thin film cerium oxide. *Surface Science* **513**, 163–173.

MUNNIK, P., DE JONGH, P. E. & DE JONG, K. P. (2015). Recent Developments in the Synthesis of Supported Catalysts. *Chemical Reviews* **115**, 6687–6718.

M. WECKHUYSEN, B. (2003a). Operando spectroscopy: fundamental and technical aspects of spectroscopy of catalysts under working conditions. *Physical Chemistry Chemical Physics* **5**, vi–vi.

———— (2003b). Determining the active site in a catalytic process: Operando spectroscopy is more than a buzzword. *Physical Chemistry Chemical Physics* **5**, 4351–4360.

NAGAI, Y, HIRABAYASHI, T., DOHMAE, K., TAKAGI, N., MINAMI, T., SHINJOH, H. & MATSUMOTO, S. (2006). Sintering inhibition mechanism of platinum supported on ceria-based oxide and Pt-oxide–support interaction. *Journal of Catalysis* **242**, 103–109.

NAGAI, YASUTAKA, HIRABAYASHI, T., DOHMAE, K., TAKAGI, N., MINAMI, T., SHINJOH, H. & MATSUMOTO, S. (2006). Sintering inhibition mechanism of platinum supported on ceria-based oxide and Pt-oxide-support interaction. *Journal of Catalysis* **242**, 103–109.

NEAGU, D., OH, T.-S., MILLER, D. N., MÉNARD, H., BUKHARI, S. M., GAMBLE, S. R., GORTE, R. J., VOHS, J. M. & IRVINE, J. T. S. (2015). Nano-socketed nickel particles with enhanced coking resistance grown in situ by redox exsolution. *Nature Communications* **6**, 8120.

NIBBELKE, R. H., CAMPMAN, M. A. J., HOEBINK, J. H. B. J. & MARIN, G. B. (1997). Kinetic study of the CO oxidation over Pt/γ-Al2O3 and Pt/Rh/CeO2/γ-Al2O3 in the presence of H2O and CO2. *Journal of Catalysis* **171**, 358–373.

NØRSKOV, J. K., STUDT, F., ABILD-PEDERSEN, F., BLIGAARD, T. & NØRSKOV, J. K. (2014). *Fundamental Concepts in Heterogeneous Catalysis*. Somerset, United States: John Wiley & Sons, Incorporated.

ONG, S. P., RICHARDS, W. D., JAIN, A., HAUTIER, G., KOCHER, M., CHOLIA, S., GUNTER, D., CHEVRIER, V. L., PERSSON, K. A. & CEDER, G. (2013). Python Materials Genomics (pymatgen): A robust, open-source python library for materials analysis. *Computational Materials Science* **68**, 314–319.

PACCHIONI, G. (2013). Electronic interactions and charge transfers of metal atoms and clusters on oxide surfaces. *Physical Chemistry Chemical Physics* **15**, 1737.

PAIDAR, M., FATEEV, V. & BOUZEK, K. (2016). Membrane electrolysis—History, current status and perspective. *Electrochimica Acta* **209**, 737–756.

PEKSEN, M. (2018). *Multiphysics Modeling: Materials, Components, and Systems*. San Diego: Elsevier Science & Technology.

PENKALA, B., PAULUS, W., AUBERT, D., KAPER, H., TARDIVAT, C. & CONDER, K. (2015). The role of lattice oxygen in CO oxidation over Ce18O2-based catalysts revealed under operando conditions. *Catalysis Science and Technology* **5**, 4839–4848.

PENNYCOOK, S. J. & NELLIST, P. D. (2011). *Scanning Transmission Electron Microscopy — imaging and analysis*. Springer.

PEREIRA-HERNÁNDEZ, X. I., DELARIVA, A., MURAVEV, V., KUNWAR, D., XIONG, H., SUDDUTH, B., ENGELHARD, M., KOVARIK, L., HENSEN, E. J. M., WANG, Y. & DATYE, A. K. (2019). Tuning Pt-CeO2 interactions by high-temperature vapor-phase synthesis for improved reducibility of lattice oxygen. *Nature Communications* **10**.

PICCOLO, L. (2020). Restructuring effects of the chemical environment in metal nanocatalysis and single-atom catalysis. *Catalysis Today*.

https://www.sciencedirect.com/science/article/pii/S0920586120301747 (Accessed May 11, 2021).

PINJARI, D. V. & PANDIT, A. B. (2011). Room temperature synthesis of crystalline CeO2 nanopowder: Advantage of sonochemical method over conventional method. *Ultrasonics Sonochemistry* **18**, 1118–1123.

PLODINEC, M., NERL, H. C., FARRA, R., WILLINGER, M. G., STOTZ, E., SCHLÖGL, R. & LUNKENBEIN, T. (2020). Versatile Homebuilt Gas Feed and Analysis System for Operando TEM of Catalysts at Work. *Microscopy and Microanalysis* **26**, 220–228.

PLODINEC, M., NERL, H. C., GIRGSDIES, F., SCHLÖGL, R. & LUNKENBEIN, T. (2020). Insights into Chemical Dynamics and Their Impact on the Reactivity of Pt Nanoparticles during CO Oxidation by Operando TEM. *ACS Catalysis* **10**, 3183–3193.

PODKOLZIN, S. G., SHEN, J., DE PABLO, J. J. & DUMESIC, J. A. (2000). Equilibrated Adsorption of CO on Silica-Supported Pt Catalysts. *Journal of Physical Chemistry B* **104**, 4169–4180.

PRIETO, G. & SCHÜTH, F. (2015). Bridging the gap between insightful simplicity and successful complexity: From fundamental studies on model systems to technical catalysts. *Journal of Catalysis* **328**, 59–71.

PUIGDOLLERS, A. R., SCHLEXER, P., TOSONI, S. & PACCHIONI, G. (2017). Increasing oxide reducibility: the role of metal/oxide interfaces in the formation of oxygen vacancies. *ACS Catalysis* **7**, 6493–6513.

QIAO, Z.-A., WU, Z. & DAI, S. (2013). Shape-Controlled Ceria-based Nanostructures for Catalysis Applications. *ChemSusChem* **6**, 1821–1833.

RAHM, J. & ERHART, P. (2020). WulffPack: A Python package for Wulff constructions. *Journal of Open Source Software* **5**, 1944.

REHR, J. J. & VILA, F. D. (2014). Dynamic structural disorder in supported nanoscale catalysts. *The Journal of Chemical Physics* **140**, 134701.

REIMER, L. (1998). Electron Scattering and Diffusion. In *Scanning Electron Microscopy: Physics of Image Formation and Microanalysis*, Reimer, L. (Ed.), pp. 57–134. Berlin, Heidelberg: Springer Berlin Heidelberg https://doi.org/10.1007/978-3-540-38967-5_3.

REIMER, L. & LÖDDING, B. (1984). Calculation and tabulation of mott cross-sections for large-angle electron scattering. *Scanning* **6**, 128–151.

REN, Z., LIU, N., CHEN, B., LI, J. & MEI, D. (2018). Theoretical Investigation of the Structural Stabilities of Ceria Surfaces and Supported Metal Nanocluster in Vapor and Aqueous Phases. *The Journal of Physical Chemistry C* **122**, 4828–4840.

ROBERTS, A., BROOKS, R. & SHIPWAY, P. (2014). Internal combustion engine cold-start efficiency: A review of the problem, causes and potential solutions. *Energy Conversion and Management* **82**, 327–350.

RODRÍGUEZ-PADRÓN, D., PUENTE-SANTIAGO, A. R., BALU, A. M., MUÑOZ-BATISTA, M. J. & LUQUE, R. (2019). Environmental Catalysis: Present and Future. *ChemCatChem* **11**, 18–38.

RONNEBERGER, O., FISCHER, P. & BROX, T. (2015). U-Net: Convolutional Networks for Biomedical Image Segmentation. In *Medical Image Computing and Computer-Assisted Intervention – MICCAI 2015*, *Lecture Notes in Computer Science*, Navab, N., Hornegger, J., Wells, W. M. & Frangi, A. F. (Eds.), pp. 234–241. Cham: Springer International Publishing.

ROSEMOUNT ANALYTICAL (2012). Fundamentals of Gas Chromatography.

ROSS, F. M. & MINOR, A. M. (2019). In Situ Transmission Electron Microscopy. In *Springer Handbook of Microscopy*, Hawkes, P. W. & Spence, J. C. H. (Eds.), p. 2. Cham: Springer International Publishing https://doi.org/10.1007/978-3-030-00069-1_3.

DE RUIJTER, W. J. & WEISS, J. K. (1992). Methods to measure properties of slow-scan CCD cameras for electron detection. *Review of Scientific Instruments* **63**, 4314–4321.

RUSKA, E. (1985). The Beginnings of Electron Microscopy. *The Beginnings of Electron Microscopy* **1983**, xvii–xix.

RUSKIN, R. S., YU, Z. & GRIGORIEFF, N. (2013). Quantitative characterization of electron detectors for transmission electron microscopy. *Journal of Structural Biology* **184**, 385–393.

SALCEDO, A. & IRIGOYEN, B. (2020). Unraveling the Origin of Ceria Activity in Water-Gas Shift by First-Principles Microkinetic Modeling. *Journal of Physical Chemistry C* **124**, 7823–7834.

SCHLÖGL, R. (2015). Heterogeneous Catalysis. *Angewandte Chemie International Edition* **54**, 3465–3520.

SCHMIDT, O., GAMBHIR, A., STAFFELL, I., HAWKES, A., NELSON, J. & FEW, S. (2017). Future cost and performance of water electrolysis: An expert elicitation study. *International Journal of Hydrogen Energy* **42**, 30470–30492.

SCHNEIDER, C. A., RASBAND, W. S. & ELICEIRI, K. W. (2012). NIH Image to ImageJ: 25 years of image analysis. *Nature Methods* **9**, 671–675.

SHARAPA, D. I., DORONKIN, D. E., STUDT, F., GRUNWALDT, J.-D. & BEHRENS, S. (2019). Moving Frontiers in Transition Metal Catalysis: Synthesis, Characterization and Modeling. *Advanced Materials* **31**, 1807381.

SHARMA, R. (2001). Design and Applications of Environmental Cell Transmission Electron Microscope for In Situ Observations of Gas–Solid Reactions. *Microscopy and Microanalysis* **7**, 494–506.

——— (2012). Experimental set up for in situ transmission electron microscopy observations of chemical processes. *Micron* **43**, 1147–1155.

SHARMA, V., CROZIER, P. A., SHARMA, R. & ADAMS, J. B. (2012). Direct observation of hydrogen spillover in Ni-loaded Pr-doped ceria. *Catalysis Today* **180**, 2–8.

SHARMA, V., EBERHARDT, K. M., SHARMA, R., ADAMS, J. B. & CROZIER, P. A. (2010). A spray drying system for synthesis of rare-earth doped cerium oxide nanoparticles. *Chemical Physics Letters* **495**, 280–286.

SHETH, D. Y., MOHAN, S., VINCENT, J. L., MANZORRO, R., CROZIER, P. A., KHAPRA, M. M., SIMONCELLI, E. P. & FERNANDEZ-GRANDA, C. (2020). Unsupervised Deep Video Denoising. *arXiv:2011.15045 [cs, eess, stat]*. http://arxiv.org/abs/2011.15045 (Accessed January 12, 2021).

SHINJOH, H., HATANAKA, M., NAGAI, Y., TANABE, T., TAKAHASHI, N., YOSHIDA, T. & MIYAKE, Y. (2009). Suppression of noble metal sintering based on the support anchoring effect and its application in automotive three-way catalysis. *Topics in Catalysis* **52**, 1967–1971.

SIGMA-ALDRICH (2019). Whatman® glass microfiber filters, Grade GF/D diam. 10 mm, pack of 100 | Sigma-Aldrich. https://www.sigmaaldrich.com/catalog/product/aldrich/wha1823010?lang=en&region=US (Accessed August 7, 2019).

DA SILVA, F. S. & DE SOUZA, T. M. (2017). Novel materials for solid oxide fuel cell technologies: A literature review. *International Journal of Hydrogen Energy* **42**, 26020–26036.

SIMONSEN, S. B., CHORKENDORFF, I., DAHL, S., SKOGLUNDH, M., SEHESTED, J. & HELVEG, S. (2010). Direct Observations of Oxygen-induced Platinum Nanoparticle Ripening Studied by In Situ TEM. *Journal of the American Chemical Society* **132**, 7968–7975.

SINCLAIR, R., LEE, S. C., SHI, Y. & CHUEH, W. C. (2017). Structure and chemistry of epitaxial ceria thin films on yttria-stabilized zirconia substrates, studied by high resolution electron microscopy. *Ultramicroscopy* **176**, 200–211.

SINGH-MILLER, N. E. & MARZARI, N. (2009). Surface energies, work functions, and surface relaxations of low-index metallic surfaces from first principles. *Physical Review B* **80**, 235407.

SMITH, D. J. (1997). The realization of atomic resolution with the electron microscope. *Reports on Progress in Physics* **60**, 1513–1580.

SMITH, D. J. (2008). Development of Aberration-Corrected Electron Microscopy. *Microscopy and Microanalysis* **14**, 2–15.

SOMORJAI, G. A. (1991). The flexible surface. Correlation between reactivity and restructuring ability. *Langmuir* **7**, 3176–3182.

SOMORJAI, G. A. & LI, Y. (2010). *Introduction to Surface Chemistry and Catalysis*. 2nd ed. Wiley https://www.wiley.com/en-us/Introduction+to+Surface+Chemistry+and+Catalysis%2C+2nd+Edition-p-9780470508237 (Accessed May 9, 2021).

SPENCE, J. C. H. (2003). *High-resolution electron microscopy*. Oxford University Press.

SPENCE, J. C. H. & ZUO, J. M. (1988). Large dynamic range, parallel detection system for electron diffraction and imaging. *Review of Scientific Instruments* **59**, 2102–2105.

VAN SPRONSEN, M. A., FRENKEN, J. W. M. & GROOT, I. M. N. (2017). Surface science under reaction conditions: CO oxidation on Pt and Pd model catalysts. *Chemical Society Reviews* **46**, 4347–4374.

SPURGEON, S. R., OPHUS, C., JONES, L., PETFORD-LONG, A., KALININ, S. V., OLSZTA, M. J., DUNIN-BORKOWSKI, R. E., SALMON, N., HATTAR, K., YANG, W.-C. D., SHARMA, R., DU, Y., CHIARAMONTI, A., ZHENG, H., BUCK, E. C., KOVARIK, L., PENN, R. L., LI, D., ZHANG, X., MURAYAMA, M. & TAHERI, M. L. (2021). Towards data-driven next-generation transmission electron microscopy. *Nature Materials* **20**, 274–279.

STAMBOULI, A. B. & TRAVERSA, E. (2002). Solid oxide fuel cells (SOFCs): A review of an environmentally clean and efficient source of energy. *Renewable and Sustainable Energy Reviews* **6**, 433–455.

SU, Y.-Q., WANG, Y., LIU, J.-X., FILOT, I. A. W., ALEXOPOULOS, K., ZHANG, L., MURAVEV, V., ZIJLSTRA, B., VLACHOS, D. G. & HENSEN, E. J. M. (2019). Theoretical Approach To Predict the Stability of Supported Single-Atom Catalysts. *ACS Catalysis* **9**, 3289–3297.

SUN, G. & SAUTET, P. (2018). Metastable Structures in Cluster Catalysis from First-Principles: Structural Ensemble in Reaction Conditions and Metastability Triggered Reactivity. *Journal of the American Chemical Society* **140**, 2812–2820.

TA, N., LIU, J. (JIMMY), CHENNA, S., CROZIER, P. A., LI, Y., CHEN, A. & SHEN, W. (2012). Stabilized Gold Nanoparticles on Ceria Nanorods by Strong Interfacial Anchoring. *Journal of the American Chemical Society* **134**, 20585–20588.

TABATABAIAN, MEHRZAD & TABATABAIAN, MERHZAD (2014). *COMSOL for Engineers*. Bloomfield: Mercury Learning & Information.

TAHERI, M. L., STACH, E. A., ARSLAN, I., CROZIER, P. A., KABIUS, B. C., LAGRANGE, T., MINOR, A. M., TAKEDA, S., TANASE, M., WAGNER, J. B. & SHARMA, R. (2016). Current status and future directions for in situ transmission electron microscopy. *Ultramicroscopy* **170**, 86–95.

TAO, F. (FENG) & CROZIER, P. A. (2016). Atomic-Scale Observations of Catalyst Structures under Reaction Conditions and during Catalysis. *Chemical Reviews* **116**, 3487–3539.

TIAN, C., FEI, L., ZHENG, W., XU, Y., ZUO, W. & LIN, C.-W. (2019). Deep Learning on Image Denoising: An overview. https://arxiv.org/abs/1912.13171v4 (Accessed January 14, 2021).

TJADEN, B., COOPER, S. J., BRETT, D. J., KRAMER, D. & SHEARING, P. R. (2016). On the origin and application of the Bruggeman correlation for analysing transport phenomena in electrochemical systems. *Current Opinion in Chemical Engineering* **12**, 44–51.

TOPSOE, H. (2003). Developments in operando studies and in situ characterization of heterogeneous catalysts. *Journal of Catalysis* **216**, 155–164.

TORSTENSSON, M. (2014). 'A comparison of the multicomponent model and the mixture averaged approximation'. M.S. Thesis, Lund University http://lup.lub.lu.se/student-papers/record/4331903.

TOULHOAT, H. (2010). Heterogeneous Catalysis: Use of Density Functional Theory. *Encyclopedia of Materials: Science and Technology* 1–7.

TROVARELLI, A. (2002). *Catalysis by Ceria and Related Materials*. 2nd ed. Trovarelli, A. (Ed.). London: Imperial College Press.

TROVARELLI, A. & LLORCA, J. (2017). Ceria Catalysts at Nanoscale: How Do Crystal Shapes Shape Catalysis? *ACS Catalysis* **7**, 4716–4735.

TSEN, S.-C. Y., CROZIER, P. A. & LIU, J. (2003). Lattice measurement and alloy compositions in metal and bimetallic nanoparticles. *Ultramicroscopy* **98**, 63–72.

UHLEMANN, S. & HAIDER, M. (1998). Residual wave aberrations in the first spherical aberration corrected transmission electron microscope. *Ultramicroscopy* **72**, 109–119.

URBAN, K., KABIUS, B., HAIDER, M. & ROSE, H. (1999). A way to higher resolution: spherical-aberration correction in a 200 kV transmission electron microscope. *Journal of Electron Microscopy* **48**, 821–826.

VASUDEVAN, R. K. & JESSE, S. (2019). Deep Learning as a Tool for Image Denoising and Drift Correction. *Microscopy and Microanalysis* **25**, 190–191.

VENDELBO, S. B., ELKJÆR, C. F., FALSIG, H., PUSPITASARI, I., DONA, P., MELE, L., MORANA, B., NELISSEN, B. J., VAN RIJN, R., CREEMER, J. F., KOOYMAN, P. J. & HELVEG, S. (2014). Visualization of oscillatory behaviour of Pt nanoparticles catalysing CO oxidation. *Nature Materials* **13**, 884–890.

VENKATRAMAN, K., LEVIN, B. D. A., MARCH, K., REZ, P. & CROZIER, P. A. (2019). Vibrational spectroscopy at atomic resolution with electron impact scattering. *Nature Physics* **15**, 1237–1241.

VESOVIC, V., WAKEHAM, W. A., OLCHOWY, G. A., SENGERS, J. V., WATSON, J. T. R. & MILLAT, J. (1990). The Transport Properties of Carbon Dioxide. *Journal of Physical and Chemical Reference Data* **19**, 763.

VINCENT, J. & CROZIER, P. (2020). Atomic-resolution *Operando* and Time-resolved *In Situ* TEM Imaging of Oxygen Transfer Reactions Catalyzed by CeO2-supported Pt Nanoparticles. *Microscopy and Microanalysis* **26**, 1694–1695.

VINCENT, J. L. & CROZIER, P. A. (2021). Fluxional Behavior at the Atomic Level and its Impact on Activity: CO Oxidation over CeO$_{2}$-supported Pt Catalysts. *arXiv:2104.00821 [cond-mat]*. http://arxiv.org/abs/2104.00821 (Accessed April 19, 2021).

VINCENT, J. L., MANZORRO, R., MOHAN, S., TANG, B., SHETH, D. Y., SIMONCELLI, E. P., MATTESON, D. S., FERNANDEZ-GRANDA, C. & CROZIER, P. A. (2021). Developing and Evaluating Deep Neural Network-based Denoising for Nanoparticle TEM Images with Ultra-low Signal-to-Noise. http://128.84.4.18/abs/2101.07770 (Accessed April 20, 2021).

VINCENT, J. L., VANCE, J. W., LANGDON, J. T., MILLER, B. K. & CROZIER, P. A. (2020). Chemical Kinetics for Operando Electron Microscopy of Catalysts: 3D Modeling of Gas and Temperature Distributions During Catalytic Reactions. *Ultramicroscopy* 113080.

WANG, C., MAO, S., WANG, Z., CHEN, Y., YUAN, W., OU, Y., ZHANG, H., GONG, Y., WANG, Y., MEI, B., JIANG, Z. & WANG, Y. (2020). Insight into Single-Atom-Induced Unconventional Size Dependence over CeO2-Supported Pt Catalysts. *Chem* **6**, 752–765.

WANG, H., ZHU, J.-J., ZHU, J.-M., LIAO, X.-H., XU, S., DING, T. & CHEN, H.-Y. (2002). Preparation of nanocrystalline ceria particles by sonochemical and microwave assisted heating methods. *Physical Chemistry Chemical Physics* **4**, 3794–3799.

WANG, Z., BOVIK, A. C., SHEIKH, H. R. & SIMONCELLI, E. P. (2004). Image Quality Assessment: From Error Visibility to Structural Similarity. *IEEE Transactions on Image Processing* **13**, 600–612.

WANG, Z., LI, C. & DOMEN, K. (2019). Recent developments in heterogeneous photocatalysts for solar-driven overall water splitting. *Chemical Society Reviews* **48**, 2109–2125.

WARD, M. R., BOYES, E. D. & GAI, P. L. (2013). In Situ Aberration-Corrected Environmental TEM: Reduction of Model Co3O4 in H2 at the Atomic Level. *ChemCatChem* **5**, 2655–2661.

WEILENMANN, M., FAVEZ, J. Y. & ALVAREZ, R. (2009). Cold-start emissions of modern passenger cars at different low ambient temperatures and their evolution over vehicle legislation categories. *Atmospheric Environment* **43**, 2419–2429.

WESTON, G. F. (1985). *Ultrahigh Vacuum Practice*. London: Butterworth & Co.

WILKE, C. R. (1950). A Viscosity Equation for Gas Mixtures. *The Journal of Chemical Physics* **18**, 517–519.

WILLIAMS, D. B. & CARTER, C. B. (2008). *Transmission electron microscopy: a textbook for materials science*. 2nd ed. New York: Springer.

WINTERBOTTOM, W. L. (1967). Equilibrium shape of a small particle in contact with a foreign substrate. *Acta Metallurgica* **15**, 303–310.

WINTTERLIN, J., VÖLKENING, S., JANSSENS, T. V. W., ZAMBELLI, T. & ERTL, G. (1997). Atomic and Macroscopic Reaction Rates of a Surface-Catalyzed Reaction. *Science* **278**, 1931–1934.

WU, Z., LI, M., HOWE, J., MEYER, H. M. & OVERBURY, S. H. (2010). Probing defect sites on CeO2 nanocrystals with well-defined surface planes by raman spectroscopy and O2 adsorption. *Langmuir* **26**, 16595–16606.

WU, Z., LI, M. & OVERBURY, S. H. (2012). On the structure dependence of CO oxidation over CeO2 nanocrystals with well-defined surface planes. *Journal of Catalysis* **285**, 61–73.

XING, X., YOON, B., LANDMAN, U. & PARKS, J. H. (2006). Structural evolution of Au nanoclusters: From planar to cage to tubular motifs. *Physical Review B* **74**, 165423.

YANG, Q., YAN, P., KALRA, M. K. & WANG, G. (2017). CT Image Denoising with Perceptive Deep Neural Networks. https://arxiv.org/abs/1702.07019v1 (Accessed January 14, 2021).

YANG, S. & GAO, L. (2006). Controlled Synthesis and Self-Assembly of CeO2 Nanocubes. *Journal of the American Chemical Society* **128**, 9330–9331.

YE, F., XU, M., DAI, S., TIEU, P., REN, X. & PAN, X. (2020). In Situ TEM Studies of Catalysts Using Windowed Gas Cells. *Catalysts* **10**, 779.

YOSHIDA, H., KUWAUCHI, Y., JINSCHEK, J. R., SUN, K., TANAKA, S., KOHYAMA, M., SHIMADA, S., HARUTA, M. & TAKEDA, S. (2012). Visualizing Gas Molecules Interacting with Supported Nanoparticulate Catalysts at Reaction Conditions. *Science* **335**, 317–319.

YOSHIDA, H., MATSUURA, K., KUWAUCHI, Y., KOHNO, H., SHIMADA, S., HARUTA, M. & TAKEDA, S. (2011). Temperature-Dependent Change in Shape of Platinum Nanoparticles Supported on CeO2 during Catalytic Reactions. *Applied Physics Express* **4**, 065001.

ZANDKARIMI, B. & ALEXANDROVA, A. N. (2019). Surface-supported cluster catalysis: Ensembles of metastable states run the show. *Wiley Interdisciplinary Reviews: Computational Molecular Science* **9**. https://onlinelibrary.wiley.com/doi/abs/10.1002/wcms.1420 (Accessed May 11, 2021).

ZHAI, H. & ALEXANDROVA, A. N. (2017). Fluxionality of Catalytic Clusters: When It Matters and How to Address It. *ACS Catalysis* **7**, 1905–1911.

——— (2018). Local Fluxionality of Surface-Deposited Cluster Catalysts: The Case of Pt $_7$ on Al $_2$ O $_3$. *The Journal of Physical Chemistry Letters* **9**, 1696–1702.

ZHANG, J., OHARA, S., UMETSU, M., NAKA, T., HATAKEYAMA, Y. & ADSCHIRI, T. (2007). Colloidal Ceria Nanocrystals: A Tailor-Made Crystal Morphology in Supercritical Water. *Advanced Materials* **19**, 203–206.

ZHANG, K., ZUO, W., CHEN, Y., MENG, D. & ZHANG, L. (2017). Beyond a Gaussian Denoiser: Residual Learning of Deep CNN for Image Denoising. *IEEE Transactions on Image Processing* **26**, 3142–3155.

ZHANG, S., PLESSOW, P. N., WILLIS, J. J., DAI, S., XU, M., GRAHAM, G. W., CARGNELLO, M., ABILD-PEDERSEN, F. & PAN, X. (2016). Dynamical observation and detailed description of catalysts under strong metal-support interaction. *Nano Letters* **16**, 4528–4534.

ZHANG, X., LU, Y., LIU, J. & DONG, B. (2018). Dynamically Unfolding Recurrent Restorer: A Moving Endpoint Control Method for Image Restoration. https://openreview.net/forum?id=SJfZKiC5FX (Accessed January 3, 2021).

ZHANG, Y., ZHU, Y., NICHOLS, E., WANG, Q., ZHANG, S., SMITH, C. & HOWARD, S. (2019). A Poisson-Gaussian Denoising Dataset With Real Fluorescence Microscopy Images. , pp. 11710–11718. https://openaccess.thecvf.com/content_CVPR_2019/html/Zhang_A_Poisson-Gaussian_Denoising_Dataset_With_Real_Fluorescence_Microscopy_Images_CVPR_2019_paper.html (Accessed January 3, 2021).

ZHANG, Z., ZANDKARIMI, B. & ALEXANDROVA, A. N. (2020). Ensembles of Metastable States Govern Heterogeneous Catalysis on Dynamic Interfaces. *Accounts of Chemical Research* **53**, 447–458.

ZHOU, K., WANG, X., SUN, X., PENG, Q. & LI, Y. (2005). Enhanced catalytic activity of ceria nanorods from well-defined reactive crystal planes. *Journal of Catalysis* **229**, 206–212.

ZHU, B., MENG, J., YUAN, W., ZHANG, X., YANG, H., WANG, Y. & GAO, Y. (2020). Reshaping of Metal Nanoparticles Under Reaction Conditions. *Angewandte Chemie - International Edition* **59**, 2171–2180.

ZIENKIEWICZ, O. C. (2000). *The finite element method*. 5th ed. Oxford ; Butterworth-Heinemann.

ZUO, J. M. (1996). Electron detection characteristics of slow-scan CCD camera. *Ultramicroscopy* **66**, 21–33.

ZUO, J. M. & SPENCE, J. C. H. (2017). *Advanced Transmission Electron Microscopy*. 1st ed. New York, NY: Springer.

APPENDIX A

SUPPLEMENTARY MATERIAL FOR CHAPTER 2: METHODS

TABLE OF CONTENTS: APPENDIX A

A.1. *OPERANDO* PELLET FABRICATION PROCESS

The annular *operando* pellets are fabricated from a commercially available grade GF/D borosilicate glass microfiber cylindrical filters intended for water filtration applications (Sigma-Aldrich, 2019). The commercial GF/D microfiber filters are 10 mm in diameter and 0.67 mm thick. The pore size published by the manufacturer is 2.7 micrometers. The fiber width and aspect ratio were not reported by the manufacturer. The reported Herzberg speed is 41 sec/100 mL.

The as-received filters were first washed by rinsing de-ionized (DI) water through them using a vacuum filtration device to provide negative pressure. Next, the washed and dried pellets were fired at 550 °C for 5 minutes in air. This high-temperature thermal treatment was performed in order to remove any residual contamination from the fibers. Heating the pellet at higher temperatures or for longer than 5 minutes at 550 °C was found to introduce softening of the pellet microfibers, leading to significant shape changes. The heat treatment for 5 minutes at 550 °C was conducted in a pre-heated clamshell furnace, by sliding the pellets into the furnace on a cleaned and pre-heated alumina crucible, firing them for the specified time, and quickly removing them to cool in ambient air. At this point in the fabrication process, it can be beneficial to isolate the cooled pellet in a dust-proof labeled container, e.g., a sealed petri dish is suitable. Additionally, it may be useful to weigh the pellet prior to loading it with catalyst particles.

The as-fired 10 mm GF/D filters were impregnated with an aqueous or an alcoholic dispersion of catalyst powder. It was found that placing the fired filters on a vacuum filtration device with negative pressure assisted in pulling the dispersion of powder through the pore network of the filter (compared with diffusion of the powder via drop-casting, for example). The fired 10 mm filter was placed on the vacuum filtration device over a thinner piece of filter paper. The vacuum was pulled, and then the catalyst dispersion was drop-cast into the center of the fired GF/D filter. Care must be taken to uniformly load the catalyst powder into a roughly 3.0 mm diameter region of the larger 10 mm diameter filter. After loading 3 – 5 drops of powder into the filter, the filter was carefully turned over, and another 3 – 5 drops of powder were impregnated into the other side. The dispersion was repeatedly sonicated throughout this process to maintain a fine dispersion of catalyst powder while loading. Typically, the dispersions consisted of ~1 mg of catalyst per 2 mL of solvent sonicated for 10+ minutes in an ultrasonicator.

After loading, the pellets were dried in air. A 3.0 mm diameter annular disk with a 1.0 mm diameter centered hole was cut from the dried, catalyst-loaded filter by the use of specialized core sampling cutting tools (Electron Microscopy Sciences, 2021). A clean cutting mat must be used to stop the core sampling tools during this process (Electron Microscopy Sciences, 2021). The 3.0 mm diameter disk is produced by cleanly slicing a 3.0 mm diameter core sampling tool through the catalyst-loaded pellet. In the center of the 3.0 mm disk, a smaller 1.0 mm diameter hole is cut (using a 1.0 mm diameter core sampling tool) to create the annular pellet. The mass of catalyst in the annular pellet can be determined by measuring the mass of the pellet with a microbalance before and after catalyst impregnation. Extreme caution must be taken to prevent any breakage of fibers which would skew the catalyst mass measurement. For the work reported in Chapter 6, the loaded mass of catalyst was determined to be 180 ± 5 μg.

A.2. Thermal and Electron-beam Induced Rates of Displacement in O and Ce Atoms

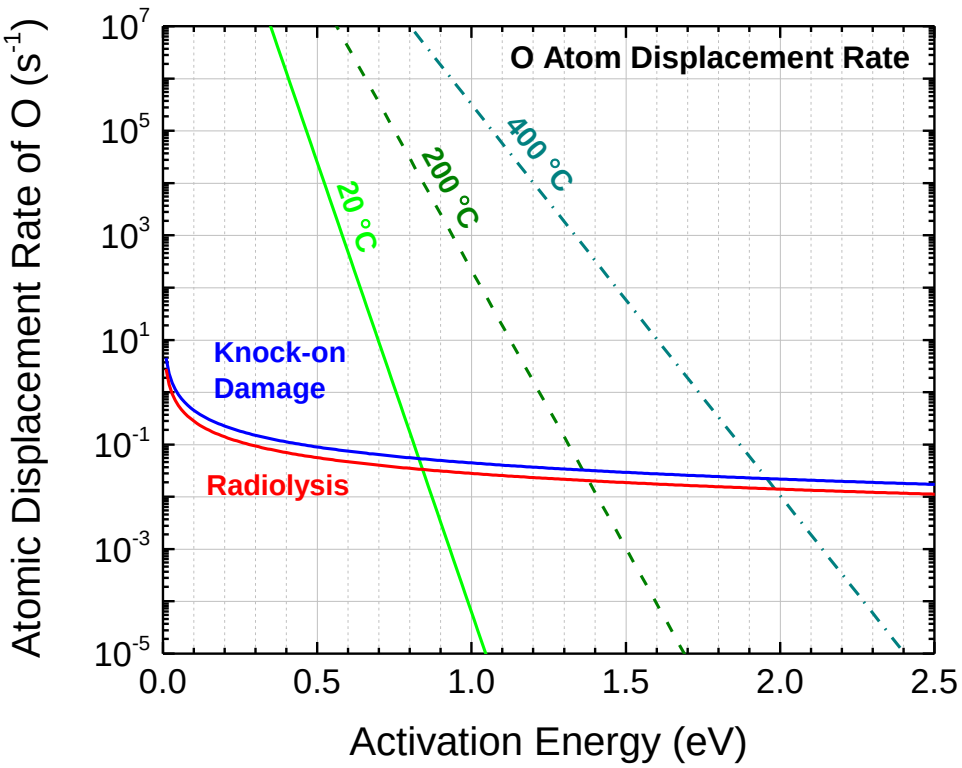

Figure A.1. Thermally-activated and electron beam-induced O atom displacement rate (displacement per atom per second) as a function of displacement activation energy. Knock-on and radiolytic damage rate shown for an incident electron flux of 5,000 e-/Å^2/sec. A radiolytic efficiency $\xi = 10^{-5}$ was used.

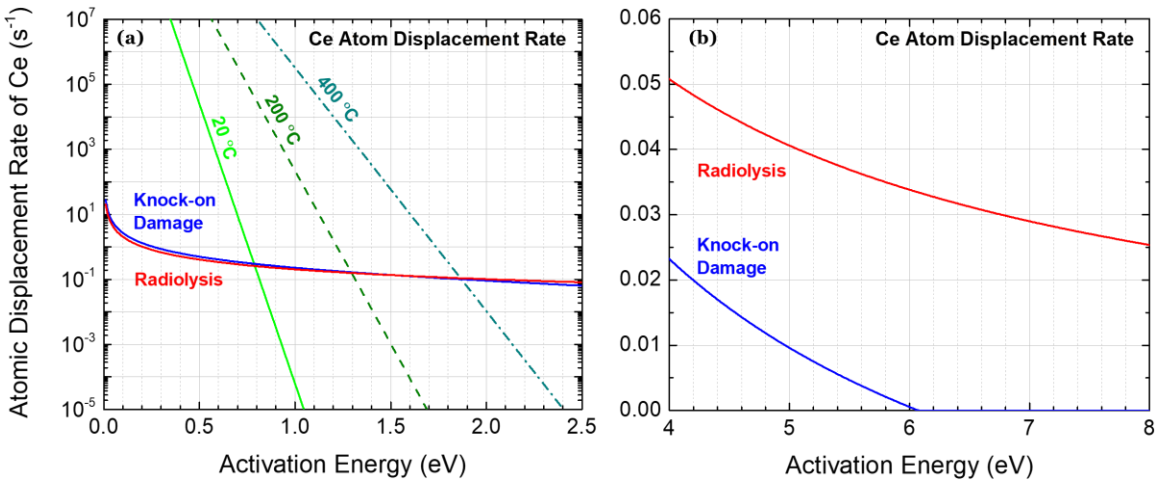

Figure A.2. Thermally-activated and electron beam-induced Ce atom displacement rate (displacement per atom per second) as a function of displacement activation energy for activation energies spanning (a) [0 – 2.5] eV and (b) [4 – 8] eV. Knock-on and radiolytic damage rate shown for an incident electron flux of 5,000 e-/Å^2/sec. A radiolytic efficiency $\xi = 10^{-5}$ was used.

APPENDIX B

SUPPLEMENTARY MATERIAL FOR CHAPTER 3: ETEM MODEL

TABLE OF CONTENTS: APPENDIX B

B.1. EXTENDED VIEW OF ETEM MODEL GEOMETRY

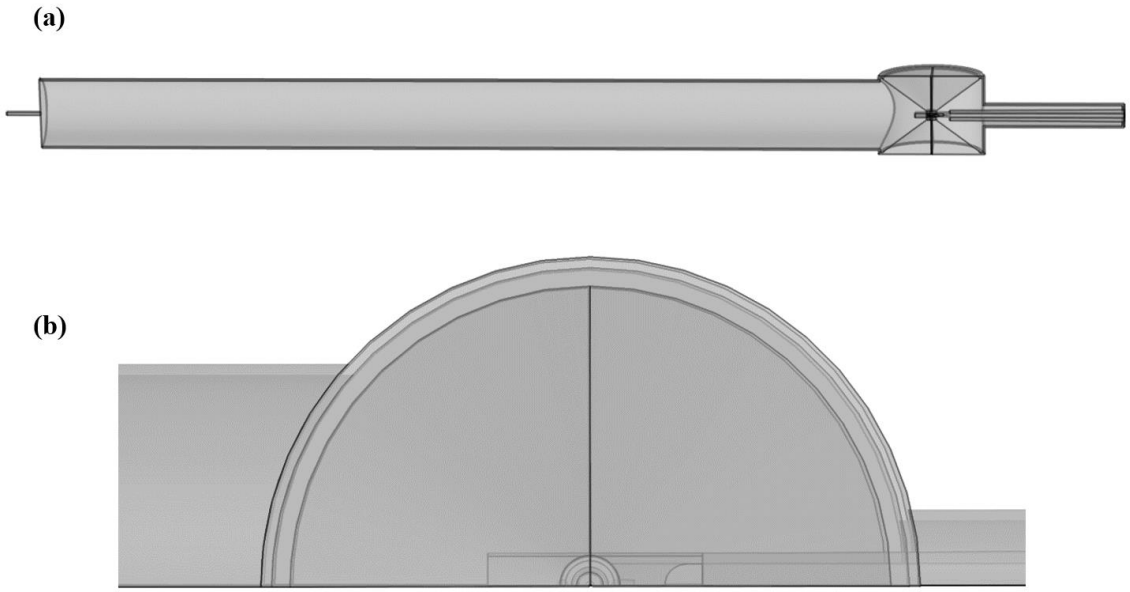

Figure B.1. (a) Full view of model geometry showing reactant gas inlet into ETEM cell which extends approximately one meter out of the cell so that the gas composition in the cell does not impact the inlet composition. (b) Top-down view of the model geometry focused on the ETEM cell and *operando* pellet reactor, which makes both the cylindrical nature of the chamber and the planar symmetry of the model more apparent.

B.2. Dimensionless Number Analysis

Mach number and numerical stability

A dimensionless number analysis was done to justify certain simplifications to the mass and heat transport equations solved by the model. First, to maintain numerical stability, the form of the Navier-stokes equations used in this model requires that the Mach number, Ma, stay below $Ma = 0.3$. The Mach number is calculated as:

Eq. B.1 $$Ma = \frac{v}{a}$$

Here a is the speed of sound in the gas and v is the linear velocity. Given that the speed of sound in gas is generally greater than 200 m s^{-1}, and that the typical gas velocities in the simulation are low around 0.2 m s^{-1}, we expect that the Mach number will stay well below $Ma = 0.3$ and that the numerical stability requirement be satisfied.

Reynolds number and laminar flow

The Reynolds number, Re, was computed to ascertain the flow regime of the gas in the ETEM cell, which is either laminar or turbulent. The Reynolds number is given by:

Eq. B.2 $$Re = \frac{\rho v L}{\mu}$$

Here ρ is the gas density, L is a characteristic length, and μ is the gas viscosity. It is generally accepted that laminar flow occurs for $Re < 100 - 2{,}000$ (Bird et al., 2006). An upper bound on the Reynolds number can be computed by considering the lowest viscosity gas at its highest density and flow rate as it flows through the inlet. Take for example O_2 gas with a room temperature viscosity of $\mu = 2.08 \times 10^{-5}$ Pa*s at low pressure. In this model the highest density is achieved at 4 Torr which provides a gaseous density of 6.83 g*m^{-3} and an inlet linear gas flow rate of 0.239 m s^{-1}. The inlet diameter is taken to be the

characteristic length and it is equal to 0.026 m. Overall this produces a Reynolds number of Re = 4.1 << 2,000. Even near the differential pumping aperture outlets, where the simulated flow is calculated to be ~100 times higher, the Reynolds number would still lie well into the laminar flow regime.

Rayleigh number and natural convection

The gravitational force in the Navier-Stokes equation was ignored on the basis that its primary effect, natural convection, was negligible. This simplification is supported by computing the Rayleigh number, Ra, which describes the significance of buoyancy-driven flow. The calculation for Ra is given by:

Eq. B.3 $$Ra = \frac{g\beta\Delta T L^3}{\upsilon\kappa}$$

Here g is the standard gravitational acceleration, β is the thermal expansion coefficient, ΔT is the temperature difference between the surface and the quiescent fluid, L is a characteristic length, υ is the kinematic viscosity, and κ is the thermal diffusivity. It is generally accepted that natural convection is insignificant for Ra < 1,000–1,700 (Bird et al., 2006). An upper bound for the Rayleigh number in the model can be computed by considering CO_2 which has a relatively low kinematic viscosity and thermal diffusivity. Consider a maximum temperature difference of ΔT = 400 °C and take the cell height for the largest possible dimension, which gives L = 0.04 m. The value of g is known to be 9.806 m s^{-2}. The thermal expansion coefficient of an ideal gas is known to be $\beta = \frac{1}{T}$, so for T = 298 K, we have that $\beta = 3.35 \times 10^{-3}$ K^{-1}. The kinematic viscosity and thermal diffusivity of CO_2 at 4 Torr and 298 K can be calculated Eq. B.6, Eq. B.13, and Eq. B.16, along with the ideal gas law. These computations yield $\upsilon = 1.59 \times 10^{-3}$ m^2 s^{-1} and $\kappa = 2.10 \times 10^{-3}$ m^2 s^{-1}. Overall this yields a Rayleigh number of Ra = 251.1 < 1,000. Considering the thermal

profiles presented in the text, a more appropriate and typical Rayleigh number would consider the dimensions between the hot furnace, where the high-temperature gas is localized, and the water-cooled pole pieces. This dimension is 0.145 cm, which yields a Rayleigh number of $Ra = 0.01 << 1{,}000$. In both cases the dimensionless number analysis suggests that natural convection is not significant. Simulations that include a gravity force and permit natural convection were observed to be essentially identical to those without, so no gravity force is included in the model.

B.3. EXPRESSIONS FOR TRANSPORT PROPERTIES

Mathematical expressions for properties relevant to heat and mass transport have been located from the literature and are summarized here. Polynomial expressions for the viscosity of CO, O_2, and CO_2 were determined from published data (AIChE, 2005; Vesovic et al., 1990; Laesecke et al., 1990) and are given in Eq. B.4, Eq. B.5, and Eq. B.6 below:

Eq. B.4 $$\mu_{CO} = -2.210 \times 10^{-11}\, T^2 + 5.796 \times 10^{-8}\, T + 2.368 \times 10^{-6} \text{ [Pa s]}$$

Eq. B.5 $$\mu_{O_2} = -2.485 \times 10^{-11}\, T^2 + 6.873 \times 10^{-8}\, T + 2.374 \times 10^{-6} \text{ [Pa s]}$$

Eq. B.6 $$\mu_{CO_2} = -1.738 \times 10^{-11}\, T^2 + 5.889 \times 10^{-8}\, T - 1.082 \times 10^{-6} \text{ [Pa s]}$$

Expressions for the binary diffusivities of CO, O2, and CO2 are found in the low pressure limit and are given in Eq. B.7, Eq. B.8, and Eq. B.9 below:

Eq. B.7 $$D_{CO,CO_2} = 5.77 \times 10^{-6}\, T^{1.803} \times \frac{101325}{p}\ [cm^2\, s^{-1}]$$

Eq. B.8 $$D_{CO,O_2} = 1.13 \times 10^{-5}\, T^{1.724} \times \frac{101325}{p}\ [cm^2\, s^{-1}]$$

Eq. B.9 $$D_{O_2,CO_2} = 1.56 \times 10^{-5}\, T^{1.661} \times \frac{101325}{p}\ [cm^2\, s^{-1}]$$

Note that $D_{i,k}$ with $i = k$ is defined as 1.

Mixture-averaged diffusivities, D_i^m, are calculated for each component i by Eq. B.10:

Eq. B.10 $$D_i^m = \frac{1-\omega_i}{\sum_{i \neq k} \frac{x_k}{D_{ik}}}$$

Here, D_i^m represents the mixture-averaged diffusivity for component i, ω_i represents the mass fraction of component i in the mixture, x_k represents the mole fraction of component k, and D_{ik} is again the binary diffusivity for components i and k, calculated in Eq. B.7 – Eq. B.9.

Polynomial expressions for the heat capacities of CO, O_2, and CO_2 are located in the literature (McBride et al., 2002) and given in Eq. B.11 – Eq. B.13 below:

Eq. B.11 $$\frac{C_{p_{CO}}}{R} = 3.02 \times 10^{-12}\, T^4 - 1.08 \times 10^{-8}\, T^3 + 1.45 \times 10^{-5}\, T^2 - 8.17 \times 10^{-3}\, T - 2.92 \times 10^{2}\, T^{-1} + 1.48 \times 10^{4}\, T^{-2} + 5.72$$

Eq. B.12 $$\frac{C_{p_{O_2}}}{R} = 1.03 \times 10^{-12}\, T^4 - 2.02 \times 10^{-9}\, T^3 - 6.83 \times 10^{-7}\, T^2 + 4.29 \times 10^{-3}\, T + 4.84 \times 10^{2}\, T^{-1} - 3.42 \times 10^{4}\, T^{-2} + 1.11$$

Eq. B.13 $$\frac{C_{p_{CO_2}}}{R} = 2.84 \times 10^{-13}\, T^4 - 7.68 \times 10^{-10}\, T^3 - 2.12 \times 10^{-7}\, T^2 + 2.50 \times 10^{-3}\, T - 6.26 \times 10^{2}\, T^{-1} + 4.94 \times 10^{4}\, T^{-2} + 5.30$$

Polynomial expressions for the unadjusted thermal conductivities of CO, O_2, and CO_2 are found as a function of temperature in the low-pressure limit (Vesovic et al., 1990; Millat & Wakeham, 1989; Laesecke et al., 1990) and are given in Eq. B.14 – Eq. B.16 below:

Eq. B.14 $$k_{0,CO} = -2.178 \times 10^{-8}\, T^2 + 8.817 \times 10^{-5}\, T + 5.410 \times 10^{-4}\ [W\, m^{-1}\, K^{-1}]$$

Eq. B.15 $$k_{0,O_2} = -1.161 \times 10^{-8}\, T^2 + 7.903 \times 10^{-5}\, T + 3.485 \times 10^{-3}\ [W\, m^{-1}\, K^{-1}]$$

Eq. B.16 $$k_{0,CO_2} = 8.309 \times 10^{-5}\, T - 8.121 \times 10^{-3}\ [W\, m^{-1}\, K^{-1}]$$

B.4. Pellet Loading Profile and Sensitivity Analysis to X_{CO}

Based on observations during *operando* TEM sample preparation, it was decided to model the loading of catalyst in the *operando* pellet with an egg-shell profile, whereby the majority of catalyst is located near the pellet's surface. We incorporate the loading profile into the model by introducing a spatial dependence on the magnitude of A, the pre-exponential factor of the reaction rate constant. All else equal, the rate of a catalytic reaction scales proportionally with the mass of catalyst involved, so factoring the loading profile into the linear term of the rate constant offers a simple way to describe the distribution of catalyst loaded into the *operando* pellet reactor. We describe the egg-shell distribution with an exponential function that depends on the depth of penetration into the pellet, as described in Eq. B.17 below:

Eq. B.17 $$A(d) = A_0 * e^{-\gamma * d}$$

Here, $A(d)$ represents the pre-exponential factor with a spatial dependence, d represents the depth of penetration into the pellet, A_o represents a constant that governs the overall magnitude of the pre-exponential factor, and γ is a parameter that controls the shape of the loading profile.

The penetration depth d at a given point within the pellet was calculated as the distance from that point to the nearest external surface of the pellet. It is possible to define a shell thickness for the egg-shell catalyst loading profile. Here, we define the shell thickness to be the distance into the *operando* pellet throughout which $1 - \frac{1}{e} \cong 63\%$ of the catalyst mass is contained. Visualizations of the catalyst loading profile for shell thicknesses ranging from 28 – 300 μm are provided in Figure B.2(a)-(d) below. As the

shell thickness was varied, the integrated magnitude of *A* was normalized in order to maintain the same amount of catalyst in all cases.

A sensitivity analysis was performed to evaluate the impact the uniformity of the catalyst loading profile had on the distribution of catalytically produced CO_2. Steady state simulations were performed for an inlet reactant gas mixture of ~2.2 Torr of stoichiometric CO and O_2 with a furnace thermocouple set point of 200 – 270 °C. Note that this corresponds to a condition when the catalyst is active and producing CO_2. The thickness of the catalyst shell was varied across an order of magnitude from 28 – 300 μm, while the mole fraction of catalytically produced CO_2 was investigated along the EELS line, at the TEM grid, and in the *operando* pellet. The mole fraction of catalytically-produced CO_2 along the EELS line, at the TEM grid, and in the *operando* pellet is plotted as a function of the catalyst shell thickness in Figure B.3.

Varying the thickness of the catalyst shell from 28 – 300 μm had a weak impact on the CO_2 mole fraction for the two temperatures explored here. For simulations conducted at 270 °C, as the shell thickness increased from 28 to 300, the value of the CO_2 mole fraction along the EELS line increased from 0.571 to 0.589 (by 0.018, or 3.1%). At 200 °C, the effect is less and the CO_2 mole fraction along the EELS line changes by about 1.2%. As seen in the graph by comparing the top and bottom curves, variations of 1 – 3% are far smaller than the changes that result from ramping up the furnace temperature. Thus, we conclude that the interpretation of the results presented in the main text are not sensitive to slight changes in the distribution of the catalyst loaded in the reactor. A shell thickness of 40 μm was used in the simulations in the main text.

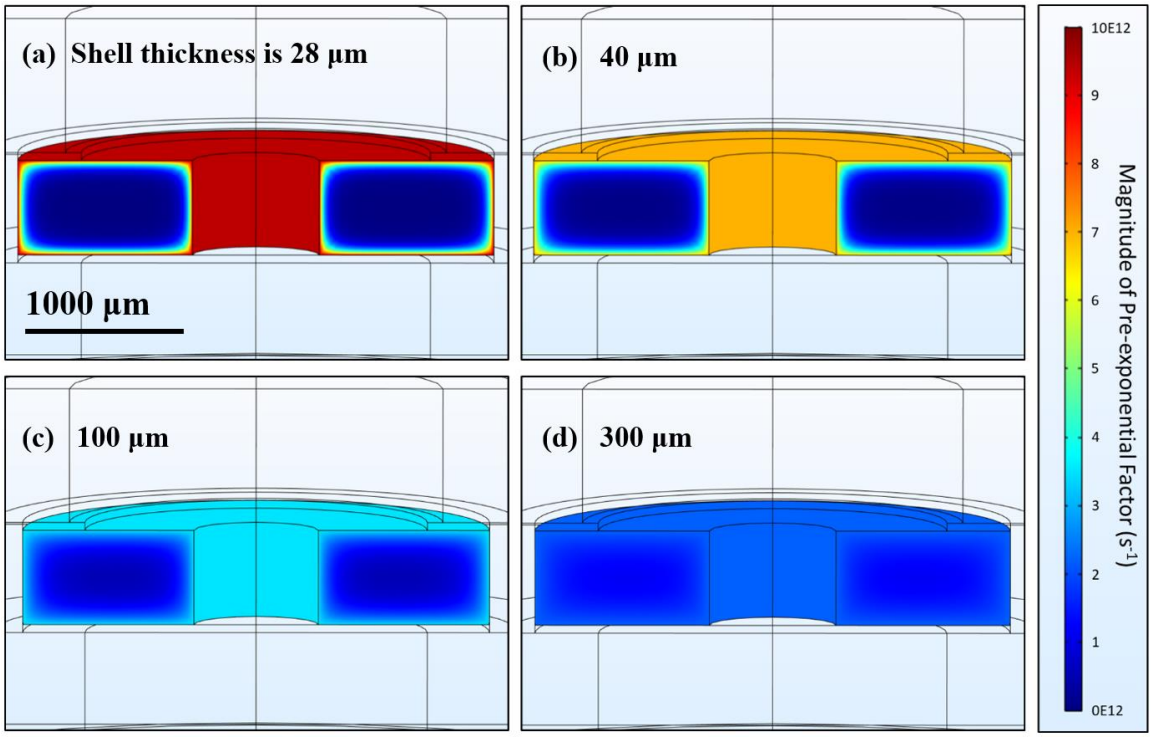

Figure B.2. Surface plots of the loading profiles of catalyst in the *operando* pellet that give catalyst shell thickness of (a) 28 µm, (b) 40 µm, (c) 100 µm, and (d) 300 µm. The quantity plotted is the magnitude of the spatially varying pre-exponential factor, *A(d)*, with the legend displaying units scaled to 1E12 s^{-1}. A spatial scale bar of 1000 µm is provided in (a). Note that as the shell thickness was changed, the integrated magnitude of *A* throughout the pellet was normalized so the total amount of catalyst modeled in the reactor remained the same. Also note that the profile for a shell thickness of 300 µm yields a catalyst loading that is highly uniform.

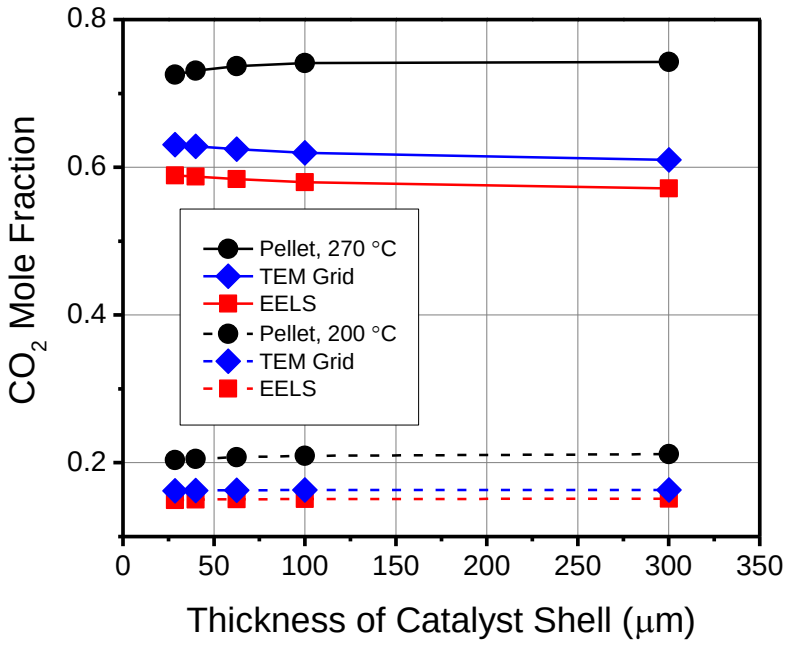

Figure B.3. Effect of varying the catalyst shell thickness on the mole fraction of catalytically-produced CO_2 in the *operando* pellet (black circles), at the TEM grid (blue diamonds), and along the EELS line (red squares). Results are shown for simulations conducted at both 270 °C (solid lines) and 200 °C (dashed lines). Note that a shell thickness of 40 μm was used in the simulations presented in the main text.

B.5. Deriving CO Conversion in Terms of CO_2 Mole Fraction

Recall from Eq. 3.15 in the main text that the CO conversion X_{CO} is defined as:

Eq. B.18 $$X_{CO} = \frac{\dot{n}_{CO,in} - \dot{n}_{CO,out}}{\dot{n}_{CO,in}}$$

Where $\dot{n}_{CO,in}$ is the molar flow rate (mol/s) of CO into the ETEM chamber, which is calculated in the model by taking a surface integral of the molar flux of CO across the inlet surface into the ETEM. The variable $\dot{n}_{CO,out}$ is the molar flow rate of CO out of the ETEM, which is calculated similarly by taking a surface integral of the molar flux of CO across the pumping aperture outlets. Notice that Eq. B.18 can be reformulated as a carbon balance – i.e., either C is in CO or it is in CO_2:

Eq. B.19 $$X_{CO} = \frac{\dot{n}_{CO_2,out}}{\dot{n}_{CO,out} + \dot{n}_{CO_2,out}}$$

Dividing both halves of the fraction by the total outlet molar flow rate, $\dot{n}_{total,out}$, we obtain the CO conversion in terms of the mole fraction of CO, y_{CO}, and of CO_2, y_{CO2}:

Eq. B.20 $$X_{CO} = \frac{\dot{n}_{CO_2,out}}{\dot{n}_{CO,out} + \dot{n}_{CO_2,out}} \div \frac{\dot{n}_{total,out}}{\dot{n}_{total,out}} = \frac{y_{CO_2}}{y_{CO} + y_{CO_2}}$$

Here, the mole fraction of species i is defined in a standard way as the number of moles of that species divided by the total number of moles of all species. For example, the mole fraction of CO_2 within a volume of interest may be calculated as:

Eq. B.21 $$y_{CO2} = \frac{n_{CO_2}}{n_{total}} = \frac{n_{CO_2}}{n_{CO} + n_{O_2} + n_{CO_2}}$$

For a stoichiometric mixture of reactants, y_{CO} can be expressed in terms of y_{CO2}:

Eq. B.22 $$y_{CO} = 1 - y_{CO_2} - y_{O_2} = 1 - y_{CO_2} - \frac{1}{2} y_{CO} = (1 - y_{CO_2}) \times \frac{2}{3}$$

Substituting this into Eq. B.20, we have that the CO conversion in terms of y_{CO2} is:

Eq. B.23 $$X_{CO} = \frac{y_{CO_2}}{(1 - y_{CO_2}) \times \frac{2}{3} + y_{CO_2}}$$

APPENDIX C

SUPPLEMENTARY MATERIAL FOR CHAPTER 4: *OPERANDO* TEM OF PT/CEO_2

TABLE OF CONTENTS: APPENDIX C

C.1. Characterization of Catalyst Structure and Activity for CO Oxidation

Bulk characterization was performed using X-ray diffraction (XRD) on a Bruker D-5000 with a Cu Kα source (λ = 0.15406 nm). The powder XRD patterns of the bare CeO_2 and Pt-loaded CeO_2 nanocubes are shown in Figure C.1. A simulated XRD pattern of an infinite crystal of CeO_2 is also shown for reference (*JCPDS* No. 34-0394). The peaks present in the XRD pattern for the bare CeO_2 nanocubes (blue line) match well with that of the simulated crystal (black line), indicating that the sample is phase-pure CeO_2 (space group Fm-3m, a = 5.41 Å). The XRD pattern for the Pt/CeO_2 nanocubes (red line) is essentially identical to that of the bare CeO_2 support.

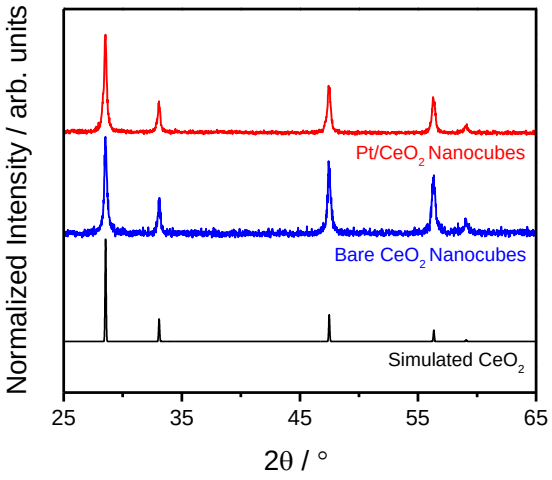

Figure C.1. Powder XRD patterns from (blue) bare CeO_2 and (red) Pt-loaded CeO_2 compared with (black) a simulated pattern from a perfect CeO_2 crystal.

The as-reduced Pt/CeO_2 catalyst powder was imaged in a probe-corrected STEM at 200 kV. High angle annular dark field (HAADF) or so-called Z-contrast images were collected of many different areas of the TEM specimen and the Pt nanoparticle size distribution was determined by measuring the size of about 500 different Pt nanoparticles. Figure C.2 displays two representative HAADF STEM images of the Pt/CeO_2 powder showing the dispersion of the Pt on the CeO_2 support along with a histogram of the size

distribution measurement. The histogram of the size distribution shows that the Pt nanoparticle population has an average size of 1.6 nm.

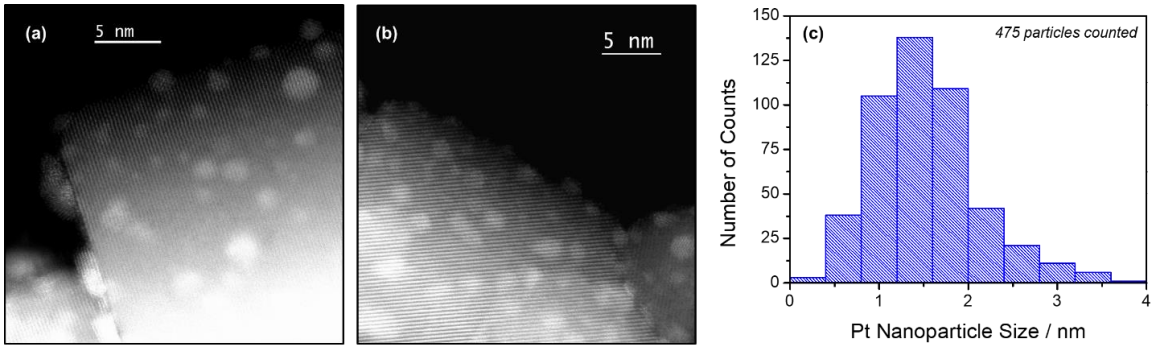

Figure C.2. (a, b) Z-contrast STEM images of a typical Pt-loaded CeO_2 nanoparticle imaged during the Pt nanoparticle size measurement, and (c) Pt nanoparticle size distribution histogram (n = 475) for the 17 wt.% Pt/CeO_2 catalyst, which exhibits an average Pt particle size of 1.6 nm.

The catalyst's activity for CO oxidation was evaluated in a packed bed plug flow reactor (further details on the experimental methodology are given in Chapter 2, Section 2.2 and Chapter 4, Section 4.2.1). The CO conversion, X_{CO}, was quantified by calculating $X_{CO} = (CO_{in}\text{-}CO_{out})/CO_{in}$, where CO_{in} and CO_{out} denote the molar flowrate of CO into and out of the reactor, respectively. A reaction rate was calculated by multiplying the conversion by the molar flow rate of CO into the reactor. Turnover frequencies were computed by normalizing the reaction rates to the estimated number of Pt atoms at the metal-support interfacial perimeter, as determined by the derivation described in the next section. We normalize to the number of Pt atoms at the perimeter as we assume that the reaction occurs through a Mars-van Krevelen mechanism at the perimeter of the metal-support interface. We note that this normalization assumes that each perimeter Pt atom is active and that the number of perimeter Pt atoms is identical both in vacuum conditions, where the number is counted, and under reaction conditions, where the catalysis takes place. Essentially, though, the TOF reported here is linearly related to the mass-normalized rate of product formation. Activation energies for CO oxidation were

calculated through an Arrhenius analysis of the activity data taken in the low-conversion regime (i.e., < 25%). Figure 4.1a of the main text shows the light-off curves for CO oxidation. Figure C.3 below shows the Arrhenius analysis of the rate data, which reveals that the Pt/CeO_2 catalyst shows an apparent activation energy E_a of 74 kJ/mol.

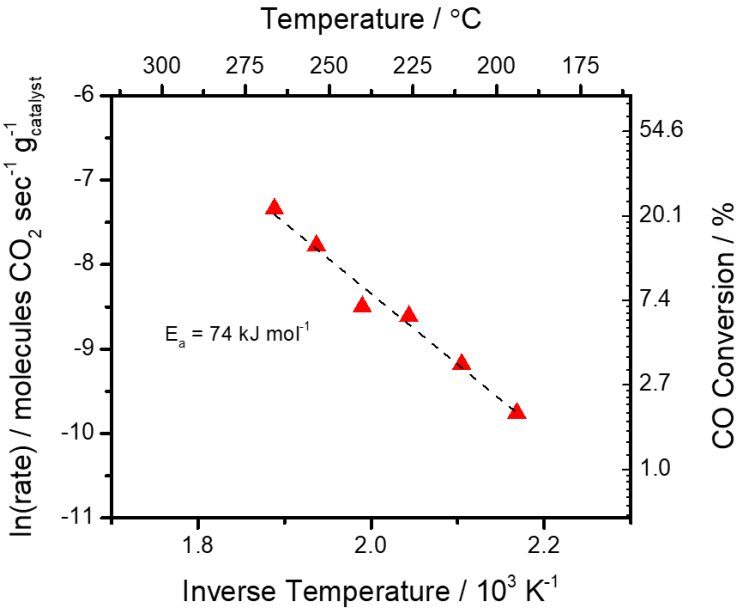

Figure C.3. Arrhenius analysis of the Pt/CeO_2 catalyst light-off conversion data (see Figure 4.1a of the main text) shows that the apparent E_a for CO oxidation is 74 kJ mol^{-1}.

C.2. Derivation of Turnover Frequency (TOF) on an Interfacial Perimeter-Site Basis from Pt Nanoparticle Size Distribution

The number of atoms of Pt at the metal-support interfacial perimeter can be determined from the particle size histogram by assuming that the Pt nanoparticles have a hemispherical shape (Ertl et al., 1997). A derivation of this quantity and a sample calculation of the TOF for a given conversion are provided below. First, we define the TOF as:

Eq. C.1 $$TOF\ [\frac{molecules\ CO_2}{perimeter\ site*second}] = \frac{F_{CO,in} \times X_{CO}}{m_{Pt/CeO_2} \times \gamma}$$

Where $F_{CO,in}$ represents the molar flowrate of CO into the *ex situ* reactor or the environmental cell, X_{CO} represents the CO conversion, m_{Pt/CeO_2} represents the mass of Pt/CeO_2 catalyst loaded into the *ex situ* reactor or *operando* pellet, and γ represents the number of atoms of Pt at the perimeter of the metal-support interface *per gram of* Pt/CeO_2 *catalyst*. The quantities $F_{CO,in}$ and m_{Pt/CeO_2} are controllable, and X_{CO} is determined experimentally. To calculate the TOF for a given X_{CO}, one simply requires an estimate of the number of perimeter sites per gram of catalyst, i.e., γ.

The value of γ was determined from HAADF-STEM measurements by assuming that the Pt nanoparticles have a hemispherical shape (Ertl et al., 1997). First, the volume, V_i, and interfacial perimeter length (i.e., circumference), L_i, was calculated for each particle i measured with diameter d_i, as described in the following equations:

Eq. C.2 $$V_i = \frac{2}{3}\pi \left(\frac{d_i}{2}\right)^3$$

Eq. C.3 $$L_i = \pi d_i$$

The total volume, V_{total}, and interfacial perimeter length, L_{total}, of all the particles measured in the data set is then computed as the sum of all n measurements (here n = 475):

Eq. C.4 $V_{total} = \sum_{i=1}^{n} V_i$

Eq. C.5 $L_{total} = \sum_{i=1}^{n} L_i$

Using the density of Pt, ρ_{Pt} = 21.45 g/cm^3, the total mass of Pt observed in the measurements is:

Eq. C.6 $m_{total} = V_{total} \times \rho_{Pt}$

This allows for a mass-specific interfacial perimeter length, L'_{total}, to be calculated as:

Eq. C.7 $L'_{total} = L_{total} \div m_{total} \times 0.17 \left[\frac{g_{Pt}}{g_{Pt/CeO_2}}\right]$

The factor of 0.17 is included since the catalyst is 17% Pt by weight. The last quantity needed to calculate the number of perimeter Pt atoms per gram catalyst is a value for the width of a Pt atom, $d_{Pt\ atom}$. Given the density of Pt, ρ_{Pt}, we can estimate a value by first calculating the number of atoms in a cubic nm of Pt, *i.e.*, the atomic volume density, φ_{Pt}:

Eq. C.8 $\varphi_{Pt} = \rho_{Pt} \div M_{Pt} \times N_{Avogadro}$

Where M_{Pt} is the molar mass of Pt, 195.08 g mol^{-1}, and $N_{Avogadro}$ is Avogadro's number, 6.02 × 10^{23} atoms mol^{-1}. The width of a Pt atom can be computed by inverting and taking the cube root of the atomic volume density:

Eq. C.9 $d_{Pt\ atom} = \left(\frac{1}{\varphi_{Pt}}\right)^{\frac{1}{3}}$

And so, the number of perimeter Pt atoms per gram catalyst, γ, is:

Eq. C.10 $\gamma = L'_{total} \div d_{Pt\ atom}$

Following this arithmetic and performing the analysis on the Pt nanoparticle size distribution plotted in Figure C.2c, a value for γ of 5.45 × 10^{19} sites g^{-1} is obtained. A TOF can now be calculated for a given conversion assuming the CO flowrate and mass of

catalyst in the reactor are known. During the *operando* TEM experiment, around 180 ug of Pt/CeO_2 catalyst was loaded into the operando pellet. The inlet flow rate of CO into the cell was 0.08 SCCM or 5.94×10^{-8} mol CO sec^{-1}, which is 3.58×10^{16} molecules CO sec^{-1}. It should be briefly mentioned here that the calculated TOF will still need to be corrected by finite element simulations in order to accurately represent the reaction rate of catalyst particles supported on the TEM grid, which is discussed at length in the following section of the Appendix. Regardless of this additional complexity, for an example CO conversion of 10%, the *in situ* TOF would be calculated as:

Eq. C.11 $$TOF = \frac{F_{CO,in} \times X_{CO}}{m_{Pt/CeO2} \times \gamma} = \frac{3.58*10^{16} \times 0.10}{180*10^{-6} \times 5.45 \times 10^{19}} \approx 0.37 \left[\frac{molecules\ CO_2}{perimeter\ site*second}\right]$$

C.3. Details of Finite Element Simulation of *Operando* ETEM Reactor for Pt/CeO_2

Finite element simulations of the *operando* ETEM reactor were performed by adapting the model described in Chapter 2, Section 2.4.2 and in Chapter 3 to the experimental situation involving Pt/CeO_2. Steady-state simulations were performed under conditions nominally identical to the *operando* ETEM experiment described in Chapter 4. A reactant gas inflow of CO and O_2 in a 1:1.375 ratio was admitted to the cell. The total inlet flowrate was adjusted to 0.08 SCCM in order achieve a cell static pressure of 0.57 Torr. The reaction was modeled as 0^{th} order, with an activation energy, E_a, of 74 kJ mol^{-1}, which was taken from the Arrhenius analysis done on the plug flow reactor data as presented in Figure C.3. The spatial distribution of catalyst in the pellet was modeled with an egg-shell profile. The furnace temperature was set in the range of 144 – 297 °C.

Here, we have employed the model to establish a framework that allows us to link the reactant conversion measured along the EELS line to the reaction rate of the catalyst on the TEM grid. The reader is referred to Chapter 3, Section 3.3.5 for detailed information on the reaction rate analysis. As discussed in those sections, one can determine the mass-normalized rate for the catalyst on the TEM grid by integrating the mass and rate along the innermost surface of the pellet (Vincent et al., 2020). This rate, which refer to as r_{grid}, is tabulated in Table C.1 as function of temperature for the conditions relevant to Chapter 4. Experimentally, the rate of product formation may be estimated from the EELS CO conversion measurement. The mass-normalized rate estimated by the EELS conversion simulation in the model is tabulated as a function of temperature in Table C.1. The CO conversion values estimated through EELS are also given for reference.

Table C.1. Summary of reaction rate analysis. The CO conversion estimated through EELS is presented as a function of the furnace temperature set point. The mass-normalized rate of CO_2 formation obtained by integrating the reaction rate and mass within a 50 μm thick layer at the surface along the inner hole in the pellet, $\boldsymbol{r_{grid}}$, which represents the rate at the TEM grid, is presented, along with the rate estimated from the EELS CO conversion measurement, $\boldsymbol{r_{EELS}}$. Finally, the ratio of the rate estimated through EELS and the rate at the TEM grid is given.

Furnace Set Point (°C)	X_{CO} Estimated from EELS (%)	r_{grid} (μmol CO_2 sec^{-1} g_{cat}^{-1})	r_{EELS} (μmol CO_2 sec^{-1} g_{cat}^{-1})	Ratio of r_{EELS} : r_{grid} (%)
144	0.11	0.26	0.21	80%
202	1.26	3.48	2.44	70%
251	7.07	19.83	13.66	69%
261	9.65	27.20	18.65	69%
271	13.01	36.89	25.16	68%
275	14.61	41.55	28.25	68%
285	19.33	55.51	37.40	67%
297	26.61	77.57	51.53	66%

It is of interest to compare the estimated – and experimentally measurable – rate of product formation, r_{EELS}, to the value which represents the rate at the TEM grid, r_{grid}. The last column of Table C.1 presents the ratio of the two values. Observe that the ratio of r_{EELS} to r_{grid} is not constant with conversion but varies by nearly 20% from 0.80 to 0.66 over the conditions explored here. Previously we have shown that under higher conversion conditions (e.g., X_{CO} > 0.70), the difference between the r_{EELS} and r_{grid} can grow beyond 200% (for instance, see Figure 3.8). This clearly demonstrates the need for and power of a model that allows one to relate the reactant conversion to the true reaction rate (i.e.,

activity) of the imaged catalyst. In the context of the present work, the true rate can be calculated correctly by scaling the rate measured through EELS by a conversion-dependent factor that is given in in the last column of Table C.1.

In addition to establishing a relationship between the measured conversion and the quantitative chemical kinetics of the catalyst, it is also important to investigate the extent of any thermal gradients that may exist within the reactor. Additional analysis (not shown here, see Vincent & Crozier, 2021) demonstrates that the temperature distributions appear largely uniform in the hot zone of the reactor were the catalyst is located. The results are similar to those reported in Chapter 3, Section 3.3.2 and suggest the reactor can be treated as isothermal.

C.4. TIME-AVERAGED IMAGE METHODOLOGY

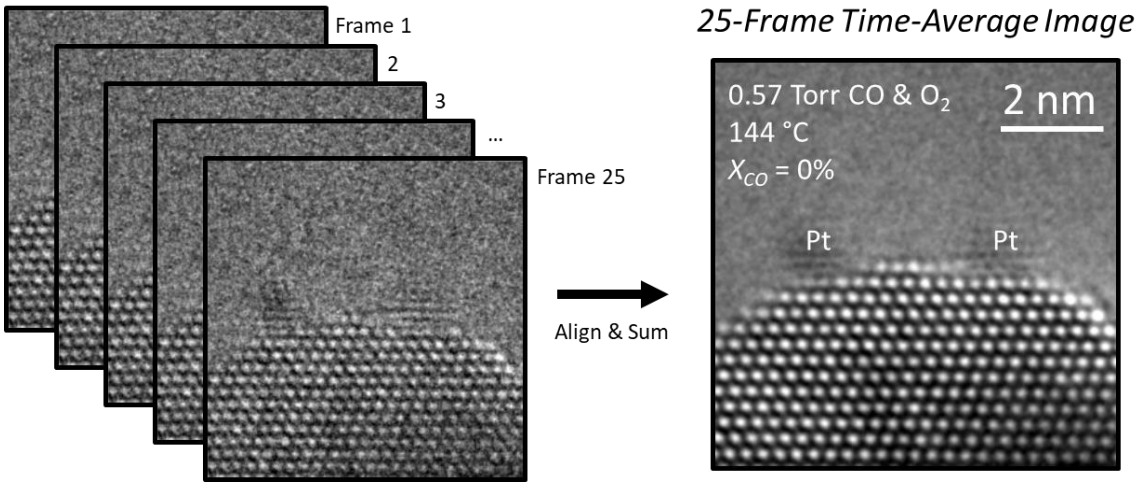

Figure C.4. Schematic of time-averaged image methodology. The limited electron flux of about 10^3 e^- $Å^{-2}$ s^{-1} used here results in a poor SNR in each individual 0.5 s exposure frame (left). To increase the SNR in the image without increasing the electron dose, multiple independent frames were selected, aligned, and summed together to produce a time-averaged image (right). Individual images were selected on the basis of bulk Ce column visibility to avoid artifacts from drift in the sample or electron optics. The time-average shown at right was constructed from 25 frames, which yields a 12.5 s time-average. The time-averaged image exhibits a marked increase in SNR available for local structural analysis.

C.5. Multislice TEM Image Simulations of Contrast Reversals in CeO_2-supported Pt Nanoparticles Undergoing Rigid-body Rotations

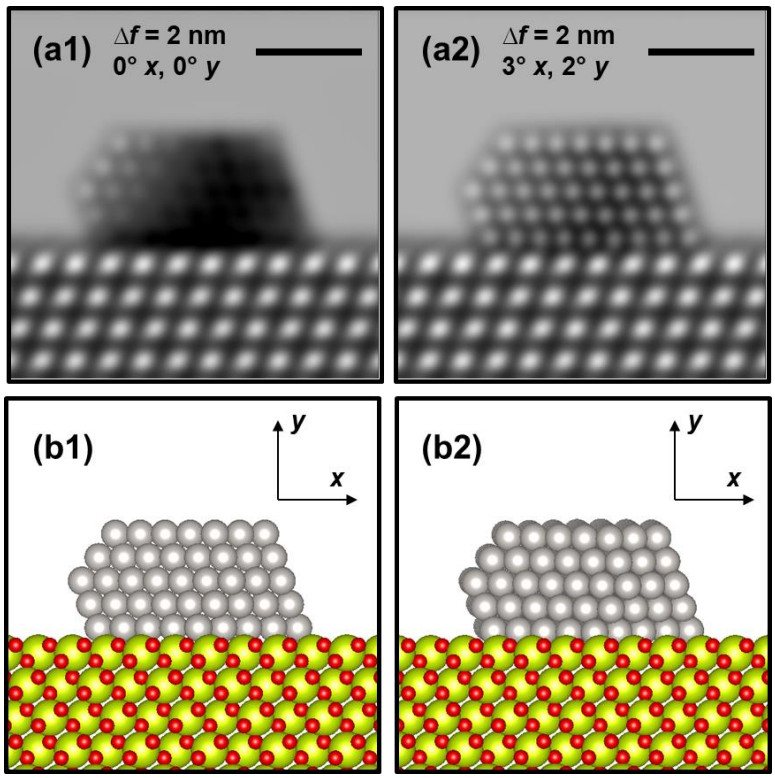

Figure C.5. Simulations of a Pt / CeO_2 (111) particle showing mixed black and white Pt atomic column contrast and contrast reversals due to rigid body rotations. Figure (a1) presents a simulation of a Pt particle oriented along the beam without any tilt, for an electron optical defocus of 2 nm. Notice the appearance of mixed black and white atomic column contrast in the Pt due to a contrast reversal occurring between the thinner sites on the edge of the particle and the thicker sites in the particle center. Figure (a2) presents another simulation at the same defocus but now for a Pt particle that has been tilted by three degrees about the horizontal *x* axis and by two degrees about the vertical *y* axis (see (b1) and (b2) for the atomic models as well as the orientation of the axes). In the case that the particle is tilted, the image simulated at a defocus of 2 nm no longer shows a mixture of black and white atomic column contrast but instead shows only white atomic column contrast, presumably due to a disruption in the electron beam channeling conditions. Simulations performed at other comparable tilts (i.e., of a few degrees) show similar behavior. An isotropic vibration envelope of 85 pm was applied during the image calculation. During the simulation, the CeO_2 support was tilted independently by 1.5° in *x* and 1.0° in *y*. The tilt information in the figure inset of (a1) and (a2) therefore denote the orientation of the Pt with respect to the incident electron beam. Scale bars in (a1) and (a2) correspond to 2 nm. In the models, Pt is gray, Ce is yellow-green, and O is red.

C.6. Analysis of Bragg Spots in FTs of Pt Nanoparticles Imaged under CO Oxidation Reaction Conditions

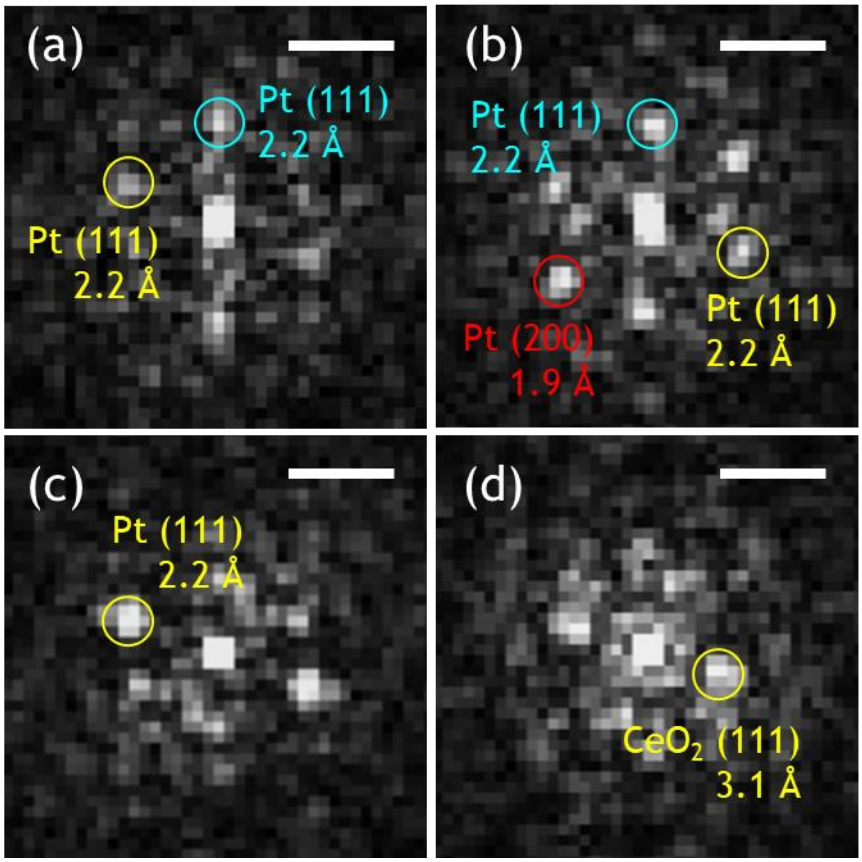

Figure C.6. Indexing major Fourier transform (FT) spots shown in Figure 4.2(f1) – (f4) in the main text. Here, (a) corresponds to (f1), (b) to (f2), and so on. Major FT spots corresponding to the (111) and/or (200) lattice plane spacings of the Pt metal phase can be seen in (a), (b), and (c), while in a spot corresponding to the CeO_2 (111) lattice plane spacing is discernable in (d). Color coding is simply for clarity. The scale bar in each subfigure corresponds to 5.0 nm^{-1}.

C.7. Dynamic Structural Response of CeO_2-supported Pt Nanoparticles at Elevated Temperatures

The analysis of the time-averaged *operando* TEM images shows that the turnover frequency for CO oxidation is correlated with structural dynamics taking place in the Pt nanoparticles and at/near the three-phase boundary (TPB). However, as the catalyst must be heated in order to be activated, it may be reasoned that the dynamics are driven by the elevated temperature of the catalyst and not the catalytic chemistry. We have therefore performed *in situ* TEM imaging experiments in inert gases at elevated temperatures, in order to investigate what may be called spectator fluxional behavior attributed only to the presence of applied heat and not to catalytic surface chemistry. Some of the results of these experiments demonstrating the lack of fluxional behavior attributed to thermal effects were presented in Chapter 4, Section 4.3.5 of the main text (see, e.g., Figure 4.8). This appendix section goes into further detail by presenting additional images of the catalyst at 20 °C and 300 °C (i.e., Figure C.7), as well as by presenting evidence for a lack of CeO_2 surface lattice expansion at elevated temperatures of 300 °C in a gas atmosphere N_2.

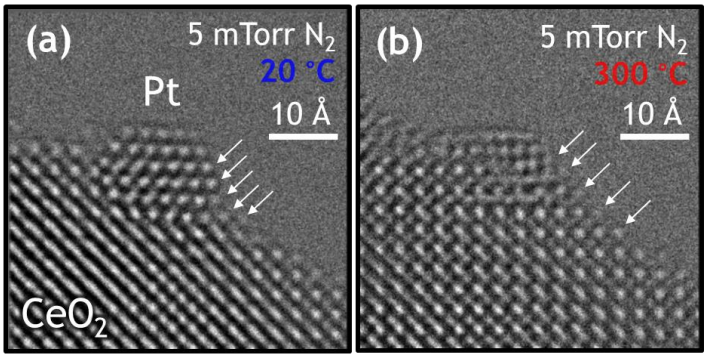

Figure C.7. Additional half-second exposure *in situ* ETEM images of the same nanoparticle of a Pt/CeO_2 catalyst in 5 mTorr N_2 at **(a)** 20 °C and **(b)** 300 °C. Clearly-resolved atomic columns bridging the Pt/CeO_2 TPB are indicated with white arrows.

We investigate the lattice plane separation distance of the top layer on the CeO_2 support near the Pt/CeO_2 interface. The surface lattice plane separation was measured

from intensity line profiles taken from the bulk of the CeO_2 toward the surface; the region over which the profiles were taken at 20 °C and 300 °C are indicated in Figure C.8a/b, and the intensity profiles are themselves given in Figure C.8c. Measurements of the surface and the sub-surface lattice plane separation distance yield 1.98 ± 0.1 Å at both temperatures. Here we note that these measurements match those obtained from the bulk of the nanoparticle and that they agree with the accepted CeO_2 (110) Miller plane spacing of 1.91 Å. Thus, the outward CeO_2 surface relaxation observed under *operando* conditions also appears to be a consequence of structural dynamics that are driven by catalytic chemistry and not heating to 300 °C alone.

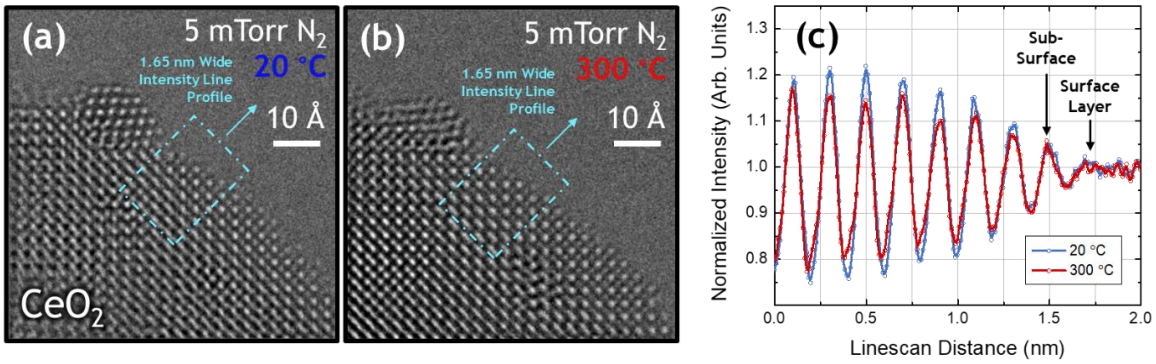

Figure C.8. Half-second exposure *in situ* ETEM images of the same nanoparticle of a Pt/CeO_2 catalyst in 5 mTorr N_2 at (a) 20 °C and (b) 300 °C, which were presented in Figure 4.8 and which are shown here again to indicate the regions over which integrated intensity line profiles were taken to measure the surface lattice plane separation distance. The regions are indicated with light blue dashed boxes; the profiles were taken in the arrowed direction which lies perpendicular to the CeO_2 (110) surface. In (c) the intensity line profiles at 20 °C (blue line) and 300 °C (red line) are plotted overtop one another. The line profiles were normalized to the average vacuum intensity; original data points are plotted as circles along with an interpolated spline function for clarity. The surface layer and the sub-surface lattice plane are indicated in the graph.

C.8. Additional *In Situ* ETEM Image Time-series of CeO2-supported Pt Nanoparticles under CO Oxidation Reaction Conditions

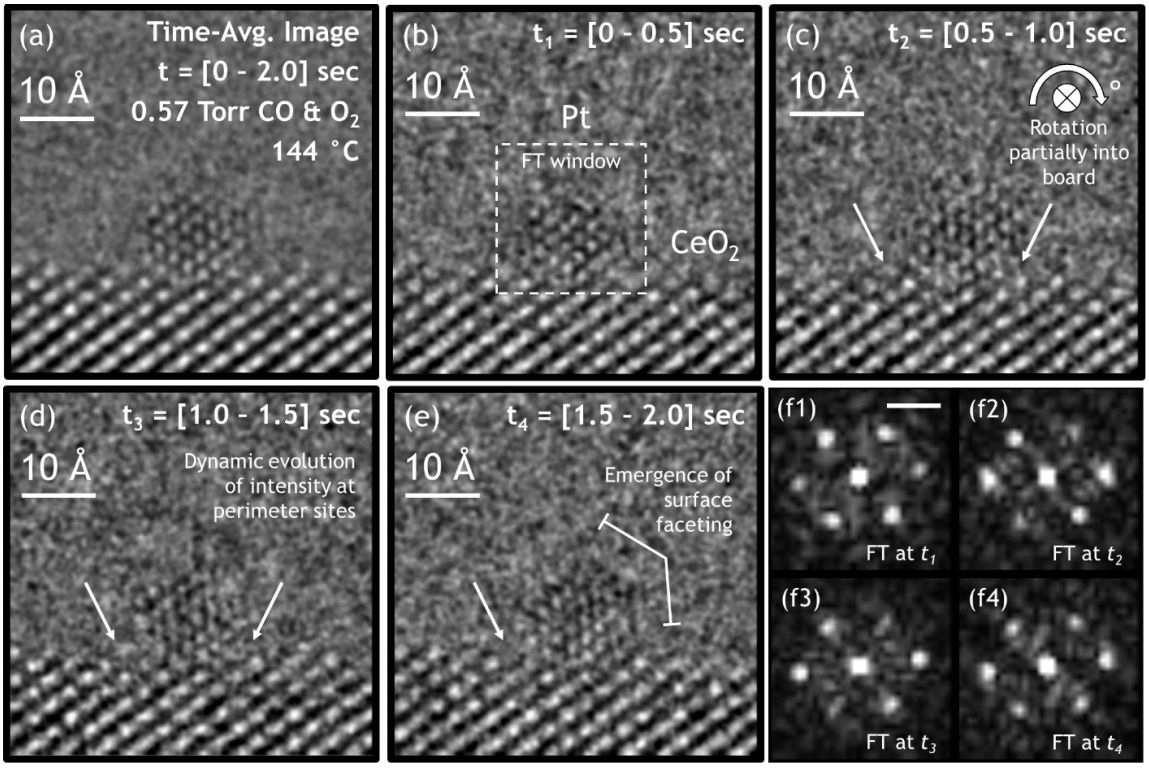

Figure C.9. *In situ* ETEM image time-series of CeO_2-supported Pt NP at 144 °C in 0.57 Torr of CO and O_2. Part (a) shows the time-averaged image of the catalyst, obtained by summing together the individual 0.5 second exposure frames over the entire over [0 – 2.0] second acquisition period. Parts (b) – (e) show the atomic-scale structural dynamics that evolve over 0.5 second intervals from t = 0 seconds to t = 2.0 seconds. Parts (f1) – (f4) display the FT taken at each time interval from the windowed region around the Pt NP, as denoted in (b). The scale bar in (f1) is 5.0 nm^{-1}. Images have been processed with a bandpass filter for clarity. FTs were produced from unfiltered, windowed images that were processed with a Hanning function to remove edge artifacts caused by windowing; the modulus of the FT is shown.

C.9. Analysis of Intensity Line Profiles in *Operando* Time-averaged Images

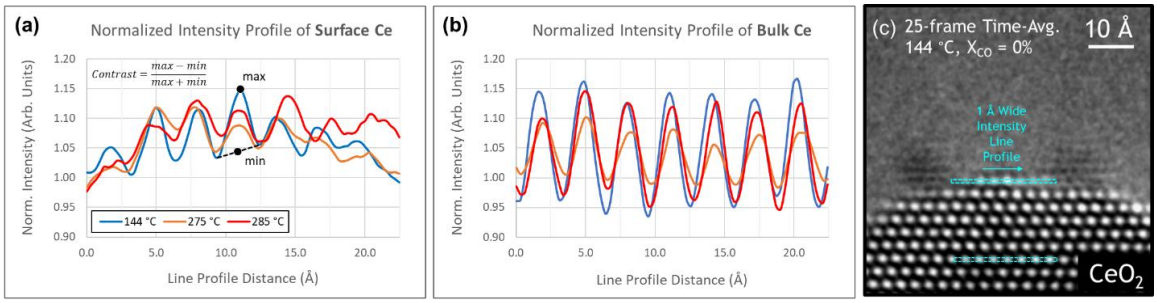

Figure C.10. Normalized intensity line profiles taken from (a) the free surface Ce columns between the Pt nanoparticles and from (b) a row of Ce cation columns several layers into the bulk of the nanoparticle. All of the intensity line profiles have been normalized to the average vacuum intensity at each condition. Intensity profiles are given for 144 °C (blue), 275 °C (orange), and 285 °C (red). The line profiles were generated over an integration window 92.1 pm wide (i.e., 3 pixels). The windows and direction are indicated in (c). In (a) the equation for calculating the contrast of a column is given, and the process for determining the maximum and minimum values is demonstrated for the middle surface Ce column at 144 °C. In (b) the fact that the CeO_2 particle has tilted at 275 °C is evident by the reduction in contrast of the orange curve. When the catalyst was heated to 285 °C, the crystal tilted back, seen by the recovered contrast in the red curve.

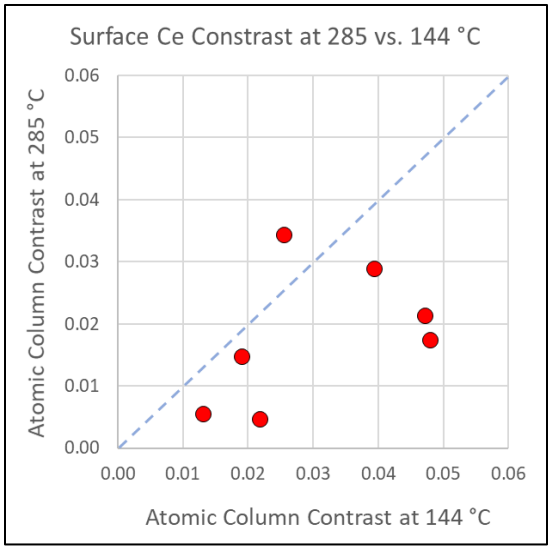

Figure C.11. The measured contrasts of the surface Ce columns at 24% CO conversion are plotted against the contrasts of the same column at 0% CO conversion. A straight dashed line is provided for reference, which shows that most Ce columns become more blurred with increasing conversion, as most points lie below the straight dashed line.

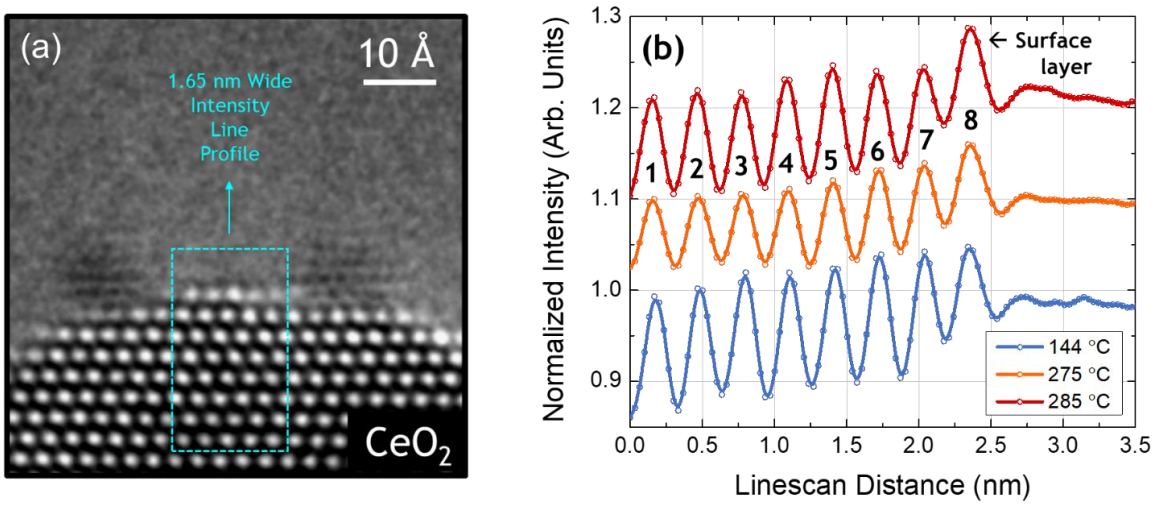

Figure C.12. Normalized intensity line profiles taken from interior of nanoparticle toward catalyst surface, revealing the outward CeO_2 (111) surface relaxation with increasing catalytic turnover. In (a) the region and direction of the intensity line scans are indicated for an example *operando* TEM time-averaged image acquired at 144 °C. The same region was used for all three conditions. In (b) the normalized intensity line profiles are plotted for 144 °C (blue), 275 °C (orange), and 285 °C (red). Original data points are plotted along with an interpolated spline which was used to measure the distances between the peaks in the profile. Numerical labels are given to the peaks to identify the measured separation distances that are provided in Table C.2.

Table C.2. Measurement of peak separation distances from intensity line profiles presented in Figure C.12. The peaks being measured are referenced with the numerical labels given in Figure C.12b (top). The outward relaxation of the CeO_2 (111) surface layer is presented in the last row of the table. The standard deviation of the measurements taken of all layers except the bulk (second to last row of the table) is used as an error bar on the measurement at each condition. Note that the averages of the sub-surface and bulk layer separation distances (third to last row of the table) are all close to the accepted CeO_2 (111) Miller plane spacing of 312 pm.

Peaks Being Measured	Separation Distance at 144 °C (pm)	Separation Distance at 275 °C (pm)	Separation Distance at 285 °C (pm)
1 – 2	305	313	307
2 – 3	313	307	306
3 – 4	308	313	310
4 – 5	311	309	315
5 – 6	303	314	307
6 – 7 (sub-surface)	312	312	319
Average of all layers except the surface	309	311	311
Std. dev. of all layers except the surface	4	3	5
7 – 8 (surface layer)	306	315	320

APPENDIX D

SUPPLEMENTARY MATERIAL FOR CHAPTER 5: TIME-RESOLVED *IN SITU* TEM OF PT/CEO_2

TABLE OF CONTENTS: APPENDIX D

D.1. EVIDENCE FOR MULTIPLY TWINNED STRUCTURE OF CeO_2-SUPPORTED PT NANOPARTICLE EXPOSED TO CO AND O_2 GAS

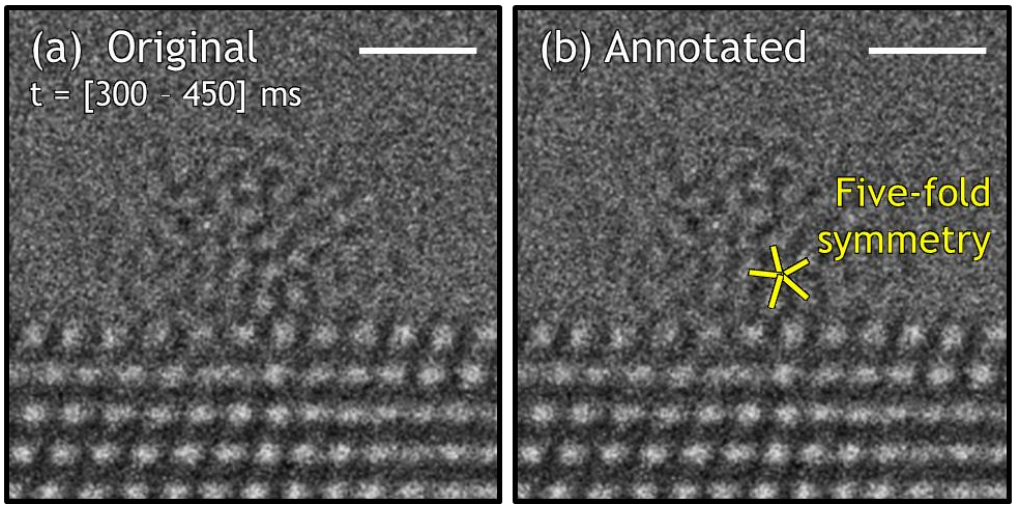

Figure D.1. *In situ* ETEM image time-average over 150 ms of CeO_2-supported Pt NP imaged at 20 °C in 10 mTorr of CO and O_2 gas, showing evidence of a five-fold symmetric site in the nanoparticle which would be consistent with a multiply twinned structure. At left in (a1) the original experimental observation is shown; at right in (a2) an annotated version is shown to mark the five-fold symmetric site. All scale bars correspond to 1.0 nm.

D.2. Additional Simulated Time-average and Comparison with Period from [300 – 450] ms in Experimental CO and O_2 *in situ* ETEM Image Time-series

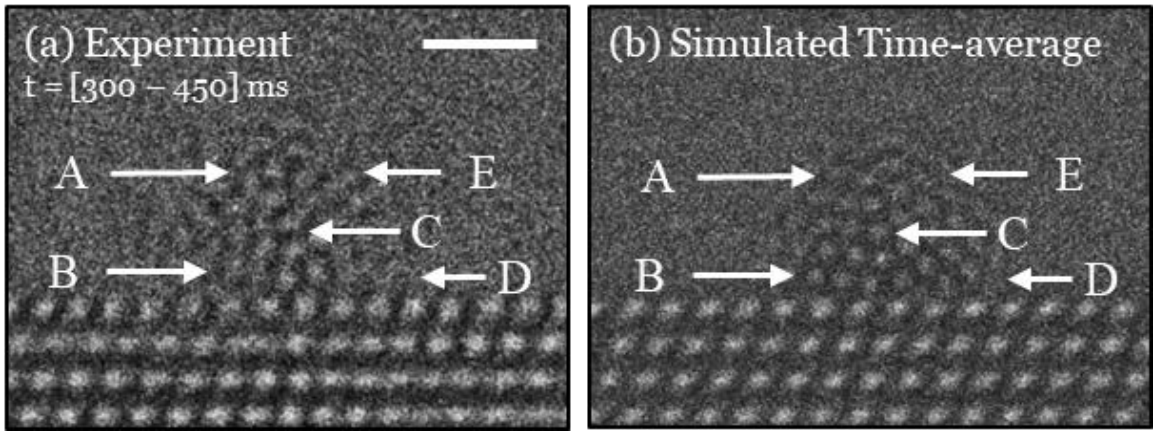

Figure D.2. Comparison between (a) experimental 150 ms time-averaged *in situ* ETEM image extracted from [300 – 450] ms during time-series in CO and O_2 and (b) simulated time-average that achieves best qualitative match to observed contrast. Lettering A, B, C, and D mark regions with prominent contrast features and a waypoint for comparison between the two images. Scale bar corresponds to 1 nm. The simulated time-average is comprised of the images generated from the structural models that are both displayed below in Figure D.3.

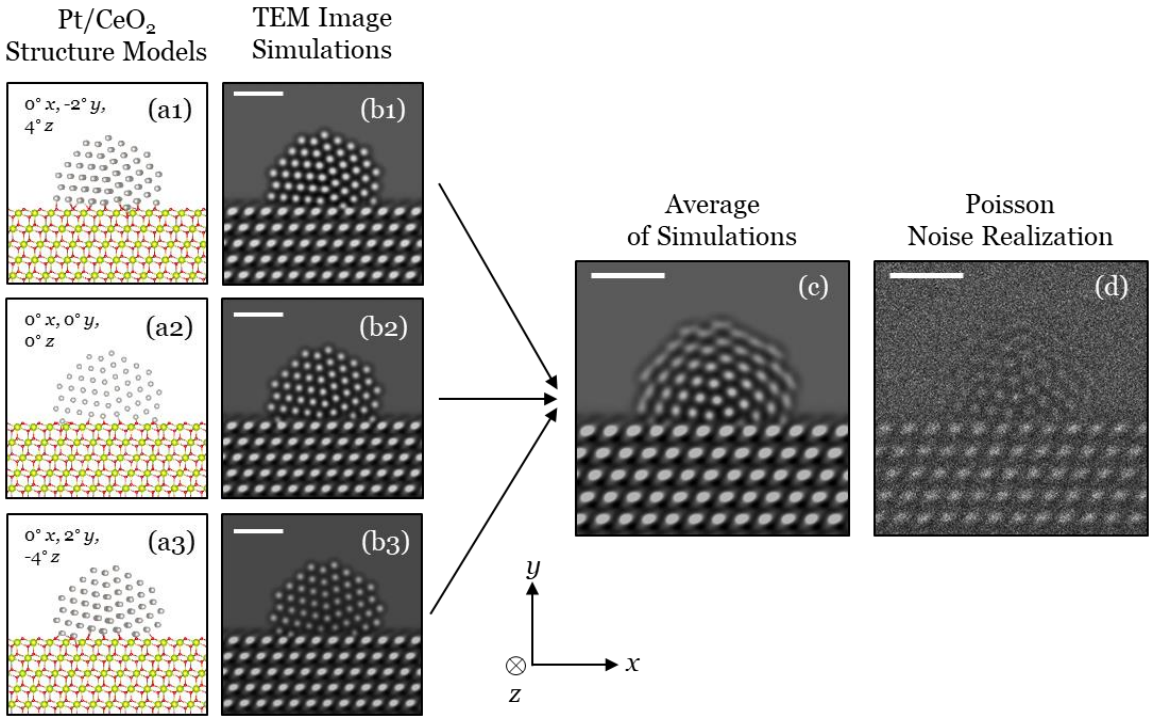

Figure D.3. (a1) – (a3) Atomic-scale structural models of CeO_2-supported multiply-twinned Pt nanoparticles used to produce the best-obtained qualitative match to the experimental image shown in Figure D.2 above. The notation in the upper left of the model subfigure inset provides the orientation of the Pt nanoparticle relative to the (110) zone axis. A tilt of 8° x corresponds to a rigid-body rotation of the Pt nanoparticle by 8° about the *x* axis, with respect to the principle tilt axes illustrated in the bottom middle of the figure. Pt atoms are shown as gray, Ce atoms as yellow-green, and O atoms as red; the CeO_2 support is also in a (110) zone axis and the nanoparticle sits on a (111) CeO_2 surface. (b1) – (b3) TEM image simulations of the Pt/CeO_2 structures. (c) Average of the three simulated images. (d) Poisson noise realization of the average simulation. All scale bars correspond to 1 nm.

D.3. Additional Observations of a Pt/CeO_2 Particle under WGS Reaction Conditions

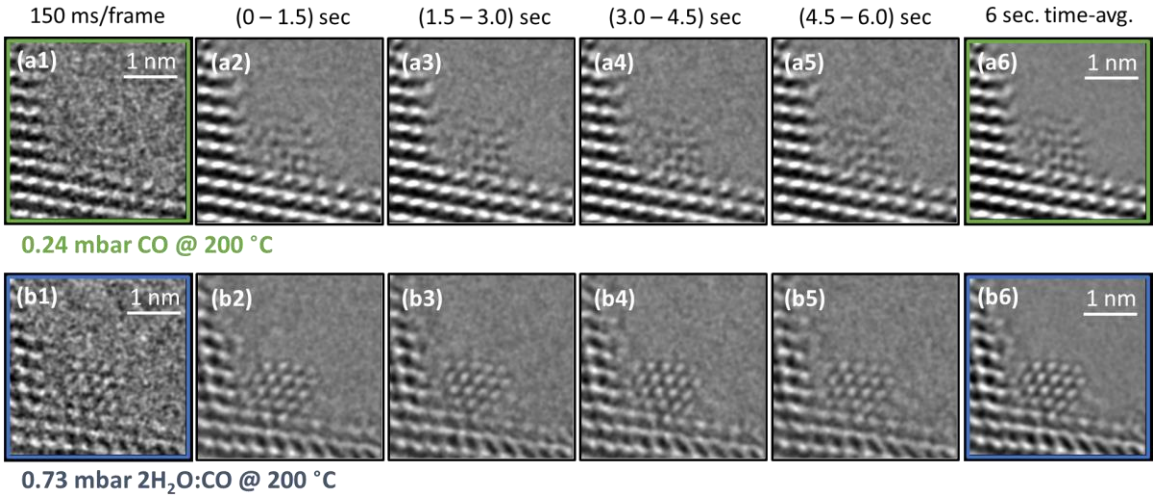

Figure D.4. Time-resolved *in situ* ETEM images showing the dynamic structural response and behavior of another CeO_2-supported Pt nanoparticle catalyst (a1) – (a6) at 200 °C in CO gas and (b1) – (b6) in WGS reaction conditions. (a1/b1) show the catalyst in a single 150 ms frame. Time-averaged image series from sequential 1.5 sec intervals are shown in (a2) – (a5) and (b2) – (b5). Time-averaged images from each condition over the entire 6.0 sec image acquisition period are shown in (a6/b6). The same Pt nanoparticle, which is different from the particle shown in the main text, is shown in all frames. The behavior shown in both figures is representative of many other particles imaged under the same conditions.

D.4. Documented Examples of Python Code

All model and image generation Python codes have been posted to the Crozier Research Group GitHub page (https://github.com/Crozier-Research-Group), and a few documented examples are given below.

Script to generate multiply twinned Pt nanoparticles

```
"""

Generates multiply twinned Pt nanoparticles.
The 'wulffpack' and 'ase' packages must be installed.
A twinned particle of a specified size will be written to.xyz file.

@author: Joshua Vincent, Arizona State University (jvincen5@asu.edu)
"""

# Import necessary modules
from wulffpack import Decahedron
from ase.build import bulk
from ase.io import write

# Specify (relative) surface energies of Pt
surface_energies = {(1, 0, 0): 2.036,
                    (1, 1, 1): 2.0,
                    (1, 1, 0): 2.5}

# Produce primitive structure from Pt lattice parameter (3.912 A)
prim = bulk('Pt', a=3.912)

# Produce a twinned particle using the Decahedron function
# A default relative twin energy of 0.04 is used
particle = Decahedron(surface_energies,
                      twin_energy=0.04,
                      primitive_structure=prim)

# Specify the size (number of atoms) of the twinned particle
particle.natoms = 325

# Write the twinned particle structure to an .xyz format file
# A file name will need to be provided where "Filename" is written
write('Filename.xyz', particle.atoms)
```

Script to rotate a supported Pt nanoparticle on a CeO_2 support

```
"""
Created on Mon Sep 28, 2020

Generate structure files (.cif) of CeO2-supported Pt particles,
where the Pt nanoparticles have been rotated by specified angles
about the principle axes of the original supercell. The anchor point
is chosen to be the center of the supercell. All permutations of tilt
are considered.

The user needs to specify (1) the range of tilts to rotate the
nanoparticle in each axis, and (2) whether to delete Pt that has
embedded in the support after rotation.

Running the script will prompt a user to choose a .cif file to load,
which should be the base file upon which all rotations are applied.

The script will then prompt the user to select a directory.
This directory is where all of the (.cif) files will be saved.

The 'pymatgen', 'tkinter', and 'tqdm' modules are required.

@author: Joshua Vincent, Arizona State University (jvincen5@asu.edu)
"""

## Import necessary modules
import pymatgen as mg
import os
from tkinter import filedialog
from tqdm import tqdm

## Initiliaze and import base structure from .cif file
structure_file = os.path.normpath(filedialog.askopenfilename())
structure_name = os.path.splitext(os.path.basename(structure_file))[0]

# Produce Immutable Structure object from specified .cif file
BaseStructure = mg.IStructure.from_file(structure_file)
BaseStructureDict = BaseStructure.as_dict()

# Determine structure indices corresponding to Pt
PtIndices = BaseStructure.indices_from_symbol("Pt")

## Choose a directory in which to save the .cif files after rotating.
```

```
save_directory = os.path.normpath(filedialog.askdirectory())

## Specify wheter to delete Pt beneath the CeO2 support surface
DeleteEmbeddedPt = True

## Initialize range of tilts to rotate the nanoparticle in each axis
a_tilts_list = [-2, 0, 2] # Amount to tilt about A axis (degrees)
b_tilts_list = [-2, 0, 2] # Amount to tilt about B axis (degrees)
c_tilts_list = [-2, 0, 2] # Amount to tilt about C axis (degrees)

## Designate an anchor point about which to perform the rotations
#  Here we choose the center of the supercell
anchor = list(0.5*supercell_dimension
              for supercell_dimension in BaseStructure.lattice.abc)

## Initalize directions of tilt axes
a_axis = [1, 0, 0] # Principle axis for A
b_axis = [0, 1, 0] # Principle axis for B
c_axis = [0, 0, 1] # Principle axis for C

#! The next step of the script is to perform the rotations.
#! Ensure that all inialization above is complete before proceeding.

## Perform rotations on Pt.
# Rotations are sequentially applied in A, B, and then C directions
for c_tilt in c_tilts_list:
    for b_tilt in tqdm(b_tilts_list):
        for a_tilt in a_tilts_list:
            # Clear RotatedStructure variable name
            RotatedStructure = None
            # Generate mutable struct from BaseStructure dictionary
            RotatedStructure=mg.Structure.from_dict(BaseStructureDict)
            # Perform specified tilts
            if a_tilt != 0:
                # Convert from deg to rad
                a_theta = a_tilt*2*3.14159/360
                # Rotate about A axis
                RotatedStructure.rotate_sites(anchor=anchor,
                                              axis=a_axis,
                                              indices=PtIndices,
                                              theta=a_theta,
                                              to_unit_cell=True)

            if b_tilt != 0:
```

```
            # Convert from deg to rad
            b_theta = b_tilt*2*3.14159/360
            # Rotate about B axis
            RotatedStructure.rotate_sites(anchor=anchor,
                                          axis=b_axis,
                                          indices=PtIndices,
                                          theta=b_theta,
                                          to_unit_cell=True)

        if c_tilt != 0:
            # Convert from deg to rad
            c_theta = c_tilt*2*3.14159/360
            # Rotate about C axis
            RotatedStructure.rotate_sites(anchor=anchor,
                                          axis=c_axis,
                                          indices=PtIndices,
                                          theta=c_theta,
                                          to_unit_cell=True)

        # Get file name after rotating
        deg_tilted=f'{a_tilt:2.1f}a_{b_tilt:2.1f}b_{c_tilt:2.1f}c'
        rotated_name = structure_name + f'_{deg_tilted}'
        rotated_name = rotated_name.replace('.', '-')

        # Delete embedded Pt if True
        if DeleteEmbeddedPt:
            sites_to_remove = []
            for index in PtIndices:
                # Remove all sites below the CeO2 surface
                if RotatedStructure[index].b < 0.48:
                    sites_to_remove.append(index)
            tuple(sites_to_remove)
            RotatedStructure.remove_sites(sites_to_remove)
            rotated_name += '_NoBuriedPt'

        # Save .cif file with rotated Pt to the save directory
        print(rotated_name)
        name=os.path.join(save_directory, rotated_name + '.cif')
        RotatedStructure.to(filename=name)
```

Script to expand supercell of model isotropically from model center

```
"""
Created on Thu Apr 8, 12:40 PM, 2021

Expands supercell by specified amount uniformly from model center.
This is useful to do prior to rotating a model in order to provide
some
padding around the model edges to avoid boundary artifacts during a
multislice TEM image simulation.

Before running, the user needs to specify (1) the expansion factor,
i.e.,
a scaling factor to specify how much to expand the supercell
dimensions,
(2) directory where the expanded supercell structure model will be
saved,
and (3) the minimum supercell dimension after expansion. The script
will
expand the model dimensions by the expansion factor, and if this
expanded
distance lies below the minimum specified threshold, the threshold
will be chosen as the supercell dimension instead.

The 'pymatgen', 'os', and 'tkinter' packages are required.

@author: Joshua Vincent, Arizona State University (jvincen5@asu.edu)
"""

## Import necessary modules
import pymatgen as mg
import os
from tkinter import filedialog

## Specify expansion factor. Setting equal to 1 results in no
change.
expansion_factor = 1.20

## Specify minimum supercell dimension, in Angstroms.
# If the expanded distance is less than this minimum, the dimension
# will be set as this minimum value instead.
min_dimension = 15

```

```
## Specify save directory
print("Please specify directory in which to save the expanded .cif
file:")
save_directory = os.path.normpath(filedialog.askdirectory())

## Initiliaze and import original structure from a .cif file
print("Please choose a .cif file that you would like to expand:")
structure_file = os.path.normpath(filedialog.askopenfilename())
structure_name =
os.path.splitext(os.path.basename(structure_file))[0]
OriginalStructure = None
OriginalStructure = mg.IStructure.from_file(structure_file)

## Create ExpandedStructure with larger supercell
ExpandedStructure = None
# Calculate expanded supercell dimension
abc = list(round(expansion_factor * lattice_param, 3)
           for lattice_param in OriginalStructure.lattice.abc)
# If expanded dimension < minimum, set dimension equal to minimum
abc = [lattice_param if lattice_param > min_dimension
       else min_dimension for lattice_param in abc]
latt = mg.Lattice.from_parameters(abc[0], abc[1], abc[2], 90, 90,
90)
# Create expanded structure object.
# One 'dummy' site (to be deleted) is necessary to initialize the
object.
ExpandedStructure = mg.Structure(latt, ["O"], [[0,0,0]])
# Remove dummy site
ExpandedStructure.remove_sites([0])

## Add every site from OriginalStructure
for site in OriginalStructure:
    ExpandedStructure.append(site.specie,
                             site.coords,
                             coords_are_cartesian=True)

# Translate all sites by a distance equal to
# half of the expansion distance in each axis
translation_vector = [0.5*(new_lat_param - old_lat_param)
                      for new_lat_param, old_lat_param
                      in zip(abc, OriginalStructure.lattice.abc)]
ExpandedStructure.translate_sites(list(range(
                                  ExpandedStructure.num_sites)),
                                  translation_vector,
```

```
86                                      frac_coords=False)
87
88 # Save ExpandedStructure as .cif file
89 expanded_name = structure_name + '_expanded'
90 save_filename = os.path.join(save_directory, expanded_name + '.cif')
91 ExpandedStructure.to(filename=save_filename)
```

Script to produce multislice TEM image simulations with Dr. Probe package

```
"""
Created on Fri Jan 22 12:23:00 2021
Purpose:    Performs multislice image simulations using Dr. Probe
    command line-based simulation software. A directory with .cel
    files is specified along with a range of defoci of interest.
    The simulations are saved in a specified output directory.
    There is an option to also save a Poisson noise realization
    of each simulated image in a separate directory.

    The 'drprobe', 'numpy', 'shutil', 'PIL', 'tkinter', and
    'tqdm' packages are required.

*/*/* OUTLINE of CODE and ALGORITHM */*/*
1. SETUP and USER INPUT
    1.1)    Import modules and set constants
    1.2)    Specify input and output directories, and defocus range
    1.3a)   Initialize parameter files
    1.3b)   Option to load parameter files from directory

2. MAIN CODE
        2.1)    Create back-up of cel file in output directory
    2.2)    Slice cel file
    2.3)    Perform multislice simulation
    2.4)    Generate TEM images
    2.5)    Delete slice directory to save space
*/*/* END CODE */*/*

@author: Joshua Vincent, Arizona State University (jvincen5@asu.edu)
"""
#%% 1.1) Import modules and set constants

# Import important modules
import drprobe as drp
import numpy as np
import os
import shutil
from PIL import Image
from tkinter import filedialog
from tqdm import tqdm

# Initialize constant parameters
```

```
ht = 300;                       # High tension is 300 kV
nx = 512; ny = 512;             # nx x ny pixels
nz = 300;                       # Structures will be cut into 300 slices
dwf = True; buni = 0.005;       # Debye-Wallar factor set B = 0.5 Ang^2
absorb = True;                  # Apply built-in absorptive form factors
output = True;                  # Give chatty output during simulations
Cs = -13000                     # Cs = -9 um
C5 = 5000000                    # C5 = 5 mm

#%% 1.2) Specify input and output directories

# Input directory containing .cel files to be simulated
print('Select input directory containing .cel files to simulate')
input_dir = os.path.normpath(filedialog.askdirectory())

# Output directory where in-progress simulations should be saved
print('Select output directory where in-progress should be saved')
output_dir = os.path.normpath(filedialog.askdirectory())

# Image directory where all the clean simulations should be saved
print('Select a directory where all simulated images will be saved')
clean_image_dir = os.path.normpath(filedialog.askdirectory())

# Directory where all the noisy simulated images should be saved
print('Select a directory where the noisy images will be saved')
noisy_image_dir = os.path.normpath(filedialog.askdirectory())

# Range of defocus in nm. Positive values indicate overfocus
defoci = [2]

# Range of vacuum levels in terms of electron counts
vac_levels = [1]
for vac_level in vac_levels:
    os.mkdir(os.path.join(noisy_image_dir,
                          f'vac_int-{vac_level:02d}counts'))

# Read lattice parameters from cel file
a, b, c = np.genfromtxt(r'\PtNp2_ceo2_4nm_0-0a_0-0b_0-0c.cel',
          skip_header=1, skip_footer=1, usecols=(1,2,3))[0]

#%% 1.3a) Option A: Initialize Parameter Files from Scratch

## Directory where initialized parameter files should be saved
prm_dir = r'\20210331_operando_paper_v2\prm'
```

```
 86
 87 # Initialize general MSA Parameter File
 88 msa_prm_gen = drp.msaprm.MsaPrm()
 89 # Electron wavelength in nm
 90 msa_prm_gen.wavelength = 0.0019687482
 91 # Focus half-spread in nm
 92 msa_prm_gen.focus_spread = 4
 93 # This is the size of the cel in nm
 94 msa_prm_gen.h_scan_frame_size = a
 95 msa_prm_gen.v_scan_frame_size = b
 96 # Tilt of crystal in x direction (degrees)
 97 msa_prm_gen.tilt_x = 0
 98 # Tilt of crystal in y direction (degrees)
 99 msa_prm_gen.tilt_y = 0
100 # Consistent with image size, usure if ultimately matters
101 msa_prm_gen.scan_columns = nx
102 msa_prm_gen.scan_rows = ny
103 # Turn off temporal coherence calculation (STEM only)
104 msa_prm_gen.temp_coherence_flag = 0
105 # Turn off spatial coherence calculation (STEM only)
106 msa_prm_gen.spat_coherence_flag = 0
107 # String of slice file, will be set iteratively later
108 msa_prm_gen.slice_files = ''
109 # Load one slice at a time
110 msa_prm_gen.number_of_slices = nz
111 # No detector effects included.
112 msa_prm_gen.det_readout_period = 0
113 # Each structure contains nz slices
114 msa_prm_gen.tot_number_of_slices = nz
115 # Set aberrations
116 msa_prm_gen.aberrations_dict = {1: (0, 0),
117                                 5: (Cs, 0),
118                                 11: (C5, 0)}
119 # Save the initailized MSA prm file
120 msa_prm_gen.save_msa_prm(prm_dir + r'\MsaPrmN2PtNP_Initialized.prm')
121
122 ## Initialize general WavImg Parameter File
123 wav_prm_gen = drp.wavimgprm.WavimgPrm()
124 # Set HT to 300 kV
125 wav_prm_gen.high_tension = ht
126 # Pixel dimensions of wave are nx by ny
127 wav_prm_gen.wave_dim = (nx, ny)
128 # Pixel size is width of cell divided by pixel dimensions
129 wav_prm_gen.wave_sampling = (a/nx, b/ny)
```

```
# Output TEM image
wav_prm_gen.output_format = 0
# Pixel dimensions of image are nx by ny
wav_prm_gen.output_dim = (nx, ny)
# Explicit TCC calculation
wav_prm_gen.coherence_model = 1
# Turn on temporal coherence. Focal spread half-width of 4 nm
wav_prm_gen.temp_coherence = (1, 4)
# Turn on spatial coherence. Beam convergence half angle of 0.2 mrad
wav_prm_gen.spat_coherence = (1, 0.2)
# Turn off detector MTF effect.
wav_prm_gen.mtf = (0, 0.5, r'F:\MTF-US2k-300.mtf')
# 50 pm isotropic vibration applied.
wav_prm_gen.vibration = (1, 0.050, 0.050, 0)
# Objective aperture essentially out, set to 250 mrad
wav_prm_gen.oa_radius = 250
# Set aberrations
wav_prm_gen.aberrations_dict = {1: (0, 0),
                                5: (Cs, 0),
                                11: (C5, 0)}
##Save the initailized WavImg prm file
wav_prm_gen.save_wavimg_prm(prm_dir+r'\WavPrmN2PtNP_Initialized.prm')

#%% 1.3b) Option B: Initialize Prm Files from ones Previously Saved

# Load MSA parameter file
msa_prm_gen = drp.msaprm.MsaPrm()
print('Specify a MSA parameter file to use during the simulations')
msa_prm_gen.load_msa_prm(filedialog.askopenfilename())

# Load WAV parameter file
wav_prm_gen = drp.wavimgprm.WavimgPrm()
print('Specify a WAV parameter file to use during the simulations')
wav_prm_gen.load_wavimg_prm(os.path.normpath(
filedialog.askopenfilename()))

#%% 2) Perform Image Simulations

# For every structure in the input directory
for cel_file in tqdm(os.listdir(input_dir)):

    ## Set-up parent directory for this structure
    # Remove the file extension to isolate the structure name
    structure_name = cel_file[:-4]
```

```
174     # Name of directory for this structure
175     structure_dir = os.path.join(output_dir, structure_name)
176     # Create structure's directory with name specified above
177     os.mkdir(structure_dir)
178
179     ## 2.1) Create back-up of cel file in output directory
180
181     # Set-up cel sub-directory
182     structure_cel_dir = os.path.join(structure_dir, 'cel')
183     # Create cel directory with name specified above
184     os.mkdir(structure_cel_dir)
185     # Name of full directory to original cel file
186     cel_original = r'"{}"'.format(os.path.join(input_dir, cel_file))
187     # The r'"{}"' is necessary to enclose path in double quotes.
188     cel_copy= '"{}"'.format(os.path.join(structure_cel_dir,cel_file))
189     # Create back-up cel in back-up directory
190     #drp.commands.cellmuncher(cel_original, cel_copy, output=True)
191
192     ## 2.2) Slice cel and save slices in \slc directory
193     # Set-up slice sub-directory
194     structure_slc_dir = os.path.join(structure_dir, 'slc')
195     os.mkdir(structure_slc_dir)
196     slice_name = structure_name + '_slc'
197     slice_path_and_name = os.path.join(structure_slc_dir,slice_name)
198
199     # Slice cel and save slices in the slice directory
200     drp.commands.celslc(cel_original, slice_path_and_name,
201                         ht, nx, ny, nz,
202                         absorb=absorb, dwf=dwf, buni=buni,
203                         output=True)
204
205
206     ## 2.3) Perform multislice simulation
207     # Parameter initialization
208     # Set up name of parameter sub-directory for this structure
209     structure_prm_dir = os.path.join(structure_dir, 'prm')
210     # Create parameter directory with name specified above
211     os.mkdir(structure_prm_dir)
212     # Load general parameter file to be edited
213     msa_prm = msa_prm_gen
214     msa_prm.tilt_x = 1.5
215     msa_prm.tilt_y = 1.0
216     # Specify location of phase gratings generated in section 2.2
217     msa_prm.slice_files = slice_path_and_name
```

```
218     # Name the MSA parameter file to be saved
219     msa_prm_name = 'MsaPrm_'+structure_name+'.prm'
220     # Path location to where the MSA parameter file should be saved
221     msa_prm_path_and_name = os.path.join(structure_prm_dir,
222 msa_prm_name)
223     # Save the parameter file with the slice locations
224     msa_prm.save_msa_prm(msa_prm_path_and_name)
225 
226     ## Set-up wave function sub-directory
227     # Set up name of wave function sub-directory for this structure
228     structure_wav_dir = os.path.join(structure_dir, 'wav')
229     # Create wave function directory with name specified above
230     os.mkdir(structure_wav_dir)
231     # Specify name (and path) of output wavefunction
232     wav_path = os.path.join(structure_wav_dir,structure_name)
233 
234     # Calculate exit surface wavefunction and save it in wav_path
235     drp.commands.msa(msa_prm_path_and_name, wav_path,
236                      ctem = True, output = True,
237                      silent = False)
238 
239 
240     ## 2.4) Generate simulated images
241     # Parameter initialization
242     # Load general wav parameter file for image simulation
243     wav_prm = wav_prm_gen
244     # Name of wav file and location after full multislice simulation
245     wav_prm.wave_files = wav_path + '_sl' + f'{nz:03d}' + '.wav'
246     # Set name of wave paramter file
247     wav_prm_name = 'WavPrm_'+structure_name+'.prm'
248     # Path location to where the wav parameter file should be saved
249     wav_prm_path_and_name = os.path.join(structure_prm_dir,
250 wav_prm_name)
251     # Save the parameter file with the slice locations
252     wav_prm_gen.vibration = (1, 0.085, 0.085, 0)
253     wav_prm.save_wavimg_prm(wav_prm_path_and_name)
254 
255     ## Set-up image sub-directory
256     # Set up name of image sub-directory for this structure
257     structure_img_dir = os.path.join(structure_dir, 'img')
258     # Create image  directory with name specified above
259     os.mkdir(structure_img_dir)
260 
261     # Simulate images
```

```
262     for defocus in defoci:
263             # Specify name of path of output image
264             img_name = structure_name + '_' + str(nz) + 'slc_' + ...
265             str(nx)+'x'+str(ny)+'_'+str(defocus)+'nmDefocus'+'.dat'
266             output_img = os.path.join(structure_img_dir,img_name)
267
268             # Calculate image
269             drp.commands.wavimg(wav_prm_path_and_name, output_img,
270                                 foc = defocus,
271                                 sil = False, output=True)
272
273             # Save the clean image as a tif file
274             clean_im = np.fromfile(output_img,
275                                    dtype=np.single).reshape((nx, ny))
276             clean_im = np.flip(clean_im,0)
277             clean_img = Image.fromarray(clean_im)
278             clean_img.save(os.path.join(clean_image_dir,
279                                         img_name[:-4] + '.tif'))
280
281             # Save a noise realizations of the image
282             for vac_level in vac_levels:
283                 noisy_img_array=np.random.poisson(clean_im*vac_level)
284                 noisy_img = Image.fromarray(noisy_img_array)
285                 noisy_img.save(os.path.join(noisy_image_dir,
286                                 f'vac_int-{vac_level:02d}',
287                                 img_name[:-4]
288                                 + f'{vac_level:02d}.tif'
289                                      )
290                                 )
291
292     ## 2.5) Clean up slice directory
293     # Delete slice sub-directory to save space
294     try:
295         shutil.rmtree(structure_slc_dir)
296     except OSError as e:
297         print ("Error: %s - %s." % (e.filename, e.strerror))
```

APPENDIX E

SUPPLEMENTARY MATERIAL FOR CHAPTER 6: TIME-RESOLVED *IN SITU* TEM OF PT/CEO_2

TABLE OF CONTENTS: APPENDIX E

E.1. Description of Structural Variation Included in Training Dataset

Four base supported Pt particle structures were incorporated in the model dataset to cover variations in the overall supported particle size and shape. The nanoparticle structures have been labeled "PtNp1" through "PtNp4", as shown below in Figure E.1.

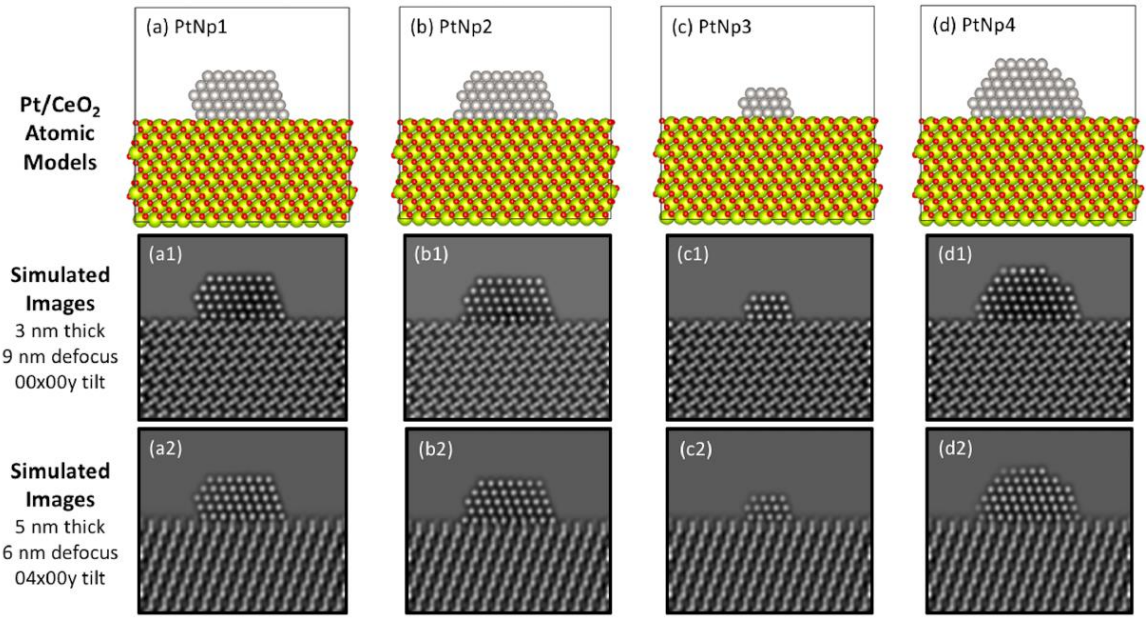

Figure E.1. Variations in the size/shape of the supported Pt nanoparticle. At top, in (a) to (d), atomic models of Pt nanoparticles PtNp1 through PtNp4, each with different size and shape, are supported on a CeO_2 slab. PtNp1 and PtNp2 correspond to supported Pt nanoparticles 2 nm in size where the difference is the appearance of an atomic column located at the interface between the Pt and the CeO_2 support; PtNp3 corresponds to a Pt nanoparticle 1 nm in size; and PtNp4 corresponds to a Pt nanoparticle 3 nm in size. In middle, from (a1) to (d1), simulated images of the modeled structures are given for a CeO_2 support thickness of 3 nm, 9 nm of defocus, and no tilt; at the bottom, in (a2) to (d2) simulations for the same models are given now for a 5 nm support thickness, 6 nm of defocus, and 4° of tilt about the *x* axis.

Furthermore, the surface character of the Pt nanoparticles was varied by introducing atomic-level defects into the structure at different surface sites. A few examples are depicted in Figure E.2. Overall, the defects can be categorized into five classes, here labeled as "D0", "D1", "D2", "Dh", and "Ds" in accordance with the models presented in Figure E.2. In regard to the terminology, D0 corresponds to the initial

structure without any introduced defects, D1 and D2 correspond to a structure in which 1 or 2 atomic columns have been removed, respectively, Dh corresponds to a structure in which a column has been reduced to half its original occupancy, and finally Ds corresponds to a structure in which a column has been reduced to a single atom. Note that the surface sites altered in the structure correspond to high-energy sites (e.g., corners and edges) which are more likely to dynamically rearrange or show variation than, say, a low-energy terrace site located in the middle of the surface.

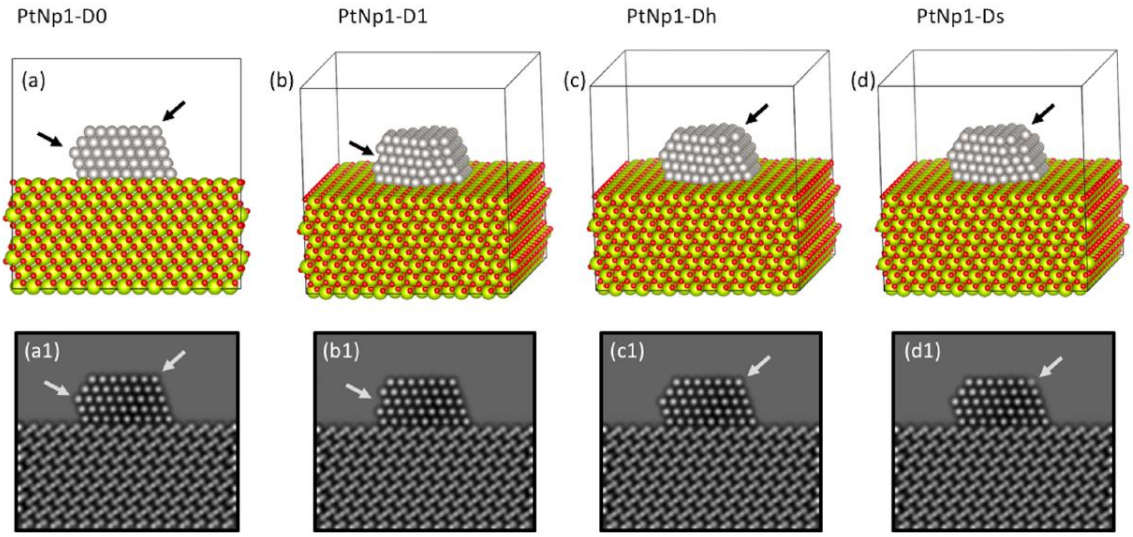

Figure E.2. Variations in the atomic-level defects present on the Pt surface. In (a) an atomic model of CeO_2-supported Pt nanoparticle PtNp1, without any introduced defects (D0) is shown. The surface of this particle has been modified in a number of ways, including by (b) removing a full atomic column (i.e., defect D1), (c) removing half of the column occupancy (defect Dh), and (d) removing all but a single Pt atom (defect Ds). Black arrows point to sites where defects have been introduced. Note that models (b), (c), and (d) have been tilted to assist in visualizing the surface defect modifications. At bottom in (a1) to (d1), simulated images of the atomic models are shown for conditions with 3 nm support thickness, 9 nm of defocus, and no tilt.

The support thickness was varied from 3 nm to 6 nm along 1 nm increments. Images showing the type of contrast variations that may occur when the support thickness is changed, and how these compare to that from changes in defocus, are given in Figure E.3 below.

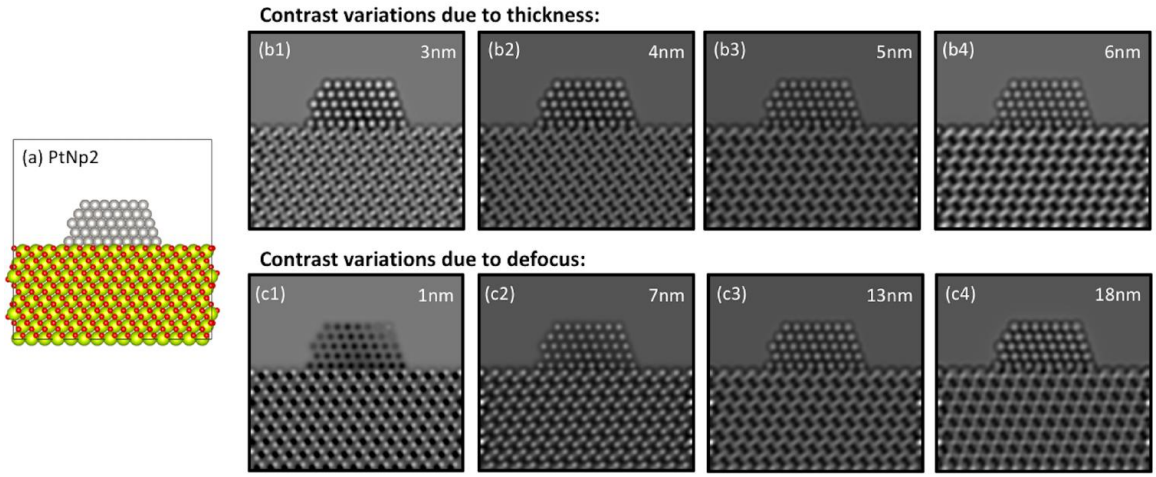

Figure E.3. Image contrast variations due to CeO_2 support thickness (top) and electron optical defocus (bottom). The model shown in (a) was used for each of the multislice simulations to isolate effects from thickness and defocus. Images (b1) through (b4) demonstrate the effect of CeO_2 support thickness on the contrast in the image, with the thickness increased from 3 nm to 6 nm in 1 nm increments and the defocus held constant at 13 nm. Images (c1) through (c4) illustrate the effect of defocus on image contrast, with the defocus increased from 1 nm to 7 nm, then 13 nm, then 18 nm, respectively, and the support thickness held constant at 5 nm.

Aside from this, the overall orientation of the structural model with respect to the incident electron beam was tilted from 0° to 4° about the x and y axes independently in increments of 1°. Thus, variations from 0° in x and 0° in y, to 4° in x and 0° in y, or 0° in x and 4° in y were considered. Accounting for the diversity in structures, in addition to the variations in crystal orientation and CeO_2 support thickness, a total of 855 atomic structural models were constructed. These structures were each used to calculate multislice simulations with defocus values ranging from 0 to 20 nm, which results in the calculation of 17,955 total images. The large variety of imaging conditions led to a variety of contrast in the resultant images. The classification of the atomic column contrast into black, white, and intermediate categories is elaborated upon and explained in Figure E.4.

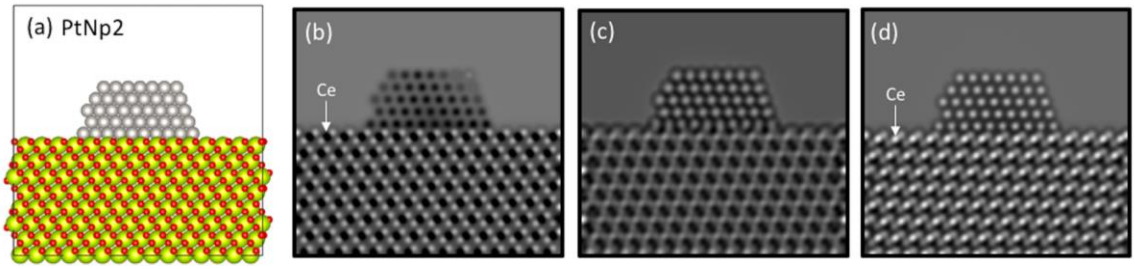

Figure E.4. Categorical classification of "black", "intermediate", and "white" atomic-column contrast. The categorization was predominately centered around the focusing condition of the Pt atomic columns, with some influence as well by the focusing condition of the Ce atomic columns. In (a) an atomic-scale structural model of CeO_2-supported Pt is presented. Parts (b) through (d) show simulated images under different defocusing conditions, emphasizing variations in the Ce and Pt column contrast. In (b), the image shows almost entirely black contrast for both Ce and Pt atomic columns. Images similar to this would be classified as "black" contrast. In (c), the Pt columns reverse contrast and now appear white, while the Ce columns become challenging to discriminate. Images similar to this would be classified as "intermediate" contrast. Finally, in (d) all of the atomic columns including the O appear with white contrast. Images similar to this one would be classified as "white" contrast.

Finally, Figure E.5 on the following page presents a schematic summary of the structural and imaging parameters varied during the modeling and image simulation process.

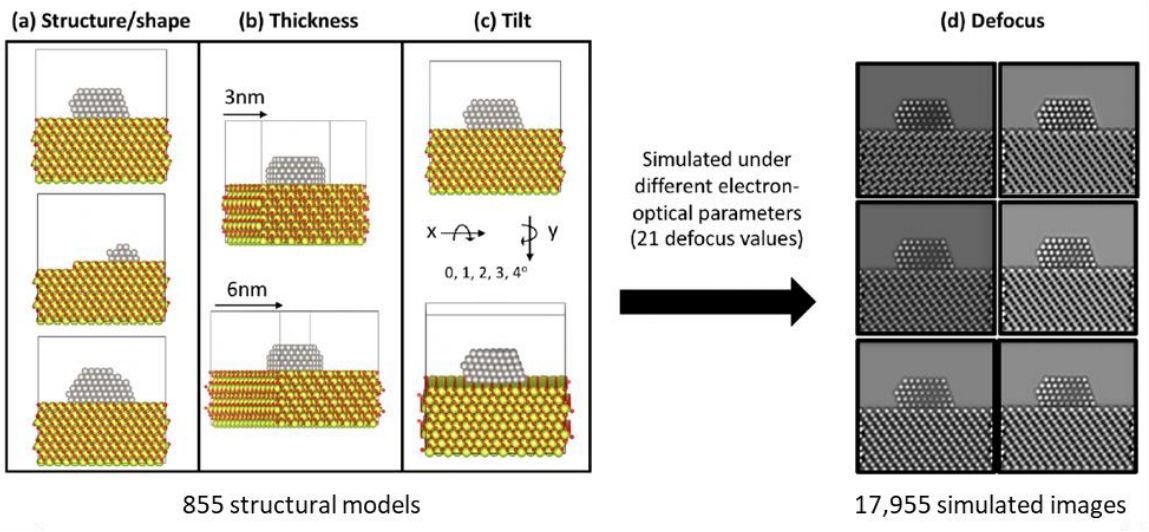

Figure E.5. Summary of structural and imaging parameters systematically varied during the modeling and image simulation process. At left is a subset of Pt/CeO_2 atomic structural models presenting variations on (a) the structure and shape of the nanoparticle and the support, (b) the thickness of the CeO_2 support, and (c) the tilt of the specimen with respect to the incident beam. The models were used to produce simulations under 21 defocus values each, as shown in (d).

E.2. Analysis of Experimental Noise Distribution

We expect the noise for images acquired on a direct electron detector operating in electron counting mode to be dominated by shot noise which can be modeled with a Poisson distribution. For counted image acquisition, the electron dose rate per pixel is sufficiently low enough that individual electron arrivals can be detected and registered. It is well known that the statistical fluctuations of such counting processes for discrete events are governed by shot noise. Additionally, we expect other sources of noise, e.g., fixed pattern noise, dark noise, and thermal noise are minimal after applying a gain correction and a dark reference to the raw image, and by cooling the detector to -20 °C, respectively. Readout noise is considered to be negligible, since the pixels on the CMOS-based detector are read out individually. Thus, we expect that the noise in the counted TEM micrographs can be modeled as Poisson. Furthermore, we have performed an analysis to verify that the noise in the experimental movie follows Poisson statistics, as shown in Figure E.6.

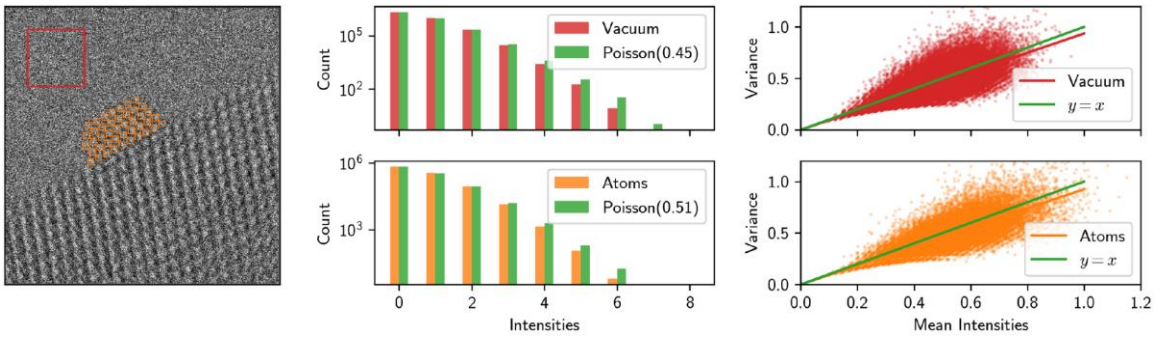

Figure E.6. In (a) a 1.000 second time-averaged image comprised of 40 frames is displayed. Part (b) displays histograms from the red and orange regions in the image representing vacuum and the Pt atomic columns, respectively. Simulated histograms taken from Poisson distributions with the indicated mean are plotted for comparison, showing good agreement in both cases. Finally, in (c) a plot of the mean and standard deviation of the pixel intensities over the 40 frames in the movie shows the data approximately follows a line with a slope of 1, as expected for Poisson distributions. The spread in the data is due to the limited number of samples (i.e., 40).

E.3. Additional Comparison of Network against Baseline Methods on Randomly Selected Simulated Data

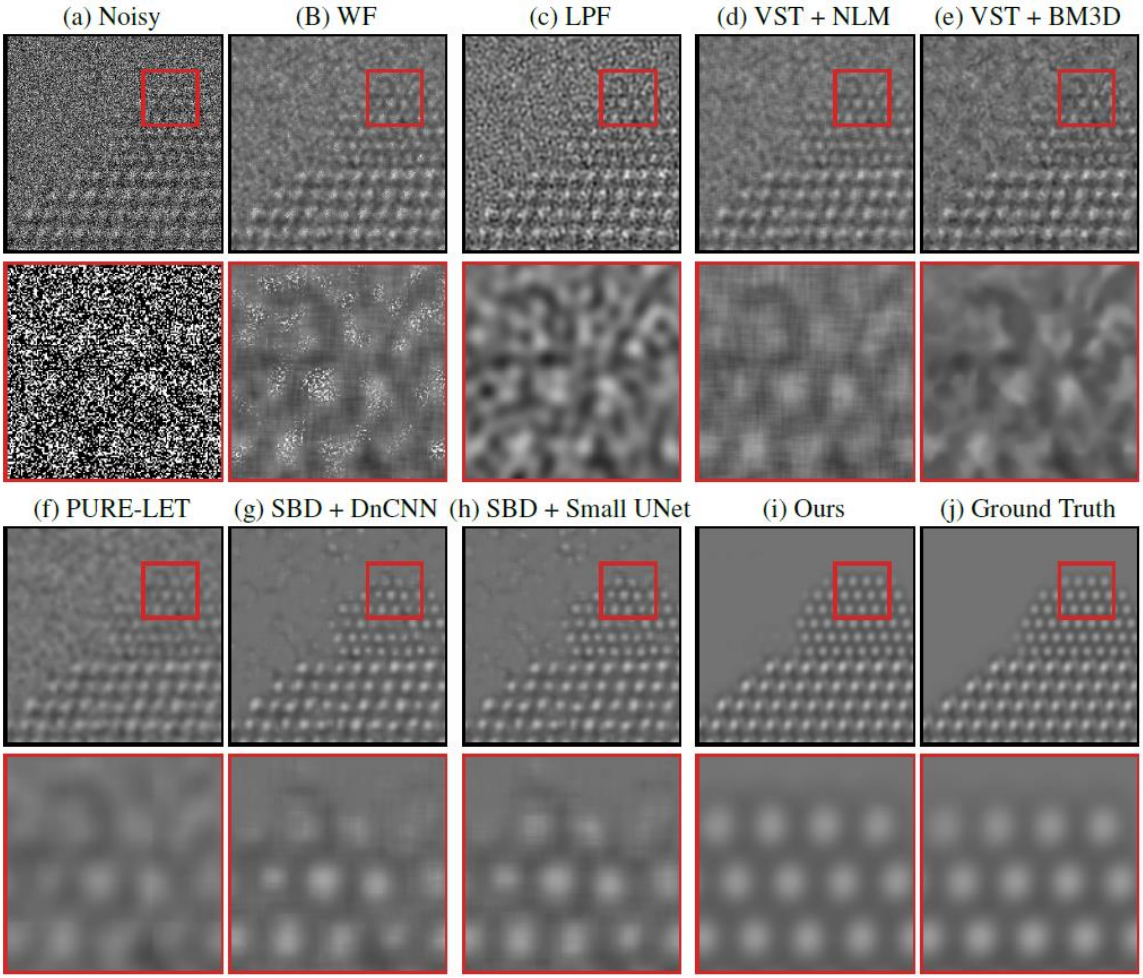

Figure E.7. Comparing the proposed network's performance on a randomly selected simulated image from the validation dataset against other baseline denoising methods, including other neural networks. See main text for an explanation of the methods. In brief, part (a) displays a noisy simulated image, along with a zoom-in on the region indicated by the red box in the figure inset. The clean simulated image is shown as a ground truth reference in (j). The baseline methods produce the denoised images shown in (b) – (h) (a description of the methods is given in Chapter 2, Section 2.4.3.1). The proposed network produces denoised images of high quality, recovering precisely the structure of the nanoparticle, even at the surface, as shown in (i).

E.4. Effect of Increasing Size of Receptive Field on Network Performance

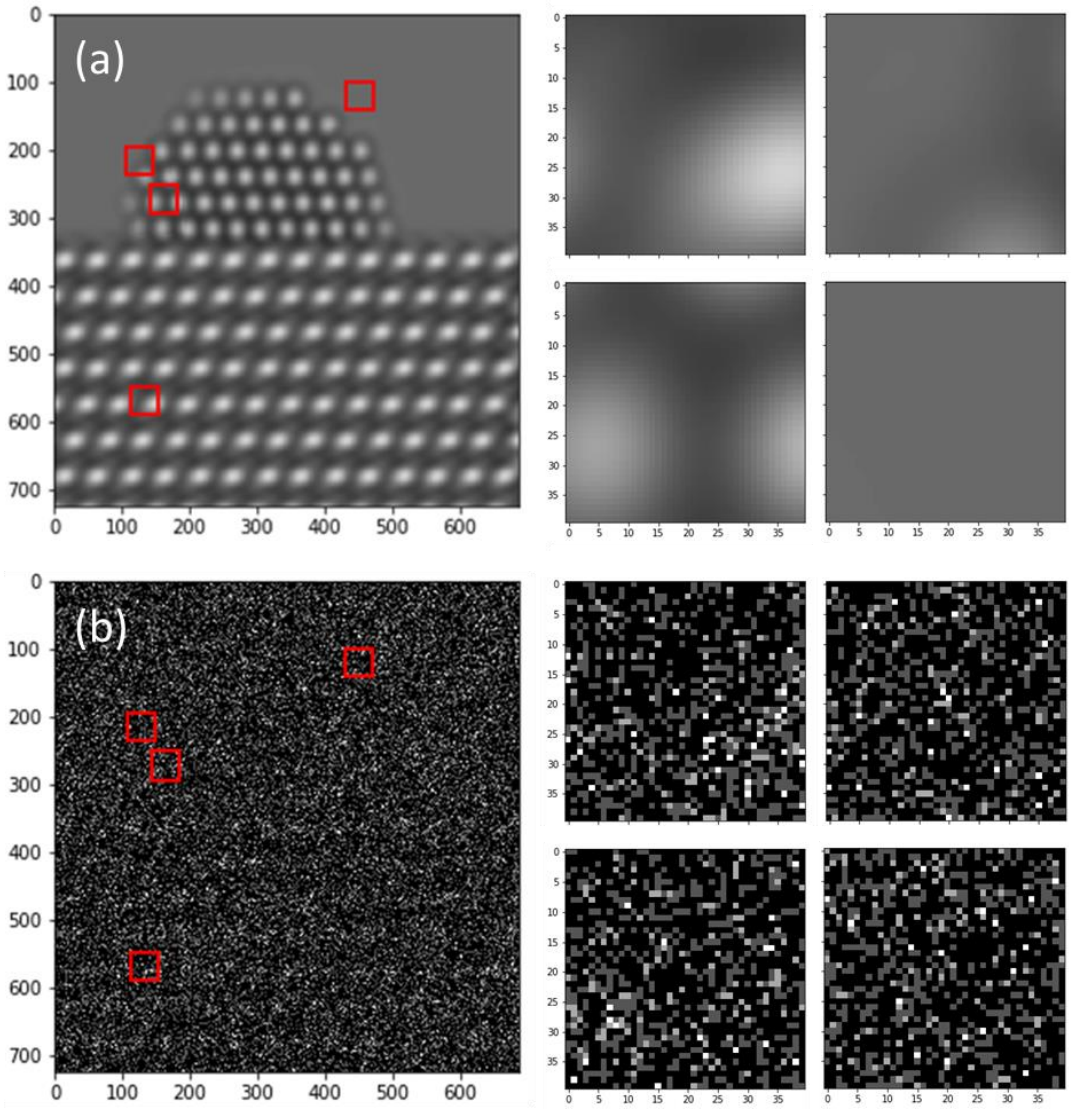

Figure E.8. With a receptive field of 41 × 41 pixels, it is challenging to see structure around the atomic columns in the clean image, which is shown in (a) with randomly selected 41 × 41 pixel regions shown at right. After severely degraded Poisson shot noise has been added to the image, as shown below in (b), differentiating the regions which contain structure from those which are taken from the vacuum becomes considerably difficult.

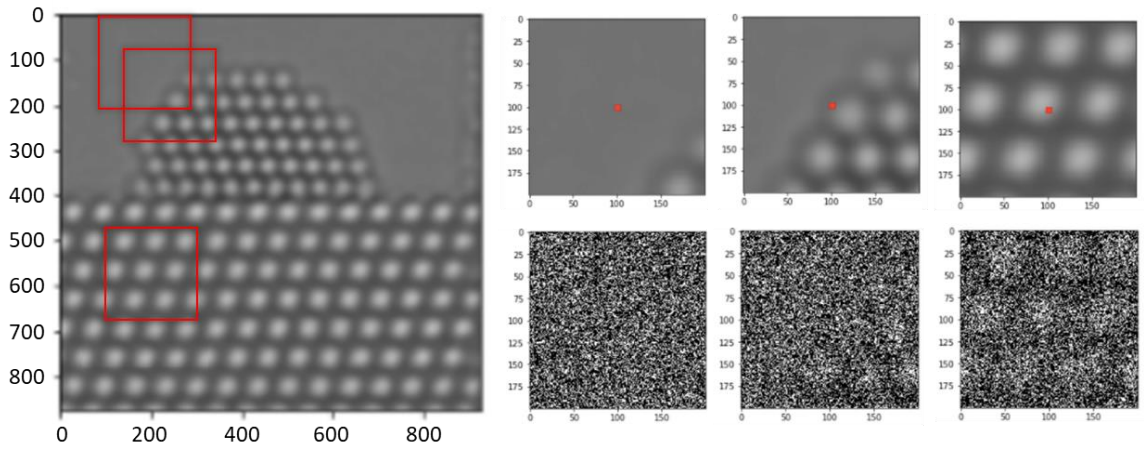

Figure E.9. Increasing the network's receptive field (e.g., here regions 1.22 nm × 1.22 nm are shown) allows the network to sense nearby atoms, while remaining sensitive to the presence of a surface or defected site. Various regions of interest are highlighted by the red boxes in the image on the right. The local structure surrounding the pixel to be denoised (small red box in windowed regions shown on top right) can clearly be seen and remains discernible after the addition of severe shot noise (bottom right).

E.5. Generalization Ability of Network to Unseen Geometries and Image Features

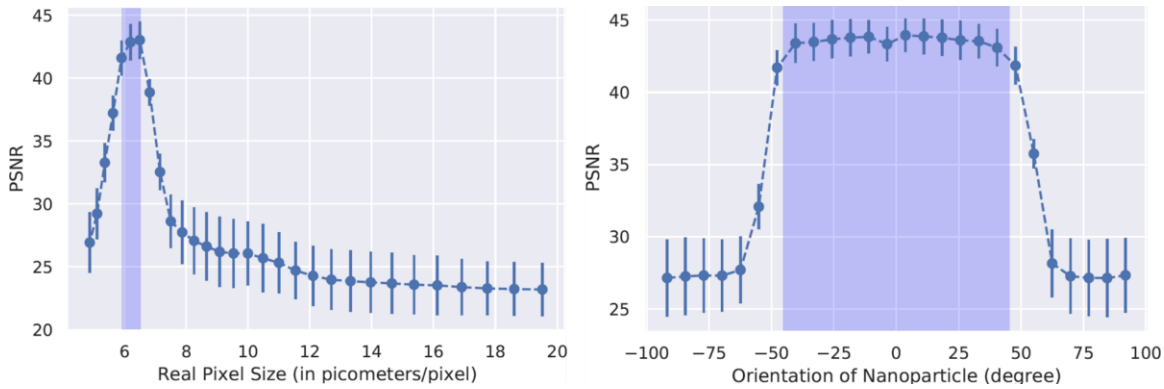

Figure E.10. Impact of training data geometry on network denoising performance. At left, the effect of image scaling (measured in terms of real-space pixel size) is investigated; at right, the influence of image orientation (measured in degrees relative to the original simulation). In both cases the network was trained on data augmented with resized and rescaled images within the regions that are shaded purple. When the network is evaluated on images outside of these regions, the performance, measured in terms of PSNR, worsens significantly. Mean values are plotted for each size/orientation, with the standard deviation of the values given as the data error bars.

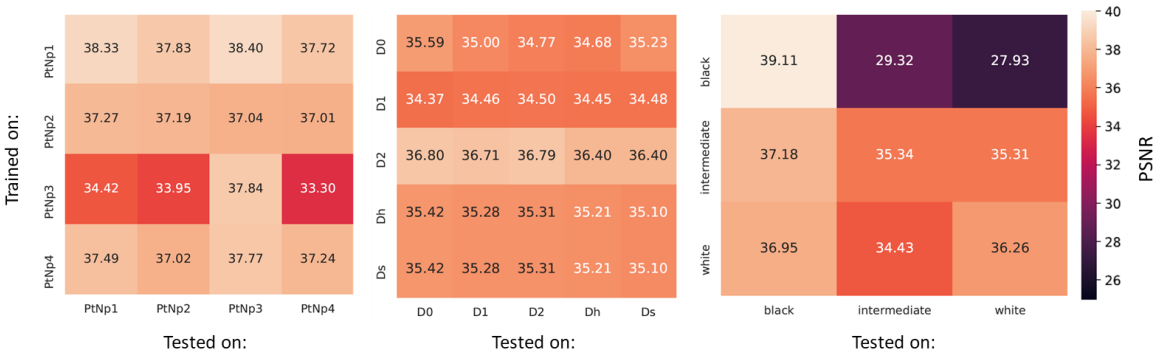

(a) Pt NP Structure (b) Pt Surface Defects (c) Column Contrast

Figure E.11. Investigating the network's generalizability to unseen (a) supported Pt nanoparticle structures (see Figure E.1), (b) atomic-level Pt surface defects (see Figure E.2), and (c) atomic column contrast (i.e., white or black-column focusing) conditions (see Figure E.3). A description of the different subsets of data that were formed for each category, as well as an explanation of the terminology, is given in the methodological section of the main text. The tables report the mean PSNR denoising performance when it is trained (rows) and evaluated (columns) on various combinations of the data subsets. For example, when the network is trained only on images with the PtNp1 structure (Table (a), row 1), the network achieves a PSNR denoising performance of 38.33 dB when it is evaluated on images of the PtNp2 structure, and a PSNR denoising performance of 37.72 dB when evaluated on images of the PtNp4 structure.

E.6. Overview of Structure Models used for Surface Structure Evaluation

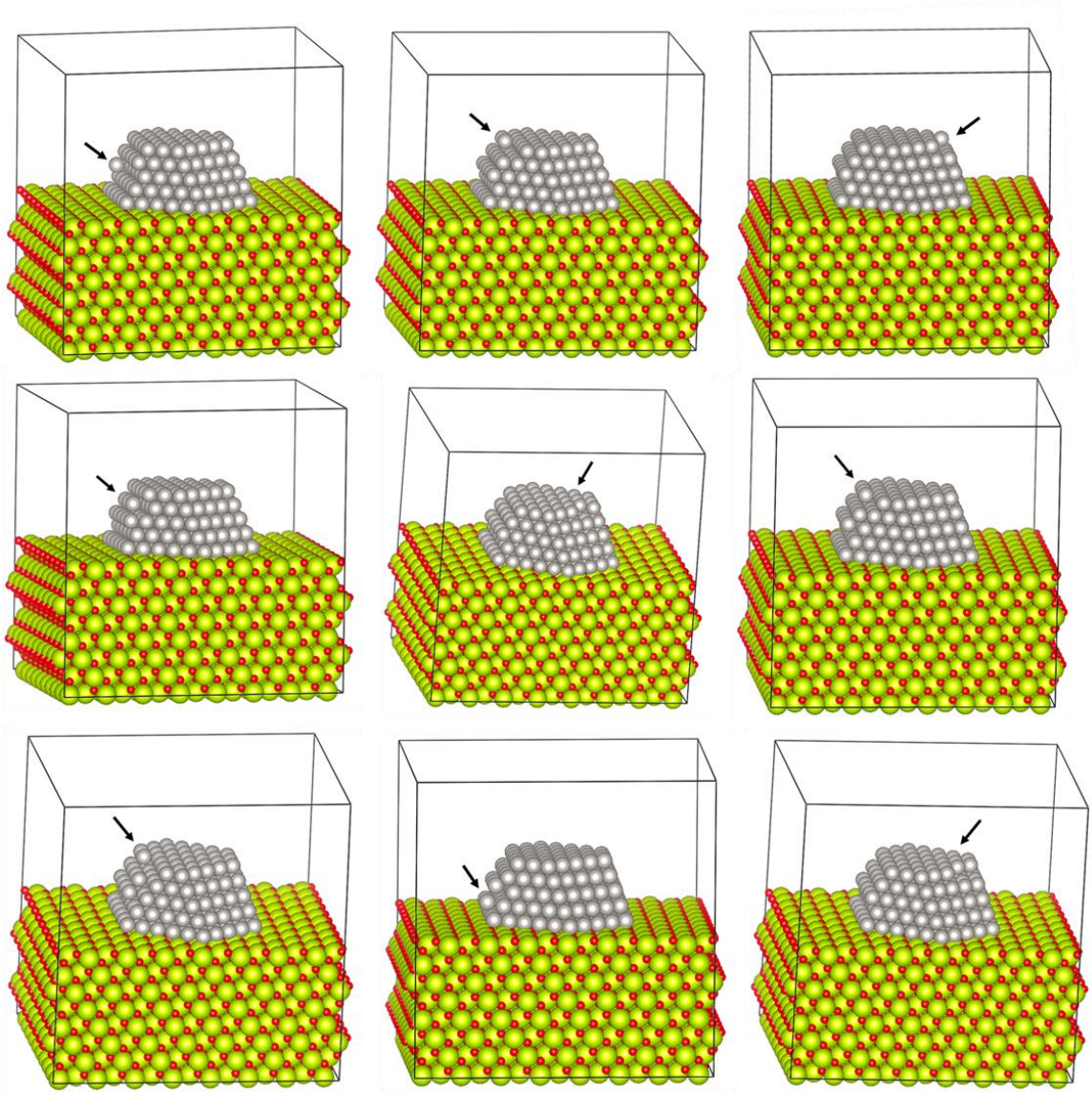

Figure E.12. Representative set of nine Pt/CeO_2 atomic structural models used in the generation of the surface evaluation dataset. Many different types of atomic-level surface defects have been introduced into the Pt models, including, e.g., the removal of an atom from a column, the removal of two atoms, the removal of all but one atom, the addition of an adatom at a new site, etc., to emulate dynamic atomic-level reconfigurations that could potentially be observed experimentally. Altered sites are indicated with black arrows.

E.7. Inspection of Noisy Data that Produced Spurious Column upon Denoising

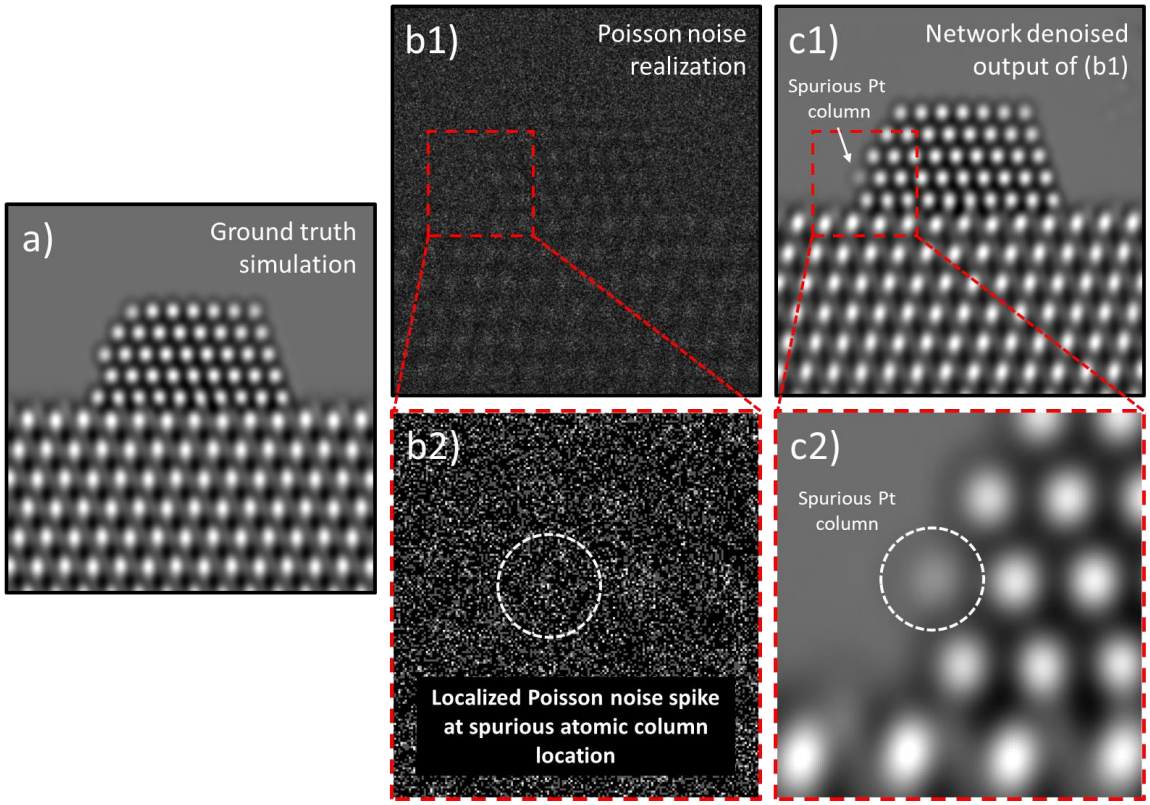

Figure E.13. Examination of Poisson noise distribution around locations where spurious atomic columns appear in denoised simulated images. Part (a) shows the original ground truth simulation in this case, (b1) shows the Poisson noise realization and (c1) shows the network denoised output. Notice the appearance of a spurious atomic column which is marked by the white arrow in (c1). Subfigures (b2) and (c2), respectively, show an enhanced view around the spurious atomic column from the windowed region marked by the dashed red box in the noisy and denoised images. In (b2) and (c2) a dashed white circle is used to mark the location of the spurious atomic column. Examining the distribution of intensity in the Poisson shot noise realization reveals the presence of a noise spike near the center of the spurious atomic column location (i.e., (b2)). This analysis suggests that the random clustering of intensity in a manner that appears to resemble a surface atomic column can lead the network to produce denoised estimates with spurious surface atomic columns.

E.8. Comparison of Likelihood Analysis with and without Averaging

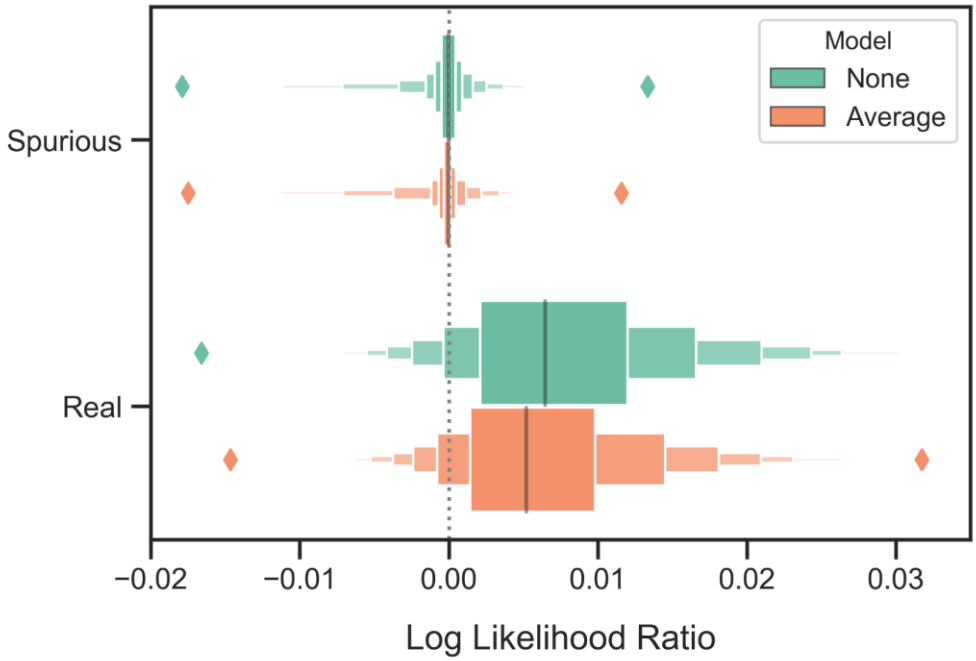

Figure E.14. Letter value or so-called boxen plots of the log-likelihood ratio distributions for spurious (top) and real (bottom) atomic columns calculated in two different ways. The distribution labeled as having a model of "Average" contains log-likelihood ratios calculated using a Poisson probability mass function (pmf) governed by a rate parameter that was obtained by *averaging* the intensity within the column, as explained in the main text. The area over which the intensity was averaged is defined by a circle that is centered on the atomic column and approximately 1.5 Å in diameter. The distribution labeled as having a model of "None" contains ratios calculated using a Poisson pmf where the rate parameter of each pixel varies and is taken to be the intensity value of the denoised pixel. Observe that the distributions differ by little.

E.9. Additional Comparison Network against Baseline Methods on Randomly Selected Experimental Data

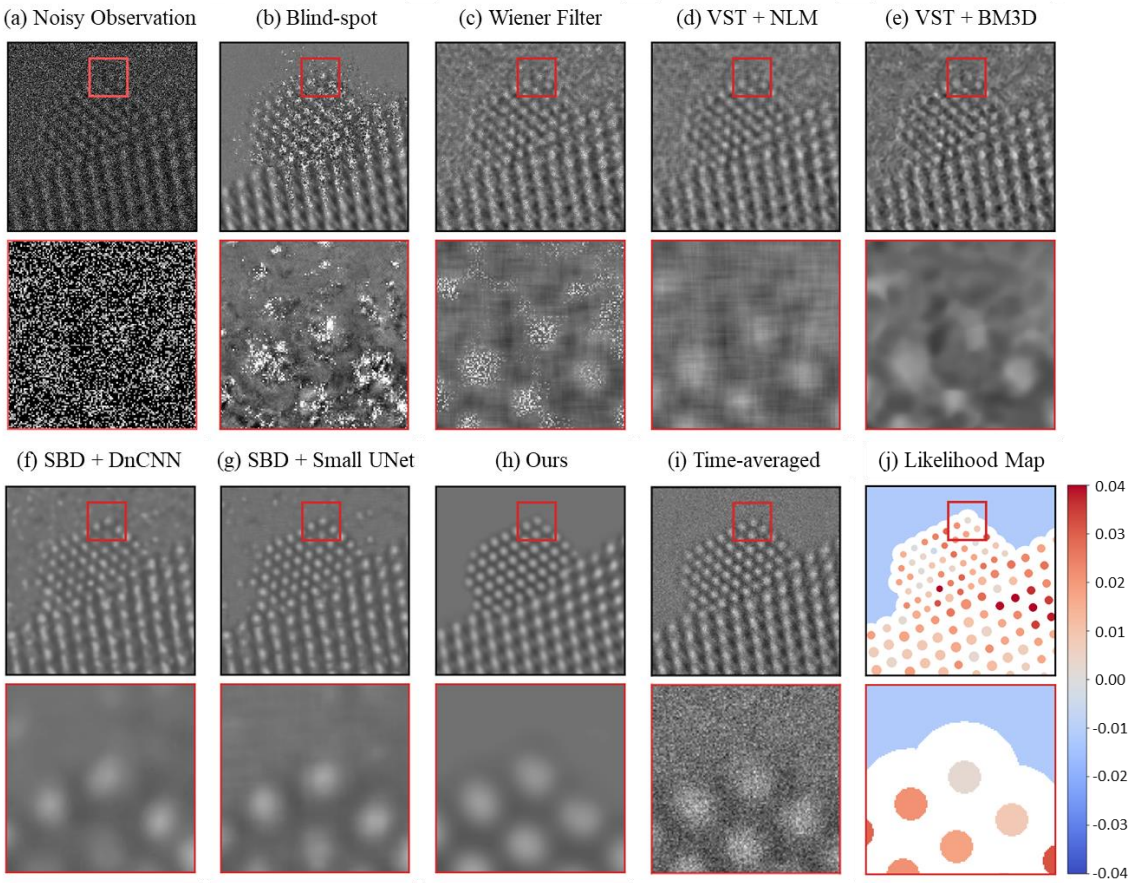

Figure E.15. Evaluating the performance of the trained network on experimental 25 ms exposure *in situ* TEM images, in comparison to current state-of-the-art methodologies. The experimental image used in this comparison is different with respect to that presented in Figure 6.6 of the main text. A raw 25 ms frame is shown in (a) along with a zoom-in image from the region marked by the red box. Denoised estimates of the same raw frame from the baseline methods are presented in (b) through (g), while (h) displays the denoised estimate from the proposed network. Part (i) presents a time-average over 40 raw frames, or 1.0 sec total, to serve as a relatively high SNR reference image. Finally, part (j) shows the likelihood map of the proposed network's output to quantify the agreement with the noisy observation.

APPENDIX F

COPYRIGHT AGREEMENTS

Copyright permissions for Figure 1.4a:

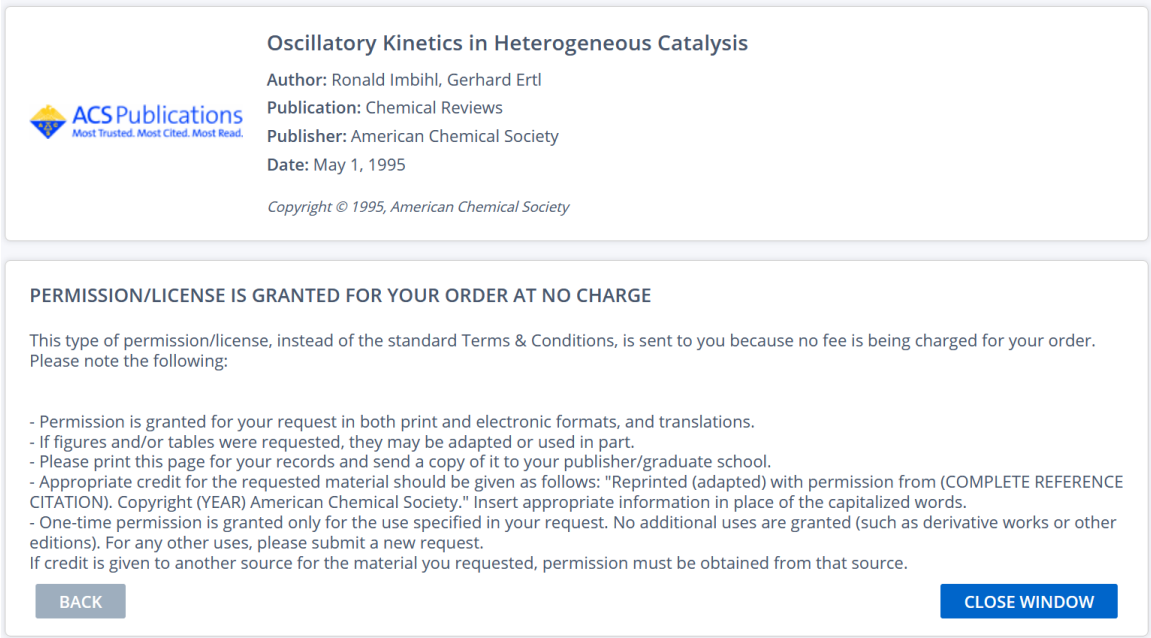

Oscillatory Kinetics in Heterogeneous Catalysis

Author: Ronald Imbihl, Gerhard Ertl
Publication: Chemical Reviews
Publisher: American Chemical Society
Date: May 1, 1995

PERMISSION/LICENSE IS GRANTED FOR YOUR ORDER AT NO CHARGE

This type of permission/license, instead of the standard Terms & Conditions, is sent to you because no fee is being charged for your order. Please note the following:

- Permission is granted for your request in both print and electronic formats, and translations.
- If figures and/or tables were requested, they may be adapted or used in part.
- Please print this page for your records and send a copy of it to your publisher/graduate school.
- Appropriate credit for the requested material should be given as follows: "Reprinted (adapted) with permission from (COMPLETE REFERENCE CITATION). Copyright (YEAR) American Chemical Society." Insert appropriate information in place of the capitalized words.
- One-time permission is granted only for the use specified in your request. No additional uses are granted (such as derivative works or other editions). For any other uses, please submit a new request.

If credit is given to another source for the material you requested, permission must be obtained from that source.

BACK CLOSE WINDOW

Copyright permissions for Figure 1.4b:

JOHN WILEY AND SONS LICENSE
TERMS AND CONDITIONS

Jun 16, 2021

This Agreement between Mr. Joshua Vincent ("You") and John Wiley and Sons ("John Wiley and Sons") consists of your license details and the terms and conditions provided by John Wiley and Sons and Copyright Clearance Center.

License Number	5091120084251
License date	Jun 16, 2021
Licensed Content Publisher	John Wiley and Sons
Licensed Content Publication	The Chemical Record
Licensed Content Title	Heterogeneous catalysis on the atomic scale
Licensed Content Author	Gerhard Ertl
Licensed Content Date	Jan 30, 2001
Licensed Content Volume	1
Licensed Content Issue	1
Licensed Content Pages	13
Type of use	Dissertation/Thesis

Requestor type	University/Academic
Format	Print and electronic
Portion	Figure/table
Number of figures/tables	1
Will you be translating?	No
Title	Atomic-resolution in situ and operando visualization of oxygen transfer reactions over CeO2-supported Pt catalysts
Institution name	Arizona State University
Expected presentation date	Aug 2021
Portions	Figure 4
Requestor Location	Mr. Joshua Vincent 522 W 14th st TEMPE, AZ 85281 United States Attn: Mr. Joshua Vincent
Publisher Tax ID	EU826007151
Total	0.00 USD

Copyright permissions for Figure 2.4:

SPRINGER NATURE LICENSE
TERMS AND CONDITIONS

Jun 16, 2021

This Agreement between Mr. Joshua Vincent ("You") and Springer Nature ("Springer Nature") consists of your license details and the terms and conditions provided by Springer Nature and Copyright Clearance Center.

License Number	5091130935680
License date	Jun 16, 2021
Licensed Content Publisher	Springer Nature
Licensed Content Publication	Springer eBook
Licensed Content Title	Physics of Electron Scattering
Licensed Content Author	R.F. Egerton
Licensed Content Date	Jan 1, 2011
Type of Use	Thesis/Dissertation
Requestor type	academic/university or research institute
Format	print and electronic
Portion	figures/tables/illustrations
Number of figures/tables /illustrations	1

Will you be translating?	no
Circulation/distribution	1 - 29
Author of this Springer Nature content	no
Title	Atomic-resolution in situ and operando visualization of oxygen transfer reactions over CeO2-supported Pt catalysts
Institution name	Arizona State University
Expected presentation date	Aug 2021
Portions	2
Requestor Location	Mr. Joshua Vincent 522 W 14th st TEMPE, AZ 85281 United States Attn: Mr. Joshua Vincent
Total	0.00 USD

Copyright permissions for Figure 2.5b:

ELSEVIER LICENSE
TERMS AND CONDITIONS

Jun 16, 2021

This Agreement between Mr. Joshua Vincent ("You") and Elsevier ("Elsevier") consists of your license details and the terms and conditions provided by Elsevier and Copyright Clearance Center.

License Number	5091140055267
License date	Jun 16, 2021
Licensed Content Publisher	Elsevier
Licensed Content Publication	Ultramicroscopy
Licensed Content Title	Current status and future directions for in situ transmission electron microscopy
Licensed Content Author	Mitra L. Taheri,Eric A. Stach,Ilke Arslan,P.A. Crozier,Bernd C. Kabius,Thomas LaGrange,Andrew M. Minor,Seiji Takeda,Mihaela Tanase,Jakob B. Wagner,Renu Sharma
Licensed Content Date	Nov 1, 2016
Licensed Content Volume	170
Licensed Content Issue	n/a
Licensed Content Pages	10
Start Page	86

End Page	95
Type of Use	reuse in a thesis/dissertation
Portion	figures/tables/illustrations
Number of figures/tables /illustrations	1
Format	both print and electronic
Are you the author of this Elsevier article?	No
Will you be translating?	No
Title	Atomic-resolution in situ and operando visualization of oxygen transfer reactions over CeO2-supported Pt catalysts
Institution name	Arizona State University
Expected presentation date	Aug 2021
Portions	figure 5
Requestor Location	Mr. Joshua Vincent 522 W 14th st TEMPE, AZ 85281 United States Attn: Mr. Joshua Vincent
Publisher Tax ID	98-0397604
Total	0.00 USD

Copyright permissions for Figures 2.6, 2.9, and 2.10a:

SPRINGER NATURE LICENSE
TERMS AND CONDITIONS

Jun 17, 2021

This Agreement between Mr. Joshua Vincent ("You") and Springer Nature ("Springer Nature") consists of your license details and the terms and conditions provided by Springer Nature and Copyright Clearance Center.

License Number	5091141063922
License date	Jun 17, 2021
Licensed Content Publisher	Springer Nature
Licensed Content Publication	Springer eBook
Licensed Content Title	The Transmission Electron Microscope
Licensed Content Author	David B. Williams, C. Barry Carter
Licensed Content Date	Jan 1, 2009
Type of Use	Thesis/Dissertation
Requestor type	academic/university or research institute
Format	print and electronic
Portion	figures/tables/illustrations
Number of figures/tables /illustrations	4

Will you be translating?	no
Circulation/distribution	1 - 29
Author of this Springer Nature content	no
Title	Atomic-resolution in situ and operando visualization of oxygen transfer reactions over CeO2-supported Pt catalysts
Institution name	Arizona State University
Expected presentation date	Aug 2021
Portions	figures related to aberration correction and eels
Requestor Location	Mr. Joshua Vincent 522 W 14th st TEMPE, AZ 85281 United States Attn: Mr. Joshua Vincent
Total	0.00 USD

Copyright permissions for Figure 2.7:

ELSEVIER LICENSE
TERMS AND CONDITIONS

Jun 17, 2021

This Agreement between Mr. Joshua Vincent ("You") and Elsevier ("Elsevier") consists of your license details and the terms and conditions provided by Elsevier and Copyright Clearance Center.

License Number	5091150034492
License date	Jun 17, 2021
Licensed Content Publisher	Elsevier
Licensed Content Publication	Ultramicroscopy
Licensed Content Title	On the benefit of the negative-spherical-aberration imaging technique for quantitative HRTEM
Licensed Content Author	C.L. Jia,L. Houben,A. Thust,J. Barthel
Licensed Content Date	Apr 1, 2010
Licensed Content Volume	110
Licensed Content Issue	5
Licensed Content Pages	6
Start Page	500
End Page	505

Type of Use	reuse in a thesis/dissertation
Portion	figures/tables/illustrations
Number of figures/tables /illustrations	1
Format	both print and electronic
Are you the author of this Elsevier article?	No
Will you be translating?	No
Title	Atomic-resolution in situ and operando visualization of oxygen transfer reactions over CeO2-supported Pt catalysts
Institution name	Arizona State University
Expected presentation date	Aug 2021
Portions	figure of simulations on SrTiO3
Requestor Location	Mr. Joshua Vincent 522 W 14th st TEMPE, AZ 85281 United States Attn: Mr. Joshua Vincent
Publisher Tax ID	98-0397604
Total	0.00 USD

Copyright permissions for part of Figure 2.11:

ELSEVIER LICENSE
TERMS AND CONDITIONS

Jun 17, 2021

This Agreement between Mr. Joshua Vincent ("You") and Elsevier ("Elsevier") consists of your license details and the terms and conditions provided by Elsevier and Copyright Clearance Center.

License Number	5091150565886
License date	Jun 17, 2021
Licensed Content Publisher	Elsevier
Licensed Content Publication	Ultramicroscopy
Licensed Content Title	Novel sample preparation for operando TEM of catalysts
Licensed Content Author	Benjamin K. Miller,Trevor M. Barker,Peter A. Crozier
Licensed Content Date	Sep 1, 2015
Licensed Content Volume	156
Licensed Content Issue	n/a
Licensed Content Pages	5
Start Page	18
End Page	22

Type of Use	reuse in a thesis/dissertation
Portion	figures/tables/illustrations
Number of figures/tables /illustrations	1
Format	both print and electronic
Are you the author of this Elsevier article?	No
Will you be translating?	No
Title	Atomic-resolution in situ and operando visualization of oxygen transfer reactions over CeO2-supported Pt catalysts
Institution name	Arizona State University
Expected presentation date	Aug 2021
Portions	figure on reactor
Requestor Location	Mr. Joshua Vincent 522 W 14th st TEMPE, AZ 85281 United States Attn: Mr. Joshua Vincent
Publisher Tax ID	98-0397604
Total	0.00 USD

Copyright permissions for Figure 2.13:

SPRINGER NATURE LICENSE
TERMS AND CONDITIONS

Jun 17, 2021

This Agreement between Mr. Joshua Vincent ("You") and Springer Nature ("Springer Nature") consists of your license details and the terms and conditions provided by Springer Nature and Copyright Clearance Center.

License Number	5091151026250
License date	Jun 17, 2021
Licensed Content Publisher	Springer Nature
Licensed Content Publication	Springer eBook
Licensed Content Title	Multislice Applications and Examples
Licensed Content Author	Earl J. Kirkland
Licensed Content Date	Jan 1, 2010
Type of Use	Thesis/Dissertation
Requestor type	academic/university or research institute
Format	print and electronic
Portion	figures/tables/illustrations
Number of figures/tables /illustrations	1

Will you be translating?	no
Circulation/distribution	1 - 29
Author of this Springer Nature content	no
Title	Atomic-resolution in situ and operando visualization of oxygen transfer reactions over CeO2-supported Pt catalysts
Institution name	Arizona State University
Expected presentation date	Aug 2021
Portions	figure on multislice method
Requestor Location	Mr. Joshua Vincent 522 W 14th st TEMPE, AZ 85281 United States Attn: Mr. Joshua Vincent
Total	0.00 USD